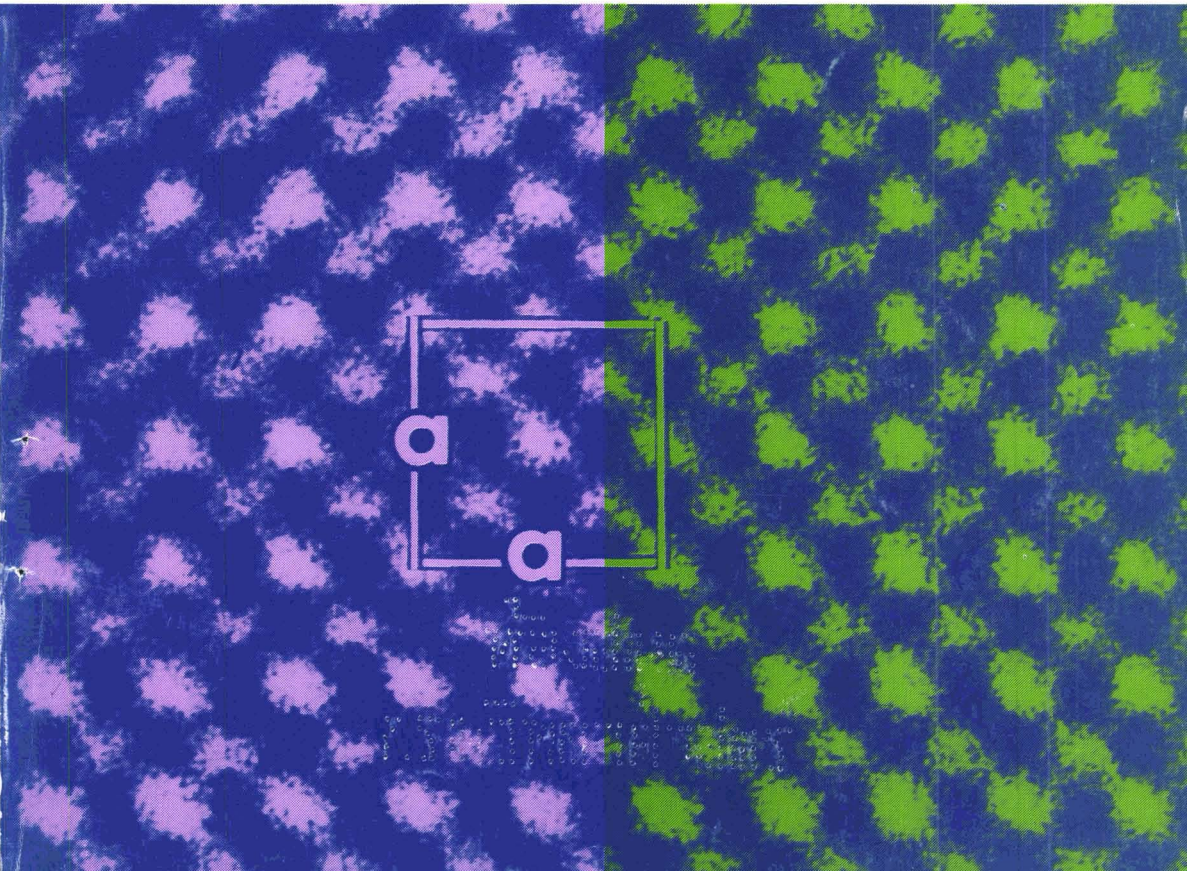


# Journal of the CERAMIC SOCIETY of Japan, International Edition

## Vol.99 Aug.1991

■ 18 Papers from Nippon Seramikkusu Kyokai Gakujutsu Ronbunshi, Vol.99 No.8 1991

NIPPON SERAMIKKUSU KYOKAI GAKUJUTSU RONBUNSHI Vol.99 1991



**Editorial Board**

- Dr. Teruo Sakaino  
Prof. Emeritus, Tokyo Institute of Technology
- Dr. Nobuyasu Mizutani  
Prof., Tokyo Institute of Technology
- Dr. Yusuke Moriyooshi  
Director, Nat. Inst. for Res. in Inorganic Materials
- Dr. Kitao Takahara  
Prof., Nagoya University
- Yukio Endo  
Chairman  
Koyo-sha Co., Ltd.
- Dr. Takashi Hanazawa  
Executive Director,  
The Ceramic Society of Japan
- Seiji Iwata  
Executive Director,  
Japan Fine Ceramics Association
- Keiji Hayashi  
Managing Editor

**Editors**

- |                   |                                 |
|-------------------|---------------------------------|
| Managing Editor   | Keiji Hayashi                   |
| Associate Editors | Kristine Roseberry              |
| Art Director      | Prof. Yuji Isa                  |
| Assistant Artists | Toshimitsu Irie<br>Misao Tomita |
| Assistant         | Kiyoe Kojima                    |
| Circulation       | Youko Matsumoto                 |
| Publisher         | Keiji Hayashi                   |

Published Monthly by  
**FUJI TECHNOLOGY PRESS LTD.**  
7F Daini Bunsei Bldg.  
11-7, Toranomon 1-chome  
Minato-ku, Tokyo 105, Japan  
Tel: 81-3-3508-0051  
Fax: 81-3-3592-0648

One year subscription  
Air Mail ¥200,000

Copyright © 1991 by  
The Ceramic Society of Japan and Fuji  
Technology Press Ltd. All rights  
reserved.

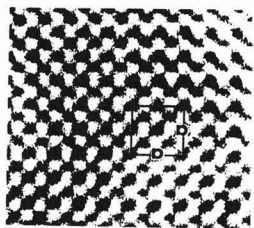
No part of this publication may be reproduced, stored in a retrieval system, or transmitted, in any form or by any means, electronic, mechanical, photo copying, recording, or otherwise, without the prior written permission of the publishers. The papers, excluding those on information and communications, reviews, etc., were originally received by Nippon Seramikkusu Kyokai Gakujutsu Ronbunshi, and translated for this journal. The responsibility for the translation lies with the publisher.

**Papers:**

- **Internal Friction and Anelastic Relaxation of ZrO<sub>2</sub> Polycrystals Containing 2 mol% Y<sub>2</sub>O<sub>3</sub>, 8 mol% Y<sub>2</sub>O<sub>3</sub> and 12 mol% CeO<sub>2</sub>** .628  
Masakuni Ozawa, Tatsuya Hatanaka and Hideo Hasegawa
- **Microstructure and Microwave Characteristics of Ba((Mg, Co)<sub>1/3</sub>Nb<sub>2/3</sub>)O<sub>3</sub>-Based Dielectrics** .633  
Shigekazu Sumita, Makoto Kobayashi, Kazuaki Suzuki, Keizo Kawamura and Taro Miura
- **Preparation of Mullite Fiber by Sol-Gel Method** .638  
Toshiyuki Nishio and Yoshinori Fujiki
- **Effect of Process-Related Oxidation on Microstructure and Mechanical Properties of β'-α' Sialon Ceramics** .644  
Kazuya Yabuta, Hiroaki Nishio and Keizo Uematsu
- **Internal Friction in MgAl<sub>2</sub>O<sub>4</sub> Spinel Doped with Gallium Oxide or Alumina** .649  
Yasuhiro Yoshimura, Takeshi Nakamura, Ken'ichi Matsushita, Taira Okamoto and Susumu Goda
- **Morphology of Diamond in Radio-Frequency Thermal Plasma CVD** .653  
Toyohiko Kobayashi
- **Sintering and Properties of CaTi<sub>4</sub>(PO<sub>4</sub>)<sub>6</sub> Prepared by Sol-Gel Process** .660  
Yutaka Miyamoto, Akira Kishioka, Kiyoshi Itatani and Makio Kinoshita
- **Densification of Plasma-sprayed Ceramic Coatings by HIP Treatment and their Cracking Behavior** .665  
Yutaka Ishiwata, Yoshiyasu Ito and Hideo Kashiwaya
- **Preparation and Thermal Expansion Behavior of Pollucite Powders by Sol-Gel Processing** .670  
Hidehiko Kobayashi, Toshihiro Terasaki, Toshiyuki Mori, Chihiro Ishihara, Shoshichi Saito, Hiroshi Yamamura and Takashi Mitamura
- **Sintering Property of Green Compacts of Si and TiC Mixed Powders in Nitrogen** .676  
Yoshiyuki Yasutomi, Masahisa Sobue, S. Shinozaki and J. Hangas
- **Preparation of High Tc Superconductors by a Plasma-Arc Melting and Rapid Quenching Method** .683  
Maruo Kamino, Kazuhiko Takahashi, Yorinobu Yoshisato and Shoichi Nakano
- **Synthesis of SiC from Fine SiO<sub>2</sub>-C Mixed Powders** .688  
Norihiro Murakawa and Mutsuo Nakajima

**Notes:**

- **Preparation of SiCl<sub>4</sub> from Rice Hull Ashes (Part 3) — FT-IR-PAS Analysis of Chlorination Mechanism of Rice Hull Ashes Containing Alkaline and Alakline Earth Metal Salts —** .693  
Takeshi Okutani, Yoshinori Nakata and Masao Hino
- **Properties of Porcelain Bodies Containing Zirconia** .696  
Kouhei Ohta, Tosio Torikai, Takanori Watari and Ohsaku Matsuda
- **Mechanical Properties of High Thermal Conductive SiC Ceramics** .699  
Yukio Takeda and Kunihiro Maeda



**Cover:**

This picture shows a high-resolution structure image of zirconia ( $ZrO_2$ ) projected along the a-axis of a cubic lattice ( $a=5.1$ ). As indicated by arrowheads in the micrograph, both zirconium (Zr) and oxygen (O) atom positions appear as strong and weak dark dots, respectively. This is the first electron microscope data in which individual oxygen positions in inorganic compounds can be directly observed as weak dark dots.

The microgram was obtained by the ultra-high-resolution, high-voltage electron microscope (Model: H-1500) developed in 1990 as NIRIM's second high-voltage electron microscope. The device has the world's highest resolution of  $1.0\text{\AA}$ , which was achieved by employing operating and applicable voltages of 1300kV and 1500kV, respectively. A very low spherical aberration coefficient for the objective ( $C_s=1.85\text{mm}$  at 1300kV) was realized by computer-aided design of the electron-magnetic lens system. This new apparatus permits the imaging of not only metal atoms but also light atoms (such as oxygen) in many inorganic materials by means of high-resolution electron microscopy.

- **Solubility of Lanthanum Oxide in Barium Titanate** . . . . .701  
Akira Hasegawa, Satoru Fujitsu, Kunihito Koumoto and Hiroaki Yanagida
- **Emission Spectra and Morphology of Carbon Films by ECR Plasma CVD** . . . . .703  
Kazunori Maruyama, Kiichiro Kamata, Tohru Inoue and Isao Tanabe
- **Preparation and Some Properties of Porous Mullite Ceramics Using Needle-like Crystals** . . . . .706  
Hiroaki Katsuki, Akihiko Kawahara, Hiromichi Ichinose, Sachiko Furuta and Ohsaku Matsuda

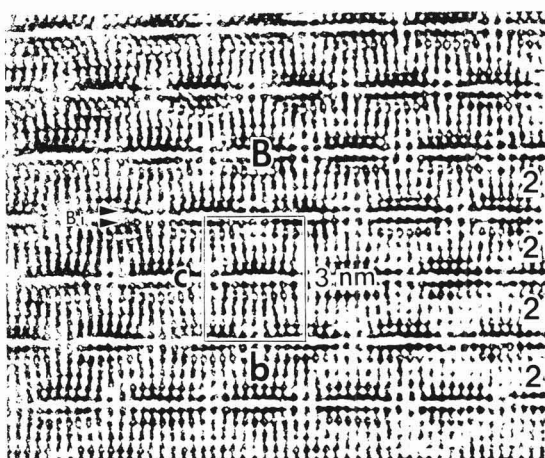
**Information & Communications**

- **News** . . . . .C-70
- **Abstracts of Articles on Ceramics from Selected Journal of the Academic Societies** . . . . .C-73

---

## Papers, Letters and Notes

---



High resolution electron microscope photograph of the modulation doped structure of  $\text{Bi}_2\text{Sr}_2\text{CaCu}_2\text{O}_y$  ( $T_c=80\text{K}$ ) in the  $[100]$  direction. Figures at right side indicate number of copper layers, symbol B indicates bismuth rich region.

# Internal Friction and Anelastic Relaxation of ZrO<sub>2</sub> Polycrystals Containing 2 mol% Y<sub>2</sub>O<sub>3</sub>, 8 mol% Y<sub>2</sub>O<sub>3</sub> and 12 mol% CeO<sub>2</sub>

Masakuni Ozawa, Tatsuya Hatanaka and Hideo Hasegawa

Toyota Central Research and Development Laboratories, Inc.  
Nagakutecho, Aichi-gun, 480-11 Japan

The comparative study of the internal friction of ZrO<sub>2</sub> polycrystals doped containing 2 mol% Y<sub>2</sub>O<sub>3</sub>, 8 mol% Y<sub>2</sub>O<sub>3</sub> and 12 mol% CeO<sub>2</sub> (2Y-TZP, 8Y-FSZ and 12Ce-TZP) was performed at high frequencies around 100kHz. The data of 2Y-TZP around 100kHz revealed an anelastic relaxation peak with the activation enthalpy  $H=82.5\pm 1.4$  kJ/mol, the relaxation strength  $\Delta=1.34\pm 0.08\times 10^{-2}$ , and  $\tau_0=5.4\pm 1.1\times 10^{-14}$  sec. The relaxation is considered to be the same as the dielectric one with  $H=79.0\pm 3.8$  kJ/mol and  $\tau_0=5.9\pm 3.1\times 10^{-13}$  sec. The internal friction for 2Y-TZP and 8Y-FSZ indicated the existence of the same relaxation process and consequently the possibility of similar local cation-anion (or vacancy) interaction in Y<sub>2</sub>O<sub>3</sub> doped ZrO<sub>2</sub> regardless of the symmetry (tetragonal and cubic). The internal friction was small for the 12Ce-TZP, but was large after the reduction and increased at elevated temperature, accompanied by the trace peak. The results indicate directly significant contribution of the oxygen vacancy to the generation of the internal friction of ZrO<sub>2</sub>.

[Received January 11, 1991; Accepted April 19, 1991]

**Key-words:** Internal friction, ZrO<sub>2</sub>, Elastic property, Debye peak, Anelastic relaxation, Dielectric relaxation, Piezoelectric resonance method

## 1. Introduction

The measurement of anelastic and dielectric loss are useful for the investigation of point defects or complexes with anelastic and dielectric dipole in materials. The application of stress or electric field to the oxide with oxygen vacancies can affect the energies of the otherwise equivalent sites for the diffusion defects, ions and complexes, resulting in the relaxations.<sup>1)</sup>

Zirconia (ZrO<sub>2</sub>) with Y<sub>2</sub>O<sub>3</sub> addition has been widely known to be good solid electrolytes at elevated temperature due to the oxygen vacancies introduced as compensation for the dopant cations.<sup>2)</sup> Recently, tetragonal zirconia polycrystals (TZP) with 2 to 3mol% of Y<sub>2</sub>O<sub>3</sub> and 12mol% CeO<sub>2</sub> were developed for ceramics materials with high strength and toughness.<sup>3)</sup> Toughness is resulted by stress induced martensitic transformation of tetragonal (t) to monoclinic (m) symmetry. However, it has been reported that thermal aging of TZP with Y<sub>2</sub>O<sub>3</sub> at 200 to 300°C leads to the degradation of the strength and toughness in the materials due to the progress of t-m transformation.<sup>4)</sup>

Several investigators<sup>5-9)</sup> have revealed the internal friction

peak in the TZP at moderate temperature range, and suggested that it was caused by the oxygen diffusion or rearrangement which are related with the transformation.

This work describes the comparative study anelastic and dielectric relaxation of ZrO<sub>2</sub> polycrystals doped with 2mol% Y<sub>2</sub>O<sub>3</sub>, 8mol% Y<sub>2</sub>O<sub>3</sub> and 12 mol% CeO<sub>2</sub> (2Y-TZP, 8Y-FSZ and 12Ce-TZP) which were measured at high frequencies around 100kHz, and discusses the contribution of oxygen defects to the internal friction and the relaxation process in the ZrO<sub>2</sub>.

## 2. Experimental and Analysis Procedure

### 2.1. Samples

The experiments were carried out on sintered polycrystalline bars of ZrO<sub>2</sub> doped with 2mol% Y<sub>2</sub>O<sub>3</sub> (2Y-TZP), 8mol% Y<sub>2</sub>O<sub>3</sub> (8Y-FSZ) and 12mol% CeO<sub>2</sub> (12Ce-TZP) which are 3×4mm in cross section and 25 to 32mm in length. The samples used in the present study are listed in Table 1. The 2Y-TZP sample contains 3.53wt.% Y<sub>2</sub>O<sub>3</sub> and trace impurities such as Al, Si and Fe. The 2Y-TZP consisted of tetragonal and trace monoclinic phases. The phase fraction did not change in the heat treatment of the measurement. The 8Y-FSZ contains 13.50wt.% Y<sub>2</sub>O<sub>3</sub> and trace impurities and consists of only cubic phase. The 12Ce-TZP sample consists of tetragonal phase with trace amount of monoclinic phase and contains 16.69wt.% CeO<sub>2</sub> and trace impurities. Furthermore, the 12Ce-TZP sample was reduced by heating at 1000°C in H<sub>2</sub> for 8hr to introduce oxygen vacancy in the crystal lattice.

### 2.2. Elastic Measurements

For elastic measurements, the resonance piezoelectric method was used on composite-bars of samples and vibrators.<sup>9,12)</sup> The piezoelectric vibrators used were -18.5°X-cut quartz for longitudinal vibration mode. Quartz vibrator bars were 3×4mm in cross section and 20 to 30mm in length for the excitation with the different frequencies of 90 to 140kHz. The composite bar of a vibrator and a sample was formed by using the inorganic adhesive.<sup>12)</sup>

The internal friction  $Q^{-1}$  of the composite bar is calculated by the following equations.

$$Q^{-1} = (1 + m_s/m_q) \{ 2(f_n - f_m)/f_R \} / (Y_m Y_n)^{1/2} / (Y_n + Y_m) \dots \dots \dots (1)$$

$$m_s f_s \tan(\pi f_R/f_s) + m_q f_q \tan(\pi f_R/f_q) = 0 \dots \dots \dots (2)$$

where  $m_s$  and  $m_q$  are the masses of the sample and of the quartz vibrator,  $Y_m$  and  $Y_n$  the admittances and  $f_m$  and  $f_n$  the frequencies corresponding to the maximum and minimum,

$f_R$  the resonant frequency of the composite bar, and  $f_s$  and  $f_q$  the resonant frequency of a sample and a quartz respectively.  $Q^{-1}$  was calibrated by the internal friction of quartz  $Q_q^{-1}$ , which was below  $10^{-5}$  at the temperature in this experiment. The difference of the resonant frequencies between samples and vibrators influences the measured data of the internal friction  $Q^{-1}$  of the samples.<sup>11)</sup> The data were calibrated by the experimental equation,

$$\ln(Q^{-1}) = \ln(Q_0^{-1}) - \alpha(f_s/f_{s0} - 1)^2 \dots \dots \dots (3)$$

where  $Q^{-1}$  and  $Q_0^{-1}$  are the observed and true value of internal friction,  $f_s$  and  $f_{s0}$  the observed and true value of the resonant frequency, and  $\alpha$  the constant (-7.5) which was determined experimentally. The temperature dependence of the resonant frequency of a quartz was calibrated by the equation with its temperature coefficients. Young's modulus was obtained from  $E = \rho(2f_l l)^2$ , where  $\rho$  is the density and  $l$  the length of samples. The temperature change of  $\rho$  and  $l$  was calibrated by the thermal expansion data of the samples.

**2.3. Dielectric Measurements**

Dielectric loss was measured with LCR meter (HP-

**Table 1.** ZrO<sub>2</sub> samples used in the present study.

Materials	Dopant content (wt%)	Impurities (wt%)	Phase	Lattice constant (nm)	Density (10 <sup>3</sup> kg/m <sup>3</sup> )	Young's modulus (GPa)
2Y-TZP	3.53 Y <sub>2</sub> O <sub>3</sub>	<0.085 (Al, Si, Fe)	t m(tr)	a=0.5098 c=0.5186	6.01	208.3
8Y-FSZ	13.5 Y <sub>2</sub> O <sub>3</sub>	<0.015 (Al, Si, Fe)	c	a=0.5139	5.84	217.5
12Ce-TZP	16.69 CeO <sub>2</sub>	<0.013 (Al, Si, Fe)	t m(tr)	a=0.5127 c=0.5222	6.15	193.2
12Ce-TZP reduced	same above	same above	t	a=0.5154 c=0.5217	6.01	191.0

t:tetragonal, m:monoclinic, c:cubic, tr:trace  
All samples were purchased from Tosoh Co. Ltd.

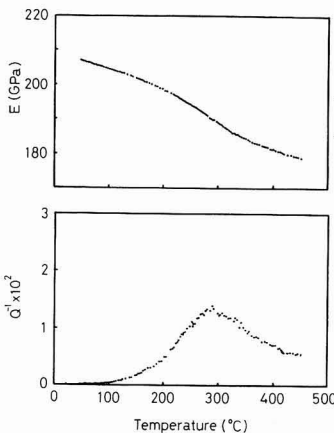


**Fig. 1**

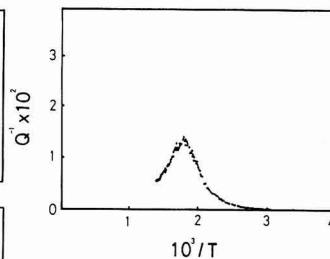


**Fig. 2**

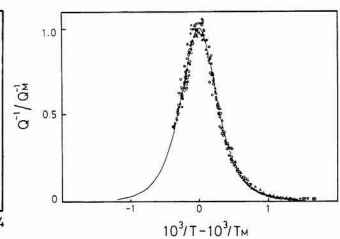


**Fig. 3**

4275A) at various frequencies  $f$  of 10k to 10MHz at elevated temperature. The samples used were thin plates (3×4×1.1mm), and the silver electrodes (2.5×3.5mm) were painted on two faces. The dielectric loss angle  $\delta$  was obtained from,

$$\tan\delta = 1/(\omega RC) \dots \dots \dots (4)$$

where  $\omega=2\pi f$ ,  $R$  the resistance and  $C$  the capacitance.

**2.4. Analysis of Debye Peak**

Anelastic or dielectric relaxation in solid gives rise to a relaxation peak which obeys the Debye equation (1),

$$\tan\delta = \Delta\omega\tau/(1 + \omega^2\tau^2) \dots \dots \dots (5)$$

where  $\delta$  is the angle for either the anelastic ( $Q^{-1} \approx \tan\delta$ ) or dielectric causes,  $\Delta$  the relaxation strength,  $\omega$  the angular frequency of the applied stress or electric field, and  $\tau$  the relaxation time. In the thermally-activated relaxation, the relaxation time  $\tau$  obeys the Arrhenius equation,

$$\tau^{-1} = \tau_0^{-1} \cdot \exp(-H/RT) \dots \dots \dots (6)$$

where  $H$  is the activation enthalpy for relaxation,  $\tau_0$  a pre-exponential factor,  $R$  the gas constant and  $RT$  the temperature. A plot of  $Q^{-1}$  versus  $1/T$  at a fixed frequency gives rise to a symmetric Debye peak with the maximum for  $\omega\tau=1$ . The peak width  $\delta(1/T)$  at half-maximum is represented by the equation for a single relaxation,

$$\delta(1/T) = 2.635P/H\delta(1/T)=2.635R/H \dots \dots (7)$$

**3. Results and Discussion**

**3.1. 2Y-TZP**

Figure 1 shows the temperature dependence of Young's modulus  $E$  and internal friction  $Q^{-1}$  in 2Y-TZP measured by a 90KHz vibrator. The data revealed the internal friction peak and the elastic anomaly around 300°C. Figure 2 illustrates the plot of the  $Q^{-1}$  data as a function of reciprocal temperature, showing a symmetric peak similar to Debye-type relaxation. The experimental data on internal friction were analyzed by a parameter fitting, by using the least squares method, after the equation (4) and (5). Table 2 summarizes the results of peak temperature, relaxation

**Fig. 1.** Temperature dependence of Young's modulus  $E$  and the internal friction  $Q^{-1}$  of 2Y-TZP measured by a 90 kHz quartz.  
**Fig. 2.** Reciprocal temperature dependence of the internal friction  $Q^{-1}$  of 2Y-TZP. The data are the same as that in Fig.1.  
**Fig. 3.** Normalized relation of  $Q^{-1}$  vs.  $T^{-1}$  with data measured at three different frequencies with 90 kHz (O), 110 kHz (●) and 130 kHz (Δ).  $Q_M^{-1}$  and  $T_M$  stand for the internal friction and temperature at maximum.

strength ( $\Delta$ ) and activation enthalpy ( $H$ ) obtained from fitting curves with experimental data of the Debye peak for 2Y-TZP, measured by the three quartz vibrators with different frequencies. **Figure 3** shows a theoretical curve and experimental data normalized on the peak height and temperature position. The data with different frequencies have good consistence on peak shape each other. The averaged  $H$  was obtained to be  $36.1 \pm 1.6$  kJ/mol from half-width data and the relaxation strength  $\Delta$  was  $1.34 \pm 0.08 \times 10^{-2}$ .

Matsushita et al.<sup>5)</sup> carried out the elastic measurement on 2Y and 3Y-TZP by the flexural vibration method. They showed Arrhenius plots of frequencies applied (1k to 5 KHz) versus peak temperatures, and obtained activation enthalpy  $H=69.3 \pm 2.0$  kJ/mol for 2Y-TZP and  $H=81.2 \pm 5.3$  kJ/mol for 3Y-TZP. Weller and Schubert<sup>6)</sup> reported  $H=90 \pm 3$  kJ/mol for 3Y-TZP, derived from an Arrhenius plot using two data measured by 2.7 Hz torsion and 3.06 kHz flexural vibrations. **Figure 4** shows the relation of applied angular frequency  $\omega$  ( $2\pi f$ ) vs. reciprocal peak temperature  $T^{-1}$  for 2Y-TZP, in which the present data around 100kHz and the data by Matsushita et al. were used. The data gave a straight line in the wide range of the applied frequency of 1k to 100kHz. The relation,  $\ln\omega = -H/RT - \ln(\tau_0)$  where  $H=82.5 \pm 1.4$  kJ/mol and  $\tau_0=5.4 \pm 1.1 \times 10^{-14}$  sec, was found to be valid for the anelastic relaxation of 2Y-TZP. The  $H$  value derived from half-width of the peak in the present work was smaller than that obtained by the Arrhenius plot. The peak observed in Fig.3 was 2.3 times broader than a single Debye peak with  $H=82.5$  kJ/mol. It

indicates the association of complex relaxation processes which can not be described by a single Debye peak.

**Figure 5** shows the temperature dependencies of the dielectric loss angle for various frequencies of 10k to 10MHz. The data revealed the peak of the dielectric loss. Its peak temperature depended on the frequency applied for the measurement. An Arrhenius plot of applied angular frequencies  $\omega$  vs. reciprocal peak temperature  $T^{-1}$  is illustrated in **Fig.6**. These data were represented by a straight line indicating thermally-activated relaxation to give  $H=79.0 \pm 3.8$  kJ/mol and  $\tau_0=5.9 \pm 3.1 \times 10^{-13}$  sec.

The activation enthalpy derived from an Arrhenius plot is the same for anelastic and dielectric relaxation within experimental error. However,  $\tau_0$  is different by a factor of 10. The  $H$  values correspond to that of oxygen ionic conduction of  $ZrO_2$ . The results suggest that the same mechanism is involved in anelastic and dielectric and dielectric relaxation, such as the movement and rearrangement of oxygen (or defect).

### 3.2. 8Y-FSZ

**Figure 7** shows the data of Young's modulus  $E$  and internal friction  $Q^{-1}$  on 8Y-FSZ measured by a 90kHz quartz. The internal friction data revealed a peak around 300°C, with the background increased with increasing temperature. They are also observed in **Fig.8**, which shows a plot of  $Q^{-1}$  vs.  $T^{-1}$ . The peak temperature increased with increasing frequency applied for the measurement. The peak strength after the subtraction of background was ca.  $1.4 \times 10^{-2}$ , and was almost the same to that for 2Y-TZP. The data suggest that the peak in 8Y-FSZ is due to the relaxation process which is activated thermally as in 2Y-TZP. The results of internal friction for 2Y-TZP and 8Y-FSZ suggest the local interaction between cation and anion (or vacancy) which induces the an elastic relaxation for  $ZrO_2$  with  $Y_2O_3$  regardless of the symmetry with long periodicity.

The local structure in cubic  $ZrO_2$  stabilized with  $Y_2O_3$  has been investigated using EXAFS technique by Catlow et al.<sup>13)</sup> They suggest the average  $Zr^{4+}$  environment being more disordered than that of  $Y^{3+}$ , i.e. the  $Zr^{4+}$  coordinated with seven oxygen ions. At elevated temperature, the high oxygen mobility results in statistical distribution of oxygen vacancies. Their result indicates that the oxygen vacancy is

**Table 2.** The data for the internal friction peaks of 2Y-TZP, analyzed by the Debye equation.

Applied frequency at peak (kHz)	Peak temperature (°C)	Half-width $\times 10^{-3}$ ( $K^{-1}$ )	Relaxation strength $\times 10^{-3}$	Activation enthalpy (kJ/mol)
85.53	292±1	0.59±0.01	12.7±0.1	37.1±0.6
112.58	311±2	0.62±0.01	13.2±0.2	35.3±0.6
120.80	312±2	0.61±0.02	14.1±0.2	35.9±1.2

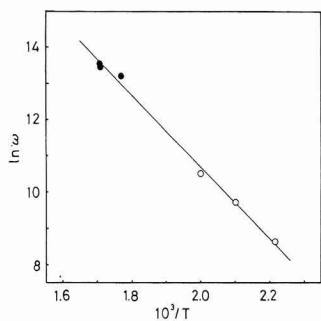


**Fig. 4**

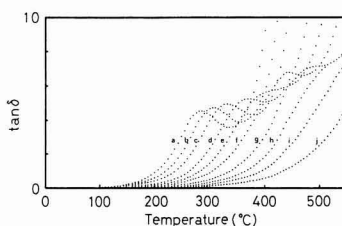


**Fig. 5**

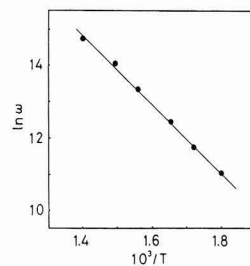


**Fig. 6**

**Fig. 4.** Arrhenius plot of  $\ln\omega$  ( $\omega$  is angular frequency) vs. the peak temperature  $T$  for the internal friction peak of 2Y-TZP. ●: present study, ○: Matsushita et al.<sup>5)</sup>

**Fig. 5.** Temperature dependence of dielectric loss  $\tan\delta$  of 2Y-TZP measured at frequencies of (a) 10k, (b) 20k, (c) 40k, (d) 100k, (e) 200k, (f) 400k, (g) 1M, (h) 2M, (i) 4M and (j) 10M Hz.

**Fig. 6.** Arrhenius plot of  $\ln\omega$  ( $\omega$  is angular frequency) vs. the peak temperature  $T$  for the dielectric loss peak of 2Y-TZP.

located around Zr cation to form (Zr<sup>4+</sup>V<sub>o</sub><sup>''</sup>) pair at low temperatures, and this pair decomposed at high temperatures. The present data supports the appearance of the local structure with an elastic dipole to give rise to the elastic relaxation peak in cubic ZrO<sub>2</sub> with Y<sub>2</sub>O<sub>3</sub>. Furthermore, the elevated background with temperature is attributed to the movement of oxygen vacancies with increasingly random distribution, which may be different cause for internal friction from the relaxation observed at 300°C.

The data of the dielectric loss on 8Y-FSZ is shown in Fig.9. It was found that the dielectric loss significantly increased upon rather low temperature and was elevated with temperature, not showing the peak. It was different from the case of the internal friction in the same sample. The results indicate that the relaxation response is more sensitive at elastic field than electric field in cubic ZrO<sub>2</sub>. The peak around 300°C is revealed by only elastic measurement, which shows that the internal friction experiment is unique for study on the relaxation.

3.3. 12Ce-TZP

The heat treatment at 1000°C in H<sub>2</sub> for 8 hours induced the loss of weight, slight expansion, the decrease of tetragonality (c/a) and the increase of the lattice volume for the TZP containing 12.6 mol% CeO<sub>2</sub>. The data for the density and the lattice constant are listed in Table 1. The weight loss of the reduced Ce-TZP sample was explained by the reduction of CeO<sub>2</sub> to Ce<sub>2</sub>O<sub>3</sub> (i.e. Ce<sup>4+</sup> to Ce<sup>3+</sup>) doped in ZrO<sub>2</sub> lattice. The change of Ce<sup>4+</sup> to Ce<sup>3+</sup> results the formation of oxygen defect to compensate the charge in the TZP and the expansion of the crystal lattice because of the increase of ionic radius of Ce with the reduction. The composition of 12Ce-TZP samples, represented by Zr<sub>0.874</sub>Ce<sub>0.126</sub>O<sub>2</sub> as received, changed to be Zr<sub>0.847</sub>Ce<sub>0.126</sub>O<sub>2x</sub> (x = 0.063) which was calculated from the weight loss with heating in H<sub>2</sub>. The reduction treatment produces the oxygen vacancy with the amount correspond-

ing to the change of the valence of Ce<sup>4+</sup> to Ce<sup>3+</sup> doped in TZP.

Figures 10 and 11 compare the results of Young's modulus *E* and the internal friction *Q*<sup>-1</sup> for the 12Ce-TZP before and after the reduction. The data for the sample without the reduction shows the linear decrease of *E* with temperature and small value for *Q*<sup>-1</sup> even at elevated temperature. For the reduced Ce-TZP, the internal friction shows the increase with elevated temperature and the trace peak around 330°C, where Young's modulus shows slightly non-linear behavior. The plot of *Q*<sup>-1</sup> with reciprocal temperature scale is demonstrated in Fig.12. The temperature dependence of the internal friction for the reduced sample are similar to that for 8Y-FSZ in Fig.8, although its absolute value is smaller than that of 8Y-FSZ. The results directly indicate the significant contribution of the oxygen vacancy to cause the internal friction of ZrO<sub>2</sub>.

3.4. Effect of the Oxygen Vacancy for the Internal Friction

The concentration of oxygen vacancy for (Zr, M)O<sub>2-x</sub> (M=Y, Ce) used in the present work is x=0.02 for the 2Y-TZP, x=0.08 for the 8Y-FSZ, x=0 for the 12Ce-TZP and x=0.06 for the reduced 12Ce-TZP. The comparative results in Figs.1, 7, 10 and 11 indicate the significant contribution of the oxygen vacancy and its concentration to cause the internal friction of ZrO<sub>2</sub>. Our results are briefly summarized as following. 1) The internal friction peak appears in the ZrO<sub>2</sub> sample with oxygen vacancy regardless of their symmetry (cubic or tetragonal), the kind of dopants (Y or Ce) and their composition. 2) The type of internal friction in the temperature range of 25°C to 450°C is summarized as two ones; the peak indicating the anelastic relaxation, and the background increased with increasing temperature. In the 2Y-TZP, the relation of *Q*<sup>-1</sup> vs. *T*<sup>-1</sup> indicates the relaxation peak defined by the parameter described earlier. Whereas in the 8Y-FSZ and the reduced 12Ce-TZP, large amount of the oxygen vacancy in ZrO<sub>2</sub> gives rise to the internal friction with high level background on which the relaxation peak is accompanied.

The results suggest that the anelastic relaxation to produce the peak of the internal friction is due to common cause in ZrO<sub>2</sub> with the oxygen defect. The introduction of trivalent cation M<sup>3+</sup> such as Y and Ce<sup>3+</sup> to ZrO<sub>2</sub> produces one oxygen vacancy V<sub>o</sub> for every M<sub>2</sub>O<sub>3</sub> molecule. In cubic ZrO<sub>2</sub> with Y<sub>2</sub>O<sub>3</sub>, as suggested by Catlow et al., the anion

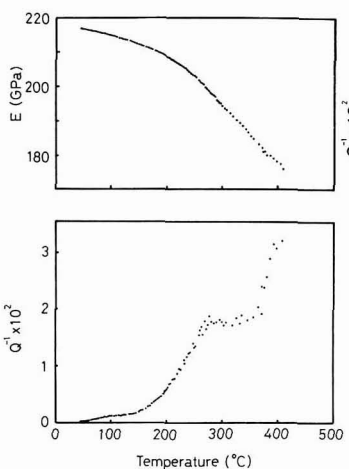


Fig. 7

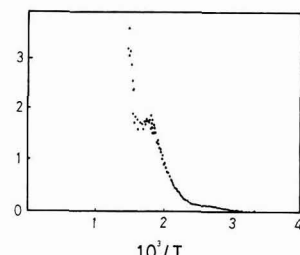


Fig. 8

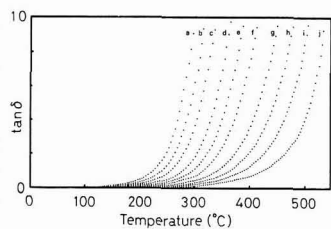


Fig. 9

Fig. 7. Temperature dependence of Young's modulus *E* and the internal friction *Q*<sup>-1</sup> of 8Y-FSZ measured by a 90 kHz quartz.  
 Fig. 8. Reciprocal temperature dependence of the internal friction *Q*<sup>-1</sup> of 8Y-FSZ. The data are the same as that in Fig.7.  
 Fig. 9. Temperature dependence of dielectric loss tanδ of 8Y-FSZ measured at frequencies of (a) 10k, (b) 20k, (c) 40k, (d) 100k, (e) 200k, (f) 400k, (g) 1M, (h) 2M, (i) 4M and (j) 10M Hz.

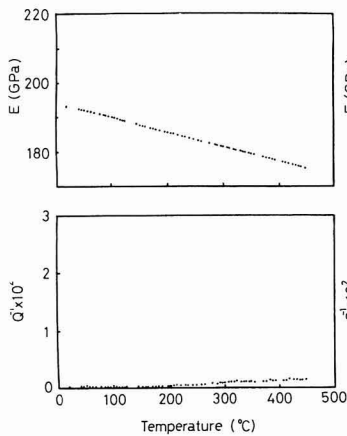


Fig. 10

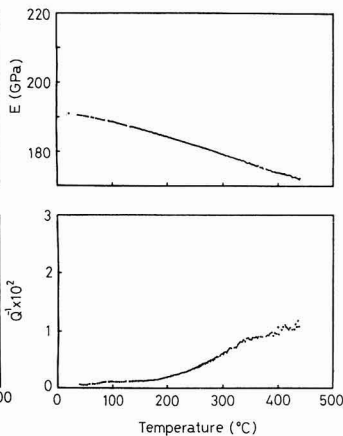


Fig. 11

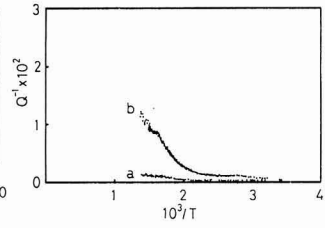


Fig. 12

Fig. 10. Temperature dependence of Young's modulus  $E$  and the internal friction  $Q^{-1}$  of 12Ce-TZP measured by a 90 kHz quartz.

Fig. 11. Temperature dependence of Young's modulus  $E$  and the internal friction  $Q^{-1}$  of the reduced 12Ce-TZP, measured by a 90kHz quartz.

Fig. 12. Reciprocal temperature dependence of the internal friction  $Q^{-1}$  of (a) 12Ce-TZP and (b) the reduced 12Ce-TZP. The data are the same as that in Fig.10 and 11.

vacancy is preferentially sited adjacent to  $Zr^{4+}$ , so that ( $Zr^{4+}Vo''$ ) pair with elastic dipole will give rise to the relaxation peak. A part of the pair in the local structure is decomposed thermally at elevated temperature. Therefore the background of the internal friction is produced by the movement of decomposed  $V_o$  in  $ZrO_2$  with large amount of oxygen defects. It is believed that the relaxation observed in 2Y-TZP and reduced 12Ce-TZP with tetragonal symmetry is caused by the local interaction similar to that in cubic  $ZrO_2$ . However, the internal friction peak in 2Y-TZP was not described by a single Debye peak. It suggests the appearance of complex relaxation processes which produce a broadened peak. For tetragonal  $ZrO_2$  with  $Y_2O_3$ , Morikawa et al.<sup>14)</sup> have discussed the local structure and proposed a  $Zr_2Y_2O_7$  cluster as a model by EXAFS. The present results suggest the appearance of the local structure including ( $Zr^{4+}V_o''$ ) and ( $Y^{3+}V_o''Y^{3+}$ ) in both tetragonal and cubic  $ZrO_2$  with oxygen vacancy.

#### 4. Conclusion

The present study is concluded as following.

- 1) The elastic measurement data of 2Y-TZP around 100kHz reveals an anelastic relaxation peak with the activation enthalpy  $H=82.5\pm 1.4$ kJ/mol, the relaxation strength  $\Delta=1.34\pm 0.08\times 10^{-2}$ , and  $\tau_0=5.4\pm 1.1\times 10^{-14}$ sec. The relaxation is considered to be due to the cause as same as that for the dielectric one with  $H=79.0\pm 3.8$ kJ/mol and  $\tau_0=5.9\pm 3.1\times 10^{-13}$ sec.
- 2) The comparative study on the internal friction for 2Y-TZP and 8Y-FSZ indicates the existence of the similar relaxation process and consequently the possibility of similar local cation-anion (or vacancy) interaction in  $Y_2O_3$  doped  $ZrO_2$  regardless of the symmetry (tetragonal and cubic).
- 3) The internal friction is small for Ce-TZP, whereas after the reduction of the sample it changes increasingly the large value with elevated temperature and is accom-

panied with the trace peak. The results directly indicate the significant contribution of the oxygen vacancy to the internal friction of  $ZrO_2$ .

#### References:

- 1) A.S. Nowick, Point defects in solids Vol.1, ed. by J.H. Crawford and L.M. Slifkin, Chap. 3, Plenum Press, New York (1972)p.151-200.
- 2) B.C.H. Steele, J. Drennan, R.K. Slotwinski, N. Bonanos and E.P. Butler, Advances in Ceramics, Vol.3, Amer. Ceram. Soc. (1981) p.286-309.
- 3) T.K. Gupta, J.H. Bechtold, R.C. Kuznicki, K.H. Cadloff and B.R. Rossing, J. Mater. Sci. 12, 2421-2426 (1977).
- 4) T. Sato, S. Ohtaki, T. Endo and S. Shimada, Advances in Ceramics, Vol.24, Amer. Ceram. Soc. (1988) p.29-37.
- 5) K. Matsushita, T. Okamoto and M. Shimada, J. Physique C10 suppl. 46, C10-549-552 (1985).
- 6) M. Weller and H. Schubert J. Am. Ceram. Soc. 69, 573-577 (1986).
- 7) S. Sakaguchi, F. Wakai and S. Matsuno, Yogyo-Kyokaiishi, 95, 476-479 (1987) in Japanese.
- 8) K. Nishiyama, M. Yamanaka, M. Omori and S. Umekawa, J. Mater. Sci. Lett. 9, 526-528 (1990).
- 9) M. Ozawa, T. Hatanaka and H. Hasegawa, *ibid.* 10, 774-5 (1991).
- 10) T. Ikeda, Atsuden zairyougaku no kiso, ohmu-sha, Tokyo (1984) in Japanese (English version "Fundamentals of Piezoelectric Materials Science," Oxford University Press, 1989).
- 11) S. Kudo and M. Ozawa, Seramikkusu-Ronbunshi, 98, 653-657 (1990) in Japanese.
- 12) M. Ozawa and S. Kudo, Seramikkusu-Ronbunshi, 98, 987-990 (1990) in Japanese.
- 13) C.R.A. Catlow, A.V. Chadwick, G.N. Greaves and L.M. Moroney, J. Amer. Ceram. Soc. 69, 272-277 (1986).
- 14) H. Morikawa, Y. Shimizu, H. Marumo, T. Harasawa, H. Ikawa, K. Tazi and Y. Udagawa, Seramikkusu-Ronbunshi, 96, 253-258 (1988) in Japanese.

# Microstructure and Microwave Characteristics of Ba((Mg, Co)<sub>1/3</sub>Nb<sub>2/3</sub>)O<sub>3</sub>-Based Dielectrics

Shigekazu Sumita\*, Makoto Kobayashi, Kazuaki Suzuki, Keizo Kawamura and Taro Miura

TDK Corporation, Materials Research Center  
570-2, Matsugashita, Minami-Hatori, Narita-shi, 286 Japan

**The microstructure of the cubic perovskite Ba((Mg, Co)<sub>1/3</sub>Nb<sub>2/3</sub>)O<sub>3</sub>-based dielectric has been investigated. The secondary phase was determined to be Ba<sub>5</sub>Nb<sub>4</sub>O<sub>15</sub>; this phase was detrimental to the microwave properties of Ba((Mg, Co)<sub>1/3</sub>Nb<sub>2/3</sub>)O<sub>3</sub>. Eliminating the secondary phase, the precise control of A-site/B-site ratio of the perovskite and long time annealing improved the microwave characteristics.**

[Received February 22, 1991; Accepted May 23, 1991]

**Key-words:** Ba((Mg, Co)<sub>1/3</sub>Nb<sub>2/3</sub>)O<sub>3</sub>, Ba<sub>5</sub>Nb<sub>4</sub>O<sub>15</sub>, Microwave dielectric, Perovskite structure, Microstructure

## 1. Introduction

Microwave application to automobile telephones and TV-receivers of satellite broadcasting has been increasing rapidly. Geographic Positioning System (GPS) for navigation of airplanes, cars, and mountain-climbers is also in the category of microwave application. Under these circumstances, the microwave dielectric properties with high-Q, low loss, as resonators and filters in the microwave equipment have been becoming extremely important. The cubic perovskite dielectrics have been studied for developing the high-Q, low loss, dielectric.<sup>1-8)</sup> In order to study the mechanisms of microwave characteristics, far infrared reflection spectra,<sup>9)</sup> phase transition,<sup>10)</sup> and the effect of secondary phase on Q-value,<sup>11)</sup> Curie-Weiss-like behavior of the loss tangent,<sup>12)</sup> the effect of dopants,<sup>13,14)</sup> Ba reduced perovskite to improve sintering density,<sup>15)</sup> B-site element control in perovskite ABO<sub>3</sub>,<sup>16)</sup> frequency and temperature dependence of grain size and density of polycrystalline perovskite,<sup>17)</sup> and the techniques for microwave measurement<sup>18)</sup> have been widely discussed. However, the relation between microstructural phases and the microwave properties has not been sufficiently discussed. The development of structural analysis equipment has made it possible to analyze the microstructures and the concentrations of constituent elements in grains and phases.<sup>19,21)</sup>

Ba((Mg, Co)<sub>1/3</sub>Nb<sub>2/3</sub>)O<sub>3</sub>-based dielectrics usually synthesized have a very low Q-value. The authors considered that this might be caused by the existence of other phases in the dielectrics. The first purpose of this study, therefore, is to analyze the microstructure of the Ba((Mg, Co)<sub>1/3</sub>Nb<sub>2/3</sub>)O<sub>3</sub>-based dielectrics usually synthesized have a very low Q-value. The authors considered that this might be caused by the existence of other phases in the dielectrics. The first purpose of this study, therefore, is to analyze the microstructure of the Ba((Mg, Co)<sub>1/3</sub>Nb<sub>2/3</sub>)O<sub>3</sub>-based

dielectrics, and to study the effects of the phases on the microwave properties of the dielectric body. The second purpose is to synthesize a high-Q, low loss, dielectric compound by controlling the A-site/B-site ratio and by long annealing process.

## 2. Experimental Procedure

Commercially available BaCO<sub>3</sub>, MgCO<sub>3</sub>, Co<sub>3</sub>O<sub>4</sub>, and Nb<sub>2</sub>O<sub>5</sub> were used for the synthesis of Ba((Mg, Co)<sub>1/3</sub>Nb<sub>2/3</sub>)O<sub>3</sub>-based dielectrics. A mixture of 40wt% concentration was ball-milled in deionized water for 17.5h, dried then calcined at 1270°C for 2h in air atmosphere. After milling with polyvinyl alcohol as an organic binder, the calcined powder was pressed into a cylindrical shape, 12.5mm in diameter and 15.0mm in height. The pressed body was sintered at 1520°C for 2h in air.

The sintered compacts were polished with 0.25μm diamond paste then chemically etched by HCl + HF solution to reveal the grains and phases for microstructural observation with a Scanning Electron Microscope (SEM: Hitachi S-800). Constituent elements of the microarea were mapped by means of a Computer-aided Micro Analyzer (CMA: Jeol JCMA-733). A Scanning Transmission Electron Microscope (STEM: Jeol JEM-2000FXII) with Energy Dispersion X-ray (EDX) was used for quantitative analysis of composition of grains and phases in the microarea. The crystal structure of each phase was determined by an X-ray Diffraction Spectrometer (XRD: Mac Science MXP<sup>3</sup>) with Cu target.

In order to evaluate the microwave characteristics, each sintered body was precisely machined into a cylindrical shape, 10.00±0.003mm in diameter and 5.00±0.01mm in height. Microwave dielectric characteristics were measured by Hakki and Coleman's dielectric resonator method,<sup>22)</sup> and the Q-value was measured at 7.3 GHz.

## 3. Results and Discussion

### 3.1. Phase Determination

Figure 1 shows a microstructure of the polished and chemically etched surface of a sintered sample. The average grain size of the principal phase, Ba((Mg, Co)<sub>1/3</sub>Nb<sub>2/3</sub>)O<sub>3</sub>, is approximately 1.2μm. The white-colored secondary phase, having straight edges and dihedral angles of 60 or 120 degrees, is stable against the HCl+HF solution. The black-colored tertiary phase with 0.2μm diameter exists on the grain boundaries, particularly at the triple points. The

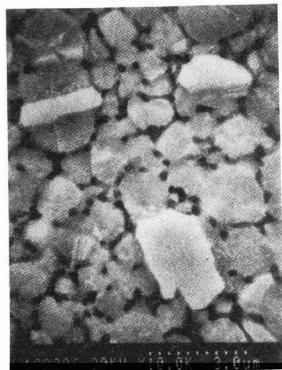


**Fig. 1.** SEM photomicrograph of polished and etched surface of  $\text{Ba}(\text{Mg}, \text{Co})_{1/3}\text{Nb}_{2/3}\text{O}_3$  body. The white-colored secondary phase, and black-colored tertiary phase on the grain boundaries are observed.

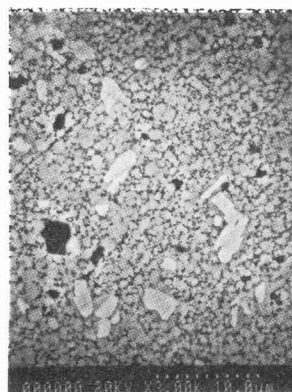
Note: Etching solution was (1:1)HCl 250ml + (1:9)HF 1ml. Etching time was 100 sec at 20°C.

tertiary phase is etched most easily by the solution among the three phases.

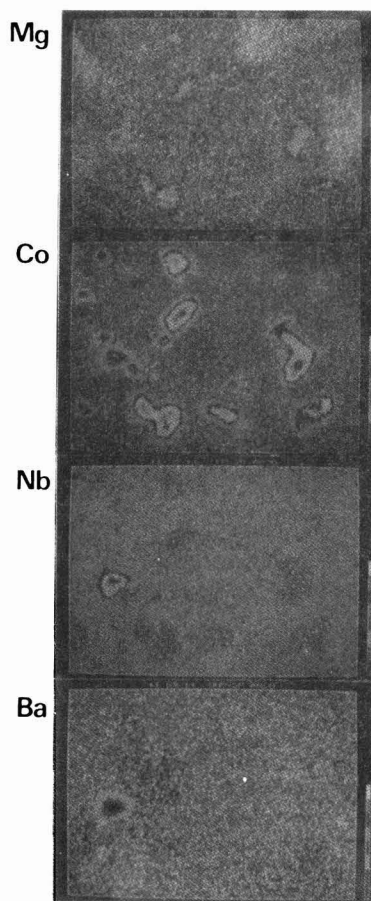
The constituent elements of the dielectric were mapped by CMA as shown in Fig.2. It is significant that the concentrations of both Mg and Co in the secondary phase are extremely small. On the other hand, the concentration of Nb is much higher than that of the principal phase. Barium, as an A-site element in perovskite structure of  $\text{ABO}_3$ , shows no noticeable difference in concentration between principal and secondary phases. The constituent elements of each phase were quantitatively analyzed by using STEM-EDX as given in Table 1. The Ba/Nb ratio of the principal phase,  $\text{Ba}(\text{Mg}, \text{Co})_{1/3}\text{Nb}_{2/3}\text{O}_3$ , is 52.04/35.95 (nearly 3/2). The secondary phase is 52.67/44.26 (nearly 5/4). Therefore, the most probable compound of the secondary phase is determined to be  $\text{Ba}_5\text{Nb}_4\text{O}_{15}$ , which is a stable compound in the  $\text{BaO-Nb}_2\text{O}_5$  binary system.<sup>23,24)</sup>

Figures 3(a) and (b) show XRD patterns of  $\text{Ba}(\text{Mg}, \text{Co})_{1/3}\text{Nb}_{2/3}\text{O}_3$ -based dielectric and the synthesized  $\text{Ba}_5\text{Nb}_4\text{O}_{15}$  (JCPDS:Card No.14-28),<sup>25)</sup> respectively. The diffraction pattern of  $\text{Ba}_5\text{Nb}_4\text{O}_{15}$  corresponds to the unknown peaks in Fig.3(a). The  $\text{Ba}_5\text{Nb}_4\text{O}_{15}$  phase was milled and intentionally added to the principal phase at the concentration of 25wt%, then the mixture was sintered at 1520°C for 2h. The resulting XRD pattern in Fig.3(c) is the same as that in Fig.3(a). however, the former shows much higher intensity of  $\text{Ba}_5\text{Nb}_4\text{O}_{15}$  than the latter. Consequently, this result convinces that the secondary phase has to be

$\text{Ba}_5\text{Nb}_4\text{O}_{15}$ . Furthermore, the hexagonal structure of  $\text{Ba}_5\text{Nb}_4\text{O}_{15}$  agreed with the microstructural shape of the



(a)



(b)

**Table 1.** Quantitative analysis by STEM-EDX (n=4).

		Concentration (at%)			
		BaO	(Nb <sub>2</sub> O <sub>5</sub> )/2	CoO	MgO
Principal phase	ave.	52.04	35.95	5.84	2.74
	σ	±1.47	±3.63	±1.68	±2.00
Secondary phase	ave.	52.67	44.26	1.19	0.30
	σ	±2.85	±2.11	±1.20	±0.54
Tertiary phase	ave.	37.98	58.22	2.17	1.43
	σ	±2.29	±1.98	±0.35	±1.00

**Fig. 2.** (a) Composition image of the etched microstructure of  $\text{Ba}(\text{Mg}, \text{Co})_{1/3}\text{Nb}_{2/3}\text{O}_3$ , and (b) Mg, Co, Nb and Ba mapping image by CMA.

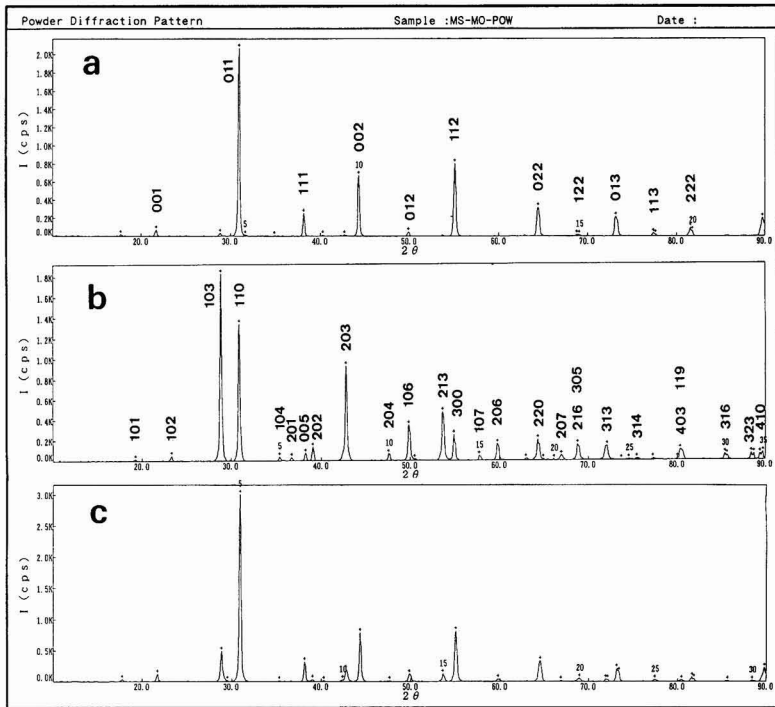


Fig. 3. X-ray diffraction spectra of (a)  $\text{Ba}((\text{Mg}, \text{Co})_{1/3}\text{Nb}_{2/3})\text{O}_3$ -based dielectric, (b)  $\text{Ba}_5\text{Nb}_4\text{O}_{15}$ , and (c)  $\text{Ba}((\text{Mg}, \text{Co})_{1/3}\text{Nb}_{2/3})\text{O}_3$  (75wt%) +  $\text{Ba}_5\text{Nb}_4\text{O}_{15}$  (25wt%). These samples were sintered at  $1520^\circ\text{C}$  for 2h in air.

secondary phase in Fig.1.

### 3.2. Model Experiment of $\text{Ba}_5\text{Nb}_4\text{O}_{15}$ -doped $\text{Ba}((\text{Mg}, \text{Co})_{1/3}\text{Nb}_{2/3})\text{O}_3$

In order to study the influence of the secondary phase, a single phase of  $\text{Ba}_5\text{Nb}_4\text{O}_{15}$  was synthesized from  $\text{BaCO}_3$  and  $\text{Nb}_2\text{O}_5$  under exactly the same processing conditions as the mother material. Below its calcination temperature of  $1270^\circ\text{C}$ ,  $\text{Ba}_5\text{Nb}_4\text{O}_{15}$  shrunk considerably. When the temperature was raised to  $1520^\circ\text{C}$  for sintering,  $\text{Ba}_5\text{Nb}_4\text{O}_{15}$  melted because the melting point of  $\text{Ba}_5\text{Nb}_4\text{O}_{15}$  is  $1320^\circ\text{C}$ .<sup>23,24)</sup> It is, thus, tenable that the secondary phase was formed during cooling process from the liquid phase.

Figure 4 shows an SEM photomicrograph of the sintered dielectric with the addition of 25wt% secondary phase. The hexagonal-shaped secondary phase with  $20\mu\text{m}$  diameter and approximately  $1\mu\text{m}$  thickness is observed. Even when the dielectric was sintered without the intentional addition of the secondary phase, the same size of the hexagonal-shaped phase was still observed; but the number of the phase was smaller.

The microwave characteristics of  $\text{Ba}((\text{Mg}, \text{Co})_{1/3}\text{Nb}_{2/3})\text{O}_3$  containing secondary and tertiary phases were evaluated. The dielectric constant  $\epsilon_r$ , the loss quality  $Q$ , and the temperature coefficient of resonating frequency  $\tau_f$  (ppm/ $^\circ\text{C}$ ) of the  $\text{Ba}((\text{Mg}, \text{Co})_{1/3}\text{Nb}_{2/3})\text{O}_3$ -based dielectric were 31.7, 1730 and 9.12, respectively, while those of  $\text{Ba}_5\text{Nb}_4\text{O}_{15}$  were 27.3, 1100, and 54.56, respectively. In other words,  $\text{Ba}_5\text{Nb}_4\text{O}_{15}$  possessed disadvantageous properties of low- $\epsilon_r$ , low- $Q$ , and high  $\tau_f$ . This case study, therefore, proves two points for improving the dielectric synthesis.

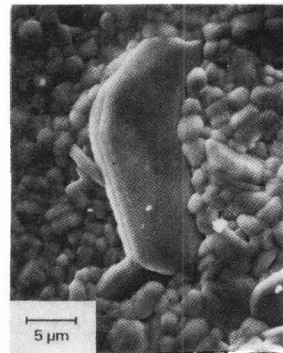


Fig. 4. SEM photomicrographs of  $\text{Ba}_5\text{Nb}_4\text{O}_{15}$  (25wt%) +  $\text{Ba}((\text{Mg}, \text{Co})_{1/3}\text{Nb}_{2/3})\text{O}_3$  (75wt%) dielectric sintered at  $1500^\circ\text{C}$

- 1) The existence of  $\text{Ba}_5\text{Nb}_4\text{O}_{15}$  in  $\text{Ba}((\text{Mg}, \text{Co})_{1/3}\text{Nb}_{2/3})\text{O}_3$  is detrimental to the microwave properties of  $\epsilon_r$ ,  $Q$ , and  $\tau_f$ . Thus,  $\text{Ba}_5\text{Nb}_4\text{O}_{15}$  has to be eliminated from the principal phase.
- 2) Both  $Q$ -values of the principal and secondary phases were low. Chemical compositions, therefore, must be precisely controlled in order to obtain a high- $Q$  microwave dielectric.

### 3.3. Effect of A-site/B-site ratio of $\text{Ba}((\text{Mg}, \text{Co})_{1/3}\text{Nb}_{2/3})\text{O}_3$

Figure 5 shows the  $Q$ -value and  $\epsilon_r$  of  $\text{Ba}((\text{Mg},$

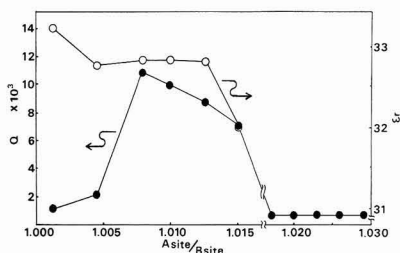


Fig. 5.  $Q$ -value and dielectric constant versus A-site/B-site ratio of  $\text{Ba}[(\text{Mg}, \text{Co})_{1/3}\text{Nb}_{2/3}]\text{O}_3$ .

Table 2. Effect of annealing on  $\epsilon_r$  and  $Q$ .

annealing (h)	$\epsilon_r$	$Q$
Conventional method		
2	32.90	8175
5	32.63	8529
10	32.82	8539
20	32.65	8743
40	32.62	9133
80	32.49	8985
A-site/B-site control		
40	32.66	11600

$\text{Co}_{1/3}\text{Nb}_{2/3}\text{O}_3$ , as a function of A-site/B-site ratio, which was determined by fluorescence X-ray analysis (Rigaku Simultics 3530). When the A/B value is over 1.018,  $Q$ -value is less than 1000; in this A-site rich zone, the porous microstructure of the dielectric was observed and thus both  $\epsilon_r$  and  $Q$  had low values. At the point where  $A/B=1.015$ , the  $Q$ -value shows approximately 7000; this improved dielectric possesses much higher  $Q$ -value than that in the model experiment sample. As the A/B ratio decreases from 1.015 to 1.008, the  $Q$ -value increases to 11000 with the reduction of  $\text{Ba}_5\text{Nb}_4\text{O}_{15}$  confirmed by XRD peak intensities. For the A/B ratio between 1.008 and 1.005, the  $Q$ -value declines dramatically to 2000; in this region, the quantity of  $\text{Ba}_5\text{Nb}_4\text{O}_{15}$  increased. On the other hand, dielectric constant shows constant value of 32.8 in the A/B area between 1.013 and 1.005. It is, therefore, concluded that the  $Q$ -value is remarkably dependent on the A-site/B-site ratio of  $\text{Ba}[(\text{Mg}, \text{Co})_{1/3}\text{Nb}_{2/3}]\text{O}_3$ .

### 3.4. Effect of Annealing

Long-time annealing was carried out to enhance the  $Q$ -value of  $\text{Ba}[(\text{Mg}, \text{Co})_{1/3}\text{Nb}_{2/3}]\text{O}_3$ , since the atomic arrangement of the constituent elements was considered to affect the microwave properties of the dielectric. Table 2 gives  $Q$ ,  $\epsilon_r$ , and annealing time of conventionally synthesized samples and those of the A-site/B-site controlled sample at 1390°C. The  $Q$ -value increases as annealing continues, although the  $\epsilon_r$  shows to be almost constant. The atomic arrangement of the dielectric during annealing enhances the  $Q$ -value. However, when the sample is over-annealed more than 80h, the  $Q$ -value decreases. Probably the composition

has been altered because cobalt has priority over other elements in the vaporization during long annealing. Based on the result, long time annealing of 40h for A-site/B-site modified sample was attempted. The result of  $Q$ -value is 11600 (Table 2), or the highest value in this experiment. The dielectric constant of this sample is almost the same as that of the conventional samples. Thus, in order to improve the microwave characteristics of  $Q$ -value, the precise control of the composition and long time annealing are of prime importance.

## 4. Concluding Remarks

The microstructure and microwave properties of the cubic perovskite  $\text{Ba}[(\text{Mg}, \text{Co})_{1/3}\text{Nb}_{2/3}]\text{O}_3$ -based dielectrics have been investigated.

- 1) The secondary phase is determined to be hexagonal  $\text{Ba}_5\text{Nb}_4\text{O}_{15}$ . This phase is detrimental to the microwave properties of  $\text{Ba}[(\text{Mg}, \text{Co})_{1/3}\text{Nb}_{2/3}]\text{O}_3$ .
- 2) The precise control of A-site/B-site ratio is significant in eliminating the secondary phase  $\text{Ba}_5\text{Nb}_4\text{O}_{15}$  and therefore in improving the  $Q$ -value of  $\text{Ba}[(\text{Mg}, \text{Co})_{1/3}\text{Nb}_{2/3}]\text{O}_3$ .
- 3) Long time annealing is also effective for the enhancement of the  $Q$ -value of  $\text{Ba}[(\text{Mg}, \text{Co})_{1/3}\text{Nb}_{2/3}]\text{O}_3$ .

### Acknowledgements

The authors thank Y. Izumi and Y. Yamamoto for their analytical support, and A. Okamoto for his comment. The advice on the sample preparation by M. Yahagi, T. Kikuchi, S. Taguchi, and Y. Iijima is also gratefully acknowledged.

### References:

- 1) S. Kawashima, M. Nishida, I. Ueda, and H. Ouchi, *J. Am. Ceram. Soc.*, 66, 421-423 (1983).
- 2) K. Endo, K. Fujimoto and K. Murakawa, *ibid.*, 70, C215-218 (1987).
- 3) H. Tamura, T. Konoike, Y. Sakabe and K. Wakino, *ibid.*, 67, C59-61 (1984).
- 4) H. Banno, F. Mizuno and T. Takeuchi, *Jpn. J. Appl. Phys.*, 24, Supplement 24-3, 87-89 (1985).
- 5) S. Nomura and F. Kojima, *ibid.*, 14, 907-98 (1975).
- 6) F. Galasso and J. Pyle, *J. Phys. Chem.*, 533-534 (1963).
- 7) Y. Hikichi, Z. Chen, R.E. Newnham and L.E. Cross, *Mat. Res. Bull.*, 17, 1371-1377 (1982).
- 8) K. Sasazawa and N. Yamaoka, *Jpn. J. Appl. Phys.*, 24, Supplement 24-2, 1022-1024 (1985).
- 9) K. Wakino, M. Murata and H. Tamura, *J. Am. Ceram. Soc.*, 69, 34-37 (1986).
- 10) G. Rupprecht and R.O. Bell, *Phys. Rev.*, 125, 1915-1920 (1962).
- 11) K. Kageyama, J. Takahashi and M. Takata, *Seramikkusu Ronbunshi*, 98, 824-830 (1990).
- 12) A.J. Pointon and R.M. Henson, *Proc. 3rd. IMF, Ferroelectrics*, 7, 359-360 (1974).
- 13) S. Neirman and I. Burn, *J. Mater. Sci.*, 19, 737-744 (1984).
- 14) B.D. Silverman, *Phys. Rev.* 125, 1921-1930 (1990).
- 15) K. Endo, M. Tsurumi and K. Murakawa, *Seramikkusu Ronbunshi*, 98, 934-937 (1990).
- 16) S.B. Desu and H.M. O'Bryan, *J. Am. Ceram. Soc.*, 68, 546-551 (1985).
- 17) S. Ikegami, *J. Phys. Soc. Jpn.*, 18, 1203-1213 (1963).
- 18) M.T. Lanagan, J.H. Kim, S-J. Jang and R.E. Newnham, *J. Am. Ceram. Soc.*, 71, 311-316 (1988).
- 19) S. Sumita, M. Ikeda, Y. Nakano, K. Nishiyama and T. Nomura, *J. Am. Ceram. Soc.*, 74, 2739-2746 (1991).

- 20) S. Sumita, *Seramikkusu Ronbunshi*, 99, 538-544 (1991).
- 21) S. Sumita, A. Fukuno, S. Yamashita and T. Yoneyama, *J. Jpn. Soc. Powder & Powder Metal.*, 32, 253-258 (1985).
- 22) B.W. Hakki and P.D. Coleman, *IRE Trans. on Microwave Theory and Techniques*, 402-410 (1960).
- 23) Phase Diagram for Ceramists, VI, p.101, Fig.6371, *Am. Ceram. Soc.* (1987).
- 24) *ibid.*, I, p.99, Fig.214, *Am. Ceram. Soc.* (1964).
- 25) Powder Diffraction file, Card No.14-28, Joint Committee on Powder Diffraction Standards.

---

This article appeared in English in *Nippon Seramikkusu Kyokai Gakujutsu Ronbunshi* (Japanese version), Vol.99, No.8, 1991.

# Preparation of Mullite Fiber by Sol-Gel Method

Toshiyuki Nishio and Yoshinori Fujiki\*

Central Research Laboratories, Unitika Co., Ltd. 23, Uji-Kozakura, Uji-shi, 611 Japan

\*National Institute for Research in Inorganic Materials. 1-1, Namiki, Tsukuba-shi, 305 Japan

Mullite fibers were prepared by a new sol-gel method from  $\text{Al}(\text{OPr})_3$ - $\text{Al}(\text{NO}_3)_3$ -TEOS- $\text{H}_2\text{O}$  system. In this system, the spinnable range varied depending on solution preparation procedures. When TEOS and  $\text{Al}(\text{OPr})_3$  were added simultaneously to an  $\text{Al}(\text{NO}_3)_3$  aqueous solution, precursor fibers could be obtained from solutions in a compositional range of  $\text{H}_2\text{O}/\text{mol}/(\text{Al}+\text{Si})/\text{mol} = 20/1 \sim 200/1$  and  $\text{Al}(\text{OPr})_3/\text{mol}/\text{Al}(\text{NO}_3)_3/\text{mol} \leq 6/1$ . On the other hand, the spinnable range was narrow, when TEOS was added to the solution of  $\text{Al}(\text{OPr})_3$  in an aqueous  $\text{Al}(\text{NO}_3)_3$ . When  $\text{Al}(\text{OPr})_3$  was added after TEOS was dissolved in an  $\text{Al}(\text{NO}_3)_3$  aqueous solution, no spinnable solutions were obtained. Aluminoxane polymer, oligomer of siloxane or that containing Si-O-Al bond, Al-O dimer,  $\text{Si}(\text{OH})_3$ -O-Si(OH)<sub>3</sub> and  $[\text{Al}(\text{H}_2\text{O})_6]^{3+}$  were observed by <sup>27</sup>Al- and <sup>29</sup>Si-NMR spectroscopy of the spinnable solutions. To the contrary, the unspinnable solutions contained  $\text{Al}_{13}^{7+}$  polycation and three-dimensional polymer having Al-O bonds. The existence of aluminoxane-polymer, Al and Si atomic scale component was deemed necessary for the appearance of spinnability. The DTA curves of all precursor fibers showed a unique and sharp exothermic peak at 1000°C, while those of gels obtained from unspinnable solutions showed only small peaks. The X-ray diffraction analysis revealed that the precursor fiber crystallizes directly from amorphous to mullite at temperature as low as 600°C. It was deduced that structure which has a similar composition to mullite exists in precursor fibers. Mullite fibers were prepared by a new sol-gel method from  $\text{Al}(\text{OPr})_3$ - $\text{Al}(\text{NO}_3)_3$ -TEOS- $\text{H}_2\text{O}$  system. In this system, the spinnable range varied depending on solution preparation procedures. The existence of aluminoxane-polymer, Al and Si atomic scale component was deemed necessary for the appearance of spinnability. The DTA curves of all precursor fibers showed a unique and sharp exothermic peak at 1000°C. The X-ray diffraction analysis revealed that the precursor fiber crystallizes directly from amorphous to mullite at temperature as low as 600°C. It was deduced that structure which has a similar composition to mullite exists in precursor fibers.

[Received October 16, 1990; Accepted April 19, 1991]

**Key-word:** Mullite fiber, Sol-Gel method, <sup>27</sup>Al-NMR, <sup>29</sup>Si-NMR, Spinnability

## 1. Introduction

Recently, ceramic fibers are playing more and more important roles as heat-resistant and refractory materials, as well as reinforcing agents for FRC's, FRM's and FRP's.

Fibrous  $\text{Al}_2\text{O}_3$ - $\text{SiO}_2$  is one of them. There are various types of  $\text{Al}_2\text{O}_3$ - $\text{SiO}_2$  fibers, of which mullite ( $3\text{Al}_2\text{O}_3 \cdot 2\text{SiO}_2$ ) fibers are well known for their resistance to creep, high strength-related properties at high temperature, resistance to chemicals and low thermal expansion coefficient. Ceramic fibers are normally prepared by the dry spinning process, in which the viscous solution of the constituent elements of the fibers are spun into precursor fibers to be fired. There are three methods known for the synthesis of  $\text{Al}_2\text{O}_3$ - $\text{SiO}_2$  fibers:

- 1) hydrolysis and condensation of metal alkoxides, such as  $\text{Al}(\text{OR})_3$  and  $\text{Si}(\text{OR})_4$  (R: alkyl group) in an alcohol-base solvent, to prepare the viscous solution,<sup>1)</sup>
- 2) mixing an aluminum salt with silica sol in an aqueous system,<sup>2)</sup> and
- 3) mixing alumina sol with polysilicate in an aqueous solution containing PVA.

Method (1), however, cannot produce uniform aluminosilicate by simply mixing the starting alkoxides, because of different polymerization/condensation rates of aluminum and silicon alkoxides. For this reason, partially hydrolyzed silicon alkoxide<sup>4)</sup> or aluminum chelate<sup>5,6)</sup> is used. These methods, however, have their own disadvantages; it is difficult to strictly control extent of partial hydrolysis for the former, and the starting materials tend to be very expensive for the latter. One of the major problems involved in methods (2) and (3) is formation of the liquid phase in the grain boundaries of sintered mullite, because aluminum and silicon atoms are not very compatible with each other in the precursor fibers.<sup>7)</sup> This lowers their mechanical strength.

In this study, the authors produced the mullite fibers by a new method in which aluminum nitrate, aluminum isopropoxide and tetrathoxysilane (TEOS) were used in an aqueous system as an approach to solve the above problems. Many researchers have discussed that mullite is produced via Al-Si spinel or directly, when metal alkoxides are used as the starting materials, depending on whether aluminum and silicon atoms form the uniform, single phase or uniform, mixed phase.<sup>7-14)</sup> This point is discussed in this article. Furthermore, the effects of starting composition on spinnability of the solution, and Al and Si bond conditions in the precursor and sintered fibers are discussed, based on the <sup>27</sup>Al- and <sup>29</sup>Si-NMR, powder X-ray diffraction, and DTA analysis results.

## 2. Experimental Procedure

### 2.1. Starting Materials

The aluminum sources for the synthesis were aluminum triisopropoxide ( $\text{Al}(\text{OPr})_3$ , purity: 99.999%) and aluminum nitrate hydrate ( $\text{Al}(\text{NO}_3)_3 \cdot 9\text{H}_2\text{O}$ , special grade), and the silica source was tetraethoxy silane ( $\text{Si}(\text{OEt})_4$ , TEOS first grade), all of which were reagents.

## 2.2. Synthesis of Precursor Fiber

### 1) Method A

Aluminum nitrate hydrate was dissolved in distilled water, to which aluminum isopropoxide and TEOS were simultaneously added, and the mixture was stirred vigorously for 24h. The molar ratio of aluminum isopropoxide to aluminum nitrate hydrate ( $\text{Al(OPr}^i)_3/\text{Al(NO}_3)_3$ ) was in a range from 1/1 to 10/1 mol/mol, and that of water to aluminum and silicon ( $\text{H}_2\text{O}/(\text{Al} + \text{Si})$ ) in a range from 20/1 to 200/1 mol/mol.

### 2) Method B

Aluminum nitrate hydrate was dissolved in distilled water, to which aluminum isopropoxide was added, and the mixture was stirred vigorously for 24h. TEOS was then added to the above solution, and the mixture was stirred again vigorously for 24h. The same molar ( $\text{Al(OPr}^i)_3/\text{Al(NO}_3)_3$ ) and ( $\text{H}_2\text{O}/(\text{Al} + \text{Si})$ ) were used.

The Al/Si molar ratio was set at 3/1 in each method. The solution prepared by each method was concentrated for around 1h using an oil bath kept at 100°C, to prepare the spinning solution. The viscous solution thus prepared was stirred with a 5mm diameter glass rod at room temperature, and the rod was manually withdrawn quickly, after the solution was considered to be spinnable by its viscosity, to prepare the precursor fiber.

## 2.3. Structural Analysis of Spinning Solution and Precursor Fibers, and Fibers during Firing Process

### 1) $^{27}\text{Al}$ - and $^{29}\text{Si}$ -NMR Analysis

The analyzer was Bruker's MSL400, operated at magnetic flux density set at 9.39T. The  $^{27}\text{Al}$  spectra were measured 100 times at intervals of 1.0s and at 1.04.27MHz by the ordinary FT NMR method, using the  $\pi/2$  pulses of 1.2 $\mu\text{s}$ . On the other hand, the  $^{29}\text{Si}$  spectra were measured 3000 times at intervals of 20s and at 79.49MHz, using the  $\pi/2$  pulses of 4.0 $\mu\text{s}$ . The chemical shifts of the  $^{27}\text{Al}$  and  $^{29}\text{Si}$  spectra were measured, using  $[\text{Al}(\text{H}_2\text{O})_6]^{3+}$  and tetraethyl silane (TMS) as the external standards. The linear analysis was also made for the  $^{27}\text{Al}$  spectra, producing good results for many components by the aid of the Lorentz function, when applied to the solution system, ?? sharpened ?? by the movement of atoms. However, the Gaussian function gave better results for some components, conceivably due to the presence of chemical shift distributions, resulting from structural disturbances.

### 2) DTA-TG and Powder X-Ray Diffraction Analysis

The DTA-TG analysis was carried out using an analyzer (Rigaku Denki's TAS200TG8110), where the sample was heated at 20°C/min. The powder X-ray diffraction analysis was carried out by the ordinary method, using a diffractometer (Rigaku Denki's D-9C).

## 3. Results and Discussion

### 3.1. Preparation of Spinning Solution for Precursor Fibers

Figure 1 gives the results by Method A, where  $\text{Al(OPr}^i)_3$  and TEOS were simultaneously added, to form the spinning solution. The axis of ordinates represents the molar  $\text{H}_2\text{O}/(\text{Al} + \text{Si})$  ratio, which had little effect on spinnability in a range tested (20 to 200). It was found that the solution was spinnable at a molar  $\text{Al(OPr}^i)_3\text{mol}/\text{Al(NO}_3)_3\text{mol}$  ratio of

8 and less.  $\text{Al(OPr}^i)_3$  and TEOS in the above ratio were simultaneously added to an aqueous solution of  $\text{Al(NO}_3)_3$ , and the mixture was stirred vigorously for several hours, to form, for the most part, a transparent solution. The solution, even when it was not transparent, became transparent when concentrated under heat in the subsequent step.

Figure 2 gives the results by Method B, where  $\text{Al(OPr}^i)_3$  and TEOS were added separately, to form the spinning solution. The solution was spinnable, when molar  $\text{H}_2\text{O}/(\text{Al} + \text{Si})$  ratio was 200 or less and  $\text{Al(OPr}^i)_3/\text{Al(NO}_3)_3$  ratio was 4 or less. The mixture of powdered  $\text{Al(OPr}^i)_3$  and an aqueous  $\text{Al(NO}_3)_3$  solution in a spinnable ratio turned, when stirred vigorously for 24hr, into a transparent solution, when molar  $\text{H}_2\text{O}/(\text{Al} + \text{Si})$  ratio was 50 or more. Addition of TEOS to the above transparent solution gave a transparent, low-viscosity solution. On the other hand, the solution tended to change from a transparent condition to opaque jelly, as  $\text{Al(OPr}^i)_3/\text{Al(NO}_3)_3$  ratio increased, when  $\text{H}_2\text{O}/(\text{Al} + \text{Si})$  ratio was kept at 20. Addition of TEOS to the above solution gave a transparent, viscous solution. Method B gave a narrower spinnable range than Method A. A method in which  $\text{Al(OPr}^i)_3$  was added after TEOS was added to the aqueous  $\text{Al(NO}_3)_3$  solution failed to form a spinnable solution for the compositional range used in this study. It was also observed that the solution formed with aqueous  $\text{AlCl}_3$  solution was either unspinnable or spinnable in a very narrow range, whether Method A or B was followed.

### 3.2. Thermal Treatment of Precursor Fibers

Table 1 shows the phases, determined by the X-ray dif-

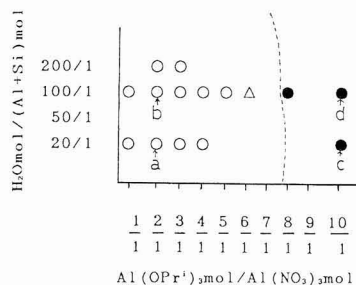


Fig. 1. Spinnable range of precursor obtained by Method A. ○: good spinnable (the obtained fiber is longer than 10cm). Δ: spinnable (fiber obtained is shorter than 10cm). ●: unspinnable.

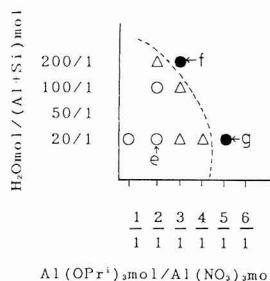


Fig. 2. Spinnable range of precursor obtained by Method B. ○: good spinnable (fiber obtained is longer than 10cm). Δ: spinnable (fiber obtained is shorter than 10cm). ●: unspinnable.

fraction analysis, found in the dried gel samples, whose names are given in Figs.1 and 2, thermally treated at 400° to 1300°C. These results indicate two important phenomena:

- 1) The mullite phase appears directly from the amorphous state, which is found in all the samples shown in the table. This is similar to the direct synthesis of mullite powder by spraying a mixture of aluminum nitrate and ethyl silicate dissolved in a mixed solvent of water and methanol into an atmosphere kept at 350° or 650°C,<sup>15,16</sup> which differs greatly from the phenomenon observed in the ordinary sol-gel process, where the starting materials are transformed into the mullite phase via the alumina phase (such as Al-Si spinel, or  $\gamma$ ,  $\eta$ -,  $\theta$ - or  $\alpha$ -Al<sub>2</sub>O<sub>3</sub>) and the silica phase (such as cristobalite).<sup>7-14</sup>
- 2) The mullite phase is found in the precursor fibers heated to 600° to 700°C, whereas the dried gel prepared from the unspinnable solution should be heated to 1100°C or more to be transformed into the mullite phase. It is accepted that heat treatment at 1100°C is required to produce the mullite phase in the ordinary sol-gel process. Such a temperature level is much higher than 600° to 700°C used in this study. **Figure 3** shows the X-ray diffraction patterns of Sample a, the precursor fibers prepared by Method A, heat-treated at various temperature levels for 1h. As discussed above, the sample heat-treated at 600°C had the mullite phase, though its pattern is broad. **Figure 4** shows the DTA curves of Samples a, d, e and f, which are the fibrous precursor and dried gel, prepared by Methods A and B, respectively. Each curve has an exothermic peak at around 1000°C. It is important to note that the DTA curves of Samples a and e, (the precursor fibers) have a sharp peak only at around 1000°C, whereas those of Samples d and f prepared from the unspinnable solutions have a very small peak at around 1000°C. The exotherm at around 1000°C has been discussed by many researchers; Suzuki et al<sup>17</sup>) and Hirata et al<sup>18</sup>) attribute it to crystallization of Al-Si spinel, Kumazawa et al<sup>16</sup>) and Yoldas et al<sup>11</sup>) to crystallization of mullite, and Hoffman et al<sup>8</sup>) and Chakravorty et al<sup>10</sup>) to crystallization of Al-Si spinel and mullite. The chemical formula proposed for the Al-Si spinel is SiO<sub>2</sub>·6H<sub>2</sub>O<sub>3</sub>, which is richer in Al<sub>2</sub>O<sub>3</sub> than SiO<sub>2</sub>·2Al<sub>2</sub>O<sub>3</sub>.<sup>14</sup> In any case, it has been demonstrated that the exotherm found at around 1000°C and intensity of the peak are strongly related to uniformity of the Al-Si bond in the structural networks. In other words, the single-phase gel mixed at atomic level has an excessive quantity of enthalpy, resulting from its structural disturbances, which is released at a stroke while the sample is heated, to generate the sharp exothermic peak, as discussed by Hoffman et al.<sup>8</sup>) By contrast, the mixed-phase gel, being formed by mixing the particles of the alumina and silica phases, has a smaller quantity of excessive enthalpy, and the reactions between the alumina and silica phases tend to be retarded by slow diffusion rate of each element, with the result that the exothermic peak is much broader than that associated with the single-phase gel. Furthermore, the transformation of each phase is involved in this system, producing two or more exothermic peaks. The precursor fibers prepared in this study have a single, sharp exothermic peak in the DTA curve, and their X-ray diffraction patterns indicate the direct transformation into the mullite phase from the amorphous phase. It is therefore con-

sidered, based on the discussions made by many researchers,<sup>7-14</sup>) that Al and Si are mixed with each other at atomic level in the precursor fibers, which is conceivably closely related to spinnability. On the other hand, the gel sample prepared from the unspinnable solution has a smaller exothermic peak at around 1000°C, suggesting that it is of mixed phase. It should be noted, however, that the direct synthesis of the mullite phase from the amorphous is indicated by the X-ray diffraction analysis,

**Table 1** Crystal phases of heat-treated precursor fibers or non-fibers produced from different sol-gel processes. Sample NO.a-g: see Figs.1 and 2 for the preparation conditions of the mullite fiber precursors.

Method	Sample NO.	Spinnability*	Calcination Temperature °C						
			400	600	700	800	1000	1300	
A	a	○	Am**	Mu	Mu	Mu	Mu	Mu	Mu
	b	○	Am	Mu	Mu	Mu	Mu	Mu	Mu
	c	×	Am	Am	Am	(Mu)	Mu	Mu	Mu
	d	×	Am	Am	Am	(Mu)	Mu	Mu	Mu
B	e	○	Am	Am	Mu	Mu	Mu	Mu	Mu
	f	×	Am	Am	Am	Am	Mu	Mu	Mu
	g	×	Am	Am	Am	(Mu)	Mu	Mu	Mu

\* ○ : spinnable, × : unspinnable  
 \*\* Am : amorphous, Mu : mullite.  
 ( ) : very poorly crystallized

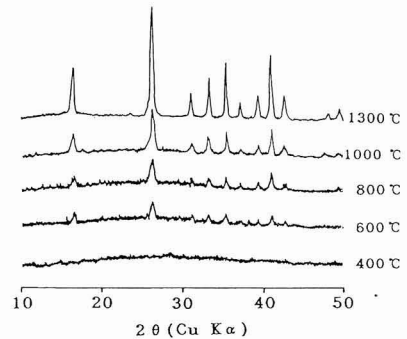


**Fig. 3.** X-ray diffraction patterns of heat-treated precursor fibers prepared from a solution of Method A(a) composition [Al(OPr)<sub>3</sub>]mol/Al(NO<sub>3</sub>)<sub>3</sub>mol=2/1 and H<sub>2</sub>Omol/(Al+Si)mol=20/1.

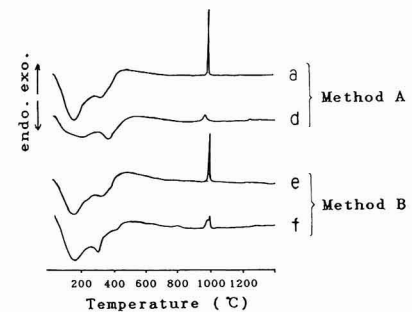


**Fig. 4.** DTA curves of solid phases obtained by Method A and Method B. a, e: spinnable, d, f: unspinnable. Sample No. a, d, e and f: see Figs.1 and 2 for the preparation conditions of the mullite fiber precursors.

by which is meant that the gel sample is different in extent of ununiformity from the mixed phases discussed so far by other researchers. It is observed in this study that the crystalline mullite phase was found in the sample heat-treated at a fairly low temperature of 600°C. This compares with around 1000°C which is generally accepted as a temperature at which the amorphous phase is crystallize into the mullite phase. This probably results from the presence of the structures close to those of mullite in the precursor fibers, which are crystallized into the mullite phase by heat-treatment carried out at as low as 600°C.

### 3.3. $^{27}\text{Al}$ - and $^{29}\text{Si}$ -NMR Analysis of Solution

#### 1) $^{27}\text{Al}$ -NMR Spectra of Spinnable and Unspinnable Solutions

Figure 5 shows the  $^{27}\text{Al}$ -NMR spectra of the spinnable, viscous solutions (a and b, so marked in Figs. 1 and 2), and the results of the linear analysis. It also shows the  $^{27}\text{Al}$ -NMR spectra of the unspinnable solutions (d and f) about to be gelled. In any case, the spinnable, viscous solutions have sharp peaks ① and ② at 0 and 4ppm, and a broad peak ③ at -15ppm. Furthermore, the solution prepared by Method A has a broad peak ④ at around -28ppm, in addition to the above. On the other hand, the unspinnable solutions have broad peaks at around 0 and 62ppm, the latter being marked with ⑤ in the figure. In general, the analysis of the bonding conditions of Al has been made with  $[\text{Al}(\text{H}_2\text{O})_6]^{3+}$  as the reference, considering that  $\text{AlO}_6$  having a peak at 10 to -20ppm to be relevant to the octahedral coordination and  $\text{AlO}_4$  having a peak at 30 to 80ppm to be relevant to the tetrahedral coordination,<sup>19)</sup> based on which the peaks found at around 0, 4, -15 and -28ppm are considered to be relevant to the octahedral coordination, and that having a peak at around 62ppm to the tetrahedral coordination. More circumstantially, the peak found at 0ppm is relevant to  $[\text{Al}(\text{H}_2\text{O})_6]^{3+}$ , and its rotational movement is prevented by the interactions with the neighboring atoms, judging from its broadness. The peak at 4ppm is relevant to  $[(\text{H}_2\text{O})_4\text{Al}(\mu\text{-OH})_2\text{Al}(\text{H}_2\text{O})_4]^{4+}$  (hereinafter referred to as Al-O dimer).<sup>20)</sup> Those found at around -15 and -28ppm are to the structures in which Al-O bonds are connected to, and interacted with, each other, like those in a polymer (such a structure is hereinafter referred to as alminoxane polymer), knowing that the Al-O bonds, when combined with each other, cause Al in the octahedral coordination to show a peak at a magnetic field higher than 0ppm and the peak is characterized by being broad.<sup>21)</sup> Here, the peak found at around 62ppm may be relevant to the tetrahedral coordination of Al consisting of Al-O-Si bonds,<sup>22)</sup> or to the tetrahedral coordination of Al positioned at the center of  $[\text{AlO}_4\text{Al}_{12}(\text{OH})_{24}(\text{H}_2\text{O})_{12}]^{7+}$  (hereinafter referred to as  $\text{Al}_{13}^{7+}$  polycation).<sup>23)</sup> The peak at 62ppm is not found in the spinnable, viscous solution, from which it is considered that it represents the tetrahedral coordination of Al positioned at the center of the  $\text{Al}_{13}^{7+}$  polycation. It is observed in the results by both Methods A and B that the  $\text{Al}_{13}^{7+}$  cation is found in the solution just short of gelation, as the  $\text{Al}(\text{OPr})_3/\text{Al}(\text{NO}_3)_3$  ratio increases, which is accompanied by linearity at around 0ppm. As a result, the solution no longer shows spinnability. It may be thus considered that expression of spinnability is prevented by the presence of the  $\text{Al}_{13}^{7+}$  polycation and formation of the three-dimensional polymer having the Al-O bond.<sup>21)</sup> The results by Method A differ from those by

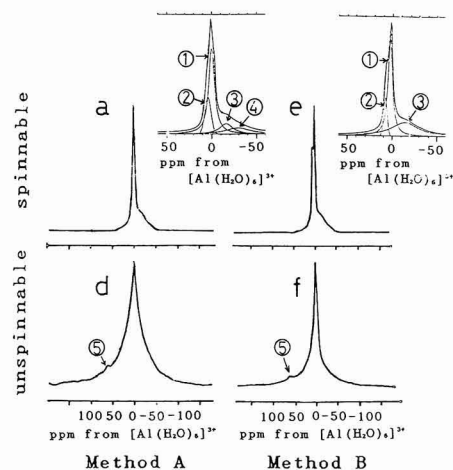


Fig. 5.  $^{27}\text{Al}$ -NMR spectra and their line shape analyses of the spinnable solutions through Method A and Method B. Sample No. a, d, e and f: see Figs. 1 and 2 for the preparation conditions of the mullite fiber precursors.

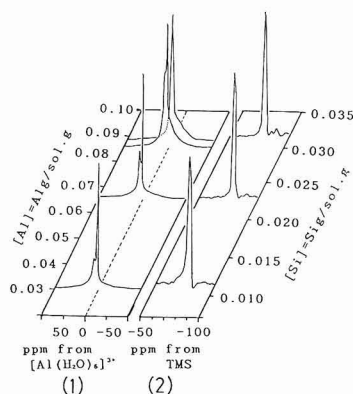


Fig. 6. Changes of  $^{27}\text{Al}$ -NMR spectra (1) and  $^{29}\text{Si}$ -NMR spectra (2) of the solution during concentration process.

Method A (a) composition  $[\text{Al}(\text{OPr})_3]_{\text{mol}}/\text{Al}(\text{NO}_3)_3_{\text{mol}} = 2/1$ ,  $\text{H}_2\text{O}_{\text{mol}}/(\text{Al}+\text{Si})_{\text{mol}} = 20/1$

Method B in an  $\text{Al}(\text{OPr})_3/\text{Al}(\text{NO}_3)_3$  ratio range from 5/1 to 7/1 mol/mol, as shown in Figs. 1 and 2. In Method B, TEOS is added to the system after aluminum isopropoxide is completely hydrolyzed with an aqueous solution containing aluminum nitrate. In Method A, on the other hand, aluminum isopropoxide and TEOS are simultaneously added to an aqueous solution containing aluminum nitrate, which causes silicon alkoxide to affect hydrolysis of aluminum alkoxide. This conceivably prevents formation of the three-dimensional polymer having the Al-O bond during the concentration process.

2) Changes in Al and Si Bonding Conditions during Concentration of Spinning Solution

Figure 6 gives changes in  $^{27}\text{Al}$ - and  $^{29}\text{Si}$ -NMR spectra

while the spinnable solution "a" (shown in Fig.1, prepared by Method A) is concentrated. The spinnable solution "e" (shown in Fig.2, prepared by Method B) has similar spectral changes during the concentration process, though not shown. First, the diluted solution ( $[Al]=0.031\text{g/g}$  of sol) has peaks at 0 and 4ppm. The peaks at 0 and 4ppm are, as discussed earlier, relevant to octahedral-coordinated Al in  $[Al(H_2O)_6]^{3+}$  and Al-O dimer structures. This solution, while being concentrated, has the peak at 4ppm increasing in its intensity and, at the same time, a broad peak at a magnetic field higher than 0ppm. The  $^{29}\text{Si}$ -NMR spectra, on the other hand, are characterized by the peak of tetraethyl silane (TMS) at -81ppm. Its peaks change little as the diluted solution ( $[Si]=0.011\text{g/g}$  of sol) is concentrated, except for very small peaks found at -88 and -93ppm. In general, the peak at -81ppm is relevant to  $Q^1$ , that at -88ppm to  $Q^2$  or  $Q^4$  (3Al), and that at -93ppm to  $Q^3$  or  $Q^4$  (2Al), where  $Q^n$  is Si bonded to the  $\text{SiO}_4$  tetrahedron, n is number of oxygen atoms bonded to the  $\text{SiO}_4$  tetrahedron,  $Q^n$  (mAl) is Al bonded to the  $\text{SiO}_4$  tetrahedron,  $0 \leq n \leq 4$ , and  $0 \leq m \leq 4$ .<sup>26)</sup> It is considered that the peaks at -81, -88 and -93ppm are relevant to, judging from their relative intensity,  $(OH)_3\text{Si-O-Si(OH)}_3$  (siloxane dimer) and an oligomer consisting of several siloxane units (hereinafter referred to as siloxane oligomer), or the siloxane dimer and a polymer consisting of several Al atoms and several siloxane units. It is also considered, if the latter is the case, that the peak of Al bonded to Si overlaps one of the peaks of Al shown in Fig.5.

To summarize: the atomic level Al and Si, such as Al-O dimer,  $[Al(H_2O)_6]^{3+}$  and siloxane dimer, are predominant in the diluted solution. Concentration of such solution is accompanied by bonding of some  $[Al(H_2O)_6]^{3+}$  units to others, to form Al-O dimer and increase its proportion in the system,<sup>27)</sup> and also by advent of oligomer or siloxane oligomer having Si-O-Al bond. Further concentration of the solution to a stage immediately before spinnable concentration ( $[Al]=0.086\text{g/g}$  of solution,  $[Si]=0.032\text{g/g}$  of solution) increases concentrations of oligomer or siloxane oligomer having Si-O-Al bond and aluminosiloxane polymer, to help the solution show spinnability. The unspinnable gel-like substance, prepared by hydrolyzing the aqueous TEOS system for concentration in the presence of nitric acid as the catalyst, has a broad peak at -115ppm, as revealed by the  $^{29}\text{Si}$ -NMR analysis. No such peak is found in the spinnable solutions prepared by Methods A and B, from which it is considered that spinnability is not affected by the Si-O bond which is incapable of forming the three-dimensional structures and remains mostly as siloxane dimer.

### 3.4. Structures of Precursor Fibers

The structures of precursor fibers are characterized by aluminosiloxane polymer, oligomer or siloxane oligomer having Si-O-Al bond, Al-O dimer, siloxane dimer and  $[Al(H_2O)_6]^{3+}$ , which are bonded to each other directly or via neighboring water molecules by hydrogen, ionic or coordination bonding. Microscopically, such a system consists of two portions, one being characterized by Al and Si which are mixed at atomic level, though not bonded to each other, and the other by these atoms which are not mixed at atomic level. The former portion is represented by Al ion and siloxane dimer, and the latter by aluminosiloxane polymer and siloxane oligomer. Heat treatment of the fibrous precursor to transform it into the mullite phase proceeds in several

steps. First, dehydration occurs at around 160°C, to deprive siloxane dimer,  $[Al(H_2O)_6]^{3+}$  and Al-O dimer, in which Al and Si are mixed with each other at nearly atomic level, of their water of hydration. Elimination of hydroxide group follows at 200 to 300°C. Those portions in which Al and Si are present in a ratio close to the mullite composition are crystallized at around 600°C, without showing definite exothermic peak in the DTA analysis, i.e., essentially without being accompanied by rearrangement of the atoms. At around 1000°C, those portions which have not been crystallized into the mullite phase are transformed into the mullite phase, which is accompanied by the sharp exothermic peak in the DTA analysis. It is also considered that aluminosiloxane and siloxane polymers, being not developed three-dimensionally, are transformed into the mullite phase in this stage.

Figure 7 presents the SEM images of the precursor fibers and those fibers fired at 1300°C for 1h, prepared by Methods A and B. Each of the precursor and fired fibers has cracks, but densified highly. It is generally observed that the reaction process of metallic ions in which diffusion is involved, being accompanied with growth of the crystallites, is characterized by the large grains present in the product, which also supports uniformity of the systems prepared in this study.

## 4. Conclusions

- 1) The mullite precursor fibers are prepared by two methods, one being characterized by the simultaneous addition of aluminum isopropoxide and TEOS to the aqueous solution containing aluminum nitrate, and the other by the separate addition of aluminum isopropoxide and TEOS,

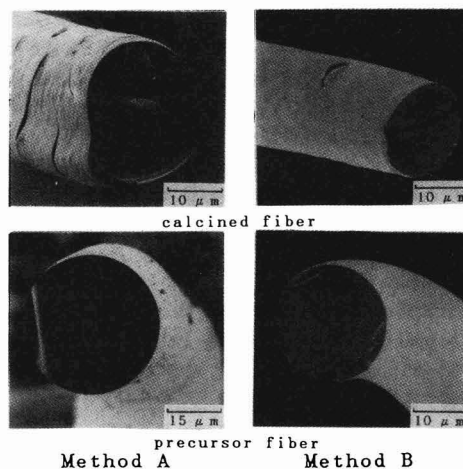


Fig. 7. SEM images of precursor and calcined fibers by Method A and Method B.

Method A:(a) composition  $[Al(OPr)_3]_{\text{mol}}/Al(NO_3)_3_{\text{mol}}=2/1$ ,  $H_2O_{\text{mol}}/(Al+Si)_{\text{mol}}=20/1$  Method B:(e) composition  $[Al(OPr)_3]_{\text{mol}}/Al(NO_3)_3_{\text{mol}}=2/1$ ,  $H_2O_{\text{mol}}/(Al+Si)_{\text{mol}}=20/1$

in this order.

- 2) The solutions prepared by the former method has a wider spinnable region, shown on the map in which molar  $H_2O/(Al + Si)$  ratio is plotted against molar  $Al(OPr^i)_3/Al(NO_3)_3$  ratio, than those prepared by the latter method, indicating that expression of spinnability is related Al and Si bonding conditions in the solution.
- 3) The precursor fiber consists of Al and Si atoms, aluminoxane polymers, and siloxane oligomer. It has a single, sharp peak at around 1000°C in the DTA curve, by which is meant that it will be transformed into the mullite phase through the rearrangement of the atoms, without being accompanied by diffusion of these atoms. When fired, it is crystallized into the mullite phase at around 600°C directly from the amorphous state, from which it is judged that it already has the structures compositionally similar to the mullite phase.

#### Acknowledgements

The authors deeply thank Dr. Y. Onoda of the Science and Technology Agency's National Institute for Researches in Inorganic materials for his valuable advice on MMR measurement.

#### Reference:

- 1) K. Kamiya, S. Sakka and N. Tashiro, *Yogyo-Kokaishi*, 84, 12, 36-40 (1976).
- 2) P. Bracke, H. Schurmans and J. Verhoest, *Inorganic Fibers and Composite Materials* Pergman Press (1984) p.40.
- 3) J.D. Birchall, *Trans. J. Br. Ceram. Soc.*, 82, 143-147 (1983).
- 4) H. Suzuki and H. Saito, *Yogyo-Kyokaishi*, 95, 7, 697-702 (1987).
- 5) L.V. Interrante and A.G. Williams, *Polymer Prepr.*, 25, 1, 13-14 (1984).
- 6) A.G. Williams and L.V. Interrante, *Better Ceramic through Chemistry* Elsevier (1984) p.151-156.
- 7) J.A. Pask, X.W. Zhang, A.P. Tomsia and B.E. Yolda, *J. Am. Ceram. Soc.*, 70, 10, 704-707 (1987).
- 8) D.W. Hoffman, R. Roy and S. Komarneni, *J. Am. Ceram. Soc.*, 67, 7, 468-471 (1984).
- 9) S. Komarneni, Y. Suwa and R. Roy, *J. Am. Ceram. Soc.*, 69, 7, C155-C156 (1986).
- 10) A.K. Chakravorty and D.K. Ghosh, *J. Am. Ceram. Soc.*, 69, 8, C202-C203 (1986).
- 11) B.E. Yoldas and D.P. Partlow, *J. Mater. Sci.*, 23, 1895-1900 (1988).
- 12) J.C. Huling and G.L. Messing, *J. Am. Ceram. Soc.*, 72, 9, 1725-1729 (1989).
- 13) C.S. Hsi, H.Y. Lu and F.S. Yen, *J. Am. Ceram. Soc.*, 72, 11, 2208-2210 (1989).
- 14) K. Okada and N. Otsuka, *ibid.*, 69, 9, 652-656 (1986).
- 15) T. Kanzaki and H. Tabata, *ibid.*, 68, 1, c6-C7 (1985).
- 16) T. Kumazawa, S. Kanzaki, J. Asaumi, O. Abe and H. Tabata, *Yogyo-Kyokaishi*, 94, 3, 485-490 (1986).
- 17) H. Suzuki, Y. Tomokiyo, Y. Suyama and H. Saito, *Nippon-Seramikkusu-Kyokai-Gakujutsu-Ronbunshi*, 96, 1, 67-73 (1988).
- 18) Y. Hirata, H. Minamizono and K. Shimada, *Yogyo-Kyokaishi*, 93, 1, 46-54 (1985).
- 19) M.H. Lewis, *Glasses and Glass Ceramics* Chapman and Hall (1989) p.6.
- 20) J.W. Akitt and B.E. Mann, *J. Magn. Reson.*, 44, 584-589 (1981).
- 21) T. Nishio and Y. Fujiki, *Nippon-Seramikkusu-Kyokai-Gakujutsu-Ronbunshi*, 98, 11, 1223-1230 (1990).
- 22) D. Mueller, D. Hoebbel and W. Gessner, *chem. Phys. Lett.*, 84, 1, 25-29 (1981).
- 23) L.F. Nazar and L.C. Klein, *J. Am. Ceram. Soc.*, 71, 2, C85-C87 (1988).
- 24) L.W. Kelts, N.J. Efinger and S.M. Melpolder, *J. Non-Cryst. Solids*, 83, 353-374 (1986).
- 25) E. Lippmaa, M. Magi, A. Samoson, G. Engelhardt and A.R. Grimmer, *J. Am. Chem. Soc.*, 102, 4889-4893 (1980).
- 26) K.A. Smith, R.J. Kirkpatrick, E. Oldfield and D.M. Henderson, *Am. Miner.*, 68, 1206-1215 (1983).
- 27) B.R. Baker and R.M. Pearson, *J. Catal.*, 33, 265-278 (1974).

---

This article is a full translation of the article which appeared in *Nippon Seramikkusu Kyokai Gakujutsu Ronbunshi* (Japanese version), Vol.99, No.8, 1991.

# Effect of Process-Related Oxidation on Microstructure and Mechanical Properties of $\beta'$ -o' Sialon Ceramics

Kazuya Yabuta, Hiroaki Nishio and Keizo Uematsu\*

Advanced Technology Research Center, NKK Corporation,  
1-1 Minami-wataridacho, Kawasaki-ku, Kawasaki-shi, 210 Japan

\*Department of Chemistry, Nagaoka University of Technology  
Kamitomioka-cho, Nagaoka-shi, 940-21 Japan

To study the effect of process-related oxidation on microstructure and mechanical properties of  $\beta'$ -o'sialon, green compacts of a Silicon nitride powder and boehmite sol were prepared through mixing, calcination and dewaxing processes, followed by sintering and HIPing. With progressive oxidation of the Silicon nitride powder in processing, the amount of o'-phase increased and the grain size of o'-phase was changed. With increasing amount of o'-phase in the sintered body, the lattice constants of  $\beta'$ -phase and hardness increased. the high temperature flexural strength of  $\beta'$ -o'sialon ceramics was governed by mixing conditions rather than by the o'-phase ratio.

[Received November 30, 1990; Accepted May, 23, 1991]

**Key-words:**  $\beta'$ -o'sialon, Silicon nitride,  $\text{Si}_3\text{N}_4$ , Boehmite, HIP, Microstructure, Strength, Hardness, Mechanical properties.

## 1. Introduction

Sialon ceramics, together with silicon carbide and silicon nitride, are promising as a material for engines.<sup>1-5)</sup> In particular,  $\beta'$ -o' sialon, produced by adding only alumina as an assistant to silicon nitride, is attracting considerable attention because of its high strength at high temperatures and its high resistance to oxidation.<sup>6-13)</sup> The recent researches on sialon have revealed that a small quantity of oxygen contained in silicon nitride changes the ratio of  $\beta'$ -phase to o'-phase and the mechanical properties.<sup>6,7)</sup> The oxygen content that has an effect on sialon should include not only the oxygen content in silicon nitride but also the oxidation of silicon nitride powder occurring in the manufacturing process before sintering. It is, therefore, important that the chemical composition of green compact to be sintered be identified as  $\text{Si}_3\text{N}_4\text{-SiO}_2\text{-Al}_2\text{O}_3$ . In determining the oxygen content by direct analysis, however, there are problems of the increase in oxygen content on grinding for analysis and the impurities entering from the grinding equipment. For this reason, it is very difficult to exactly determine the oxygen content by wet analysis in each process of usual method for manufacturing ceramics, including mixing, drying, pressing, dewaxing, and sintering.

The authors reported<sup>9)</sup> that we found a method for determining the o'-phase in sialon, that the oxygen content in a sample can be estimated indirectly from the amount of o'-phase found in sintered body, that the process-related oxidation can be investigated, and that the oxygen content can be

represented by the amount of o'-phase in HIPed body. This method is easy to understand because the amount of o'-phase can be dealt with as one parameter in studying the effect of mixing and dewaxing conditions on the sintered body. In this work, we prepared three kinds of samples under varied manufacturing conditions and evaluated the relationship between the manufacturing conditions and the microstructure and mechanical properties in terms of the amount of o'-phase.

## 2. Experimental Method

Figure 1 shows the process flow for preparing samples. The starting material used in this experiment were  $\alpha\text{-Si}_3\text{N}_4$  powder (Ube Industries, Ltd., oxygen content: 1.1wt%) and alumina sol (Nissan Chemical Industries, Ltd.). The alumina content in the alumina sol was determined from the residual quantity after calcining at 1200°C. Two materials were weighed so that the residual quantity of  $\text{Al}_2\text{O}_3$  is 9wt%, and then mixed with deionize water. The mixing was performed by using an attrition mill (hard) for 6hrs and using a ball mill (soft) for 20hrs. The mixture was dried at 110°C and calcined in the air at 500°C or 900°C for 2hrs after being passed through a 0.5mm screen. This calcined mixture was again mixed with deionized water by means of the above described ball mills. Then, the mixture was dried at 110°C, passed through a 0.5mm screen, and prepressed into 25×80×20mm sample under 30MPa by using a metal mold. After that, the sample was pressed by CIP under 300MPa. This compact was dewaxed and sintered in the air at 500°C and 900°C for 2hrs each. Table 1 gives the process conditions for different samples. The obtained compact was

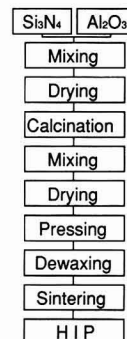


Fig. 1  $\beta'$ -o' sialon process flow.

**Table 1.**  $\beta'$ - $\alpha'$  sialon process conditions.

process	Mixing Method	Calculated Temp. (°C)	Dewaxed Temp. (°C)
A	Soft	500	500
B	Hard	900	500
C	Hard	900	900

**Table 2.** Density and  $\alpha'$ -phase ratio after HIPing in  $\beta'$ - $\alpha'$  sialon.

process	Density after HIP (g/cm <sup>3</sup> )	$\alpha'$ ratio after HIP (vol%)
A	3.123	19.4
B	3.083	24.1
C	3.033	32.0

sintered at 1900°C under 1MPa of N<sub>2</sub> for 2hrs, and then HIPed at 1900°C under 190MPa of Ar-N<sub>2</sub> mixture gas (N<sub>2</sub> partial pressure:20MPa) to yield  $\beta'$ - $\alpha'$  sialon measuring about 20×65×15mm. The quantitative analysis of  $\alpha'$  sialon was performed by the analysis method reported previously on the basis of the X-ray diffraction peak. For X-ray diffraction, the cut surface that has been mirror polished was irradiated directly with X-rays. The  $\alpha'$ -phase ratio of the sintered body was determined from the reflection integral strength on (101), (210) planes of  $\beta'$ -Si<sub>3</sub>N<sub>4</sub> and (110), (020) planes of Si<sub>2</sub>N<sub>2</sub>O by using the following equation.

$$(\alpha' - \text{ratio}) = \frac{|\alpha'_{110}| + |\alpha'_{020}|}{|\alpha'_{110}| + |\alpha'_{020}| + |\beta'_{101}| + |\beta'_{210}|} \times 100$$

The  $\alpha'$ -phase ratio in volume of each sample was determined by using the relationship<sup>6)</sup> between the  $\alpha'$ -phase ratio obtained from the X-ray diffraction and the  $\alpha'$ -phase ratio obtained from the image analysis results of EPMA photographs. In addition, the shape of  $\alpha'$ -phase was investigated by observing the polished surface by EPMA. Part of sintered body was ground, and the lattice constant of  $\beta'$ -phase was measured by X-ray diffraction with metallic silicon as an internal standard. To evaluate mechanical properties, Vickers hardness was measured under a load of 20kg for 15seconds, and three-point bending test was made at 1350°C in the atmosphere in accordance with JIS.

To investigate the phase produced in sintering, the phase was identified by X-ray diffraction on the samples prepared by sintering at 1750°C for 5 minutes or 1800°C for 5minutes or 1900°C for 2hrs under 1MPa of N<sub>2</sub> for the samples obtained by processes A and B in Table 1.

Additionally, to find the average composition of each phase of HIPed specimen, the HIPed specimen prepared by process B was observed with a TEM. For grains identified as  $\beta'$ -phase and  $\alpha'$ -phase by electron diffraction in transmission electron microscopy, five grains for each sample were analyzed to determine the Al concentration by wt% under the condition that the sum of Si and Al is 1.

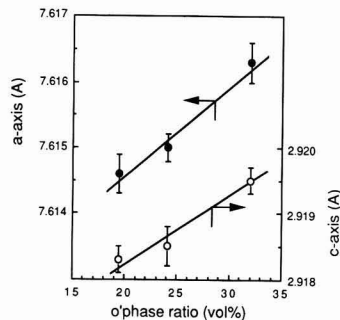
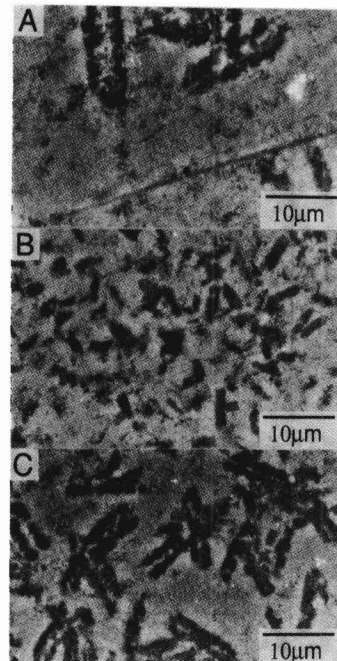
### 3. Results

**Table 2** gives the density and  $\alpha'$ -phase ratio after HIPing for the samples prepared by different processes. The conditions of mixing and heating are severer in that order of

process A, B, and C, severer oxidation occurring. In this table, the density decreases in that order; conversely,  $\alpha'$ -phases ratio increases in that order.

**Figure 2** shows the relationship between  $\alpha'$ -phase ratio and  $\beta'$ -phase lattice constant for the sample prepared for different processes. The lattice of  $\beta'$ -phase increases almost linearly for both a- and c-axis as the  $\alpha'$ -phase ratio increases, though there are some deviations. The lattice constant of  $\alpha'$ -phase increased with the increase in  $\alpha'$ -phase ratio, with large deviations (the result is not shown in the figure).

**Figure 3** shows the electron-probe microanalyzer pictures of  $\beta'$ - $\alpha'$  sialons after polishing for samples prepared by different processes. As the  $\alpha'$ -phase ratio increases, the area ratio of  $\alpha'$ -phase corresponding to the dark portions in the picture, and its size increase. The size of  $\alpha'$ -phase was

**Fig. 2.** Effect of  $\alpha'$ -phase contents on  $\beta'$ -sialon lattice constants for the HIPed specimen.**Fig. 3.** Electron-probe microanalyzer pictures of  $\beta'$ - $\alpha'$  sialons after polishing. (A): process A, (B): process B, (C): process C.

about 15 $\mu\text{m}$  for process A producing 19.4vol%  $\text{o}'$ -phase ratio, about 3 $\mu\text{m}$  for process B producing 24.1vol%, and about 8 $\mu\text{m}$  for process C producing 32.0vol%.

**Table 3** gives the average Al content of five grains of  $\beta'$ -phase and  $\text{o}'$ -phase obtained by TEM analysis. The Al content ranged 8–13wt% for  $\beta'$ -phase, and 2–4wt% for  $\text{o}'$ -phase.

**Figure 4** shows the effect of  $\text{o}'$ -phase content on three-point bending strength at 1350°C and Vickers hardness for the HIPed specimen. These values are denoted by block circles and black triangles, respectively. As the  $\text{o}'$ -phase ratio increases, the hardness increase proportionally, but the high-temperature strength has a peak value, which is 650MPa for process B of 24.1vol%.

**Table 4** gives the phase composition of the specimen prepared by processes A and B with different sintering conditions. The sintering conditions were 1700°C for 5minutes, 1800°C for 5minutes, and 1900°C for 2hrs. The  $\alpha$ -phase is detected for process A but not for process B at a sintering temperature of 1800°C. The  $\text{o}'$ -phase is not detected even at 1800°C for process A, but is detected at 1700°C for process B.

## 4. Discussion

### 4.1. Difference in Density of HIPed Specimen with Process

As shown in Table 2, the density after HIPing changes

**Table 3.** EDX analysis of the specimen prepared by process B condition.

	Al content (wt%)
$\beta'$ -sialon grain	8-13
$\text{o}'$ -sialon grain	2-4

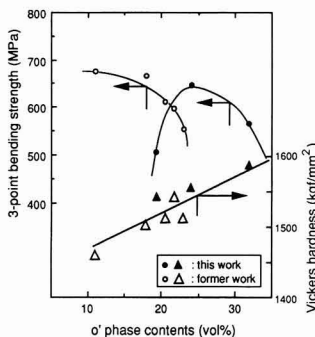


**Fig. 4.** Effect of  $\text{o}'$ -phase contents on 3-point bending strength at 1350°C and Vickers hardness for the HIPed specimen.

**Table 4.** Phase compositions of the specimen prepared by processing (A) and (B) with different sintering temperature.

Process	Sintering Conditions		
	1700°C 5min	1800°C 5min	1900°C 2hour
A	$\alpha, \beta, x$	$\alpha, \beta, x$	$\beta, \text{o}$
B	$\alpha, \beta, x, \text{o}$	$\alpha, \beta, \text{o}$	$\beta, \text{o}$

greatly with the manufacturing process. In the electron-probe microanalyser picture in Fig.3, pores are not found; the specimens are fully dense for all processes. Judging from the fact that the density of  $\text{o}'$ -phase is 2.815g/cm<sup>3,14</sup> and that of  $\beta'$ -phase ( $Z=1$ ) is 3.123g/cm<sup>3,15</sup> the difference in intensity may depend on the  $\text{o}'$ -phase ratio in the structure.

On the other hand, since any process uses the same starting materials, it is considered that the difference intensity results from the oxidation of silicon nitride yield in the manufacturing process. In this study, the oxidation of silicon nitride powder occurs mainly in the alumina sol mixing process, calcination process in the air, re-mixing process after calcination, and dewaxing process. Naturally, process C where dewaxing is done of 900°C produces higher oxygen content than process B where dewaxing is done at 500°C. In process A, oxidation of silicon nitride is restricted more than process B in mixing, calcination, and re-mixing processes; therefore, lower oxygen content is provided. The difference in oxygen content produces the change in the amount of  $\text{o}'$ -phase, and in turn the change in the density of HIPed specimen.

### 4.2. Increase in Oxidation and $\beta'$ -phase Lattice Constant Due to Process

**Figure 5** shows a part of the phase diagram reported by Naik et al.<sup>16</sup> and the starting materials in the present work (point a). Since the silicon nitride powder for raw material contains 1.1wt% of oxygen, the starting composition is represented as Si<sub>3</sub>N<sub>4</sub> 89.1wt%, SiO<sub>2</sub> 1.9wt%, and Al<sub>2</sub>O<sub>3</sub> 9.0wt%. Since the ratio of cation (Si/Al) is kept constant even when oxidation occurs in the process, it is considered that only the ratio of anion (O/N) changes. The average composition of the system shifts from point a to point b, c and d toward SiO<sub>2</sub> side as the oxidation proceeds. All these points in Fig.5 are in the region where  $\beta'$ -phase and  $\text{o}'$ -phase co-exist. It is considered that a tie lines (lines connecting the equilibrium composition of  $\beta'$ -phase to that of  $\text{o}'$ -phase) exist as shown in Fig.5. These tie lines move to the opposite side of Si<sub>3</sub>N<sub>4</sub> as the oxygen content increases, i.e. point a shifts to point d; the intersection of the tie line and  $\beta'$ -phase moves gradually in the direction apart from Si<sub>3</sub>N<sub>4</sub>. Since this intersection is the composition of  $\beta'$ -phase existing for equilibrium of a, b, c, and d point compositions, the Z value at the  $\beta'$ -phase (Si<sub>6-Z</sub>Al<sub>2</sub>O<sub>2</sub>N<sub>8-Z</sub>) may increase with the increase in oxygen content. Mitomo et al. reported that the  $\beta'$ -phase lattice expands with the increase in the Z value of  $\beta'$ -phase.<sup>14</sup> It is considered, therefore,

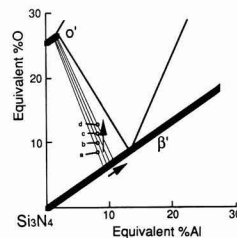


**Fig. 5.** Compositions investigated in present work shown as a part of Si<sub>3</sub>N<sub>4</sub>-SiO<sub>2</sub>-Al<sub>2</sub>O<sub>3</sub>-AlN phase diagram.

a: Composition calculated from starting materials.

b-d: Compositions of sintered bodies having various oxygen contents.

that the expansion of lattice with the increase in  $\alpha'$ -phase results from the increase in the Z value of  $\beta'$ -phase existing in equilibrium.

Considering that the tie lines in fig.5 do not cross, and that the Z value increases with the increase in the amount of  $\alpha'$ -phase as shown by the experimental results, the dissolution limit of  $\text{Al}_2\text{O}_3$  into the  $\alpha'$ -phase must be lower than the  $\text{Al}_2\text{O}_3$  content in the starting composition; lower than  $x=0.167$  when representing as  $\text{Si}_{2x}\text{Al}_x\text{O}_{1+x}\text{N}_{2x}$ . This agrees with the result obtained by Trigg et al.<sup>4)</sup> that the dissolution limit is  $x=0.15$  in  $\text{Si}_{2x}\text{Al}_x\text{O}_{1+x}\text{N}_{2x}$ . In the present experiment, the lattice constant of  $\alpha'$ -phase slightly increased as the  $\alpha'$ -phase increased. However, the change in this phase should be studied in the future because the diffraction peak was low and the measurement error was large in the present experiment.

#### 4.3. Difference in Oxidation and Structure with Process

As shown by EPMA in Fig.3, the size of  $\alpha'$ -phase definitely differs between process A and process B. The possible reasons for this difference are (1) the difference in mixing effect and (2) the difference in oxygen content. Process A of insufficient mixing may produce large size of  $\alpha'$ -phase, and process B of uniform mixing may produce small size of  $\alpha'$ -phase. As reported previously, however, on the specimen whose amount of  $\alpha'$ -phase was changed by mixing under the same condition and changing the oxidation conditions, the average longer diameter of  $\alpha'$ -phase decreased with the increase in  $\alpha'$ -phase ratio in the range of 11.0 to 23.1vol%.<sup>6)</sup> In the present work as well, the same trend as that described in the previous report is found for process A of 19.4vol%  $\alpha'$ -phase and process B of 24.1vol%. Therefore the difference in size of  $\alpha'$ -phase can be explained in terms of either the difference in mixing effect or the difference in oxygen content.

The phase given in Table 4 are the phase found when the specimen are cooled to normal temperature after sintering. The x-phase may exist as liquid phase during sintering and then deposit during cooling since this phase does not exist in the phase diagram of Naik et al.<sup>16)</sup> at 1800°C. The results given in Table 4 indicate that  $\alpha'$ -phase is less prone to deposit for process A than process B, prolonging the life of liquid phase. This fact may result from the difference in mixing, that is, the prolonged liquid phase may be ascribed to poorer mixing in process A than in process B. However, this fact can also be explained in terms of the oxygen content. The liquid phase yielded on sintering may have a composition in which a small amount of silicon nitride dissolve into the oxide of  $\text{Al}_2\text{O}_3$  and  $\text{SiO}_2$ . Since the sample of process B, which oxidizes vigorously in the process, has a higher  $\text{SiO}_2$  content than the sample of process A, the yielded liquid phase has a lower Al content. As described in 4.2, the Al content of  $\alpha'$ -phase is lower than the average composition. Considering the cation ratio (Si/Al), the liquid phase produced by process B has a composition closer to that of  $\alpha'$ -phase than the liquid phase produced by process A. From the fact that process B which has a small difference in composition between liquid phase and  $\alpha'$ -phase, provides more rapid deposition than process A with a larger difference in composition, the difference in the life of liquid phase can be understood.

#### 4.4. Relative Ratio and Mechanical Properties

The three-point bending strength at 1350°C reaches its

maximum value for 24.1vol%  $\alpha'$ -phase. This fact must be investigated in terms of both the effect of mixing and the oxygen content as discussed in 4.3. In Fig.4, the white circles and triangles denote the three-point bending strength and hardness, respectively, at 1350°C for the specimen whose oxygen content is controlled by dewaxing at different temperatures.<sup>7)</sup> In the experiment, the same raw materials as those in the present experiment were used. The materials were mixed in a ball mill for 20hrs, and then a binder was added to them to produce grains by spray drying. Therefore, the powder packing in the compact may be more uniform than that for process A in the present experiment. In the specimen system used in the previous experiment, the mixing condition of silicon nitride and alumina was kept constant because the dewaxing temperature was the only parameter. The results of previous work reveals that the three-point bending strength at 1350°C decreases in accordance with the amount of  $\alpha'$ -phase if the mixing condition is equal. In the present experiment, the samples of processes B and C are mixed in nearly the same condition by using the same stirring type ball mill, and have different oxygen content. The higher strength of sample of process B than that of process C results from a smaller amount of  $\alpha'$ -phase in the HIPed specimen; that is, the difference in strength is ascribed to the difference in oxygen content. From the viewpoint of the amount of  $\alpha'$ -phase, the three-point bending strength for process A is expected to be higher than that for process B; nevertheless, the strength was found to be lower in the present experiment. This may be because of nonuniform mixing. At normal temperature, five specimens for each process were subjected to the bending test. The result showed a large variation, so that no difference in strength with process was not found. The SEM observation of fracture surface at normal temperature revealed that on almost all specimens, fracture started at a surface defect that might be formed in preparing the specimen. It was, therefore, judged that the normal-temperature strength did not represent the difference in process. For this reason, the test result of normal-temperature strength has been excluded from this report. For the test at 1350°C, the variation in strength is within about 5% for all processes. It is, therefore, judged that the strength at 1350°C represents the difference in process. The SEM observation of fracture surface at 1350°C did not identified the origin of fracture because the fracture surface oxidized.

The hardness increased linearly as the amount of  $\alpha'$ -phase increased in both the previous and present experiments. This fact agrees with the fact reported by Larker et al.<sup>17)</sup> that the  $\alpha'$ -phase has higher hardness than the  $\beta'$ -phase. The hardness may depend mainly on the phase ratio and not be affected greatly by other factors.

## 5. Conclusions

Dense sialon samples were prepared by changing the mixing, calcination, and dewaxing conditions from silicon nitride and alumina sol to study the relationship between these conditions and microstructure and mechanical properties. The results are as follows:

- 1) As the oxidation in process is violent, the amount of  $\alpha'$ -phase in the sintered body increases.
- 2) Even if the same starting materials are used, the deposi-

tion behavior of  $\alpha'$ -phase and the life of transient liquid phase producing in sintering differ greatly with the difference in process.

- 3) As the amount of  $\alpha'$ -phase in the sintered body increases, the lattice constant of  $\beta'$ -phase increases.
- 4) The hardness depends on the phase ratio, whereas the high-temperature strength is affected by not only the phase ratio but also the mixing condition.

**References:**

- 1) K.H. Jack, J. Mater. Sci., 11, 1135-1158 (1976).
- 2) Y. Koyama and O. Kamigaito, *Yogyo-Kyokaishi*, 80, 327-336 (1972).
- 3) Z.K. Haug, P. Greil and G. Petzow, *Ceramics International*, 10, 14-17 (1984).
- 4) M.B. Trigg and K.H. Jack, Proc. Int. Sympo. on Ceramic Components for Engines, 199-207 (1983).
- 5) D.P. Thompson, W.-Y. Sun and P.A. Walls, *ibid.*, 643-650 (1988).
- 6) K. Yabuta, H. Nishio and K. Uematsu, J. Ceram. Soc. Jpn., 99, 2, 173-177 (1991).
- 7) K. Yabuta, H. Nishio and K. Uematsu, J. Am. Ceram. Soc. 74, 884-886 (1991).
- 8) S. Umeyayashi, K. Kishi, E. Tani and K. Kobayashi, *Yogyo-Kyokaishi*, 92, 45-51 (1984).
- 9) E. Tani, H. Ichinose, K. Kishi, S. Umeyayashi and K. Kobayashi, *ibid.*, 92, 675-679 (1984).
- 10) K. Kishi, S. Umeyayashi, E. Tani and K. Kobayashi, *ibid.*, 93, 629-635 (1985).
- 11) K. Kishi, S. Umeyayashi and K. Kobayashi, J. Ceram. Soc. Jpn, 96, 546-550 (1988).
- 12) K. Kishi, S. Umeyayashi and E. Tani, J. Materials Sci., 25, 2780-2784 (1990).
- 13) K. Yabuta, H. Nishio and H. Okamoto, Proc. Int. Sympo. on Ceramic Components for Engines, 622-630 (1988).
- 14) JCPDS Powder Diffraction File No.33-1162, International Centre for Diffraction Data (1983).
- 15) M. Mitomo and N. Kuramoto, *Yogyo-Kyokaishi*, 87, 141-146 (1979).
- 16) I.K. Naik, L.J. Gaucker and T.Y. Tien, J. Am. Ceram. Soc. 61, 332-335 (1978).
- 17) R. Larker, B. Loberg and T. Johansson, Proc. Int. Sympo. on Ceramic Components for Engines, 503-512 (1988).

---

This article is a full translation of the article which appeared in *Nippon Seramikkusu Kyokai Gakujutsu Ronbunshi* (Japanese version), Vol.99, No.8, 1991.

# Internal Friction in MgAl<sub>2</sub>O<sub>4</sub> Spinel Doped with Gallium Oxide or Alumina

Yasuhiro Yoshimura, Takeshi Nakamura\*, Ken'ichi Matsushita\*\*, Taira Okamoto\*\* and Susumu Goda\*\*\*

Mechanical Engineering Research Lab., Hitachi Ltd., 502 Kandachi-cho Tsuchiura-shi, 300 Japan

\*Kumano Technical College, 2800 Arima-cho Kumano-shi, 519 Japan

\*\*ISIR Osaka Univ., 8-1 Mihogaoka Ibaraki-shi, 567 Japan

\*\*\*Faculty of Eng. and Sci., Kinki Univ., 3-4 Kowakae, Higashi-Osaka-shi, 577 Japan

**Internal friction and shear modulus in MgAl<sub>2</sub>O<sub>4</sub> spinel doped with gallium oxide or alumina were measured from room temperature to 1473K. An internal friction peak was observed at 1123K and the peak area was proportional to the concentration of gallium oxide or alumina in the spinel. The activation energy of the stress induced diffusion of cation vacancies increases from 200kJ/mol to 450kJ/mol with increasing gallium oxide concentration. Effects of ionic radius and gallium and aluminum ion concentration on internal friction peaks have been discussed.**

[Received December 11, 1990; Accepted May 23, 1991]

**Key-words:** Internal friction, Spinel, Elastic modulus, Ion, Vacancy, Diffusion

## 1. Introduction

Oxides, nitrides etc. are industrially used as aids for the sintering of ceramics. Such sintering aids react with themselves and matrix, then form double oxides and oxy-nitrides. Tertiary and quaternary compounds added as sintering aids either combine with compounds formed during sintering (producing more complicated double oxides and oxy-nitrides) or dissolve in compounds. If an oxide dissolves in a double oxide formed by the reaction to sintering aids in case of the valency of metallic ion in oxide as an sintering aid differ to that of double oxide, ion vacancies are formed in double oxide. Internal friction peak are observed in such compounds having ion vacancies.

Magnesium aluminate (MgAl<sub>2</sub>O<sub>4</sub>) spinel is a compound produced by the reaction of alumina with magnesium which often used as a sintering aid for alumina ceramics. The spinel dissolves alumina and gallium oxide.<sup>2,3)</sup>

The present work is studied on the effect of concentration and ion radius of gallium and aluminum ion in spinel ceramics doped with gallium oxide and alumina, which is trivalent metallic oxide with different ion radius, on internal friction peak.

## 2. Experimental Procedure

The specimens were made as follows: magnesium aluminate powder was mixed with 5 to 50 mol% gallium oxide powder (99.9%, made by Kojundo Kagaku) and

alumina powder (AKP-30, Sumitomo Chemical) as shown in Table 1, with a small quantity of ethanol, for 12h in ball mills with 5mm zirconia balls. The mixtures were dried and about 10g of each was compressed into a block 2 × 10 × 100(mm) under a pressure of 20MPa in a hand press mold 10 × 100(mm). Compressed powder blocks were sintered at 1923K in air for 3h. Specimen H was heated at 2123K for 3h after sintering. It was then cooled down in the furnace to dissolve alumina in magnesium alumina spinel. Thus, dense sintered blocks were obtained with about a 30% volume reduction achieved by sintering. The surface were ground with a diamond grinding wheel and finally the specimens were made into form of plate about 1.5 × 8 × 70(mm).

Measurements were made on internal friction and shear modulus of the samples in the temperature range from room temperature to 1473K in an argon atmosphere by using the torsional pendulum with frequencies of 1 to 20Hz. Heating and cooling rate during measurements were 5K per minutes. A peak shift method were used to calculate the activation energy of internal friction peaks and an X-ray diffraction method were used to determine the spinel lattice constants and the structural phases in the samples.

## 3. Results and Discussion

Figure 1 shows the X-ray diffraction pattern for sample E doped with 50mol% gallium oxide into spinel. This pattern shows no diffraction peaks from gallium oxide as an additive but those completely from spinel. Also for samples, A, B, C, D, E, G and H, the X-ray diffraction peaks were identical to those from spinel. As the relation between additive concentration and spinel lattice constant, the lattice

**Table 1.** Chemical composition and internal friction characteristics of the spinel ceramics doped with gallium oxide or alumina.

Sample	Ga <sub>2</sub> O <sub>3</sub> (mol%)	Al <sub>2</sub> O <sub>3</sub> (mol%)	ΔM/2M (X10 <sup>-2</sup> )	Q <sup>1</sup> peak (X10 <sup>-3</sup> )	Half width (K)	T <sub>p</sub> (K)
A	5	-	8.6	8.4	151	1101
B	10	-	8.9	8.9	151	1108
C	20	-	15.8	12.9	157	1111
D	30	-	25.9	16.2	156	1116
E	50	-	32.7	23.4	171	1159
F	-	5	12.9	12.5	134	1111
G	-	20	47.4	57.1	148	1131
H	-	40	74.9	77.9	172	1143

constant increases in proportion to gallium content and decreases in proportion to alumina content as shown in Fig.2. According to the phase diagrams shown by G. Katz et al., spinel dissolves gallium oxide by about 70mol% at 1923K and by about 52mol% at 1273K.<sup>4)</sup> According to other phase diagrams and results by Y. M. Chiang et al., spinel dissolve alumina by 30mol% at 1973K.<sup>2,5)</sup> All this suggests that the gallium oxide and alumina in the samples in the present work were completely dissolved in spinel.

Figure 3 shows the temperature dependence of the internal friction and shear modulus measured with a frequency of 15Hz for sample C having 20mol% gallium oxide dissolved in spinel. As the temperature rises, the internal friction increases gradually at first, then rapidly at temperatures above around 923K, reaching a maximum of  $24.5 \times 10^{-3}$  at 1123K. It then decrease in the temperature range up to around 1300K and subsequently turns upward again. The internal friction peaks observed during heating and cooling were coincided within the experimental error which was less than  $0.1 \times 10^{-3}$ . No temperature hysteresis was observed in the temperature dependencies of internal friction. No temperature hysteresis are also observed in internal friction of the samples, A, B, D, E, F and G. Figure 3 also shows the temperature dependence of the shear modulus measured at the same time. As the temperature rises, the shear modulus decreases gradually. At around 700K, the temperature coefficient of shear modulus begins to increase, then reach a maximum at around 1123K which is the internal friction peak temperature. Temperature coefficients of shear modulus at 1200K or above are close to that at 1000K. The temperature curve of shear modulus varies reversibly

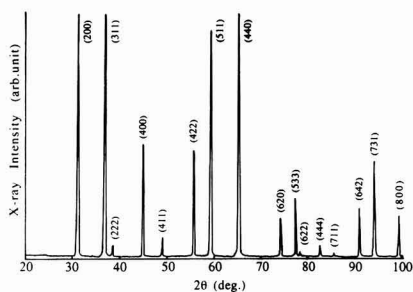


Fig. 1. X-ray diffraction pattern showing that samples E consist of the spinel only.

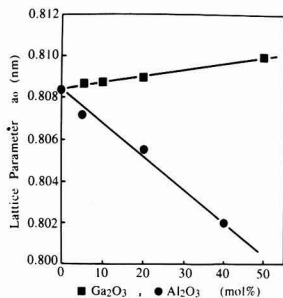


Fig. 2. Gallium oxide and alumina concentration dependencies of the lattice parameter of spinel.

without the temperature hysteresis as same as that of internal friction. The temperature coefficient of shear modulus to be large in the internal friction peak temperature range was observed in all samples. It is known as the  $\Delta M$  effect, which denotes decreases in shear modulus related with internal friction value at the peak. The values of  $\Delta M$  effect are shown in Table 1.

Figure 4 shows the temperature dependence of the internal friction measured with 17.3 and 10.5Hz for samples B and C respectively, which differ in gallium oxide content. The temperature and value of the internal friction peak for sample B are 1138.8K and  $15 \times 10^{-3}$  respectively and those for sample C are 1128.3K and  $26 \times 10^{-3}$  respectively. Peak temperatures depends on the measurement frequency. As the measuring frequency increases, the peak temperature shifts toward the high temperature side. The peak temperatures at a frequency of 16Hz were calculated from the relation between frequencies and peak temperatures measured with 4 frequencies, as shown in Table 1. As the gallium oxide content increases, the peak temperature rises. On the assumption that the background of internal friction increases exponentially, the backgrounds for samples B and C are shown by dotted and dashed lines respectively as shown in Fig.4.<sup>6)</sup> For the other samples, backgrounds of internal friction were determined likewise. The background levels were deducted from the measured values to obtain peak values. The results is shown in Table 1.

The relation between internal friction peak values ( $Q^{-1}_{\text{peak}}$ ) and  $\Delta M$  effect for samples A through H nearly agree with the following equation:

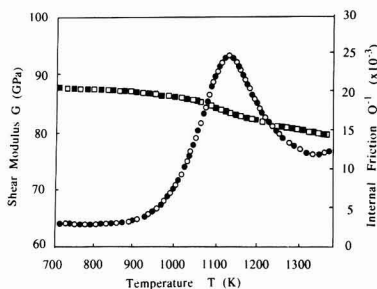


Fig. 3. Temperature dependence of internal friction and shear modulus in sample C. Open and closed circles are measured points obtained on heating and on cooling, respectively.

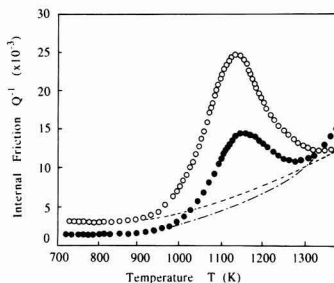


Fig. 4. Temperature dependence of internal friction in samples B and C. B: closed circle, C: open circle

$$Q^{-1}_{\text{peak}} = 1/2(\Delta M/M) \dots \dots \dots (1)$$

This proves that internal friction peaks observed with MgAl<sub>2</sub>O<sub>4</sub>-Ga<sub>2</sub>O<sub>3</sub> and MgAl<sub>2</sub>O<sub>4</sub>-Al<sub>2</sub>O<sub>3</sub> samples are nearly a single relaxation type. As shown in Table 1, the internal friction peak increases as the gallium oxide content increases. Also as shown in Table 1, the half widths of internal friction peaks are 151K and 157K for samples B and C respectively; as the gallium oxide content increases, the half width of the internal friction peak also increases. The half width of the internal friction peak also increases as the alumina content increases. **Figure 5** shows the dependence

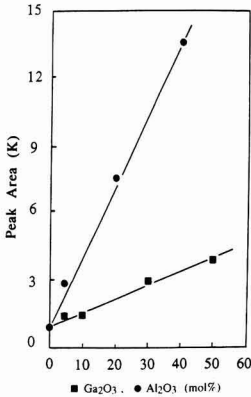


Fig. 5. The effect of gallium oxide concentration on internal friction peak area.

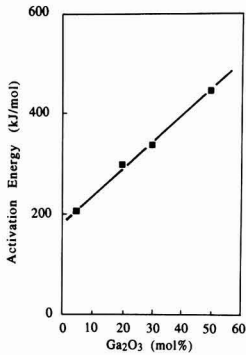


Fig. 6. The effect of gallium oxide concentration on activation energy of internal friction peaks.

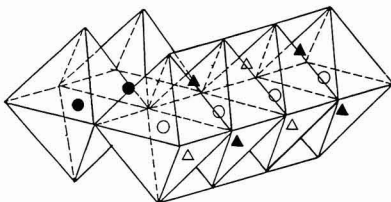


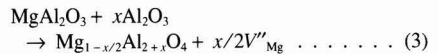
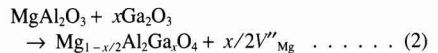
Fig. 7. Occupied (closed symbols) and unoccupied (open symbols) octahedral (circles) and tetrahedral sites (triangles) in the spinel structure.

of internal friction peak area on gallium oxide and alumina content. The internal friction peak area increases in proportion to the content of gallium oxide dissolved in spinel. Comparing with the effect of gallium oxide and alumina content on peak area, the internal friction peak area per 1mol% of alumina and of gallium oxide are 0.311 and 0.060K, respectively. The former is about 5 times of the latter.

**Figure 6** shows the dependence of activation energy of internal friction peaks on gallium oxide content. With a 5mol% gallium oxide sample, activation energy is 220kJ/mol and with a 50mol% gallium oxide dissolved sample, the activation energy of the internal friction peak is nearly twice the value of Sample A. As the content of dissolved gallium oxide increases, the activation energy increases markedly.

It is known that as the content of dissolved alumina increases, the spinel lattice constant decreases linearly.<sup>7)</sup> Variations in lattice constants for samples F, G and H under the present work show that alumina as the additive was completely dissolved in spinel. On the other hand, the lattice constant of spinel contained the gallium oxide increases in proportion to gallium content. The ion radius of gallium (0.062nm) is larger than that of aluminum (0.050nm) and smaller than that of magnesium (0.065nm). The increment of lattice constant of the spinel doped with gallium suggests that gallium substitute the sites of aluminum ions. If all aluminum ions are replaced with gallium ions, no ion vacancies were not formed owing to trivalent gallium ions substituted trivalent aluminum ions. As reported by A. Nsvrotsky et al., however, a spinel structure with magnesium ions which occupy tetrahedral sites and aluminum ions which occupy octahedral sites are exchanged with each other.<sup>8)</sup> The decrement of lattice constant of the spinel doped with alumina is considered to be a result of aluminum ions being replaced with magnesium ions which have a larger radius than that of aluminum ions.

Samples showing internal friction peaks are ones having a spinel doped excessively with trivalent metallic ions as compared with a stoichiometric spinel. If excessively contained gallium or aluminum ions substitute the sites of magnesium ions which occupy tetrahedral sites, cation vacancies are formed as follows to keep electrical neutrality:



The results in Fig.5 show that internal friction peaks are proportional to the ion vacancy concentrations formed by gallium and aluminum ions dissolved in spinel as shown in equations (2) and (3).

As shown in **Fig.7**, the spinel structure shows that there are space between magnesium ions occupying the tetrahedral sites and adjoining magnesium ions. Probably, ions diffuse through these space shown by open circles in Fig.7.<sup>9)</sup> As the gallium concentration increases, the activation energy of internal friction peaks increases. This tendency may be due to the change of in the diffusion route of ions as follows:

The radius of the gallium ion is larger than that of the aluminum ion and as the gallium ion concentration increases, the space shown by open circles may possibly

diminish. When trivalent gallium ions occupy the sites of bivalent magnesium ions, the electron concentration changes and lattice distortion could be grown owing to the concentration of cations having a different radius increases. Such change in spinel may cause the activation energy of ion diffusion to increase.

When the spinel is doped with gallium ions different in radius from aluminum and magnesium ions as components of spinel, its lattices distort around the gallium ions. When the spinel is doped with trivalent aluminum and gallium ions as shown in Fig.5, the peak areas depends on the kinds of ions. Aluminum and gallium ions are trivalent and the forming ion vacancy concentrations are probably identical. As shown in Fig.2, the absolute value of the lattice constant change per 1mol% of gallium oxide dissolved is smaller than that of alumina. This implies that when alumina is dissolved, local distortion around its ions is larger than when gallium oxide is dissolved. As the result ions and atoms move to relax the external alternate stress, relaxation type internal friction peaks were observed. The greater the distortion relaxed by the movement of one atom or ion, the larger the internal friction peak was observed.<sup>10)</sup> Therefore, in the spinel doped with alumina, the local distortion around aluminum ions occupying magnesium sites is larger than with gallium ions occupying magnesium ion sites. The external stress relaxed by the movement of one ion is larger in the spinel doped with alumina than in the spinel doped

with gallium oxide. This probably makes the internal friction peak intensity higher in the spinel doped with alumina than in the spinel doped with gallium oxide.

#### References:

- 1) J. Woigrard, P. Mazot and M. Halbwachs, *J. de Physique*, C10, 533-555(1985).
- 2) Y. M. Chiang and W. D. Kingery, *J. Am. Ceram. Soci.*, 72, 271-277 (1989).
- 3) R. A. Weeks and E. Sonder, *ibid.*, 63, 92-95 (1980).
- 4) G. Katz and R. Roy, *ibid.*, 48, 450-452 (1965).
- 5) E. M. Levin and H. F. McMurdie, *Phase Diagrams for Ceramists*, Am. Ceram. Soc. (1975) 114.
- 6) S. Sakaguchi, N. Murayama and F. Wakai, *Yogyo-Kyokaiishi*, 95, 1219-1222 (1987).
- 7) C. C. Wang, *J. Appl. Phys.*, 40, 3433-3444 (1969).
- 8) A. Navrotsky, B. A. Wechsler, K. Geisinger and F. Seifert, *J. Am. Ceram. Soci.*, 69, 418-422 (1986).
- 9) K. Mocala and A. Navrotsky, *J. Am. Ceram. Soci.*, 72, 826-832 (1989).
- 10) A. S. Nowick and B. S. Berry, *Anelastic Relaxation in Crystalline Solids*, Chap. 8, Academic Press, New York (1972) 176-224.

---

This article is a full translation of the article which appeared in *Nippon Seramikkusu Kyokai Gakujutsu Ronbunshi* (Japanese version), Vol.99, No.8, 1991.

# Morphology of Diamond in Radio-Frequency Thermal Plasma CVD

Toyohiko Kobayashi

Tokai Carbon Co., Ltd., Fuji Research Laboratory  
394-1, Subashiri, Oyama-cho, Sunto-gun, 410-14 Japan

**Morphology of diamond which was deposited on a molybdenum substrate by a radio-frequency thermal plasma CVD method in methane, hydrogen and argon atmosphere was investigated using a scanning electron microscope (SEM). It was found that with increasing deposition temperature the habit changed from octahedral to cubic, via intermediate cubo-octahedral forms. Columnar-like crystals of half-octahedron and of multiple twin were grown at low and high deposition temperatures, respectively at a  $\text{CH}_4/\text{H}_2$  ratio of 0.04. Twins such as a spinel twin and a 5-fold twins were observed. Growth layers such as triangles on  $\{111\}$  and  $\{100\}$  faces, well-defined composite spirals with 4-fold rotation axis and closed loops were observed.**

[Received January 7, 1991; Accepted May 23, 1991]

**Key-words:** Morphology, Diamond, Radio-frequency thermal plasma CVD, Columnar-like crystal, Twins, Growth layers

## 1. Introduction

Diamonds, which have been widely used as dies, cutting tools, and abrasives because of their high hardness and wear resistance, are now expected to find applications as heat sinks, optical materials, and semiconductor materials as attention has been given to their thermal conductivity, light transmittance, and electrical properties. In some field, industrial production of diamond is being planning. Since the method for synthesizing diamond from gas phase has been developed recently, the studies have been actively carried out for the purpose of utilizing these excellent properties of diamond in a thin film form.

For the early studies on the synthesis of diamond from gas phase, Eversole filed his patent<sup>1)</sup> in 1958, Augus et al.<sup>2)</sup> and Derjaguin et al.<sup>3)</sup> presented their reports in the 1960s, and Matsumoto et al.<sup>4,5)</sup> presented their reports in 1981 on the detailed method for synthesizing diamonds by the hot filament method. Since then, many synthesizing methods have been developed until now.

The methods for synthesizing diamonds are broadly classified into two groups: the hot filament<sup>4,5)</sup> and the combustion method<sup>6)</sup> using thermal excitation and the plasma CVD method<sup>7-11)</sup> using excitation due to electric discharge. The deposition form, shape and property of diamond synthesized by these methods are common though the depositing conditions are different. However, the difference in morphology is found between the diamond synthesized by the low-pressure plasma method reported by Kobashi et al.<sup>12)</sup> and the diamond synthesized by the CTR method reported by Spit-

syn et al.<sup>13)</sup> Also, it has been reported that the high-speed synthesis using thermal plasma produces columnar diamond.<sup>11,14)</sup> When radio-frequency thermal plasma is used to deposit diamonds, columnar-like crystals are formed,<sup>14)</sup> and various growth layers are found. These aspects are different from the morphology that was reported previously. This report describes the morphology of diamond that is deposited by the radio-frequency thermal plasma CVD method with the deposition temperature, deposition time, and  $\text{CH}_4/\text{H}_2$  ratio being varied.

## 2. Experiment

### 2.1. Experimental Equipment

The radio-frequency thermal plasma equipment is made up of a radio-frequency power source with a frequency of 4MHz and a maximum plate input power of 100KW, a reactor, a gas supply system, and an evacuation system. The reactor comprises a plasma torch, water-cooled substrate holder, and a water-cooled chamber.

**Figure 1-A** shows the outline of the plasma torch. The plasma torch is so constructed as to have a water-cooled

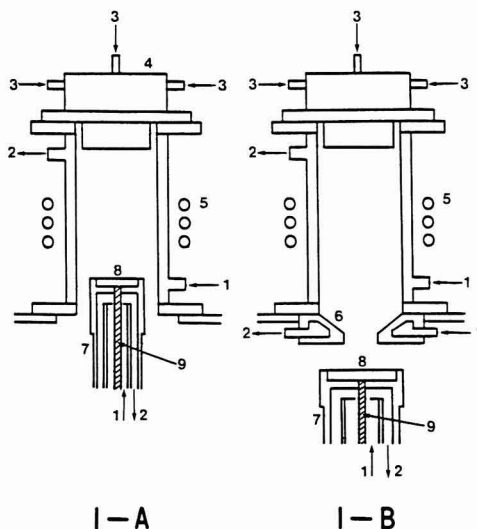


**Fig. 1.** Schematic views of a radio-frequency plasma torch (A: normal type) and with a nozzle at bottom side of it (B): (1) cooling water inlet, (2) cooling water outlet, (3) gas inlet, (4) gas supply, (5) induction coil, (6) nozzle, (7) substrate holder, (8) substrate, and (9) optical sensor.

quartz double tube with an inner diameter of 60mm around which three turns of induction coil are wound and has a gas supply at its upper part. It was also used as a torch with nozzle<sup>14)</sup> by attaching a water-cooled copper nozzle at the bottom side of torch (Fig.1-B)

The water-cooled substrate holder had a mechanism for vertical movement. The center of the holder incorporates an optical sensor 1.27mm in diameter that connects to the external measuring instrument via optical fiber. When the substrate is wrapped in plasma flame, it is difficult to measure the surface temperature of substrate with an optical pyrometer. Therefore, the bottom surface temperature of substrate plated in the disk-shaped recess on the holder was measured by the optical sensor. The temperature thus measured was taken as the substrate temperature.<sup>15)</sup>

The substrate used in this experiment was a 1.5mm-thick, 20mm-diameter molybdenum plate polished with diamond paste of mean grain size of 10 $\mu$ m. When deposition was performed by using the torch with nozzle, a 3mm-thick, 40mm-diameter molybdenum substrate polished in the same manner as described above was used.

### 2.3.2. Experimental Method

The deposition experiments were made by using the torch without nozzle (Fig.1-A) and the torch with nozzle (Fig.1-B). The procedure for depositing diamonds with the torch without nozzle is as follows: First, the torch and chamber are evacuated. After replacing with Ar, radio-frequency power is applied under a reduced pressure, and plasma is ignited. Then, while sheath gas (Ar+H<sub>2</sub>) and plasma gas (Ar) are supplied, the power is increased. The gas flow rate and the power are set. When the pressure in the chamber exceeds the atmospheric pressure, the discharge valve opens. Next, a substrate is inserted in the torch, and the substrate temperature is set. CH<sub>4</sub> gas is supplied from the gas supply to deposit diamond on the substrate.

The procedure for using the torch with nozzle was the same as the above except that the substrate is not inserted in the torch, and that the deposition is performed under a reduced pressure in the chamber.

The deposition experiment was performed with the flow rate of sheath gas and plasma gas kept constant and with the substrate temperature, deposition time, and CH<sub>4</sub>/H<sub>2</sub> ratio being varied. The substrate temperature was regulated by changing the contact area between the substrate and the holder. The plasma generating condition (input power, gas flow rate, etc.) and the position of substrate in the torch were kept constant. The contact area between the substrate and the holder was changed by changing the width and number of 0.05mm-deep grooves on the holder.<sup>15)</sup>

Tables 1 and 2 give the conditions of deposition test with the normal torch (without nozzle), and Table 3 gives those with the torch with nozzle. The morphology was observed by using a scanning electron microscope (SEM), and the identification of diamond was performed by Raman spectrometry.

## 3. Results and Discussion

### 3.1. Morphology of Diamond Deposited by Using Normal Torch

The deposition was performed for 1hour by using the

Table 1. Conditions of deposition test with the normal torch.

No	Substrate temp. (°C)	Gas flow rate		CH <sub>4</sub> /H <sub>2</sub>	Deposition time (min)
		CH <sub>4</sub>	H <sub>2</sub> (l/min)		
1-1	720 - 697	0.24	6	0.04	60
1-2	804 - 788	0.24	6	0.04	60
1-3	888 - 855	0.24	6	0.04	60
1-4	852 - 831	0.12	6	0.02	60
1-5	839 - 803	0.40	6+2*	0.05	60

Pressure = 1 atm. \* : H<sub>2</sub> flow rate of 6 l/min mixed with the sheath gas and that of 2 l/min from the center nozzle of supply

Table 2. Conditions of deposition test with the normal torch.

No	Substrate temp. (°C)	Gas flow rate		CH <sub>4</sub> /H <sub>2</sub>	Deposition time (min)
		CH <sub>4</sub>	H <sub>2</sub> (l/min)		
2-1	856 - 762	0.24	6	0.04	300
2-2	817 - 708	0.20	6	0.033	300
2-3	831 - 765	0.16	6	0.027	300
2-4	740 - 695	0.16	6	0.027	220

Pressure = 1 atm.

Table 3. Conditions of deposition test by the torch with a nozzle.

H <sub>2</sub> flow rate : 8 l/min
CH <sub>4</sub> flow rate : 0.32 l/min
CH <sub>4</sub> /H <sub>2</sub> : 0.04
Substrate temperature : 900° - 892 °C
Deposition time : 60 min
Torch pressure : 580 Torr

normal torch. The experiment conditions were 52KW of plate power, 8 and 6l/min of hydrogen flow rate, and 0.4, 0.24, and 0.12l/min of methane flow rate. The position of substrate in the torch was kept constant, and the initial substrate temperature was varied from 720°C to 886°C. At this time, the substrate temperature decreased by 20 to 30°C in 1hour. The reason for this may be that the quantity of heat transferring from the top surface of diamond to the bottom surface of substrate decreases as the film thickness increase. The observed morphology of deposits in the center and periphery areas is shown in Fig.2, and the conditions of deposition are listed in Table 1. The numerals in Table 1 and Fig.2 correspond to each other. The symbols of (c) and (p) in Fig.2 denote the center and periphery area, respectively.

When the CH<sub>4</sub>/H<sub>2</sub> ratio is kept constant, being 0.04, and the substrate temperature is increased from No.1-1 to 1-3, the morphology in the center differs from that in the periphery areas. The morphology appearing in the center was similar to that in the periphery areas of specimen deposited at higher substrate temperature. This may result from the temperature distribution on the substrate (the temperature is high in the center and become lower in the periphery area).

Regarding the morphology in the center, columnar-like crystals with {111} face only were deposited when the substrate temperature was low (Fig.2, 1-1a(c)). On that face, small crystals with {111} face only were formed. When the substrate temperature was high, crystal faces with many growth layers and {100} faces were observed (Fig.2, 1-

2a(c)). At much higher temperatures, cubic twins (Fig.2, 1-3a(c), b(c)), multiple twins (c(c)), and crystals (d(c)) in which the area corresponding to the {111} face of cubo-octahedral crystal was depressed and the generation of new faces was found were observed. The growth layer were observed on these faces.

In No.1-4 with a  $\text{CH}_4/\text{H}_2$  ratio of 0.02, growth layers

(bottom right of Fig.2, 1-4b(c), c(p), d(p); and e(p)) were observed on {111} and {100} faces, and stripe lines were observed on the {111} face.

The morphology of No.1-5, unlike that of 1-1 through 1-4, was obtained by using a different gas supply method, in which 6l/min of hydrogen flow rate of 8l/min was mixed to the sheath gas and 2l/min was blown onto the substrate

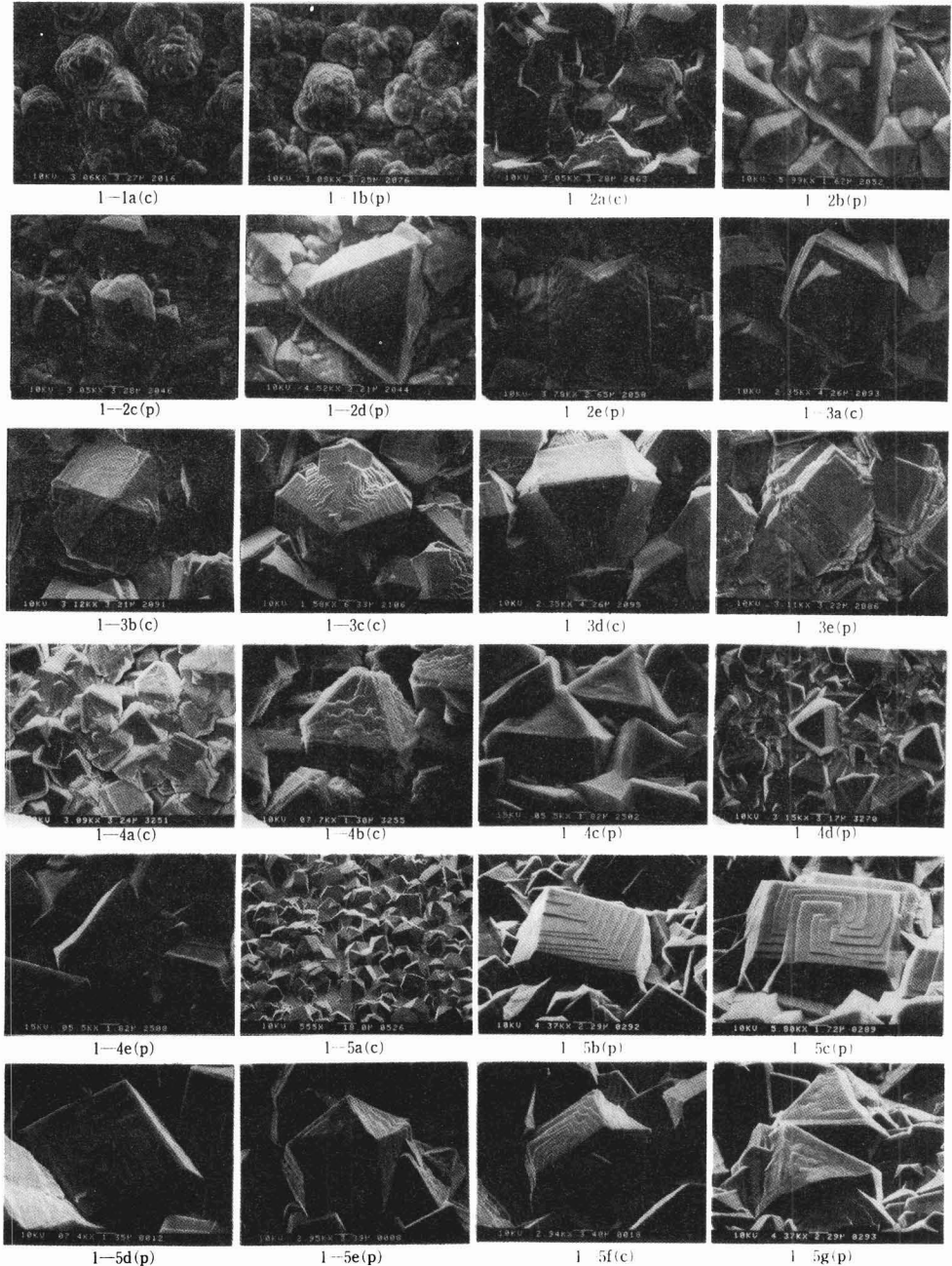


Fig. 2. Morphology of the diamond deposited on center (c) and periphery areas (p) of substrate surface by the normal torch.

through the center nozzle in the gas supply. As a result, the actual  $CH_4/H_2$  ratio on the substrate may be considerably low. This specimen, unlike other ones, had the center (Fig.2, 1-5a(c)) with no film, cubo-octahedrons, cubo-octahedron twins, and 5-fold twins being observed. On the {100} face, many growth layers (b(p), c(p), d(p), e(p), f(p)) were observed.

The observation results in the center and periphery areas described above suggest that with increasing substrate temperature the habit changes from octahedral to cubic via intermediate cubo-octahedral forms.

Next, the morphology was observed for 5hour deposition to investigate the change in morphology with time after the start of deposition. The results are shown in Fig.3. In the experiment, the plate power was a constant 52kW and the hydrogen flow rate was a constant 6l/min. The  $CH_4/H_2$  ratio was change from 0.027 to 0.04. The position of substrate in the torch was kept constant as with the 1hour deposition experiment. The substrate temperature decreased with time.

For No.2-4, the substrate temperature decreased to 700°C or lower by the deposition for 220 minutes, when the deposition experiment was suspended. The conditions of experiment is given in Table 2. In this experiment, observation was made by paying attention to the change of morphology from the periphery area to the center of substrate.

In No.2-2, where the  $CH_4/H_2$  ratio was 0.033 and the substrate temperature decreased from 817°C to 708°C, the change of morphology from the periphery area to the center (Figs.3, 2-2, 1→5) was from the deposits having vague shape (1) to the columnar crystals with {111} face only (2, 2'), the crystals with {100} face at its end (2, 3), the crystals with expanded and inclined {100} face, and the crystals with {100} face at the opposite side of inclined {100} face (4, 5).

In addition, the change of {100} face generated at the end of columnar crystal with {111} face only was observed in detail in No.2-3 (Fig.3, 2-3, 1→4). The {100} face generated at the end of columnar crystal grew at the area

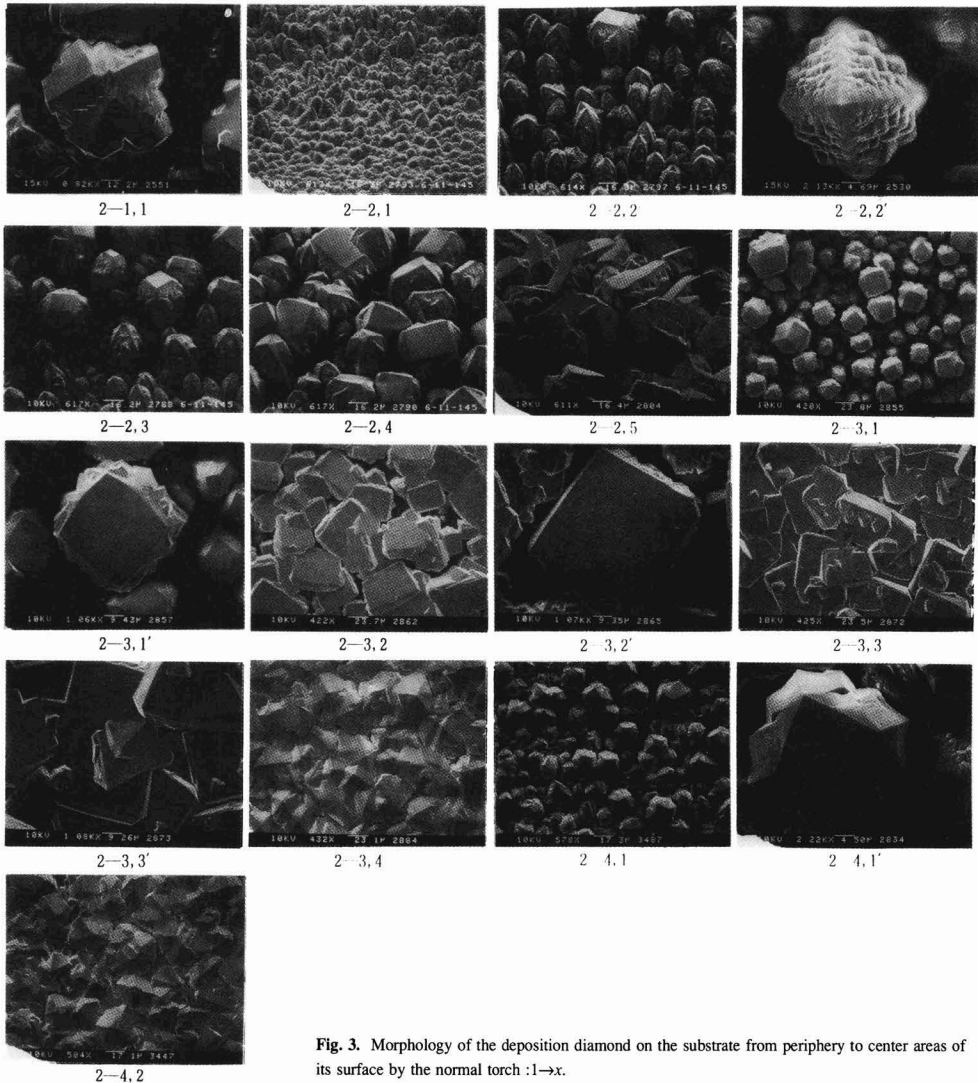


Fig. 3. Morphology of the deposition diamond on the substrate from periphery to center areas of its surface by the normal torch :1→x.

closer to the center. Some had bent and octagonal {100} face (1') was also observed. This face inclines more than that of crystal far from the center. The crystals that possibly combined with the adjacent crystals at the initial stage incline less than those that did not combine. At the opposite side of {100} face with a large inclination, the appearance of {100} face (2) was observed. Growth layers were found on the {100} face from the time when the crystals combine (2, 2'). In the area where most crystals had combined, the secondary grains were produced on the crystal face (3, 3'). At the center, a different morphology was found that comprised crystals depositing with the corner facing upward (4).

At the center of No.2-1 with a  $\text{CH}_4/\text{H}_2$  ratio of 0.04, columnar multiple twins were deposited (Fig.3, 2-1, 1). At the center of No.2-4 with a  $\text{CH}_4/\text{H}_2$  ratio of 0.027, columnar crystals were not found and the crystals with the corner facing upward (Fig.3 2-4, 2) were found. In the periphery areas of substrate of this specimen, the crystals with {111} face only and the multiple twins that were produced by the development of the {111} face (1') were observed. These observations suggest that there are two conditions for producing columnar crystals; the condition where the  $\text{CH}_4/\text{H}_2$  ratio is high and the initial substrate temperature is low and the condition where  $\text{CH}_4/\text{H}_4$  ration is high and the initial substrate temperature is high. When the substrate temperature is low, columnar crystals with {111} face only are produced. When the substrate temperature is high, columnar multiple twins with growth layers and secondary grains growing on the crystal surface are produced. As described above, the substrate temperature decreases during deposition. This phenomenon is also found when a torch with nozzle is used. After the deposition was suspended when rapid decrease in substrate temperature than ordinary occurred, the deposition of small amounts of carbon was found in the center on the surface of diamond film (Imm-thick columnar crystal film).<sup>15</sup> Since carbon deposits when the substrate temperature exceeds the temperature range in which diamond is deposited, the decrease in substrate temperature means the increase in the surface temperature of diamond. This is why the form of crystal tip changes with increasing film thickness.

The production of columnar crystals depends on the difference in experiment conditions between the thermal plasma CVD and methods of hot filament and low-pressure plasma. The present experiment was carried out with higher  $\text{CH}_4/\text{H}_2$  ratio than latter methods. Therefore, there might be highly concentrated active species associating with the production of diamond in the plasma gas. Also, since the present experiment was performed in the atmosphere, concentration boundary layers might be formed on the substrate surface. The mechanism in which columnar crystals are formed under such experimental conditions may be as fol-

lows: when the  $\text{CH}_4/\text{H}_2$  ratio is high and the substrate temperature is low, the crystals with {111} face only deposits first, and the crystal becomes columnar because the crystal corner projecting in the gas with concentration gradient becomes a nucleation point of crystal. As described later in Section 3.3, the growth layer observed when the substrate temperature and the  $\text{CH}_4/\text{H}_2$  ratio were low was generated from the corner at the highest position facing the plasma gas flow. In the present experiment with a high  $\text{CH}_4/\text{H}_4$  ratio, the secondary grains were generated on the {111} face. When the substrate temperature is high, the reaction at the crystal tip in the gas with concentration gradient may become violent, so that the generation of two-dimensional nucleus occurs frequently at the crystal face together with the generation of nucleus at the corner or edge of crystal, which may produce columnar-like crystals.

As described above, when the  $\text{CH}_4/\text{H}_2$  ratio is high and the substrate temperature is high or low, the crystals becomes columnar. However, the formation of columnar crystals can be prevented and a thick film as shown in Fig.4(a) can be obtained if, for example, the  $\text{CH}_4/\text{H}_2$  ratio is 0.033 and the substrate temperature during deposition is changed continuously from 833°C to 717°C by regulating the plasma input power (to keep the surface temperature of diamond film constant). Fig.4 shows sectional view of fracture surface of periphery area for a film with a thickness of 430µm at the center. Fig.4a shows the center of fracture surface, and Fig.4b shows the end. The end area has columnar crystals. This is probably because the substrate temperature at this area is lower than that in the center. Although the experimental results are not shown here, the formation of columnar crystals decreases (the substrate temperature range in which the film does not become columnar) when the  $\text{CH}_4/\text{H}_2$  ratio is reduced or when the  $\text{CH}_4/\text{H}_2$  ratio is constant and the flow rate of  $\text{H}_2$  is increased. Therefore, the degree of substrate temperature is a relative parameter depending on the  $\text{CH}_4/\text{H}_2$  ratio and the flow rate of  $\text{H}_2$ .

### 3.2. Morphology of Diamond Deposited by Using Torch with Nozzle

The 1hour deposition experiment was performed by using a torch with nozzle. The experiment conditions were 52kW of plate power, 8l/min of hydrogen flow rate, and 0.32l/min of  $\text{CH}_4$  flow rate. The substrate temperature was changed from 900°C to 892°C. In this experiment, an area showing different morphology concentrically appeared on the substrate. Table 3 gives the conditions of deposition, and Fig.5 shows the morphology obtained in this experiment.

At the outermost periphery area of substrate (1→), spherically-shaped crystals with vague shape were deposited. At the positions closer to the center on the substrate surface, columnar crystals with {111} face only and columnar crystals with {100} face at its tip appeared. On the {111} face of these crystals, many small crystals with {111} face only were produced. The {100} face at the tip is larger on the crystal closer to the center, and an area where {100} face appeared remarkably was produced. This {100} face had a larger inclination on the crystal closer to the center, and the number of crystals that deposited with their corners upward increased. Also, twins were found. At the positions closer to the center, many growth layers were formed on the crystal face, and their height increased. Also, the generation of secondary grains was observed on the

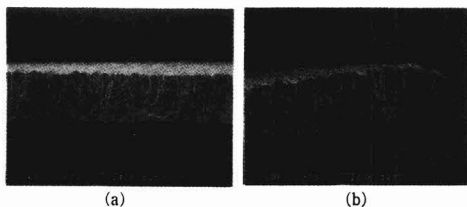


Fig. 4. Center (a) and edge parts (b) of a diamond film fracture surface.

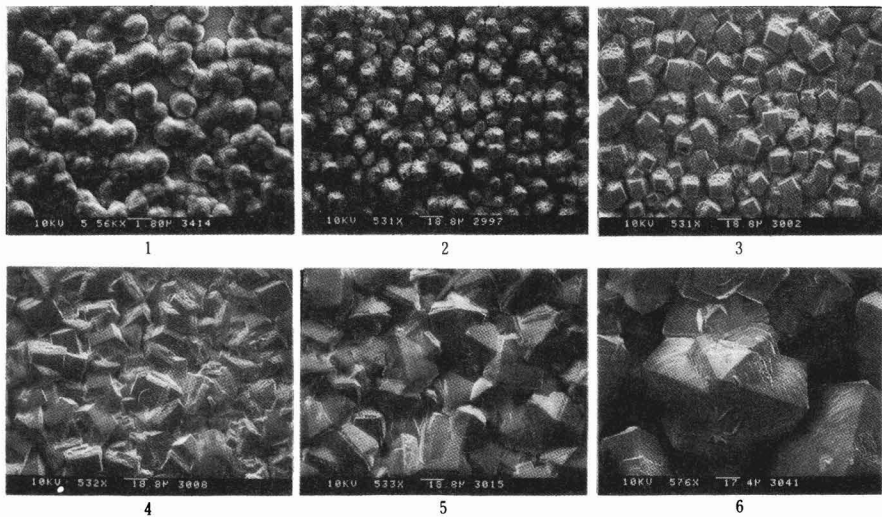


Fig. 5. Morphology of the deposition diamond on the substrate from periphery to center areas of its surface by the torch with a nozzle: 1→8.

crystal face. At the center, columnar multiple twins with growth layers on the crystal face appeared (→6). Figure 6 shows the Raman spectra in the center. The difference in morphology is probably due to the temperature distribution in the plasma flame and on the substrate, as with the case using the normal torch.

### 3.3. Twins and Growth Layers

In depositing diamonds, twins are deposited together with single crystals. So far, spinel type twins, 5-fold twins, and 20-fold twins have been observed by the hot filament method and low-pressure plasma method.<sup>16,17)</sup> Spitsyn et al. took the twin consisting of single-crystalline unit of 2, 5, and 20 as a nucleation twin, and the twin produced subsequently on the crystal face as a growth twin. They also reported that the growth twins were observed on {111} and {100} faces, and macrosteps appeared around the twin on the crystal face on which the growth twins appeared.<sup>13)</sup> Kobashi et al. observed steps on the {100} face of grain that developed unusually in the experiment using a microwave, and reported that the {100} face was produced by the step growth mechanism.<sup>12)</sup> Sunagawa paid attention to the surface microphotography<sup>18)</sup> in Fig.4 presented in the above-mentioned report of Spitsyn et al.,<sup>13)</sup> and pointed out that the growth layer on {111} face had an inverted triangle form in relation to that on the {111} face, which was opposite to the orientation of growth layer found on the {111} face produced naturally or by high-temperature, high-pressure synthesis, and the growth layer on the {100} face was slightly different from that on the {100} face produced by high-temperature, high-pressure synthesis. He reported<sup>20)</sup> that the morphology of diamond synthesized from gas phase had characteristics exactly opposite to those produced by high-temperature, high-pressure synthesis, and it was farthest from the morphology expected from the periodic bond chain (PBC) analysis.<sup>19)</sup>

On the diamond obtained in this experiment, the growth layers were frequently observed. The growth layers observed on the {111} face parallel to the substrates of 1-2d

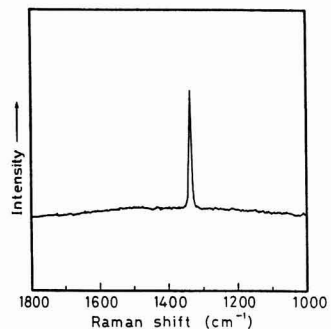


Fig. 6. Raman spectra of the diamond deposited by the torch with a nozzle.

and 1-2e in Fig.2 and the {111} face of spinel twin had an inverted triangle form in relation to the triangle on the {111} face. In this case, the face on which the growth layers were found was a face facing the direction of plasma gas flow, and no growth layers were found on other {111} faces. The rough surface of 1-2a in Fig.2 is also thought to be the {111} face on which the growth layers develop. The growth layers on the {111} face are also found on the {111} face of 5-fold twin (right of Fig.7). The growth layer on the {100} face were formed with the crystal produced on the crystal face being as the center (2-3,3 and 2-3, 3' of Fig.3, or Fig.7). The growth layer were observed when there were no crystals of formation center on the crystal face.

The observations described above were made under the condition of  $\text{CH}_4/\text{H}_2$  ratio of 0.04, so that most growth layers were irregular. For the  $\text{CH}_4/\text{H}_2$  ratio of 0.02, most growth layers were regular. When the  $\text{CH}_4/\text{H}_2$  ratio is 0.02 (fig.2, No.1-4), stripe lines are found on the {111} face, and the growth layers produced on the concave {111} face differs from those for the  $\text{CH}_4/\text{C}_2$  ratio of 0.04. The growth layers found on the {100} face have a regular shape. The morphology of 1-4e in Fig.2 indicates that the growth layer

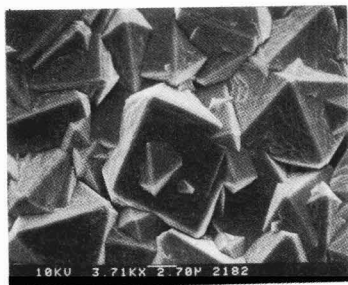


Fig. 7. Morphology of the deposition diamond.  $\text{CH}_4$  =0.24l/min,  $\text{H}_2$ =6l/min, the substrate temperature =845→824°C, and the deposition time=60min.

produced from the crystal formed on the face. The growth layers that were possibly formed from the screw dislocation (bottom right of Fig.2, 1-4d) were also observed.

In the morphology of diamond shown in Fig.2, 1-5a-1-5g deposited possibly with a lower  $\text{CH}_4/\text{H}_2$  ratio by the different gas supply method, the polygonal composite spiral growth layers with 4-fold rotation axis starting from the screw dislocation (1.5c and d have inverted orientation each other) and the growth layers that possibly expanded onto the entire face from the nucleation point of corner that was highest among four corners of {100} face (1-5b) were found. For the growth layers of this type, no growth layers that had a nucleation point on the edge were found. In 1-5e, growth layer of closed loop was observed. On the {111} face of cub-octahedron, the growth layers of the triangle of same orientation with that of {111} face were found (1-5f). This suggests that the {100} face under these experiment conditions is produced by the lateral growth, and the growth mechanisms are the spiral growth mechanism and the two-dimensional nucleus growth mechanism. Whereas, the growth layers observed on the {100} face when the  $\text{CH}_4/\text{H}_2$  ratio is 0.04 are, though irregular in shape, similar to those in Fig.2, 1-5b. The {100} face under these conditions may be produced by the two-dimensional nucleus growth mechanism.

#### 4. Conclusions

To investigate the morphology of diamond by the radio-frequency thermal plasma CVD method, experiments were performed by varying the substrate temperature,  $\text{CH}_4/\text{H}_2$  ratio, and deposition time. The observation of morphology led to the following conclusions:

- 1) As the deposition temperature increases, the habit changed from octahedral to cubic, via intermediate cubo-octahedral forms.
- 2) Octahedral, cubo-octahedral, and cubic twins were ob-

served.

- 3) When the  $\text{CH}_4/\text{H}_2$  ratio was high and the substrate temperature was low, columnar-like crystals with {111} face only were observed. When the  $\text{CH}_4/\text{H}_2$  ratio was high and the substrate temperature was high, columnar multiple twins on which growth layers and secondary grains were generated on the crystal face were observed.
- 4) Various growth layers were observed on the crystal face. This suggests that both {111} and {100} faces are produced by the lateral growth under these conditions of deposition.

#### References:

- 1) W.G. Eversole, U. S. Patent No. 3030187 and No. 3030188 Apr. 17, (1962).
- 2) J.C. Angus, H.A. Will and W.S. Stanko, *J. Appl. Phys.*, 39, 2915-2922 (1968).
- 3) B.V. Derjaguin, D.V. Fedoseev, V.M. Lukyanovich, B.V. Spitzin, V.A. Ryabov and A.V. Lavrentyev, *J. Cryst. Growth*, 2, 380-384 (1968).
- 4) S. Matsumoto, Y. Sato, M. Kamo and N. Setaka, *Jpn. J. Appl. Phys.*, 21, L183-L185 (1982).
- 5) S. Matsumoto, Y. Sato, M. Tsutsumi and N. Setaka, *J. Mater. Sci.* 17, 3106-3112 (1982).
- 6) Y. Hirose and M. Mitsuizumi, *New Diamond*, 4, 34-35 (1988).
- 7) M. Kamo, Y. Sato, S. Matsumoto, and N. Setaka, *J. Cryst. Growth*, 62, 642-644 (1983).
- 8) K. Suzuki, A. Sawabe, H. Yasuda and T. Inuzuka, *Appl. Phys. Lett.*, 50, 728-729 (1987).
- 9) S. Matsumoto, M. Hino and T. Kobayashi, *Appl. Phys. Lett.*, 51, 737-739 (1987).
- 10) K. Kurihara, K. Sasaki, M. Kawarada and N. Koshino, *ibid.*, 52, 437-438 (1988).
- 11) N. Ohtake and M. Yoshikawa, *J. Electrochem. Soc.*, 137, 717-722 (1990).
- 12) K. Kobashi, K. Nishimura, Y. Kawate and T. Horiuchi, *Phys. Rev. B*, 38, 4067-4084 (1988).
- 13) B.V. Spitsyn, L.L. Bouilov and B.V. Derjaguin, *J. Cryst. Growth*, 52, 219-226 (1981).
- 14) T. Kobayashi and S. Ono, *Seramikkusu, Ronbunshi*, 99, 119-123 (1991).
- 15) T. Kobayashi, *Koon Gakkaishi*, 17, 42-45 (1991).
- 16) Research Report, *Nat. Inst. Resear Inorg. Mater.*, No.39, 26-46 (1984).
- 17) S. Matsumoto and Y. Matsui, *J. Mater. Sci.*, 18, 1785-1793 (1983).
- 18) I. Sunagawa, *J. Crystal Growth*, 6, 166-179 (1980).
- 19) P. Hartman and W.G. Perdok, *Acta. Cryst.*, 8, 49-52, 521-529 (1955).
- 20) I. Sunagawa, Gauseki Kobutsu Kosho Gakkaishi, Special Issue No.3, 129-142 (1982).

This article is a full translation of the article which appeared in Nippon Seramikkusu Kyokai Gakujutsu Ronbunshi (Japanese version), Vol.99, No.8, 1991.

# Sintering and Properties of $\text{CaTi}_4(\text{PO}_4)_6$ Prepared by Sol-Gel Process

Yutaka Miyamoto, Akira Kishioka, Kiyoshi Itatani and Makio Kinoshita

Dept. of Chemistry, Faculty of Science and Technology, Sophia University  
7-1, Kioi-cho, Chiyoda-ku, Tokyo, 102 Japan

A precursor gel powder with the composition of  $\text{CaTi}_4(\text{PO}_4)_6$  (CTP) was prepared by sol-gel process. On heating, this powder was amorphous up to 700°C and changed into a single phase of CTP at about 800°C. The relative density showed that the sinterability of the amorphous powder was better than that of the crystallized powder. Some precursor gels with excess amounts of  $\text{P}_2\text{O}_5$  (1wt%-9wt%) were also prepared by the same process. The presence of a small amount of  $\text{P}_2\text{O}_5$  was effective for the sintering of compacts. Sintered body with relative density of 94% and bending strength of 72MPa was fabricated in the presence of 4wt% of  $\text{P}_2\text{O}_5$ . [Received January 24, 1991; Accepted May 23, 1991]

**Key-words:** Low thermal expansion, Calcium titanium phosphate, Sol-gel process, Sintering, Ceramics

## 1. Introduction

A number of researchers have been discussing that Ti(IV)-containing double phosphate, represented by the general formula  $\text{M}^{\text{I}}\text{Ti}_2(\text{PO}_4)_3$  or  $\text{M}^{\text{II}}\text{Ti}_4(\text{PO}_4)_6$  is, like Zr(IV)-containing double phosphate, a promising new material for its high ionic conductivity and low thermal expansion.<sup>1-6)</sup> Their powders, however, are difficult to sinter, and attempts to prepare the sintered bodies of sufficient mechanical properties in the absence of sintering aid have been mostly unsuccessful. Oota et al. discussed bending strength of the sintered body from the Zr-containing phosphate,<sup>9,10)</sup> but few discuss sinterability of the Ti-containing phosphate.

Two methods are available for the synthesis of double phosphate powders, solid-state reaction and sol-gel processes. The former needs a long heating time, and gives the powder which cannot be sintered at all in the absence of sintering aid. The latter, on the other hand, is capable of synthesizing, efficiently in a short time, the desired microparticles of crystalline double phosphate and, at the same time, amorphous one having exactly the same chemical composition during the heating process.

The authors have attempted first to synthesize calcium tetratitanium hexakis orthophosphate  $\text{CaTi}_4(\text{PO}_4)_6$  (hereinafter referred to as CTP) as the double phosphate by the sol-gel process, to investigate properties and sinterability of both crystalline and amorphous product powders. Further, the powder containing an excess amount of  $\text{P}_2\text{O}_5$  as the sintering aid was also synthesized, to make the similar investigations. As a result, it was found that the amorphous powder is more sinterable than the crystalline powder calcined at a higher temperature. It was also found that the sintered body from the amorphous powder containing an

excess amount of  $\text{P}_2\text{O}_5$  has fairly good relative density, bending strength and structures at the fracture surface.

## 2. Experimental Procedures

### 2.1. Synthesis of Gell Powder

The starting materials were titanium tetrabutoxide  $\text{Ti}(\text{OC}_4\text{H}_9)_4$  (Wako Junyaku, first-grade reagent), calcium dihydrogen phosphate monohydrate  $\text{Ca}(\text{H}_2\text{PO}_4)_2 \cdot \text{H}_2\text{O}$  (Wako Junyaku, first-grade reagent) and diammonium hydrogen phosphate  $(\text{NH}_4)_2\text{HPO}_4$  (Wako Junyaku, special-grade reagent). These reagents were mixed in such a way to give 20g of CTP as the double phosphate, where 500cm<sup>3</sup> of a 1-butanol solution of  $\text{Ti}(\text{OC}_4\text{H}_9)_4$  was stirred vigorously, to which 75cm<sup>3</sup> of an aqueous nitric acid solution (pH=3) containing  $\text{Ca}(\text{H}_2\text{PO}_4)_2 \cdot \text{H}_2\text{O}$  and  $(\text{NH}_4)_2\text{HPO}_4$  was added, and the mixture was stirred for 1h. The resultant white gel was centrifugally separated, washed with acetone 3 times and dried at around 50°C on a hot plate, to prepare the dried gel powder. The gel powder containing  $\text{P}_2\text{O}_5$  1 to 9% in excess of the content predicted from the CTP composition of  $\text{CaO} \cdot 4\text{TiO}_2 \cdot 3\text{P}_2\text{O}_5$  in a similar manner with  $(\text{NH}_4)_2\text{HPO}_4$ .

### 2.2. Changes in Gell Powder under Heating

All of the gell powders prepared in this study were heated for the differential thermal analysis and thermogravimetric analysis (DTA-TG). The phases formed during the thermal analysis were identified by the powder X-ray diffraction analysis, in which each sample for this purpose was heated in an electrical furnace at the same rate as used for the thermal analysis (10°C/min) and then allowed to cool in the furnace to room temperature as soon as it reached a given temperature level. The identification as made by the JCPDS cards.

### 2.3. Specific Surface Area of Powder

The gell powder sample was heated from 500° to 800°C to determine its specific surface area by the BET method with nitrogen gas, in order to investigate changes in its specific surface area, where approximately 1g of each sample placed in an alumina crucible was heated in an electrical furnace to a given temperature at which it was held for 1h, and then allowed to cool in the furnace to room temperature.

### 2.4. Calcination of Gell Powder

The gell powder sample, each weighing approximately 2g was heated to 500°, 600° or 800°C at which it was held for 1h, or to 500°C at which it was held for 3h. The powder sample containing an excess amount of  $\text{P}_2\text{O}_5$  was heated to 500°C at which it was held for 3h. They were heated at

10°C/min for the stoichiometric composition and at 10°C/h for the one containing an excess amount of  $P_2O_5$ .

## 2.5. Forming and Sintering of Calcined Powders

The following three types of the green bodies were prepared, in order to investigate their sinterability. They were sintered for 5h at 5 different temperature levels in a range from 1000° to 1300°C, in order to investigate the effects of calcination and sintering temperature on sinterability. For Sample Type 1, each was held at 1150°C for one of four time levels in a range from 1 to 10h. All sample were heated at 10°C/min.

- 1) Sample Type 1: These were for the analysis of relative density, each formed under 100MPa into a disc of 10mm in diameter and approximately 3mm in thickness. These were also used for the analysis by a scanning electron microscope (SEM) to observe sintered structure.
- 2) Sample Type 2: These were for the analysis of thermal expansion, each formed under the same pressure as the above into a cylinder of 5mm in diameter and approximately 4mm in height.
- 3) Sample Type 3: These were for the analysis of bending strength, each formed under 50MPa into a rectangular bar, 45×5×4mm in size.

## 2.6. Properties of Sintered Samples

- 1) Relative density: Relative density was bulk density relative to true density determined by a pycnometer with 1-butanol as the medium. True density of the sintered bodies were determined with the heated powder under the same conditions as those. Bulk density were calculated by measuring the weight and dimensions of each samples.
- 2) Texture of sintered bodies: The fracture surface of each sample was analyzed by an SEM, after having been polished and thermally etched.
- 3) Thermal expansion: This property was measured for a temperature range from room temperature to 1200°C.
- 4) Bending strength: This property was measured by the 3-point bending strength test.

## 2.7. Analyzers and Analysis conditions

The following analyzers were used, and the conditions under which they were operated are given in the parentheses:

Rigaku Denki's differential thermobalance for TG-DTA analysis at high temperature (sample mass: approximately 25mg, standard sample:  $\alpha$ - $Al_2O_3$ , heating rate: 10°C/min, operating in air, TG sensitivity: 20mg, DTA sensitivity:  $\pm 100\mu V$ ).

Rigaku Denki's RAD-IIA type powder X-ray diffractometer (CuK $\alpha$  irradiation, applied voltage: 40kV, tube current: 35mA, full-scale count: 10,000-cps). Hitachi's S-430 scanning electron microscope (applied voltage: 25kV). Rigaku Denki's high-temperature type thermomechanical analyzer (heating rate: 10°C/min, operating in air). Yasuda Seiki Sisakusho's No.216 YZ-500-1-PC autostrain (load application rate: 0.5mm/min, span: 20mm).

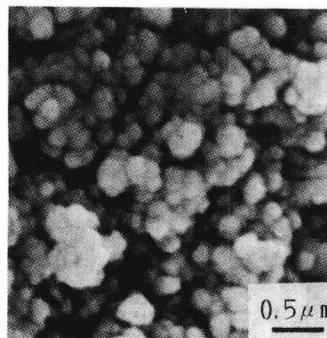


Fig. 1. SEM image of the precursor gel powder.

## 3. Results and Discussion

### 3.1. Powder Properties

Figure 1 shows the SEM image of the dried precursor gel powder. The powder was white, consisting of agglomerated microparticles of 0.1 to 0.3 $\mu m$  in size. Figure 2 shows the X-ray diffraction patterns, indicating the changes in the phases formed as a result of heat treatment of the precursor powder. It was amorphous at 700°C, and transformed into the single-phase double phosphate of CTP at 800°C.<sup>11)</sup> The single phase was maintained up to 1100°C, and the diffraction peak of  $TiO_2$  appeared at 1200°C, though very slightly. The precursor gel, when heated from room temperature, weight loss as soon as the heating process started, as a result of dehydration which was accompanied by an endothermic peak continuing up to around 200°C, as shown in Figure 3 (DTA-TG curves). The exothermic changes, accompanied by weight loss, were found to occur at 230° to 300°C and 330° to 380°C, which resulted from elimination and decomposition of ammonium ions and butanol remaining in the gel structure. The weight loss was no longer observed at above 500°C. It is considered, based on the powder X-ray diffraction analysis results, that the exothermic change occurring at 760°C resulted from the crystallization of the sample. Decomposition of CTP started at around 1200°C or more, as evidenced by the observed presence of  $TiO_2$  diffraction peak and slight weight loss on the TG curve. The top of the broad halo peak, characteristic of amorphous solid, shifted, when the dried precursor gel was heated, from at  $2\theta=28^\circ$  (indicated by the arrow) to at  $25^\circ$  (also indicated by the arrow), very close to  $25.5^\circ$  at which the most intense peak of CTP was observed. It is considered, based on the above results, that the dried precursor gel is changed during heating to have the random structure similar to that of the double phosphate, which is then changed to the regular structure characteristic of the crystalline solid. This is probably accompanied by the structural rearrangement, occurring simultaneously with diffusion of the ions. Figure 4 shows specific surface area of the precursor powder, changing with calcination temperature. It decreased rapidly at 600° to 750°C, which resulted from rapid growth of the grains during the transition period in which the amorphous state was changed into crystalline.

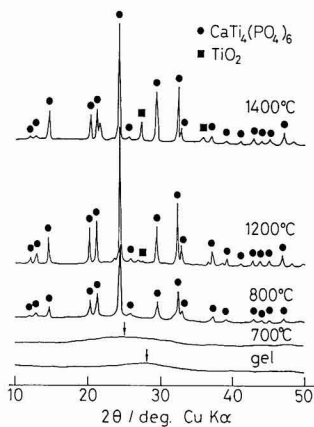


Fig. 2

Fig. 2. XRD patterns of the precursor gel and the heated powder.

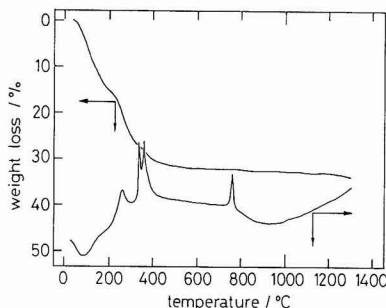


Fig. 3

Fig. 3. DTA-TG curves of the precursor gel powder.

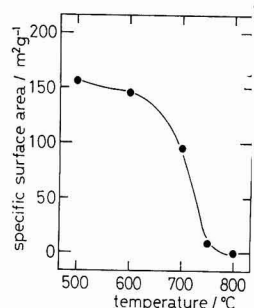


Fig. 4

Fig. 4. Specific surface area of calcinated powder calcinating time; 1h.

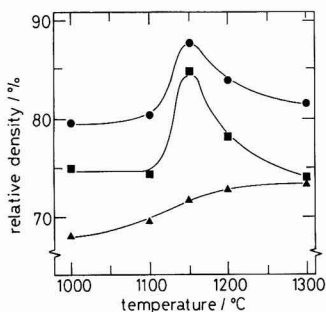


Fig. 5

Fig. 5. Relationship between relative density and firing temperature of the compacts, calcinating temperature ●; 500°C ■; 600°C ▲; 800°C.

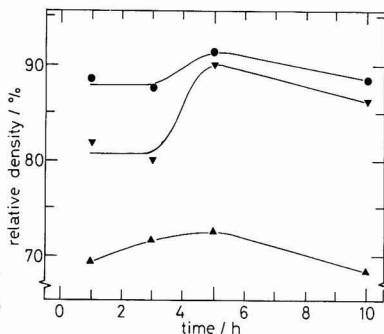


Fig. 6

Fig. 6. Change of the relative density with firing time calcinating temperature ●; 500°C ■; 600°C ▲; 800°C firing temperature; 1150°C.

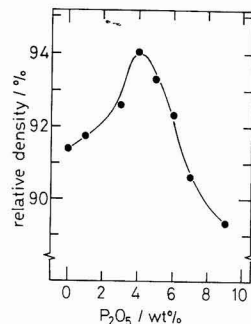


Fig. 7

Fig. 7. Effect of relative density of the compacts with excess amounts of P<sub>2</sub>O<sub>5</sub>.

### 3.2. Sinterability of Powder

It is expected that difference observed between the amorphous and crystalline powders in properties will affect their sinterability. Figure 5 shows the effects of firing temperature on relative density of the three types of double phosphate powders calcinated at different temperatures, which were fired for 3h at 5 different temperature levels in a range from 1000° to 1300°C. The samples calcinated at a lower temperatures showed a higher relative density, when fired, at all firing temperature levels tested than the one calcinated at a higher temperature. It is particularly noted that the green body calcinated at 500°C, a temperature level at which no growth of the grains was yet observed, was densified to the highest level, when fired at 1150°C. This probably resulted from the structural rearrangement accompanied by diffusion of ions, which accelerated bonding of the grains to each other and densification, since the transformation from the amorphous to the crystalline state occurred during the heating process. No such a phenomenon would be ex-

pected with the powder calcinated at 800°C or more, in which grain growth and crystallization were already completed. Figure 6 shows the effects of firing time on relative density of the sintered body, where the same green body was fired at 1150°C. Relative density increased with time, attaining a maximum (92%) at 5h.

The green body containing an excess amount of P<sub>2</sub>O<sub>5</sub>, calcinated at 1150°C for 5h, was fired at 1150°C for 5h. Relative density attained a maximum of 94% at 4wt% in excess of the stoichiometric P<sub>2</sub>O<sub>5</sub> content, showing in Fig.7 that P<sub>2</sub>O<sub>5</sub> is an effective sintering aid for the double phosphate system. The power X-ray diffraction analysis results indicate, as shown in Fig.8, that firing of the green body containing an excess amount of P<sub>2</sub>O<sub>5</sub> caused formation TiP<sub>2</sub>O<sub>7</sub>, in addition to the double phosphate. As a result, this powder body had a smaller amount of TiO<sub>2</sub> than the stoichiometric composition of the double phosphate. It is not known at present under what conditions excess amounts of CaO and P<sub>2</sub>O<sub>5</sub> are present in the system. It is, however, considered

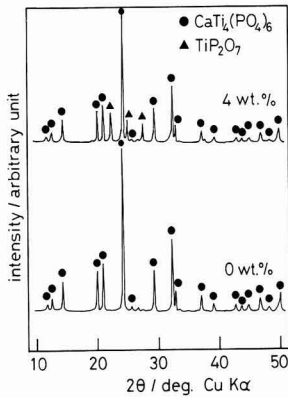


Fig. 8. XRD patterns of CTP and CTP with 4wt% excess of  $P_2O_5$ .

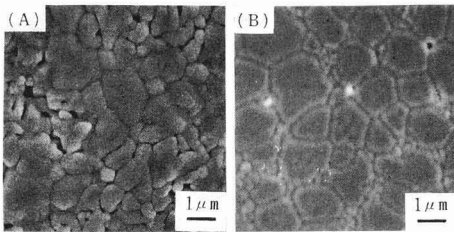


Fig. 9. SEM images of sintered compacts (A) CTP composition (B) 4wt% excess of  $P_2O_5$  polished and thermally etched surface.

that formation of  $TiP_2O_7$  accelerates diffusion of ion species constituting the powder particles, thereby contributing to densification by firing. **Figure 9** shows the SEM images of the polished and thermally etched surfaces of the sintered bodies. The texture of stoichiometric composition (A) has less uniformly sized grains and larger quantity of pores than the texture containing an excess amount of  $P_2O_5$  (B), indicating the effects of  $P_2O_5$  as the sintering aid.

### 3. 3. Properties of the Sintered Bodies

#### 3.3.1 Bending Strength

**Figure 10** shows the effects of firing temperature on bending strength of the sintered bodies. Both sintered bodies from the amorphous green body calcined at 500°C and the crystalline one calcined at 800°C had the highest bending strength, when fired at 1150°C. Decreased bending strength of the sintered bodies fired at 1200°C resulted conceivably from partial decomposition of the double phosphate. The green body calcined at 800°C was not sufficiently sintered to have a low bending strength of 17MPa at the highest, whereas that calcined at 500°C was sintered fairly sufficiently to have a bending strength of 57MPa at the highest. The green body containing 4wt% excess amount of  $P_2O_5$ , calcined at 500°C, had a still higher bending strength of 72MPa (indicated by the blank circle in

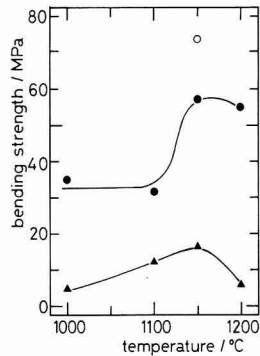


Fig. 10. Relationship between bending strength and sintering temperature of the compacts, calcinating temperature ●: 500°C ▲: 800°C ○: 4wt% excess of  $P_2O_5$  calcined at 500°C.

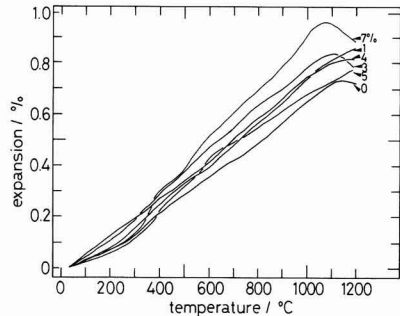


Fig. 11. Thermal expansion curves of sintered compacts with and without  $P_2O_5$  firing temperature; 1150°C, 5h.

Fig.10), when calcined at the same conditions as used for the stoichiometric composition.

#### 3.3.2. Thermal Expansion

**Figure 11** shows the thermal expansion curves for the sintered bodies from the stoichiometric composition and the green bodies containing excess amounts of  $P_2O_5$ . All of the sintered bodies containing excess amounts of  $P_2O_5$  were higher than the stoichiometric composition in thermal expansion, which, however, increased with temperature in a similar manner, irrespective of  $P_2O_5$  content. This indicates the complex effects of  $P_2O_5$  on the texture of sintered body, and possibility that thermal expansion coefficient may vary depending on conditions under which the sintered bodies are fired. The average thermal expansion coefficient in a range from room temperature to 800°C is  $6.5 \times 10^{-6}/^{\circ}C$  for the sintered body of the stoichiometric composition and  $8.2 \times 10^{-6}/^{\circ}C$  for the sintered body containing 4wt% excess amount of  $P_2O_5$ . The future research themes, therefore, will be to decrease thermal expansion coefficient, and to further improve mechanical properties by enhancing sinterability of the powder.

## 4. Conclusions

The amorphous and crystalline powders of the CTP composition, prepared by the sol-gel process, were investigated for the relationship between properties of the dried precursor gel and sinterability.

- 1) The dried precursor gel consisted of the agglomerated particles of 0.1 to 0.3 $\mu\text{m}$ . It was crystallized, when heated to 760°C, into the single-phase CTP. The crystallization was accompanied by rapid growth of the grains.
- 2) The amorphous green body, calcined at 500°C, was more sinterable than the one calcined at 800°C. The amorphous green body was fired at 1150°C for 5h into the sintered body having a relative density of 92%, bending strength of 57MPa and thermal expansion coefficient of  $6.5 \times 10^{-6}/^\circ\text{C}$  (room temperature to 800°C).
- 3) The green body containing 4wt% excess amount of  $\text{P}_2\text{O}_5$  as fired at 1150°C for 5h into the sinter having a relative density of 94%, bending strength of 72MPa and thermal expansion coefficient of  $8.2 \times 10^{-6}/^\circ\text{C}$ . The sintered body was characterized by more uniformly sized grains and a smaller quantity of pores, indicating the effects of  $\text{P}_2\text{O}_5$  as the sintering aid.

(The above results were presented at the 3rd Autumn symposium of the Ceramic Society of Japan held in September, 1990).

### Acknowledgements

The authors thank Mr. Hitoshi Okuda, then student of Sophia University, for his cooperation in the experiments.

### References:

- 1) L. Hagmann and P. Kierkegaard, *Acta Chem. Scand.*, 22, 1822 (1968).
- 2) R. Roy, D.K. Agrawal, J. Alamo and R.A. Roy, *Mat. Res. Bull.*, 19, 471 (1984).
- 3) J.B. Goodenough, N.Y.P. Hong and J.A. Kafalas, *ibid.*, 11, 203 (1976).
- 4) D.K. Agrawal and V.S. Stubican, *ibid.*, 20, 22 (1985).
- 5) R.D. Shannon, B.E. Taylor, A.D. English and T. Berzins, *Electrochim. Acta*, 22, 783 (1977).
- 6) T. Oota and I. Yamai, *J. Am. Ceram. Soc.*, 69, 1 (1986).
- 7) M. Inoue, A. Kishioka and M. Kinoshita, *J. Chem. Soc. Jpn.*, 1752 (1982).
- 8) M. Inoue, S. Kondou, A. Kishioka and M. Kinoshita, *ibid.*, 1752 (1982).
- 9) T. Oota and I. Yamai, *Yogyo-Kyokaiishi*, 95, 531 (1987).
- 10) T. Oota and I. Yamai, *J. Am. Ceram. Soc.*, 68, 273 (1985).
- 11) JCPDS card 35-740.

---

This article is a full translation of the article which appeared in *Nippon Seramikkusu Kyokai Gakujutsu Ronbunshi* (Japanese version), Vol.99, No.8, 1991.

# Densification of Plasma-sprayed Ceramic Coatings by HIP Treatment and their Cracking Behavior

Yutaka Ishiwata, Yoshiyasu Ito and Hideo Kashiwaya

Toshiba Corporation, Heavy Apparatus Engineering Labo.  
2-4, Suehiro-cho, Tsurumi-ku, Yokohama-shi, 230 Japan

The hot isostatic pressing (HIP) treatment of plasma-sprayed ceramic coatings was studied in order to improve the coating characteristics, such as micro-structure and bonding strength. Stabilized  $ZrO_2$ ,  $Al_2O_3$  and  $Y_2O_3$  were coated by plasma-spraying on two kinds of metal substrates (Nb and Type 304 stainless steel). HIP treatment was performed at from 1100°C to 1300°C under fixed pressure (98.1MPa) for 1hour. The porosity and bonding strength of ceramic coatings were measured. The residual stress analysis was carried out and compared with the cracking of ceramic coatings. The experimental results indicated that, for Nb substrate specimens, the porosity remarkably decreased and the bonding strength increased with increasing HIP temperature. But the cracks were observed at high HIP temperature. Such cracking behavior of HIP treated ceramic coatings was explained by the residual stress calculated by FEM analysis. On the other hand, no crack was observed in coatings on Type 304 substrate, because of the compressive residual stress in coatings induced by HIP treatment. But the bonding strength decreased with increasing HIP temperature.

[Received February 18, 1991; Accepted August 23, 1991]

**Key-words:** Ceramics coating, Residual stress, Cracking, Porosity, Densification, HIP, Plasma-spray, Solid state bonding

## 1. Introduction

Ceramic coating on metal surfaces is effective in improving the resistance against heat, corrosion and wear and has been utilized in various industrial fields in recent years. The plasma spraying, above all, has the feature that thick coating is possible even in large parts with comparatively complicated shapes, contrary to PVD or CVD. However, plasma sprayed coatings contains many pores,<sup>1,2)</sup> and may be useful as the insulating coating, but not necessarily so for the parts which call for high resistance against corrosion and wear, where there are cases that demand high bonding strength to metal substrates as well as the same density as in sintered ceramics. There are some reports<sup>3-6)</sup> on the usefulness of the HIP treatment as a mean to improve the characteristics of ceramic coatings formed by such plasma spraying, but many of these reports cover only the limited combination of such materials as  $ZrO_2/Ni$  or  $Al_2O_3/Fe$  and others, and are not necessarily prepared for the combination of metals and ceramics in wide ranges.

On the other hand, the writers have already carried out the analytical investigation on the residual stress charac-

teristics caused by the HIP treatment on ceramic coatings over the metal substrates,<sup>7)</sup> in which we clarified the trend that the dimensionless maximum stress  $\sigma_c (1-\mu_c)/[E_c(\alpha_c-\alpha_s)\Delta T]$  inducing on coatings decreases in proportion to the increase in the ratio of thickness between the substrate and coating ( $hc/hs$ ) as well as of Young's modulus ( $E_c(1-\mu_c)/[E_s(1-\mu_s)]$ ), where  $\sigma_c$ :the value of maximum stress caused on the coating,  $\mu_c$ : Poisson's ratio of the coating,  $\mu_s$ : Poisson's ratio of the substrate,  $E_c$ :Young's modulus of the coating,  $E_s$ :Young's modulus of the substrate,  $\alpha_c-\alpha_s$ :the difference of the thermal expansion coefficients between the coating and substrate, and  $\Delta T$ :the difference in temperature. We further estimated the critical temperature, at which crack does not generate on the coating, from the value of residual stress on the coating and the bending strength of the coating materials. This report deals with the comparison between the residual stress analysis and the experimental results on the fractures of coatings, and confirmed the feasibility of this comparison. We further measured the porosity and bonding strength of the coating with regards to the characteristics of the sprayed coating improved by the HIP treatment, and examined on the appropriate conditions for the HIP treatment.

## 2. Experimental Procedures

The combinations of metal substrates and sprayed coatings used for the experiment are shown in Table 1. The coatings were formed by plasma-spraying  $Al_2O_3$ ,  $Y_2O_3$ , and 8 mol%  $Y_2O_3$ -stabilized  $ZrO_2$  on metal substrates. For the metal substrates, we selected Nb which generates tensile residual strength on the sprayed coatings after the HIP treatment because of the smaller thermal expansion coefficient than the sprayed coats and Type 304 stainless steel which has, on the contrary, larger thermal expansion coefficient than the coats and generates compressive residual stress. Table 2 lists the chemical compositions of the ceramic spray powders and the metal substrates used for the experiment. The test specimens were prepared by blasting the #60 white alundum on one surface of the Nb and Type 304 substrates

Table 1. Constitution of specimens and thermal expansion coefficients.

Substrates	Nb			SUS 304	
	8.1%			19.0*	
Coatings	$8Y_2O_3$	$Al_2O_3$	$Y_2O_3$	$8Y_2O_3$	$Al_2O_3$
	$-ZrO_2$			$-ZrO_2$	
	10.7*	8.8*	8.6*	10.7*	8.8*

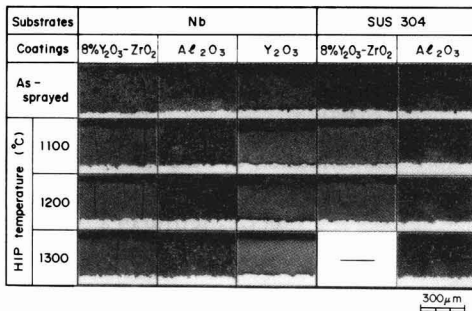
\*:  $\times 10^{-6}/^{\circ}C$ , at 1000°C

**Table 2.** Chemical compositions of material used .

Materials	Substrates				Coatings						
	Nb		SUS304		81 Y <sub>2</sub> O <sub>3</sub> -ZrO <sub>2</sub>		Al <sub>2</sub> O <sub>3</sub>		Y <sub>2</sub> O <sub>3</sub>		
Chemical compositions (Wt. %)	Ni	0.005	Ni	8.13	Y <sub>2</sub> O <sub>3</sub>	13.78	SiO <sub>2</sub>	0.05	SiO <sub>2</sub>	1.2	ppm
	Cr	0.001	Cr	18.21	CaO	0.02	Fe <sub>2</sub> O <sub>3</sub>	0.01	Fe <sub>2</sub> O <sub>3</sub>	2.7	ppm
	V	0.01	Mn	1.31	Na <sub>2</sub> O	0.014	Na <sub>2</sub> O	0.06	CaO	2	ppm
	Mo	0.003	Si	0.48	Al <sub>2</sub> O <sub>3</sub>	0.27	HgO	0.09	ZrO <sub>2</sub>	<2	ppm
	Ta	0.02	C	0.06							

**Table 3.** Plasma-spraying condition.

Spray distance	100 mm
Feed rate	30 g/min.
Plasma gas	Ar: 18.9 l/min He: 5.7 l/min
Power	750 A, 49 V

**Fig. 1.** Cross sections of as-sprayed and HIP treated ceramic coatings.

of 25.4mm in diameter and 5mm in thickness, and after degreasing they were plasma-sprayed in open air. The conditions used for plasma spraying are shown in **Table 3**. In preparing the sprayed test specimens, ceramics were sprayed directly on metal substrates without bond coats, and the coat thickness was fixed at 250 µm for every materials.

The test specimens after the plasma spraying were filled into cans of mild steel together with boron nitride powders, and after the 1hr baking at 1000°C in vacuum, they were filled in vacuum for the HIP treatment. The HIP treatment used the Ar gas as the pressure medium and was conducted at three temperatures of 1100°C, 1200°C and 1300°C. In the HIP treatment, the pressure was fixed at 98.1MPa for the retention time of 1hr, and the temperature was first raised to 800°C at which temperature the cans were fully softened, and then both the temperature and the pressure were increased simultaneously.

After the HIP treatment, we scrutinized the surfaces of specimens and their sections cut at the center on optical and scanning type electron microscopes, and evaluated the fractures in the coats and peelings induced by the HIP treatment. Then we measured the porosity on the coatings by the X-ray diffraction and image analyzing equipment (LUZEX made by NIRECO) on the as-spray coating and the HIP treated ceramic coatings, in order to clarify the improvements in the characteristics of the plasma-sprayed coating by the HIP treatment. The porosity was obtained by averaging the results of measurements at three places on the cut section at the center of the specimens. In addition, the bonding

strength of the coatings was measured in accordance with the ASTM standard,<sup>8)</sup> that is, the tensile strength test by fixing with thermosetting adhesives the tensile strength testing jig on the surface of coatings.

### 3. The Results of The Experiment

#### 3.1. Cracks on HIP Treated Ceramic Coats

**Figure 1** shows collectively the microstructures to the direction of coat thickness of cut sections at the center of the HIP treated specimens under the fixed conditions of 98.1 MPa retained for 1hr, with temperatures alternated at 1100°C to 1300°C. Fig.1 also shows the broken structure of as-sprayed coats for comparison sake. As the figure evidently shows, along with small pores of several µm, many large holes of several tens in µm were noticed in ceramic coats which might have been caused by entrapping the gas during the plasma-spraying<sup>5)</sup> or by the falling-off of grains during grinding because of weak binding force between them. On the other hand, the number of holes was markedly reduced after the HIP treatment, indicating that the HIP treatment caused the sprayed coats to densify. Moreover, in the as-spray coats, the melt ceramic grains did not fill into microscopic concave parts of the substrate surface, so that many voids generated in the boundary between the substrate and the coat, serving to be the factor to low bonding strength in sprayed coats. However, such interfacial voids were hardly observed after the HIP treatment.

Although no large crack was recognized in appearance in as-sprayed coats, we observed several linear cracks with wide opening on the HIP treated ceramic coat, of stabilized ZrO<sub>2</sub> on Nb substrate, while bent hairlike cracks were recognized in ceramic coats of Al<sub>2</sub>O<sub>3</sub> and Y<sub>2</sub>O<sub>3</sub> in the high temperature HIP treatment. Most of the cracks were vertical reaching to the substrate from the coat surface and were presumably caused by the residual stress generated during the cooling in the HIP treatment, since the direction of these cracks was vertical to the direction of maximum stress of the tensile residual stress as indicated in the previous report.

**Table 4** shows the cracks generated on ceramic coats summarized from Fig.1. Cracks generated distinctly in all HIP treated ceramic coated of stabilized ZrO<sub>2</sub>, which differs markedly in the thermal expansion coefficient from the Nb substrate. The opening width of these cracks tends to be wider as the temperature of the HIP treatment becomes higher, and we could observe cracks distinctly even in naked eyes in HIP ceramic coats treated at 1300°C. We recognized no cracks, or at best very tiny cracks in HIP coats of Al<sub>2</sub>O<sub>3</sub>

**Table 4.** Results of HIP treatment for ceramic coatings.

Substrates	Nb			SUS 304	
	8%Y <sub>2</sub> O <sub>3</sub> -ZrO <sub>2</sub>	Al <sub>2</sub> O <sub>3</sub>	Y <sub>2</sub> O <sub>3</sub>	8%Y <sub>2</sub> O <sub>3</sub> -ZrO <sub>2</sub>	Al <sub>2</sub> O <sub>3</sub>
As - sprayed	○	○	○	○	○
HIP Temp. (°C)	1100	×	△	○	○
	1200	×	△	△	○
	1300	×	×	×	—

○, No cracking ; △, Micro cracking ; ×, Cracking

or  $Y_2O_3$  treated at  $1100^\circ C$  which had smaller difference from Nb in the thermal expansion coefficient than  $ZrO_2$ , although we observed distinct cracks in either HIP coats treated at  $1300^\circ C$ .

On the other hand, no crack generated by the HIP treatment at  $1100$ - $1300^\circ C$  in sprayed coating of stabilized  $ZrO_2$  and  $Al_2O_3$  on Type 304 substrates which have higher thermal expansion coefficient than the coats, and it is evident that cracks are hard to generate in the combination of a coat and a substrate which generates compressive residual stress in coats. By the way, peelings in the coating of several hundreds  $\mu m$  in depth were observed in specimen of HIP treated Type 304 substrate along the interface at the end of the boundary between the coat and the substrate. This could be attributed to the tensile residual stress generated near the interface at the joined boundary end in the combination of materials in which the thermal expansion coefficient for the metal substrate is larger than for the coating. However, this tensile residual stress does not depend upon the size of metal substrates, and becomes almost zero at the distance of about 3 to 5 times of the coat thickness to the inside from the end surface.<sup>7)</sup> This stress may deteriorate the strength of the metal/ceramics composites,<sup>3,4)</sup> but does not become the major problem in the case of such a thin film coating as in this case, since this can be removed by the finishing work at the joined boundary end.

### 3.2. Comparison Between the Analysis and Actual Results

The previous report<sup>7)</sup> analyzed the results by FEM through changing the coefficients (Young's modulus and thermal expansion coefficient) and coat thickness. And it further sought the critical heating temperature in order that no crack will not generate, under the assumption that a crack generates in coats when the maximum tensile residual stress working on the ceramic coating reaches the fracture strength of the coat. **Figure 2** shows the critical heating temperatures calculated using the values of 10%, 30%, 50% and 70% of fracture probability from the Weibull's plot on test results of 4-point bending on sintered bodies of stabilized  $ZrO_2$ ,  $Al_2O_3$  and  $Y_2O_3$  as the fracture strength of the coating, as well as the experimental results of the Table 4. The calculation indicates that the critical heating temperature in either coating tends to be higher as the coat thickness ( $hc/hs$ ) increases. Although the bending strength was high, the critical heating temperature was generally low for stabilized  $ZrO_2$  (average bending strength 432 MPa), in which the difference in the thermal expansion coefficient from Nb is

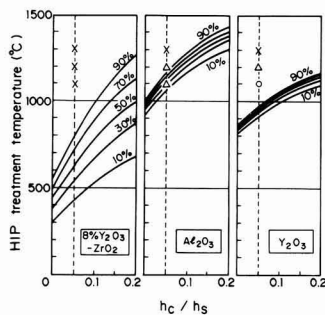


**Fig. 2.** Critical heating temperature and cracking of HIP treated coatings.

**Table 5.** Crystalline phases determined by X-ray powder diffractometer.

	Starting powder	As-sprayed	HIP temperature ( $^\circ C$ )		
			1100	1200	1300
8% $Y_2O_3$ - $ZrO_2$	cubic tetragonal monoclinic	cubic tetragonal	cubic tetragonal	cubic tetragonal	cubic tetragonal
$Al_2O_3$	$\alpha$ - $Al_2O_3$	$\eta$ - $Al_2O_3$ ( $\alpha$ - $Al_2O_3$ )	$\alpha$ - $Al_2O_3$ $\delta$ - $Al_2O_3$	$\alpha$ - $Al_2O_3$	$\alpha$ - $Al_2O_3$
$Y_2O_3$	cubic	cubic	cubic	cubic	cubic

large, and in the comparison between  $Al_2O_3$  and  $Y_2O_3$ , which have almost same thermal expansion coefficient as the substrate, the critical heating temperature was a little higher for  $Al_2O_3$  which have higher bending strength. On the other hand, the value of  $hc/hs$  was 0.05 and the temperatures were  $1100^\circ C$ - $1300^\circ C$  for the HIP treatment in this experiment, and the stabilized  $ZrO_2$  was treated at far higher temperature for the HIP treatment than the critical heating temperature, so that remarkable cracks were naturally recognized in all HIP treated specimens. Moreover, it appeared to us that the experimental results almost agree with the analytical results in  $Y_2O_3$  and  $Al_2O_3$ . From the above observation we can roughly grasp the behavior of cracks generating in ceramic coats through residual stress analysis, although we adopted the bending strength of the sintered products for the fracture strength of a coat and no provision was made for the phase transformation of the coating or the plastic deformation of the substrate.

## 4. Discussion

From the result of the previous Chapter, it became clear to us that the approach from the residual stress analysis is effective in deciding the temperature of the HIP treatment in order not to generate a crack in ceramic coating. However, when the temperature of the HIP treatment is low, it is good enough for the prevention of crack in the coat, but a problem remains in that the original purpose of the HIP treatment to improve the density of the coat and bonding strength cannot be fully attained. Therefore, we gave thoughts, in the following paragraphs, on the conditions for the adequate HIP treatment from the view points of improving the characteristics of spray coatings.

By the way, it is known that a thermally unstable phase is formed by the plasma spraying, since the ceramic grains were sprayed on the substrate in molten form and quickly quenched.<sup>9)</sup> **Table 5** indicates the results of X-ray diffraction on the surface of ceramic coats.  $ZrO_2$  spray powders used in this experiment were predominantly of biphasic composition of cubic and tetragonal phases, although they contained a few monoclinic. And this phase composition was not almost different either in as-spray coating or in the HIP treated ceramic coating.<sup>3)</sup> And  $Y_2O_3$  spray powders were monophasic only of cubic phase, and the phase composition retained the monophasic of cubic phase, whether in as-sprayed coat or whether in the HIP treated ceramic coat. On the other hand, we recognized some phase transformation in the  $Al_2O_3$ , in that although the spray powders were monophasic of  $\alpha$ - $Al_2O_3$ , in addition to  $\alpha$ - $Al_2O_3$ ,  $\eta$ - $Al_2O_3$ , which were stable at the high temperature, were formed in the as-spray coat, because they were rapidly quenched from

the molten status. Furthermore,  $\eta$ - $\text{Al}_2\text{O}_3$  was transformed into biphased of  $\alpha$ - $\text{Al}_2\text{O}_3$  and  $\delta$ - $\text{Al}_2\text{O}_3$  after the HIP treatment at  $1100^\circ\text{C}$ , and after the HIP treatment at  $1200^\circ\text{C}$  thermally unstable  $\delta$ - $\text{Al}_2\text{O}_3$  was again which is stable at room temperature. And a volumetric constriction can be expected during the phase transformations of from  $\eta$ - $\text{Al}_2\text{O}_3$  to  $\alpha$ - $\text{Al}_2\text{O}_3$  and  $\delta$ - $\text{Al}_2\text{O}_3$  and from  $\delta$ - $\text{Al}_2\text{O}_3$  to  $\alpha$ - $\text{Al}_2\text{O}_3$  in the HIP treatment. Therefore, it will be necessary to consider such a phase transformation, in deciding the critical heating temperature for the ceramic coating using the residual stress analysis as indicated in the last chapter. Additionally, it is clearly possible for such a material as  $\text{Al}_2\text{O}_3$ , in which plasma spraying may form thermally unstable coating, to stabilize the phase as well as the improvements on the mechanical characteristics of the coating through the HIP treatment.

Figure 3 shows the porosity for the as-spray coats and for HIP coats, treated at  $1100^\circ\text{C}$ - $1300^\circ\text{C}$ , with stabilized  $\text{ZrO}_2$ ,  $\text{Al}_2\text{O}_3$  and  $\text{Y}_2\text{O}_3$  on Nb substrates, which evidently indicates that porosity in any coating was around 10% in as-spray status, but decreased markedly after the HIP treatment. The effect of densification on the ceramic coating by the HIP treatment was pronouncedly evident with the increase in the treating temperature, and the porosity in any ceramic coating decreased below 1% after the HIP treatment at  $1300^\circ\text{C}$  and 98,1MPa for 1 hour, although the stabilized  $\text{ZrO}_2$  needs higher treating temperature because of its poorer capability in sintering than  $\text{Al}_2\text{O}_3$  and  $\text{Y}_2\text{O}_3$ , if the same degree of densification is required. From this results, it became clear to us that the necessary temperature for the HIP treatment in order to reduce the porosity to less than 1% must exceed  $1200^\circ\text{C}$  for  $\text{Al}_2\text{O}_3$  or  $\text{Y}_2\text{O}_3$  and  $1300^\circ\text{C}$  for stabilized  $\text{ZrO}_2$ ,<sup>5)</sup> and that the porosity decreases with the increase in the treating temperature. This is in reverse relationship with the critical heating temperature to prevent cracks on the coat.

The bonding strength of the stabilized  $\text{ZrO}_2$ ,  $\text{Al}_2\text{O}_3$  and  $\text{Y}_2\text{O}_3$  coats on Nb substrates are shown in Fig.4(a), and those of stabilized  $\text{ZrO}_2$  and  $\text{Al}_2\text{O}_3$  coats on Type 304 substrates in Fig.4(b). The measured values marked with arrows in these figures indicate that these bonding strength must be regarded to be higher because the specimens were fractured at the location of adhesives. In either materials, the bonding strength of as sprayed coating was 10–25 MPa

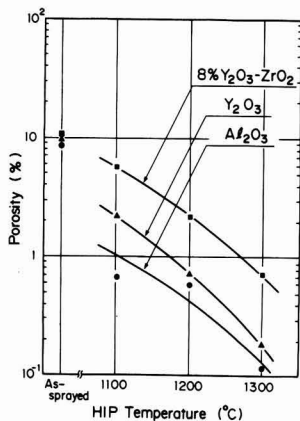


Fig. 3. Porosity measured in as-sprayed and HIP treated ceramic coatings.

with comparatively wide variation. And we can say that the bonding strength was the lowest at the boundary of the sprayed coat and the substrate, since fractures took places at this boundary. Fig.4(a) indicates the tendency to improve the bonding strength of the stabilized  $\text{ZrO}_2$  and  $\text{Y}_2\text{O}_3$  coats on Nb substrate along with the increase in the temperature of the HIP treatment. The fact that the locations of fractures were either inside the coats or the adhesives indicates that the HIP treatment improved the bonding strength between the coat and the substrate. Since we could not recognize distinctly the reaction phase in the boundary of the coat and the substrate after the HIP treatment by EPMA analysis, we think that the improvement on the bonding strength between the coat and substrate by the HIP treatment is affected greatly by the improvement of the anchoring effect of the coat itself due to the reduction, by the plastic flow of the metal substrate, of voids formed in the boundary between the coat and the substrate during the spraying, as well as the raised strength of the coat itself increased by the densification.<sup>3)</sup> On the other hand, the  $\text{Al}_2\text{O}_3$  coating on Nb substrate showed, contrary to other ceramic coating, high bonding strength (60MPa) in HIP specimens treated at  $1100^\circ\text{C}$ , but HIP specimens treated at  $1200^\circ\text{C}$  or  $1300^\circ\text{C}$  contrarily

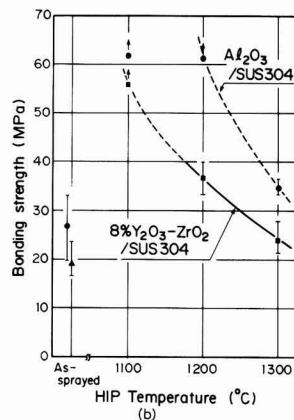
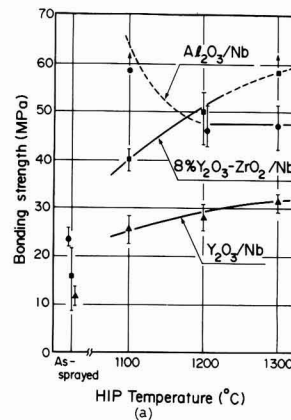


Fig. 4. Bonding strength of ceramic coatings measured by tension test with epoxy cement.

(a) Nb substrate specimens and (b) Type 304 substrate specimens

showed a tendency to lower the bonding strength. It is possible that the lowering in the bonding strength of the  $\text{Al}_2\text{O}_3$  sprayed HIP coat treated at high temperature was influenced greatly by the inside stress caused by phase transformation, since the  $\text{Al}_2\text{O}_3$  coat cause a phase transformation, contrary to stabilized  $\text{ZrO}_2$  or  $\text{Y}_2\text{O}_3$ , as shown in **Table 5**. Fig.4(b) shows the bonding strength of stabilized  $\text{ZrO}_2$  and  $\text{Al}_2\text{O}_3$  coating on Type 304 substrates. In either ceramic coating, the bonding strength was improved by the HIP treatment but showed a tendency to decrease as the treating temperature increases. Fractures on HIP specimens treated at  $1100^\circ\text{C}$  which showed high bonding strength inside the coat or inside the adhesives, but cracks generated from the coat and the substrate in many HIP specimens treated at  $1300^\circ\text{C}$ , and spread over to the boundary of the coat and the substrate. The study<sup>7)</sup> of the writers et al. clarified that the distribution of the residual stress in stabilized  $\text{ZrO}_2$  or  $\text{Al}_2\text{O}_3$  coat on Type 304 substrate causes compressive stress to the direction of coat thickness inside the coating, but high tensile residual stress to the direction of coat thickness at the boundary end. Accordingly, we are led to believe that the bonding strength was decreased in appearance by the concentration of this tensile residual stress at the boundary end.

## 5. Conclusion

We carried out the experiment mainly focussing in the residual stress regarding the appropriate conditions for the HIP treatment in which no crack generates in the ceramic coating by the combined application of plasma spraying and HIP treatment. Hereunder are the results of our experiment.

- 1) We recognized a tendency in stabilized  $\text{ZrO}_2$ ,  $\text{Al}_2\text{O}_3$  and  $\text{Y}_2\text{O}_3$  coats on Nb substrates, in that hexagonal cracks generated more remarkably with the increase in the temperature of the HIP treatment. We think that the HIP treatment induces the tensile residual stress in ceramic coatings. The results on the residual stress analysis enabled us to estimate the critical heating temperature which would not cause cracks on this coating.
- 2) We did not recognize on the coats any cracks induced by the HIP treatment in the stabilized  $\text{ZrO}_2$  and  $\text{Al}_2\text{O}_3$  coatings on Type 304 substrate. This is probably due to the fact that the thermal expansion coefficient is smaller for the coat than for the substrate, so that the compressive residual stress generated on the coat. However, we observed the peeling in the coat around the joined boundary

because of the tensile residual stress generated on joined boundary ends.

- 3) The crystalline construction of the stabilized  $\text{ZrO}_2$  and  $\text{Y}_2\text{O}_3$  coating was almost same in the as-spray status and after the HIP treatment. However, that of the  $\text{Al}_2\text{O}_3$  coat transformed from  $\eta\text{-Al}_2\text{O}_3$  and  $\alpha\text{-Al}_2\text{O}_3$  in as-sprayed status to  $\delta\text{-Al}_2\text{O}_3$  and  $\alpha\text{-Al}_2\text{O}_3$ , as the temperature increases in the HIP treatment.
- 4) About 10% of pores existed inside the sprayed coating in as-spray status, but the porosity in any coating was reduced to less than 1% by the HIP treatment at  $1300^\circ\text{C}$ , 98.1MPa and for 1hr. There was a tendency that this porosity in ceramic coating decreases with the increased temperature for the HIP treatment. The coatings of  $\text{Al}_2\text{O}_3$  and  $\text{Y}_2\text{O}_3$  densified at lower HIP temperature than stabilized  $\text{ZrO}_2$  coating.
- 5) The bonding strength of stabilize  $\text{ZrO}_2$  and  $\text{Y}_2\text{O}_3$  coatings formed on Nb substrate improved along with the increased temperature of the HIP treatment, but the bonding strength of  $\text{Al}_2\text{O}_3$  coating on Nb substrate and of stabilized  $\text{ZrO}_2$  coating and  $\text{Al}_2\text{O}_3$  coating formed on Type 304 substrates showed the tendency to decrease along with the temperature rise in the HIP treatment.

## References:

- 1) T. Chida, S. Amada, S. Uematsu and S. Sato, Nihon-Youseitu-Gakkaishi, 40, 8-12 (1988).
- 2) Y. Ito, Y. Ishiwata and H. Kashiwaya, Seramikkusu-Ronbunsi, 98, 561-566 (1990).
- 3) H. Kuribayashi, K. Suganuma, Y. Miyamoto and M. Koizumi, J. Am. Ceram. Soc., 65, 1306-1310 (1986).
- 4) K. Suganuma, T. Okamoto, M. Shimada and M. Koizumi, High Temp. Science, 20, 127-139 (1985).
- 5) H. Kuribayashi, K. Suganuma, Y. Miyamoto and M. Koizumi, Proc. 3rd Int. Conf. Isostatic-Pressing, Vol.1 (1986) paper 30.
- 6) Y. Ishiwata, Y. Ito and H. Kashiwaya, Nihon-Kinzokugakkai-Kouen-gaiyou, 358 Apr., 1988 and 523 Oct. 1988.
- 7) Y. Itoh, Y. Ishiwata and H. Kashiwaya, Seramikkusu-Ronbunshi, 97, 747-752 (1989).
- 8) Am. Nat. Standard, Adhesion or Con-Sive Strength of Frame-Spread Coatings, ASTM C633-79, 799-805 (1997).
- 9) G.F. Hurtley, F.D. Gac, Ceram. Bull. 58, 509-511 (1979).
- 10) B.C. Lippens and H.H. Bower, Acta Cryst., 17, 1312-1321 (1964).

# Preparation and Thermal Expansion Behavior of Pollucite Powders by Sol-Gel Processing

Hidehiko Kobayashi, Toshihiro Terasaki, Toshiyuki Mori\*, Chihiro Ishihara\*, Shoshichi Saito\*, Hiroshi Yamamura\* and Takashi Mitamura

Department of Applied Chemistry, Faculty of Engineering, Saitama University  
255 Shimo-ohkubo, Urawa-shi, 338 Japan

\*Advanced Materials Research Laboratory, TOSOH Co., Ltd.  
2743-1 Hayakawa, Ayase-shi, 252 Japan

Pollucite ( $\text{Cs}_2\text{O}\cdot\text{Al}_2\text{O}_3\cdot 4\text{SiO}_2$ ) powders were prepared from a combination of  $\text{Al}_2\text{O}_3$  sol,  $\text{SiO}_2$  sol and  $\text{CsNO}_3$  starting materials by sol-gel processing, and a stable region of single phase pollucite was investigated. The pollucite powders of single phase were synthesized when  $\text{Cs}_2\text{O}/\text{SiO}_2$  and  $\text{Al}_2\text{O}_3/\text{SiO}_2$  molar ratios were 0.91–1.02:4 and 0.96–2.38:4, respectively, by standardizing  $\text{SiO}_2$  molar ratio. The lattice parameters at room temperature were affected mainly by the  $\text{Cs}_2\text{O}/\text{SiO}_2$  ratio. It was confirmed by a high-temperature X-ray diffractometry that the thermal expansion for the pollucite powders is greatly affected by the change of compositions: the thermal expansion coefficient decreased with decreasing  $\text{Cs}_2\text{O}/\text{SiO}_2$  ratio from room temperature to 200°C and increased with increasing  $\text{Al}_2\text{O}_3/\text{SiO}_2$  ratio above 600°C. An increasing tendency of the latter has turned out to be caused by a slight amount of  $\alpha\text{-Al}_2\text{O}_3$  formed in the course of calcination. However, such behavior was not observed at the  $\text{Al}_2\text{O}_3/\text{Cs}_2\text{O}$  ratio of less than 1.

[Received February 27, 1991; Accepted April 19, 1991]

**Key-words:** Pollucite powder,  $\text{Al}_2\text{O}_3$  sol,  $\text{SiO}_2$  sol,  $\text{CsNO}_3$ , Sol-gel processing, High-temperature XRD

## 1. Introduction

Pollucite ( $\text{Cs}_2\text{O}\cdot\text{Al}_2\text{O}_3\cdot 4\text{SiO}_2$ ) as one of aluminosilicate compounds is known for its ability to fix radioactive isotope  $^{137}\text{Cs}$ .<sup>1)</sup> It is of cubic crystalline structure over a wide temperature range above room temperature, and has favorable characteristics as low-expansion type ceramic material, whose thermal expansion coefficient is close to zero in a range from 200° to 600°C.<sup>2)</sup> The other low-expansion type aluminosilicates include cordierite,  $\beta$ -spodumene and eucryptite. It is known that the thermal expansion characteristics of  $\beta$ -spodumene can be controlled by changing  $\text{SiO}_2$  content,<sup>3)</sup> and cordierite has a limited compositional range.<sup>4)</sup> Thus, the low expansion characteristics of aluminosilicates change with their chemical compositions. For pollucite, on the other hand, few researchers have discussed synthesis of the powder,<sup>5-8)</sup> or relationship between powder composition and thermal expansion behavior.

In this study, therefore, an attempt was made to synthesize the pollucite powder by the sol-gel process, to investigate the single-phase pollucite region. The pollucite powder thus prepared was analyzed by a high-temperature type powder X-ray diffractometer, to follow its thermal ex-

pansion behavior. Further, the changes in chemical composition in the single-phase pollucite region were followed, to investigate their effects on thermal expansion behavior.

## 2. Experimental Procedure

### 2.1. Synthesis of Sample Powders

The starting materials were  $\text{Al}_2\text{O}_3$  sol (Nissan Chemical, Alumina Sol 200),  $\text{SiO}_2$  sol (Nissan Chemical, Snowtex O) and  $\text{CsNO}_3$  (Kojundo Kagaku Kenkyusho, purity: >99%).  $\text{Al}_2\text{O}_3$  sol and  $\text{SiO}_2$  sol were mixed in a given ratio ( $\text{Al}_2\text{O}_3/\text{SiO}_2 = 1$  to 6 mol/mol), where pH of each sol was adjusted at 5.5 with ammonia water.<sup>9)</sup> The mixture was stirred by a dynamic stirrer for 24h, and then treated by a rotary evaporator, to remove water. The mixed gel was further treated by a rotary evaporator, after having been dispersed in an ethanol solution, in order to further remove a small quantity of water remaining in the gel, and then dried. The dried gel was thermally treated at 550°C for 2h.

The heat-treated gel was crushed in a plastic pot with  $\text{Al}_2\text{O}_3$  balls for 24h in the presence of ethanol, to which powdered  $\text{CsNO}_3$  was added in a ratio to give a given composition as  $\text{Cs}_2\text{O}$ , and the mixture was again ball-milled for 24h in the presence of ethanol. It was then dried, by removing the solvent, and thermally treated by a Tamman oven at 750°C for 10h. The mixed powder, after having been further mixed by an agate mortar, was calcined by a box-type high-temperature air oven at 1000°C to 1400°C for a given time (2 to 96h).

The calcined powder was analyzed by a powder X-ray diffractometer (Rigaku Denki,  $\text{CuK}\alpha$ , 40kV, 30mA, RAD-C System), to identify the phases formed. The crystalline phases formed by the heat treatment were identified a high-temperature type powder X-ray test attachment (Rigaku Denki, Sample High-temperature Equipment CN2311B1), where each sample was heated at 10°C/min, and tested at a scanning rate of 4°/min in a range  $2\theta=15$  to 35°. The lattice parameters of pollucite at room temperature were determined by Rigaku Denki's application software for the (332), (431), (440), (611), (444) and (721) planes, with silicon as the outer standard. The measurement conditions were a scanning rate of 1°/min and sampling angle  $2\theta$  of 0.02°. The mixed powder was also analyzed by a TG-DTA analyzer (Rigaku Denki, TAS-200) for the thermal decomposition process and crystallization temperature, where the sample was heated at 10°C/min from room temperature to 1000°C.

## 2.2. Thermal Expansion Coefficient

Lattice parameters at various temperature levels of the pollucite powders synthesized were determined by a high-temperature type powder X-ray diffractometer, from which thermal expansion coefficients were determined. The analysis conditions were a scanning range of  $2\theta=25$  to  $55^\circ$ , scanning rate of  $1^\circ/\text{min}$ , and heating rate of  $10^\circ\text{C}/\text{min}$ . The measurement was done at intervals of  $50^\circ\text{C}$  in a range between  $50^\circ$  and  $300^\circ\text{C}$  and at intervals of  $100^\circ\text{C}$  in a range between  $400^\circ$  and  $1000^\circ\text{C}$ . Each diffraction peak at various temperature levels was analyzed for the  $2\theta$  value from the center point of the half-width, for the one appearing at room temperature, and processed by the least-square method to find the lattice parameter.

## 2.3. Chemical Analyses

The chemical analysis methods used in this study were absorption spectroscopy for the  $\text{Cs}_2\text{O}$  composition (after atomic  $\text{SiO}_2$  was removed), weight analysis for  $\text{SiO}_2$  (the  $\text{SiO}_2$  composition was dissolved in sodium carbonate and then treated with perchloric acid fume, to prepare the sample), and the EDTA titration method for the  $\text{Al}_2\text{O}_3$  composition (after  $\text{SiO}_2$  was removed).

## 3. Results and Discussion

### 3.1. Synthesis of Pollucite Powder

The dry powder of the starting  $\text{Al}_2\text{O}_3/\text{SiO}_2$  gel mixture ( $\text{Al}_2\text{O}_3/\text{SiO}_2 = 1/4$  mol/mol) was analyzed by the TG-DTA method. The TG-DTA curves were characterized the broad exothermic peak and weight loss at up to around  $500^\circ\text{C}$ , resulting from combustion of adsorbed ethanol. They remained unchanged at above  $500^\circ\text{C}$ , based on which the dry powder of the mixed gel was thermally treated at  $550^\circ\text{C}$  for 2h, to which the  $\text{CsNO}_3$  powder was added, to prepare the mixed powder of the pollucite composition (hereinafter referred to as Mixed Powder).

Figure 1 presents the TG-DTA curves of mixed powder. The sharp endothermic peak found at around  $150^\circ\text{C}$  results from the phase transformation of  $\text{CsNO}_3$  from the hexagonal to cubic system,<sup>10</sup> the exothermic peak at  $200^\circ$  to  $300^\circ\text{C}$  from the combustion of adsorbed ethanol, and the endothermic peak at  $500^\circ$  to  $700^\circ\text{C}$ , associated with a weight loss,

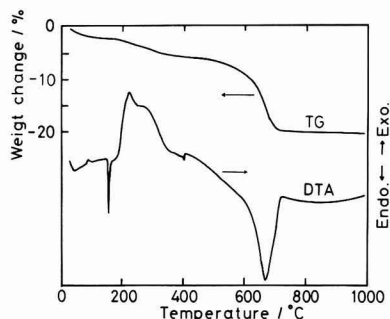


Fig. 1. TG-DTA curves of pollucite composition powder.

from thermal decomposition of  $\text{CsNO}_3$ .<sup>10</sup> For the thermal decomposition of the nitrate to be completed, it is necessary to hold the sample for a long time at sufficiently high temperature at which it is thermally decomposable, e.g., at  $600^\circ$  to  $700^\circ\text{C}$  for 12h.<sup>11</sup>

An attempt was made, therefore, to analyze the dry powder of the mixed gel by the TG-DTA method, after thermally treating the sample at  $600^\circ\text{C}$  for 10h or at  $750^\circ\text{C}$  for 10h. The results are given in Fig.2. Mixed powder thermally treated at  $600^\circ\text{C}$  for 10h had a weight loss at around  $700^\circ\text{C}$ , indicating that the above conditions were insufficient for the thermal decomposition of  $\text{CsNO}_3$ . For mixed powder thermally treated at  $750^\circ\text{C}$ , the weight loss resulting from thermal decomposition of  $\text{CsNO}_3$  at around  $700^\circ\text{C}$  was not found not on the TG curve, and there was an exothermic peak at around  $950^\circ\text{C}$  on the DTA curve. It was found that the exothermic peak appearing at around  $950^\circ$  to  $1000^\circ\text{C}$  varied with extent of thermal decomposition  $\text{CsNO}_3 \rightarrow \text{Cs}_2\text{O} + \text{NO}_2$  occurring at  $500^\circ$  to  $700^\circ\text{C}$ .<sup>10</sup>

In order to identify the exothermic peak, mixed powder thermally treated at  $750^\circ\text{C}$  for 10h was analyzed by a high-temperature type powder X-ray diffractometer. The results are given in Fig.3. Mixed powder remained amorphous at up to  $900^\circ\text{C}$ , but the pollucite phase appeared at above  $950^\circ\text{C}$ , from which it was judged that the exothermic peak found at around  $950^\circ\text{C}$  on the DTA curve was the crystallization peak of the pollucite phase. The diffraction peak of the  $\text{CsAlSiO}_4$  phase was also found, in addition to that of the pollucite phase, at above  $1000^\circ\text{C}$  in the X-ray diffraction patterns given in Fig.3. Presence of the  $\text{CsAlSiO}_4$  phase became clearer as crystallization of mixed powder proceeded. This phase, however, disappeared when calcination temperature for mixed powder was increased to above  $1300^\circ\text{C}$ , as shown in Fig.4, and therefore powder of the single pollucite phase was synthesized.

The conventional method to synthesize pollucite powders is based on the liquid-phase process using aluminum nitrate,  $\text{SiO}_2$  (or ethyl silicate) and cesium carbonate as the starting materials, the product being kept at  $1100^\circ$  to  $1200^\circ\text{C}$  for 3 to 6 days, to prepare the single phase.<sup>5,6</sup> Importance of mixing the starting materials uniformly is also pointed out.<sup>7</sup> Therefore, mixed powder was calcined at  $1000^\circ\text{C}$  for 2 to 100h, to investigate the relationship between relative intensity of the (400) plane of pollucite and half width. The results are given in Fig.5. The powder, when calcined at  $1000^\circ\text{C}$  for 2h, was almost amorphous, and relative intensity of the pollucite phase increased with calcination time, attaining a constant level at 50h or longer.

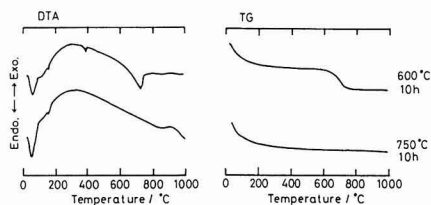


Fig. 2. TG-DTA curves of each pollucite composition powder after heat treatment.

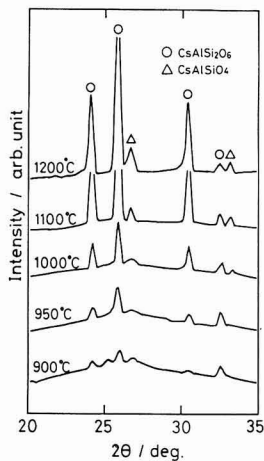


Fig. 3

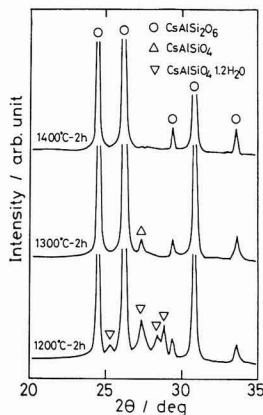


Fig. 4

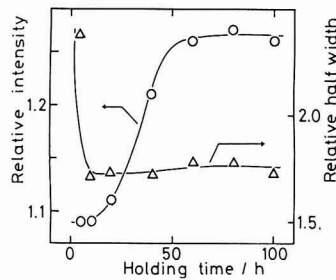


Fig. 5

Fig. 3. X-ray powder diffraction patterns of pollucite composition powder at various temperatures by high-temperature XRD with CuK $\alpha$ .

Fig. 4. X-ray powder diffraction patterns of pollucite composition powder calcined at various temperatures, with CuK $\alpha$ . Holding time was 2h.

Fig. 5. Effect of holding time on the relative intensity and half width of pollucite powder.

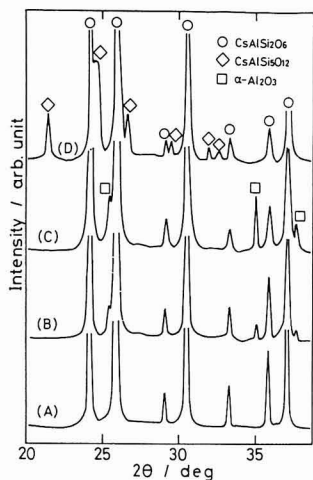


Fig. 6

Fig. 6. X-ray powder diffraction patterns of (A) Cs<sub>2</sub>O:SiO<sub>2</sub>:Al<sub>2</sub>O<sub>3</sub> = 1:4:1, (B) Cs<sub>2</sub>O:SiO<sub>2</sub>:Al<sub>2</sub>O<sub>3</sub> = 1:4:2.5, (C) Cs<sub>2</sub>O:SiO<sub>2</sub>:Al<sub>2</sub>O<sub>3</sub> = 1:4:4 and (D) Cs<sub>2</sub>O:SiO<sub>2</sub>:Al<sub>2</sub>O<sub>3</sub> = 1:6:1 composition powders, with CuK $\alpha$ . Calcined at 1400°C, 5h.

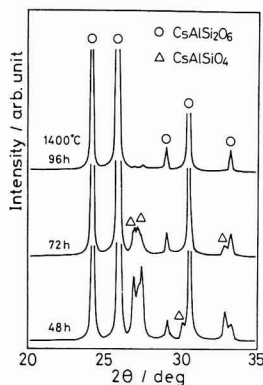


Fig. 7

Fig. 7. X-ray powder diffraction patterns of Cs<sub>2</sub>O:SiO<sub>2</sub>:Al<sub>2</sub>O<sub>3</sub> = 10:4:1 composition powder calcined at 1400°C for various times, with CuK $\alpha$ .

It may be therefore concluded that calcination temperature of at least 1000°C is needed to synthesize the powder of the single pollucite phase, and that required holding time decreases as calcination temperature increases.

### 3.2. Single-Phase Pollucite Region

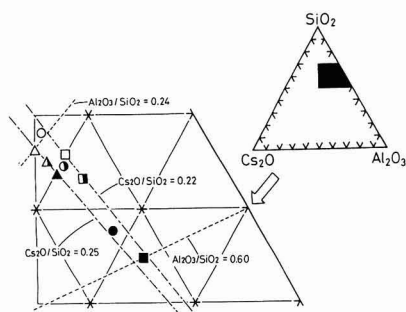
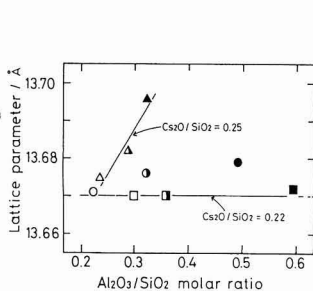
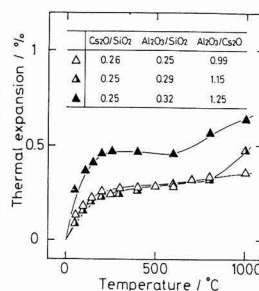
The powder samples in which each of Cs<sub>2</sub>O, SiO<sub>2</sub> and

Al<sub>2</sub>O<sub>3</sub> was present in excess of the stoichiometric content were prepared, and were calcined at 1400°C for 5h, to investigate the single pollucite phase region by analyzing the products by a powder X-ray diffractometer.

Figure 6 presents the powder X-ray diffraction patterns of the products prepared from the sample powders of varying Cs<sub>2</sub>O:SiO<sub>2</sub>:Al<sub>2</sub>O<sub>3</sub> molar ratio. The composition of

**Table 1.** Composition of starting material and heat treatment condition and chemical composition of each pollucite powder after heat treatment.

Composition of starting material Cs <sub>2</sub> O:SiO <sub>2</sub> :Al <sub>2</sub> O <sub>3</sub> (molar ratio)	Heat treatment time (h) at 1400°C	Chemical composition after heat treatment	
		Cs <sub>2</sub> O:SiO <sub>2</sub> :Al <sub>2</sub> O <sub>3</sub> (molar ratio)	Mark in Fig. 8-13
1 : 4 : 1	5	0.91 : 4 : 0.96	○
1.33 : 4 : 1.33	10	0.91 : 4 : 1.27	●
2 : 4 : 2	20	0.97 : 4 : 1.97	●
1 : 4 : 1.25	5	0.87 : 4 : 1.20	△
1 : 4 : 1.5	5	0.88 : 4 : 1.44	▲
1 : 4 : 2.5	5	0.90 : 4 : 2.38	▲
6 : 4 : 1	48	1.02 : 4 : 1.01	□
8 : 4 : 1	72	1 : 4 : 1.15	■
10 : 4 : 1	96	1.01 : 4 : 1.27	■

**Fig. 8****Fig. 9****Fig. 10**

**Fig. 8.** Pollucite composition region of the Cs<sub>2</sub>O-SiO<sub>2</sub>-Al<sub>2</sub>O<sub>3</sub> system. The symbols in this figure are the same as those in Table 1.

**Fig. 9.** Lattice parameter of various pollucite composition powders. The symbols in this figure are the same as those in Table 2.

**Fig. 10.** Relation between temperature and thermal expansion for pollucite powder obtained from various Al<sub>2</sub>O<sub>3</sub>/SiO<sub>2</sub> and Al<sub>2</sub>O<sub>3</sub>/Cs<sub>2</sub>O molar ratios at Cs<sub>2</sub>O/SiO<sub>2</sub>=0.25.

Cs<sub>2</sub>O:SiO<sub>2</sub>:Al<sub>2</sub>O<sub>3</sub> = 1:6:1, higher in SiO<sub>2</sub> content than the stoichiometric pollucite composition, had the CsAlSi<sub>5</sub>O<sub>10</sub> phase in addition to pollucite, and the Al<sub>2</sub>O<sub>3</sub>-rich composition (Cs<sub>2</sub>O:SiO<sub>2</sub>:Al<sub>2</sub>O<sub>3</sub> = 1:4:4) had the α-Al<sub>2</sub>O<sub>3</sub> phase, in addition to pollucite. The Cs<sub>2</sub>O:SiO<sub>2</sub>:Al<sub>2</sub>O<sub>3</sub> = 1:4:2.5 composition, on the other hand, had only a trace of diffraction peak of α-Al<sub>2</sub>O<sub>3</sub> and hence was of almost single-phase. By contrast, the Cs<sub>2</sub>O-rich composition of Cs<sub>2</sub>O:SiO<sub>2</sub>:Al<sub>2</sub>O<sub>3</sub> = 10:4:1 had the pollucite and CsAlSi<sub>4</sub>O<sub>8</sub> phases, as identified by the powder X-ray diffraction analysis (Fig.7), when calcined at 1400°C for 48h. Intensity of the diffraction peak of the CsAlSi<sub>4</sub>O<sub>8</sub> phase tended to diminish as calcination time increased, and the powder of the single pollucite phase was prepared by increasing calcination time to 96h.

**Table 1** summarizes the Cs<sub>2</sub>O:SiO<sub>2</sub>:Al<sub>2</sub>O<sub>3</sub> compositions and the calcination conditions therefore that gave the single pollucite phase, and the chemical compositions of the heat-treated products, determined by the chemical analysis. The Cs<sub>2</sub>O/SiO<sub>2</sub> molar ratio was varied around the stoichiometric pollucite ratio in a range from 1/4 to 10/4. The Cs<sub>2</sub>O/SiO<sub>2</sub> ratio of the calcined products, however, were fairly close to the stoichiometric ratio to vary in a range from 0.85/4 to 1.02/4, because of the evaporation of the Cs compound during the calcination process.<sup>12)</sup> Next, the Al<sub>2</sub>O<sub>3</sub>/SiO<sub>2</sub> ratio was varied from 1/4 to 2.5/4, and the calcined ratio was 0.96/4 to 2.38/4. Thus, the powder of the single pollucite phase resulted from the Al<sub>2</sub>O<sub>3</sub>-rich composition.

**Figure 8** shows the single pollucite phase region, drawn

using the data shown in Table 1. The single phase region expanded in the direction of increasing Al<sub>2</sub>O<sub>3</sub>/SiO<sub>2</sub> ratio and of slightly decreasing Cs<sub>2</sub>O/SiO<sub>2</sub> ratio, where SiO<sub>2</sub> was at the stoichiometric content.

### 3.3. Effects of Changed Composition on Lattice Parameter of Pollucite

The effects of changed Cs<sub>2</sub>O:SiO<sub>2</sub>:Al<sub>2</sub>O<sub>3</sub> composition on lattice parameter of the single pollucite phase were investigated using the lattice parameter levels varying with the Al<sub>2</sub>O<sub>3</sub>/SiO<sub>2</sub> ratio. The results are given in Fig.9. The lattice parameter varied significantly with Al<sub>2</sub>O<sub>3</sub>/SiO<sub>2</sub>, when the Cs<sub>2</sub>O/SiO<sub>2</sub> ratio was set at the stoichiometric ratio of 0.25mol/mol. By contrast, it was essentially irrespective of the Al<sub>2</sub>O<sub>3</sub>/SiO<sub>2</sub> ratio, when the Cs<sub>2</sub>O/SiO<sub>2</sub> ratio was set at 0.22, which was slightly lower than the stoichiometric level.

Next, the effects of Cs<sub>2</sub>O/SiO<sub>2</sub> ratio on the lattice parameter were investigated, based on the pollucite structure. The pollucite structure is characterized by Cs<sup>+</sup> ion being coordinated in the three-dimensional aluminosilicate network where the SiO<sub>4</sub> and AlO<sub>4</sub> tetrahedrons share the apexes, and size of the Cs<sup>+</sup> ion in the network structure makes the system cubic at room temperature.<sup>5)</sup> In other words, pollucite structure characterized by the Cs<sup>+</sup> ion will vary in lattice parameter with Cs<sub>2</sub>O/SiO<sub>2</sub> and Al<sub>2</sub>O<sub>3</sub>/SiO<sub>2</sub> ratios, the latter being related to the aluminosilicate network structure. **Table 2** summarizes the Cs<sub>2</sub>O/SiO<sub>2</sub> and Al<sub>2</sub>O<sub>3</sub>/SiO<sub>2</sub> ratios, and corresponding lattice parameters,

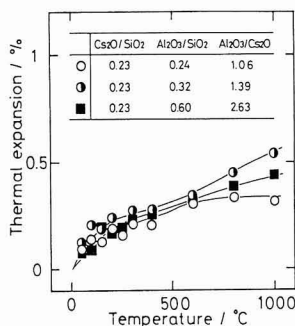


Fig. 11

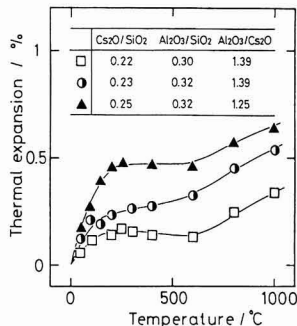


Fig. 12

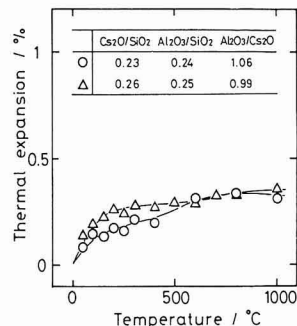


Fig. 13

**Fig. 11.** Relation between temperature and thermal expansion for pollucite powder obtained from various  $\text{Al}_2\text{O}_3/\text{SiO}_2$  and  $\text{Al}_2\text{O}_3/\text{Cs}_2\text{O}$  molar ratios at  $\text{Cs}_2\text{O}/\text{SiO}_2=0.23$ .

**Fig. 12.** Relation between temperature and thermal expansion for pollucite powder obtained from various  $\text{Cs}_2\text{O}/\text{SiO}_2$  and  $\text{Al}_2\text{O}_3/\text{Cs}_2\text{O}$  molar ratios at  $\text{Al}_2\text{O}_3/\text{SiO}_2=0.32$ .

**Fig. 13.** Relation between temperature and thermal expansion for pollucite powder obtained from various  $\text{Cs}_2\text{O}/\text{SiO}_2$  and  $\text{Al}_2\text{O}_3/\text{Cs}_2\text{O}$  molar ratios at  $\text{Al}_2\text{O}_3/\text{SiO}_2=0.24$ .

from which it is judged that the parameter is affected more by  $\text{Cs}_2\text{O}/\text{SiO}_2$  than by  $\text{Al}_2\text{O}_3/\text{SiO}_2$ , and that volumes of the  $\text{AlO}_4^-$  and  $\text{SiO}_4$  tetrahedrons relative to that of  $\text{Cs}^+$  in the pollucite structure ( $\text{Cs}^+$  ion is fairly larger than the  $\text{SiO}_4$  tetrahedron, but large than the  $\text{AlO}_4^-$  tetrahedron only slightly) determine the  $\text{Cs}_2\text{O}/\text{SiO}_2$  and  $\text{Al}_2\text{O}_3/\text{SiO}_2$  ratios, to vary lattice parameter level.

### 3.4. Changes in Pollucite Composition and Thermal Expansion Behavior

Lattice parameter of the pollucite powder at room temperature varies with the  $\text{Cs}_2\text{O}:\text{SiO}_2:\text{Al}_2\text{O}_3$  compositional change which reflects relative size of  $\text{Cs}^+$  ion, and  $\text{AlO}_4^-$  and  $\text{SiO}_4$  tetrahedrons. It is expected that the compositional change also affects the pollucite structure whose thermal expansion behavior will be different from that of the pollucite powder discussed earlier.<sup>5,6)</sup> In order to confirm this, thermal expansion behavior of the single-phase pollucite powders of different compositions, shown in Fig.8, was investigated.

**Figure 10** shows thermal expansion of the pollucite powders whose  $\text{Cs}_2\text{O}/\text{SiO}_2$  ratio was set at almost the stoichiometric ratio of 0.25. The sample powder having almost the stoichiometric composition ( $\text{Cs}_2\text{O}:\text{SiO}_2:\text{Al}_2\text{O}_3=1.02:4:1.01$ , marked with  $\Delta$ ) had thermal expansion coefficient increasing positively as temperature increased from room temperature to 200° but essentially constant in a temperature range from 200° to 600°C. Such behavior is in agreement with that discussed earlier.<sup>5,6)</sup> Increasing temperature further increased the coefficient, though at a much lower rate than observed at from room temperature to 200°C.

The sample powders having higher  $\text{Al}_2\text{O}_3/\text{SiO}_2$  and  $\text{Al}_2\text{O}_3/\text{Cs}_2\text{O}$  ratios than the stoichiometric ratios (marked with  $\Delta$ ,  $\blacktriangle$ ) had thermal expansion coefficient increasing notably in a temperature range from room temperature to 200°C and above 600°C. Increasing  $\text{Al}_2\text{O}_3$  relative to  $\text{Cs}_2\text{O}$  and  $\text{SiO}_2$  from the stoichiometric ratios increased thermal expansion coefficient more notably, and, in particular, decreased temperature at which the coefficient started to

increase at above 600°C.

**Figure 11** shows thermal expansion of the pollucite powders whose  $\text{Cs}_2\text{O}/\text{SiO}_2$  ratio was set at 0.23 which was lower than the stoichiometric ratio. In such a case, the coefficient increased slowly with temperature, almost insensitive to  $\text{Al}_2\text{O}_3/\text{SiO}_2$  in a range from room temperature to 200°C. At above 600°C, the coefficient tended to increase in the  $\text{Al}_2\text{O}_3$ -excess region. Richerson et al. attribute increased thermal expansion coefficient at above 600°C to the presence of unreacted  $\text{Al}_2\text{O}_3$  and  $\text{SiO}_2$ .<sup>6)</sup> It is considered that the increased thermal expansion coefficient at above 600°C, observed in this study, is attributable to trace quantities of  $\alpha$ - $\text{Al}_2\text{O}_3$  present in the sample powders, though not detected by the X-ray diffraction analysis of the single-phase powders, judging from the dependence of the coefficient on excess  $\text{Al}_2\text{O}_3$  ratio and formation of the  $\alpha$ - $\text{Al}_2\text{O}_3$  when  $\text{Al}_2\text{O}_3$  is present in an excessive quantity, as discussed in Section 3.3.

**Figure 12** shows thermal expansion coefficient of the sample powders having an  $\text{Al}_2\text{O}_3/\text{SiO}_2$  ratio of 0.32. It decreased as  $\text{Cs}_2\text{O}/\text{SiO}_2$  decreased from the stoichiometric level at room temperature to 200°C. It is therefore expected that decreasing  $\text{Cs}_2\text{O}/\text{SiO}_2$  ratio affects thermal movement of the open 4-member rings in which no  $\text{Cs}^+$  ion is coordinated in the aluminosilicate network structure.<sup>5)</sup>

**Figure 13** shows thermal expansion coefficient of the single-phase pollucite powder of almost the stoichiometric

**Table 2.** Composition and lattice parameter of pollucite powder after heat treatment.

Mark in Fig. 9-13	$\text{Cs}_2\text{O}/\text{SiO}_2$ molar ratio	$\text{Al}_2\text{O}_3/\text{SiO}_2$ molar ratio	Lattice parameter (Å)
□	0.22	0.30	13.670
■	0.22	0.36	13.670
○	0.23	0.24	13.671
●	0.23	0.32	13.676
■	0.23	0.60	13.672
●	0.24	0.49	13.679
▲	0.25	0.29	13.682
▲	0.25	0.32	13.697
△	0.26	0.25	13.675

composition. The coefficient was 0.35% or less in a temperature range from room temperature to 1000°C, when the  $\text{Al}_2\text{O}_3/\text{SiO}_2$  and  $\text{Cs}_2\text{O}/\text{Al}_2\text{O}_3$  ratios were close to the stoichiometric levels. In particular, the moderate increase in the coefficient at above 600°C conceivably results from inclusion of trace quantities of  $\alpha\text{-Al}_2\text{O}_3$  in the lattices to decrease its quantities.

In summary, thermal expansion of the pollucite powder is affected by its compositional change. It is necessary to keep the  $\text{Cs}_2\text{O}/\text{SiO}_2$  ratio below the stoichiometric level and  $\text{Al}_2\text{O}_3/\text{SiO}_2$  ratio close to the stoichiometric level, in order to synthesize the pollucite powder of low thermal expansion.

#### 4. Conclusions

The pollucite powder was synthesized by the sol-gel process, to investigate the single-phase region and the effects of compositional change on thermal expansion behavior.

- 1) Crystallization of the pollucite phase starts at around 1000°C. It is necessary to control calcination conditions, in order to produce the single pollucite phase.
- 2) The single-phase pollucite region extends in the direction of excessive quantities of  $\text{Cs}_2\text{O}$  and  $\text{Al}_2\text{O}_3$  relative to  $\text{SiO}_2$ , in a  $\text{Cs}_2\text{O}/\text{SiO}_2$  range from 0.91/4 to 1.02/4 and an  $\text{Al}_2\text{O}_3/\text{SiO}_2$  range from 0.96/4 to 2.38/4.
- 3) Lattice parameter of the pollucite powder at room temperature is determined mainly by the  $\text{Cs}_2\text{O}/\text{SiO}_2$  ratio, which conceivably results from relative volumes of  $\text{Cs}^+$  ion, and  $\text{AlO}_4^-$  and  $\text{SiO}_4$  tetrahedrons in the pollucite structure.

- 4) Thermal expansion of the pollucite powder is affected greatly by the compositional change. Thermal expansion coefficient tends to decrease as the  $\text{SiO}_2/\text{Cs}_2\text{O}$  ratio decreases at room temperature to 200°C. It is also observed that the coefficient increases as the  $\text{Al}_2\text{O}_3/\text{SiO}_2$  ratio increases at above 600°C. This is attributable to trace quantities of  $\alpha\text{-Al}_2\text{O}_3$  present, and is controlled by keeping  $\text{Cs}_2\text{O}/\text{Al}_2\text{O}_3 \leq 1$ .

#### References:

- 1) For example, T. Kanno, *Nendo Kagaku*, 25, 1-10 (1985).
- 2) S. Udagawa and H. Ikawa, *Seramikkusu*, 14, 967-976 (1979).
- 3) W. Ostrerag, G.R. Fischer and J.P. Williams, *J. Am. Ceram. Soc.*, 51, 651-654 (1968).
- 4) R.J. Beals and R.L. Cook, *J. Am. Ceram. Soc.*, 35, 53-57 (1952).
- 5) D. Taylor and C.M.B. Henderson, *Am. Mineral.*, 53, 1476-1489 (1968).
- 6) D.W. Richerson and F.A. Hummel, *J. Am. Ceram. Soc.*, 55, 269-273 (1972).
- 7) S.A. Gallagher and G.J. McCarthy, *J. Inorg. Nucl. Chem.*, 43, 1773-1777 (1981).
- 8) V.E. Plyushev, *Doki. Akad. Nauk SSSR*, 124, 642-645 (1959).
- 9) H. Kobayashi, N. Ishibashi, T. Akiba and T. Mitamura, *Seramikkusu Ronbun-shi*, 98, 703-708 (1990).
- 10) A.G. Solomah and R. Odoj, *J. Am. Ceram. Soc.*, 67, C50-51 (1984).
- 11) G.J. McCarthy and R. Roy, *J. Am. Ceram. Soc.*, 54, 639-640 (1971).
- 12) R. Odoj and K. Hilpert, *High Temp. High Press.*, 12, 93-98 (1980).
- 13) S.A. Gallagher and G.J. McCarthy, *Mater. Res. Bull.*, 17, 89-94 (1982).

---

This article is a full translation of the article which appeared in *Nippon Seramikkusu Kyokai Gakujutsu Ronbunshi* (Japanese version), Vol.99, No.8, 1991.

# Sintering Property of Green Compacts of Si and TiC Mixed Powders in Nitrogen

Yoshiyuki Yasutomi, Masahisa Sobue, S. Shinozaki\* and J. Hangan\*

Hitachi Research Laboratory, Hitachi, Ltd.  
4026, Kuji-cho, Hitachi-shi, 319-12 Japan

\*Scientific Research Laboratories, Ford Motor Company  
Dearborn, Michigan 48121, U.S.A.

The sintering property of powder mixture compacts of TiC and Si in a nitrogen atmosphere at 1350°C is discussed. TiC formed TiN and free carbon on reaction with nitrogen, and a small portion of this free carbon was converted into  $\beta$ -SiC on reaction with Si. A large portion of the Si formed  $\text{Si}_3\text{N}_4$  on reaction with nitrogen. Approximately half of the TiC remained unreacted when heated for 10h at the final sintering temperature of 1350°C. Thus, composite ceramics having a composition of TiC·TiN· $\text{Si}_3\text{N}_4$ ·C· $\beta$ -SiC were obtained. The porosity of this composite was much smaller than that of ordinary  $\text{Si}_3\text{N}_4$  bonded ceramics because of the volume increase caused by the conversion of Si to  $\text{Si}_3\text{N}_4$  and additionally of TiC to TiN, C and  $\beta$ -SiC. Carbon, in particular, seemed to have a remarkable effect on reducing the number of pores in the sintered body. The sample dimensions increased in the sintering stage partly because TiC particles formed porous clusters of TiN by reacting with nitrogen.

[Received March 7, 1991; Accepted May 23, 1991]

**Key-words:** Composites, Nitridation, Silicon nitride bonded ceramics, Gas phase reaction, Titanium carbide, Reaction-bonding, Low porosity, Near-net-shape sintering

## 1. Introduction

We have studied the  $\text{Si}_3\text{N}_4$ -bonding process of inorganic compounds by heating the green compacts made of Si powders and various inorganic compound particles in a nitrogen atmosphere, in which process the  $\text{Si}_3\text{N}_4$  for bonding is produced as a reaction product. With this process, we developed  $\text{Si}_3\text{N}_4$ -bonded SiC of high strength having a small dimensional change during sintering.<sup>1,2)</sup>  $\text{Si}_3\text{N}_4$ -bonded TiN having an electrical conductivity,<sup>3)</sup> and  $\text{Si}_3\text{N}_4$ -bonded ZrN.<sup>4)</sup> Since the particles of SiC, TiN and ZrN used as the raw materials are inorganic compounds stable at the nitridation temperature of Si, they do not change themselves chemically during sintering, therefore, they do not change in their particle shapes.<sup>3-5)</sup>

As sintering processes of ceramics based on a chemical reaction, not only the gas phase reaction bonding process utilizing nitrogen gas above mentioned and other gases, but also the solid-liquid phase reaction bonding process utilizing the liquid phase and the self-propagating high temperature synthesis process utilizing reaction heat between ceramic particles involved are already known.<sup>6,7)</sup> However, most of these processes are based on the utilization of a reaction

with metallic elements, and the possibility of a reaction bonding process utilizing special inorganic compound particles, for instance, transition metal carbide, which easily become nitride at high temperature, has been little studied. If this process is applied to the afore-mentioned  $\text{Si}_3\text{N}_4$ -bonded sintered bodies, we might expect that the particle shape of inorganic compounds changes due to their own chemical changes at high temperature, thereby affecting the sintering property and the microstructure of the sintered body.

From this viewpoint, we chose TiC powders as the inorganic compound in our current study because they are known to react with nitrogen at high temperature in a nitrogen atmosphere.<sup>8-11)</sup> We carried out experiments mixing them with Si powders and heating the green compacts in a high temperature nitrogen atmosphere in the same manner as in our previous studies. We investigated the sintering property and the microstructure of the sintered bodies, and finally discussed the sintering mechanism.

## 2. Experimental Procedure

### 2.1. Preparation of Test Samples

The experimental procedure starting from the raw materials used until the sintered bodies are obtained is described in detail in the following.

We observed the raw materials with a scanning electron microscope (SEM). Some micrographs are shown in Fig.1. Metallic Si powders used were fine particles having a wide size distribution and a mean size of 1 $\mu\text{m}$ . Inorganic compound powders were TiC powders having a wide size distribution and a mean size of 10 $\mu\text{m}$ . The TiC powders contained various impurity materials; Fe: 0.02wt%, N: 1.26wt% and O: 1.18wt%. TiC has a density (4.92Mg/m<sup>3</sup>), which is the lowest among various electrical conductive

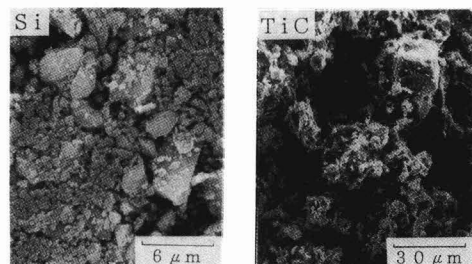


Fig. 1. SEM micrographs of Si and TiC powders.

compounds commercially applicable, a high oxidation resistance, and a low electrical resistivity ( $0.61\mu\Omega\text{m}$ ). As an additional feature, TiC is known to react with nitrogen to form Ti nitride in a nitrogen atmosphere above  $1500^\circ\text{C}$ .<sup>8-11)</sup>

We put Si and TiC powders in a pot mill together with methanol and balls made of  $\text{Si}_3\text{N}_4$ , and mixed them for 24h. These two kinds of powders were mixed in various ratios of Si/TiC such as (1) 65.5/34.5wt%, (2) 41.5/58.5wt%, (3) 32.1/67.9wt%, (4) 24./760wt% and (5) 16.9/83.1wt%. After drying these mixed materials at the room temperature, we added a polyethylene thermoplastic resin as a binder, kneaded them for 5h with a pressure-loaded kneader. The addition ratio of the binder was fixed at 19.4vol%. After cooling the kneaded materials, we crushed them to less than 10mesh. These materials were put in a metal mold which was preheated at  $140^\circ\text{C}$ . Green compacts were formed at a pressure of 98MPa. They were 50mm in diameter and about 10mm thick. The green compacts were placed in a dewaxing kiln and the resin content removed by heating (heating rate:  $5^\circ\text{C}/\text{h}$ ) from room temperature to  $500^\circ\text{C}$  in an Ar atmosphere. After that, using graphite induction heater type kiln, we fired the dewaxed compacts in a nitrogen gas atmosphere at the gas pressure of 0.88MPa by stepping up the firing conditions from  $1100^\circ\text{C} \times 20\text{h}$  to  $1200^\circ\text{C} \times 20\text{h}$ ,  $1250^\circ\text{C} \times 10\text{h}$ ,  $1300^\circ\text{C} \times 10\text{h}$  and  $1350^\circ\text{C} \times 10\text{h}$ .

## 2.2. Evaluation of Characteristics of Samples

Regarding the characteristics of the green compacts and the sintered bodies obtained, we considered the following items.

### 1) Dimensional change during sintering:

Based on the dimensions of dewaxed compacts after resin removal, we calculated the dimensional change during sintering. A slide caliper having an accuracy of  $1/100\text{mm}$  was used to measure sample dimensions.

$$\text{dimensional change during sintering (\%)} = \frac{\text{dimensions of sintered body} - \text{dimensions of dewaxed compact}}{\text{dimensions of dewaxed compact}} \times 100$$

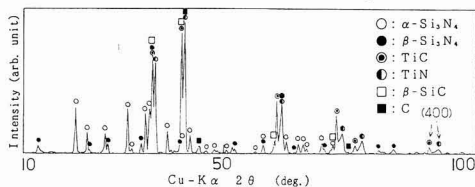


Fig. 2. Result of X-ray diffraction of sintered body (Si/TiC=32.1/67.9wt%)

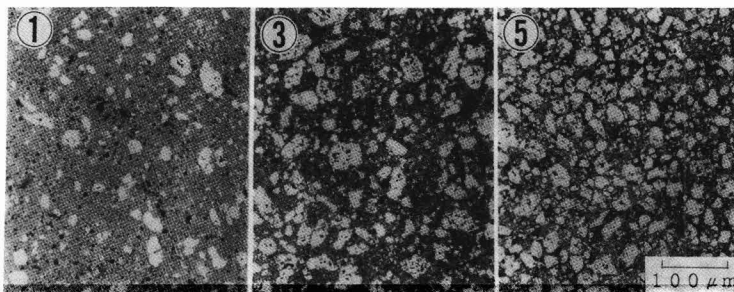


Fig. 3. Optical micrographs of polished surface of the sintered bodies (sample: Si/TiC=①; 65.5/34.5wt%, ③; 32.1/67.9wt%, ⑤; 16.9/83.1wt%)

$\times 100$

### 2) Porosity of sintered body:

Porosity of the sintered bodies was measured with a porosimeter.

### 3) Analyses of sintered body texture:

The sintered bodies were crushed into powder using a mortar made of tungsten carbide. We identified their constituents by powder X-ray diffraction analysis. Microstructure was analyzed using an optical microscope, an SEM (Hitachi model S-900), and a transparent electron microscope (TEM) (Hitachi model H-800 and JEOL model 2000FX).

### 4) Analysis of free carbon in sintered body:

Powder samples (0.5g) prepared by crushing the sintered bodies in the tungsten carbide mortar were heated under an oxygen stream. Carbon was oxidized to  $\text{CO}_2$ , which was determined with an infrared absorption spectrophotometer (Horiba model EMIA-110).

### 5) Bending strength of sintered body:

Test specimens of the sintered bodies were prepared in a square rod shape ( $40 \times 4 \times 3\text{mm}$ ), as defined by was measured the JIS R1621 standard, and the bending strength by three-point bending test method. Test conditions were a supporting point distance of 30mm and a cross-head speed of  $8.33 \times 10^{-6}\text{m/s}$ .

### 6) Young's modulus of sintered body:

Young's modulus of the sintered bodies was measured by an ultrasonic pulse method. The test specimens were plate shaped ( $20 \times 20 \times 1\text{mm}$ ).

## 3. Results and Discussion

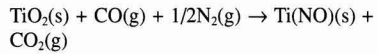
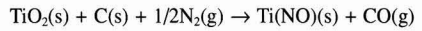
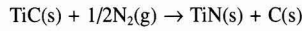
### 3.1. Microstructural Analysis

By comparing the X-ray diffraction patterns of the sintered bodies obtained in our test with JCPDS cards on known substances, we confirmed the presence of TiC originating from the raw materials  $\alpha\text{-Si}_3\text{N}_4$  and  $\beta\text{-Si}_3\text{N}_4$  which were nitrides of Si originating from the raw materials, and also TiN,  $\beta\text{-SiC}$  and C. Figure 2 shows the X-ray diffraction analysis for sample (3) (Si/TiC = 32.1/67.9wt%). The presence of TiN and  $\beta\text{-SiC}$  respectively suggests that TiC powders contained in the raw materials were converted to TiN on reaction with nitrogen during firing, and a part of free C was converted to  $\beta\text{-SiC}$  on reaction with Si. TiC is known to form nitride easily at  $1500^\circ\text{C}$ .<sup>8-11)</sup> Although the atmospheric firing temperature of  $1350^\circ\text{C}$  was lower than that we assume that the nitridation

of TiC progressed because nitridation of Si is of exothermic (about 670KJ/mol<sup>12</sup>) in the and the firing time is long.

**Figure 3** shows optical micrographs of the polished surfaces of three kinds of sintered bodies. Black parts correspond to pores, and white spotted parts to Ti compounds. We analyzed the same polished surfaces by SEM and EPMA (electron probe microanalysis) and the results are shown in **Fig.4**. The pore-like structures in the SEM micrographs correspond to the white parts in Fig.3. Much Ti was detected in these parts, while Si was detected elsewhere. To examine these white parts, we observed the fracture surface of the sintered bodies using a high magnification SEM. Results are shown in **Fig.5**. We also applied a TEM analysis to the white parts, and these results are shown in **Fig.6**. Figure 5 shows the porous bodies were produced around the unreacted TiC particles, and the electron beam diffraction pattern given in Fig.6 proves that these porous bodies consist of TiN. Furthermore, electron energy-loss spectroscopy (EELS) analysis (resolution: 5-10nm) of the surface layer part of the TiC particles by peaks of Ti, C and N. This result

suggests that an intermediate product of Ti(CN) solid solution<sup>10</sup> was formed from the surface layer of TiC particles in wards in the same manner as gradient composite materials are formed. In addition, whisker-like substances formed in the surface layer part of TiC particles, as seen in **Fig.7**, and they were identified as Ti(NO) by EELS analysis. We assume that Ti(NO) was formed by the reactions shown below, in which TiC to forms TiN and generates free C, Ti oxide films at the surface of TiC particles are reduced by this free C and nitrided to form Ti(NO), and CO gas produced in these reduction and nitridation reactions reacts with Ti oxide films to form Ti(NO).



Parts other than the white parts in Fig.3 were proven to be include  $\alpha\text{-Si}_3\text{N}_4$  and  $\beta\text{-Si}_3\text{N}_4$  based on the X-ray diffraction pattern in Fig.2 and the EPMA analysis results in Fig.4. But it was confirmed from the TEM image and the electron beam diffraction pattern shown in **Fig.8** that  $\beta\text{-SiC}$  particles were also present as based on the X-ray diffraction pattern shown in Fig.2. We assume that this  $\beta\text{-SiC}$  was formed by the reaction of Si with free C produced in the nitridation of TiC, or with CO gas produced by the reaction of free C with Ti oxide film and atmospheric oxygen. Reactions to form

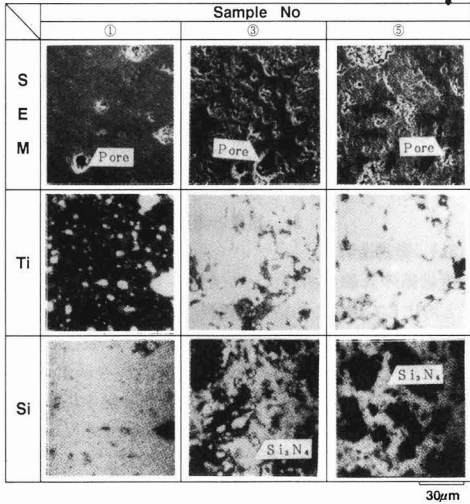


**Fig. 4.** SEM micrographs and EPMA analysis of the sintered bodies (sample: Si/TiC=①; 65.5/34.5wt%, ③; 32.1/67.9wt%, ⑤;16.9/83.1wt%)

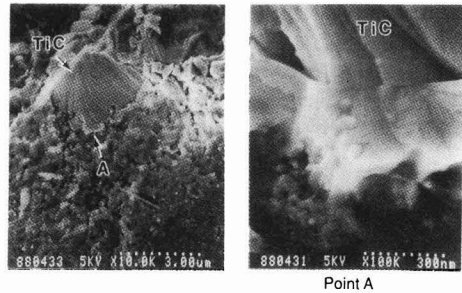


**Fig. 5.** SEM micrographs of fracture surface of sintered body.

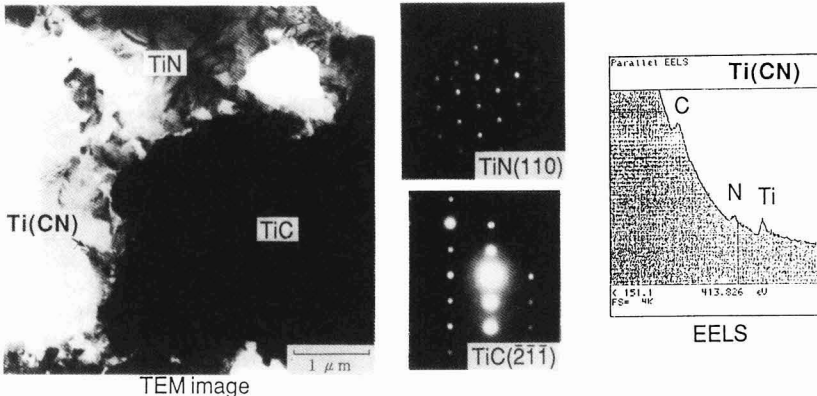


**Fig. 6.** Typical TEM image, diffraction pattern and electron energy loss spectroscopy of the sintered body.

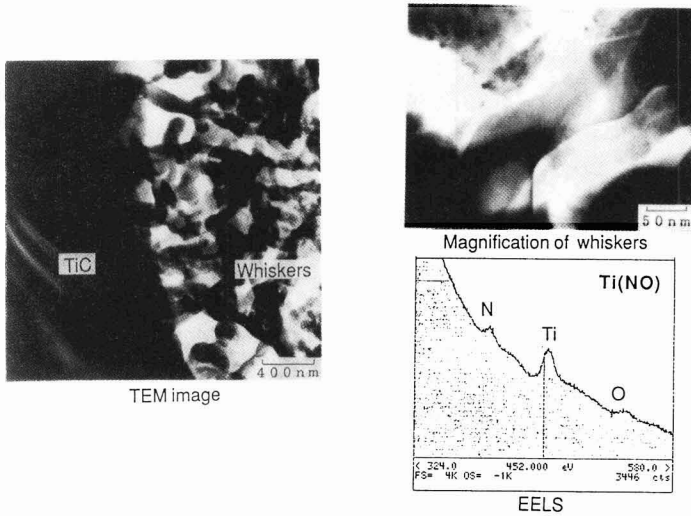


Fig. 7. TEM image and electron energy-loss spectroscopy showing whiskers on the TiC particle in the sintered body.

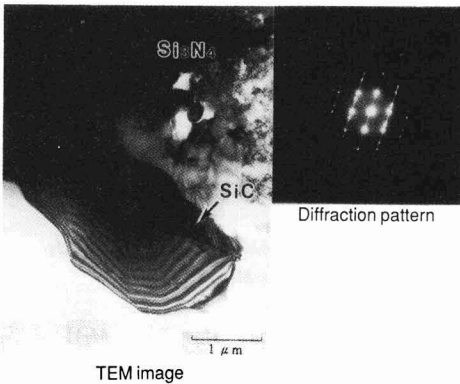
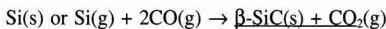
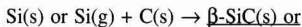


Fig. 8. TEM image and micro-diffraction pattern showing  $\beta$ -SiC in the sintered body.

$\beta$ -SiC are given below.



These  $\beta$ -SiC particles are in a dispersed state in the Si-rich parts in Fig.4, which are the parts other than the white parts in Fig.3.

From TEM analysis, we also confirmed the presence of free C in the sintered bodies, which was detected by the X-ray diffraction analysis in Fig.2. The TEM image is given in Fig.9. The free C was produced in the nitridation of TiC to form TiN. It is observed in Fig.9 that the respective crystal lattices of  $\text{Si}_3\text{N}_4$  and C conform to each other. We suppose these free C particles are dispersed in the porous substances around TiC particles as well as in the  $\text{Si}_3\text{N}_4$  particles.

In summarizing these experimental results, we confirmed that, by firing the compacts prepared with Si and TiC mixed powders in a nitrogen atmosphere at 1350°C, TiN, SiC, C and  $\text{Si}_3\text{N}_4$  were formed in the sintered bodies, and that unreacted TiC and intermediate products of Ti(CN) solid solu-

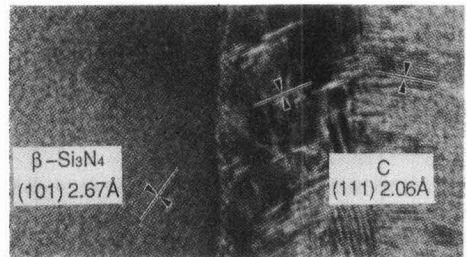


Fig. 9. High resolution TEM image showing interface between C and  $\text{Si}_3\text{N}_4$  in the sintered body.

tion and Ti(NO) were also contained in the sintered bodies. The model of a sintered body is schematically illustrated in Fig.10.

We expect that composite ceramics mainly consisting of  $\text{TiNSiCSi}_3\text{N}_4\text{C}$  will be obtained we extend the firing time, or increase the firing temperature.

### 3.2. Sintering Characteristics

The dimensional changes of the compacts during sintering are shown in Fig.11 in relation to the mixing ratio of TiC powders. For comparison, the dimensional changes of  $\text{Si}_3\text{N}_4$ -bonded  $\text{SiC}$ ,<sup>1)</sup>  $\text{Si}_3\text{N}_4$ -bonded TiN,<sup>3)</sup> and  $\text{Si}_3\text{N}_4$ -bonded  $\text{ZrN}$ ,<sup>4)</sup> are shown in the same figure. Small dimensional changes, around -0.1% for the ceramic materials compare with dimensional changes as large as +0.3 to 0.7% during sintering for compacts with added TiC powders. Changes increase remarkably with larger mixing ratio of TiC powders. We attribute the different behaviors of our tested compacts to the formation of porous TiN phase around the TiC particles (Fig.5) and the formation of free C, with a large specific volume through the nitridation of TiC; Most of this free carbon remains in the sintered body.

Figure 12 compares the measured porosities of sintered bodies with those of the ceramic materials. For the latter, porosity increases remarkably with larger mixing ratio of respective inorganic compound particles. This behavior is

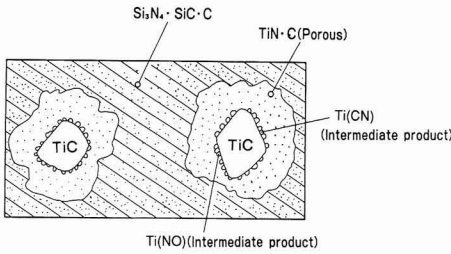


Fig. 10. Schematic illustration of microstructure.

attributed to the decreased Si content in the compact, because Si causes a as large volume expansion (22%) during nitridation and fills voids in the compacts. By contrast, for compacts sintered in our tests, the porosity remains low (8 and 11vol%) even when the mixing ratio of TiC powders was increased. We attribute such low porosity to the presence of low density, free C, as is discussed next.

3.3. Densification Phenomenon

We consider why the sintering characteristics of our TiC-added materials differ from those of ordinary Si<sub>3</sub>N<sub>4</sub>-bonded ceramic materials. Figure 13 shows the reaction processes of TiC-added materials. We neglected the formation of Ti(CN) solid solution and Ti(NO) and the loss of free C to the outside through its conversion to CO gas.

$\alpha$ ,  $\beta$  and  $\gamma$  respectively express the conversion ratios of Si to SiC, TiC to TiN and C to SiC, and the bracketed values indicate the mole quantity of the respective materials and products. With these symbols, we can quantitatively express the products produced from Si( $M_s$  mole) and TiC( $M_T$  mole), as shown in Fig.13.

C and Si react with each other at a mole ratio of 1:1 to form SiC:

$$M_s \cdot \alpha = M_T \cdot \beta \cdot \gamma$$

This is transformed to,

$$\alpha = (M_T \cdot \beta \cdot \gamma) / M_s \dots \dots \dots (1)$$

Volume increase ratio  $R_v$  of the compacts due to the nitridation reaction can be calculated from volumes of respective constituents, which were obtained from the respective mole quantities. It is expressed as,

$$R_v = \left\{ [Si_3N_4] \cdot 1/3M_s \cdot (1 - \alpha) + [SiC] \cdot itaicM_T + [TiN] \cdot M_T \cdot \beta + [TiC] \cdot M_T \cdot (1 - \beta) - ([Si] \cdot M_s + [TiC] \cdot M_T) \right\} / ([Si] \cdot M_s + [TiC] \cdot M_T) \dots \dots \dots (2)$$

Here, figures enclosed with heavy brackets indicate the respective molar volumes of the constituents. By introducing equation (1) into equation (2), the volume increase ratio  $R_v$  can be expressed as the function of  $M_s$ ,  $M_T$ ,  $\beta$  and  $\gamma$ .

We calculated the volume increase ratio  $R_v$  by applying the weight change ratio, the dimensional change ratio and the experimental porosity obtained in the sintering process of dewaxed compacts. Then, after introducing this volume increase ratio  $R_v$  together with the respective mixing ratios ( $M_s$  and  $M_T$ ) of the raw materials and the nitridation ratio ( $\beta$ ) of TiC to TiN into equation (2), we calculated the conversion ratio ( $\gamma$ ) of free C to SiC, and obtained the residual ratio (1- $\gamma$ ) of free C in the sintered bodies. Table 1 shows the calculation and analysis results in the sintered bodies.

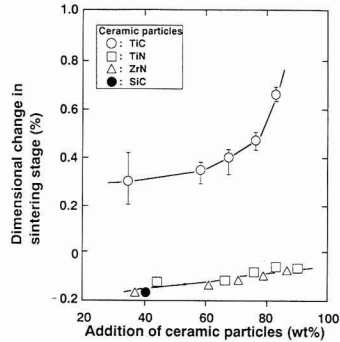


Fig. 11. Comparison of dimensional change in sintering stage among various Si<sub>3</sub>N<sub>4</sub> bonded ceramics.

The nitridation ratio ( $\beta$ ) of TiC to TiN given in Table 1 was obtained from the intensity ratio on the (400) plane in the X-ray diffraction pattern in Fig.2. The calculated values of free C are close to the analysis values, therefore, we think the reaction processes illustrated in Fig.13 are acceptable. The nitridation ratio ( $\beta$ ) of TiC to TiN was almost constant around 55%, and independent on the mixing ratio of TiC particles in the raw materials.

Table 2 shows the composition (vol%) of various sintered bodies, which we get using the above calculated results. We neglected Ti(CN) solid solution and Ti(NO), because both were very small quantities. The respective

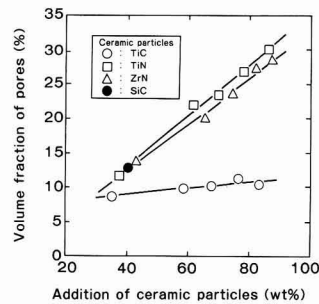


Fig. 12. Comparison of volume fraction of pore in the sintered bodies among various Si<sub>3</sub>N<sub>4</sub> bonded ceramics.

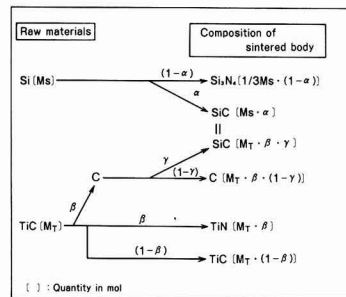


Fig. 13. Nitridation process of mixed powder compact of Si and TiC,  $\alpha$ : change ratio from Si to SiC,  $\beta$ : nitridation ratio of TiC,  $\gamma$ : change ratio from free carbon to SiC.

**Table 1.** Quantitative analyses for nitridation of mixed powder of Si and TiC.

Sample	Experimental values			Calculated values			Analytical value
	$\beta$ : Nitridation ratio of TiC (%)	$R_V$ : Volume increase in sintering (vol%)	$\gamma$ : Change ratio from free carbon to SiC (%)	$(1-\gamma)$ : Residual ratio of free carbon (%)	$\alpha$ : Change ratio from Si to SiC (%)	Free carbon (wt%)	Free carbon (wt%)
①	53	21.3	2.7	97.3	0.3	5.4	5.9
②	54	20.9	2.4	97.6	0.8	11.7	11.0
③	49	20.0	2.0	98.0	0.9	13.8	12.8
④	56	20.8	2.4	97.6	1.9	19.2	17.5
⑤	55	20.3	2.6	97.4	3.2	22.8	19.8

**Table 2.** Calculated composition of the sintered bodies.

Sample	Composition of sintered bodies				
	Si <sub>3</sub> N <sub>4</sub> (vol%)	TiC(vol%)	TiN(vol%)	C(vol%)	SiC(vol%)
1	80.6	7.6	8.0	3.6	0.2
2	60.7	15.0	16.4	7.5	0.4
3	51.2	21.0	18.8	8.6	0.4
4	40.2	21.6	25.7	11.8	0.7
5	30.0	26.0	29.6	13.5	0.9

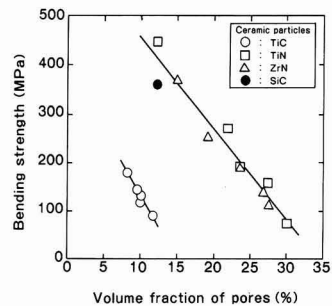
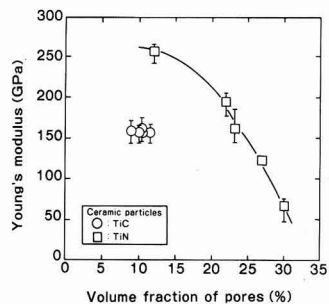
qualities of free C and SiC produced increase with larger TiC additions. As we previously mentioned, reaction-bonded sintered bodies having a low porosity, or a densified structure, were produced in our current experiments. The main reason for such a densified structure is due to of about 98% of the free C produced in the sintering bodies in the nitridation process of TiC, remaining in the product.

### 3.4. Mechanical Characteristics

**Figure 14** shows the relationship between porosity of the sintered bodies and bending strength. Various reaction-bonded ceramics Si<sub>3</sub>N<sub>4</sub>-bonded SiC, Si<sub>3</sub>N<sub>4</sub>-bonded TiN and Si<sub>3</sub>N<sub>4</sub>-bonded ZrN are also compared in the same figure. In the case of the latter materials, bending strength increased with the decrease of porosity. For the sintered bodies in our current tests, bending strength also increased with the decrease of porosity, but the bending strength was smaller than that of the comparison materials. **Figure 15** shows the relationship between porosity of the sintered bodies and Young's modulus. Young's modulus of the sintered bodies was about half that of Si<sub>3</sub>N<sub>4</sub>-bonded TiN in the same porosity range. We attributed these small mechanical characteristics to the presence of a large quantity of free C in the sintered bodies.

## 4. Conclusion

- When compacts of mixed powders of Si and TiC were fired in a nitrogen atmosphere at 1350°C, Si formed  $\alpha$ -Si<sub>3</sub>N<sub>4</sub> and  $\beta$ -Si<sub>3</sub>N<sub>4</sub>, and, at the same time, TiC particles gave TiN and free C. A part of this free C reacted with Si to form  $\beta$ -SiC, and composite ceramics, mainly consisting of Si<sub>3</sub>N<sub>4</sub>:TiC:TiN:C- $\beta$ -SiC, resulted.
- Since free C, having a large specific volume, was produced by nitridation of TiC, and most of the free C produced remained in the sintered bodies, sintered bodies having a small porosity (8 to 11vol%) were obtained. Such small porosity has been difficult to obtain in conventional reaction-bonded ceramic materials.
- Dimensions of the sintered bodies increased by 0.8% at maximum during sintering, because the porous phase

**Fig. 14.** Relation between volume fraction of pore and bending strength.**Fig. 15.** Relation between volume fraction of pore and Young's modulus.

consisting of TiN and other phases was formed around the TiC particles by nitridation and decomposition of TiC, and also free C having a large specific volume was formed.

- On the surface of TiC particles, Ti(NO) formed in addition to TiN and Ti(CN) solid solution, which were formed by the reaction of TiC with nitrogen. We supposed the Ti(NO) was formed by reduction and nitridation of Ti-oxide films at the surface of the TiC particles.
- Regarding the free C formed, a part of it changed to SiC, but the major part, about 98%, remained in the sintered bodies, according to our calculation. This value agreed with the analysis value.
- Bending strength of the sintered bodies was as small as 200MPa. We assume that these low strengths were caused by the residual free C.

### References:

- Y. Yasutomi, H. Kita, K. Nakamura and M. Sobue, *Seramikkusu Ronbunshi*, 96, 783-788 (1988).
- Y. Yasutomi, M. Sobue and T. Miyoshi, *Proc. 1st Jpn. Int. Soc. for*

- the Advancement of Material and Process Engineering Sympo., Nov.28-Dec.1, (1989) 339-344.
- 3) Y. Yasutomi, K. Nakamura, M. Sobue and H. Kubo, *Seramikkusu Ronbunshi*, 97, 148-154 (1989).
  - 4) Y. Yasutomi, M. Sobue and H. Kubo, *ibid.*, 97, 721-727 (1989).
  - 5) Y. Yasutomi, M. Sobue, S. Shinozaki and J. Hangas, *ibid.*, 98, 429-438 (1990).
  - 6) Y.M. Chiang, J.S. Haggerty, R.P. Messner and C. Demetry, *Am. Ceram. Soc. Bull.*, 68, 420-428 (1989).
  - 7) J.S. Haggerty and Y.M. Chiang, *Proc. 14th Ann. Conf. on Composites and Advanced Ceramics, Engineering Ceramics Division Meeting, Am. Ceram. Soc., Cocoa Beach, FL, January 1990, to be published.*
  - 8) H.J. Bossz, *Metall*, 10, 130-136 (1956).
  - 9) R.B. Kotelbnikov et al., *Chokoyuten Zairyo Binran*, (Japanese version) Nisso Tsushinsha (1977), 258-269.
  - 10) P. Duwez and F. Odell: *J. Electrochem. Soc.*, 97, 299-304 (1950).
  - 11) H. Hashiba and H. Mitani, *Funmatsu Yakingaku, Korona-sha* (1985) 135.
  - 12) Y. Yasutomi, K. Nakamura and M. Sobue, *Seramikkusu Ronbunshi*, 96, 561-565 (1988).

---

This article is a full translation of the article which appeared in *Nippon Seramikkusu Kyokai Gakujutsu Ronbunshi* (Japanese version), Vol.99, No.8, 1991.

# Preparation of High Tc Superconductors by a Plasma-Arc Melting and Rapid Quenching Method

Maruo Kamino, Kazuhiko Takahashi, Yorinobu Yoshisato and Shoichi Nakano

Functional Materials Research Center, Sanyo Electric Co.  
1-18-13, Hashiridani, Hirakata-shi, 573 Japan

High Tc superconductors have been prepared using a plasma-arc melting and rapid quenching (PMQ) method. Homogeneous and dense superconductors were obtained by this method through the crystallization of a superconducting phase from an amorphouslike state.

Particularly in  $\text{YbBa}_2\text{Cu}_3\text{O}_x$ , a relative density of  $7.14\text{g}/\text{cm}^3$  (98% of the theoretical density  $7.24\text{g}/\text{cm}^3$ ) and a large activation energy, 1.5eV, which was related to the flux pinning, were realized by this method.

Furthermore, the formation of insulating  $\text{Yb}_2\text{BaCuO}_5$  films on the PMQ processed  $\text{YbBa}_2\text{Cu}_3\text{O}_x$  substrate was attempted by rf magnetron sputtering. No deterioration of the  $\text{YbBa}_2\text{Cu}_3\text{O}_x$  substrate was observed.

It was found that the new method produces a dense and homogenous high Tc superconductor for device applications.

[Received March 20, 1991; Accepted May 23, 1991]

**Key-words:** Superconductor, Oxide, Amorphous phase, Crystallization, Rapid quenching, Magnetization measurement, Substrate

## 1. Introduction

In the application of high temperature oxide superconductors to wires and devices, they must have high density and homogeneity which are hard to obtain under the conventional solid phase reaction method. Therefore, many fabrication methods such as sol-gel method,<sup>1)</sup> partially melting method<sup>2)</sup> and the likes have been investigated.

Among them is the high temperature melting and rapid quenching method, in which solutions of oxide powders melt at 1300 to 1400°C are coagulated on steel or other plates, and then synthesized into dense superconductors by the subsequent heat treatment.<sup>3)</sup> However, it is difficult to obtain homogeneous products with good reproducibility, since the difference in melting points of oxide materials makes it hard to get homogeneously melt solution, and the unstable process of rapid quenching forms products of multi-phase.<sup>4)</sup>

Therefore, we developed independently the plasma-arc melting and rapid quenching method (called PMQ hereafter),<sup>5)</sup> which can produce highly dense and highly homogeneous superconductors with good reproducibility by instantly melting and quenching at the temperature exceeding 3000°C at one stage of synthesizing process of homogeneous solid solution containing amorphous phase and by subsequent crystallization.

Using this method, we attempted to form a superconductors of  $\text{LnBa}_2\text{Cu}_3\text{O}_x$  replacing with Y and other systems

(Ln), and carried out the study of their adaptability and the comparison of their characteristics.

And we selected the  $\text{YbBa}_2\text{Cu}_3\text{O}_x$  which is the most dense product among Ln systems, and investigated the possibility of improving the magnetizing characteristics in this process. We further considered on the application to superconductive substrates for devices, and investigated the surface stability and others. We found its superiority of this products, as reported hereunder.

## 2. Experimental Procedures

Figure 1 is the schematic diagram of the apparatus for the Plasma-arc Melting and Rapid Quenching Method. We used as the starting materials 4 N of  $\text{Ln}_2\text{O}_3$  (Ln=Y, Nd, Sm, Eu, Gd, Dy, Ho, Er and Yb),  $\text{BaCO}_3$ , and  $\text{CuO}$ . We mixed these materials to the given ratio ( $\text{LnBa}_2\text{Cu}_3\text{O}_x$ ), and formed into discs of 20mm in diameter and 5mm in thickness. The specimens were placed on the water-cooled copper hearth inside the bell jar. The bell jar was once made to vacuum, and the Ar gas was introduced. Then the jar was put to 10 to 100 Torr under the Ar gas, and plasma was generated by charging high voltage between the electrodes. The plasma charging output was 10 to 20kW. The specimens were melt instantly in 3 to 5 sec. by this plasma of over 3000°C, then rapid quenching was carried out by the water cooled copper hearth. The rapid quenched melt specimens were then sliced vertically in about 0.5 to 1.0mm and heat treated in oxygen for 1 to 3 hours at 920 to 1000°.

Next the superconductors thus obtained were mirror ground, and were coated with insulating film of  $\text{Yb}_2\text{BaCuO}_5$  on the surface with a rf magnetron sputtering. We used the sintering target with the ratio of 2:1:1 for Yb:Ba:Cu, and carried out the sputtering under  $\text{Ar}:\text{O}_2=1:1$ , 4Pa of gas pressure, 50W of input power and 650°C of substrate temperature. The film was formed for about 10min. at the coating speed of 20Å/min.

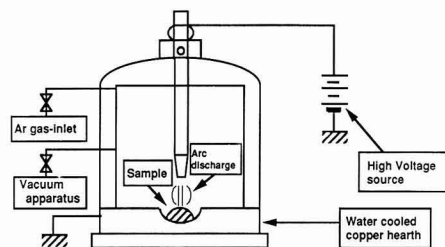


Fig. 1. Schematic diagram of the apparatus for the plasma-arc melting and rapid quenching (PMQ) method.

We examined the crystallization process of rapid quenched melt specimens by the thermal analyzing method and powder X-ray diffraction method, and measured the electric resistance with the direct current 4-terminal method and magnetized characteristics with a sample vibrating type magnetometer.

We further carried out the scrutiny on the microstructures with a scanning type electron microscope (SEM) for the surface observation and X-ray microanalyzer (EPMA) for the composition and Auger electron spectroscopy (AES) for the boundary analysis.

### 3. Experimental Results and Discussion

#### 3.1. Preparation of $\text{LnBa}_2\text{Cu}_3\text{O}_x$ Superconductors

Figure 2 shows sample patterns of X-ray diffraction of  $\text{YBa}_2\text{Cu}_3\text{O}_x$  specimens immediately after being melt and rapidly quenched, and Fig.3 indicates the DTA and TG measurements of the same specimens. Although we noted that crystalline phase was separated from these specimen, the rising background in the diffraction patterns and the exothermic peak presumably corresponding with the crystallization around  $340^\circ\text{C}$  in the DTA curves implies the existence of nonequilibrium or amorphous-like phase. The endothermic peak around  $850^\circ\text{C}$  was caused by the crystallization of  $\text{YBa}_2\text{Cu}_3\text{O}_x$ .

Figure 4 shows the relationship between the formation of impurity phase of other than  $\text{YBa}_2\text{Cu}_3\text{O}_x$  and the heat treatment temperature, by carrying out the heat treatment on the specimens immediately after the rapid quenching at 920 to  $1000^\circ\text{C}$  for 3hr in oxygen. Each vertical axis points to the peak ratio in X-ray diffraction of  $\text{Y}_2\text{BaCuO}_5$  and  $\text{BaCuO}_2$  against  $\text{YBa}_2\text{Cu}_3\text{O}_x$ , and used the diffraction peaks

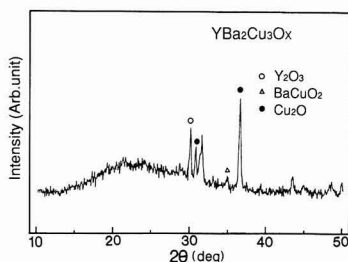


Fig. 2. X-ray powder diffraction pattern at room temperature of the quenched  $\text{YBa}_2\text{Cu}_3\text{O}_x$ .

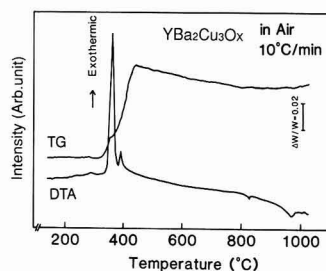


Fig. 3. Thermogravimetric analysis and differential thermal analysis for the quenched  $\text{YBa}_2\text{Cu}_3\text{O}_x$ .

from the plane [101] for  $\text{YBa}_2\text{Cu}_3\text{O}_x$  phase, from the plane [002] for  $\text{Y}_2\text{BaCuO}_5$  phase and from the plane [600] for  $\text{BaCuO}_2$  phase.

It shows us that there is a few impurity phases of  $\text{Y}_2\text{BaCuO}_5$  and  $\text{BaCuO}_2$  at the temperature of  $970^\circ\text{C}$  for the heat treatment, at which temperature the critical temperature registered the maximum temperature of 91K. From this fact, we set the most suitable temperature for the heat treatment after the rapid quenching at  $970^\circ\text{C}$ , and prepared the specimens of other Lanthanoid systems. Figure 5 indicates the degrees of diamagnetism of the prepared specimens measured by the vibrating sample type magnetometer and their relative density measured by Archimedeian method. We also shows the results on  $\text{YBa}_2\text{Cu}_3\text{O}_x$  specimens prepared by the solid phase method for comparison. As the figure points to, almost all specimens prepared by the PMQ method exceed those prepared by the solid phase method in the degree of diamagnetism and in relative density. The critical temperatures for these remain in 90 to 91K. This shows that a good oxide superconductor can be fabricated within a short time of 3hr using the PMQ method. We can obtain the products with very high density of 98% of the theoretical density especially in  $\text{YbBa}_2\text{Cu}_3\text{O}_x$ . This is probably due to the fact that the nature of Yb to easily form the solid solution with Ba at comparatively low temperature is suitable to the PMQ method which goes through the molten status in its process.

#### 3.2. Critical Electric Field Density of $\text{YbBa}_2\text{Cu}_3\text{O}_x$

We examined the superconductive characteristics on the

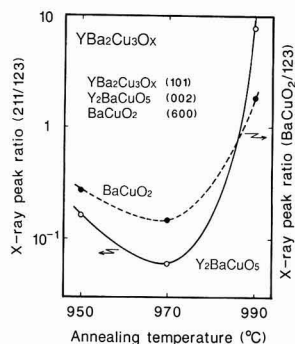


Fig. 4. Annealing temperature dependence of generation of other phase. X-ray peak ratios of  $\text{Y}_2\text{BaCuO}_5(002)/\text{YBa}_2\text{Cu}_3\text{O}_x(101)$  and  $\text{BaCuO}_2(600)/\text{YBa}_2\text{Cu}_3\text{O}_x(101)$  in  $\text{YBa}_2\text{Cu}_3\text{O}_x$  annealed at temperatures between  $950^\circ\text{C}$  and  $990^\circ\text{C}$ .

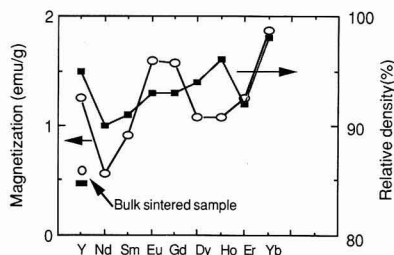


Fig. 5. Magnetization and the relative density of  $\text{LnBa}_2\text{Cu}_3\text{O}_x$  superconductors prepared by the PMQ method.

most highly dense  $\text{YbBa}_2\text{Cu}_3\text{O}_x$  products by the PMQ method.

Figure 6 shows the measurements of the magnetic ratio in DC range at 77K of  $\text{YbBa}_2\text{Cu}_3\text{O}_x$  prepared with heat treatments at 950°C, 970°C and 990°C.

When the temperature raised to 970°C from 950°C in the heat treatment, the degree of diamagnetism increases suddenly and the hysteresis ( $\Delta M$ ) also increases at the same time, but the specimens with the temperature further raised to 990°C in the heat treatment showed the tendency to decrease both the degree of diamagnetism and  $\Delta M$ . The sudden increase in the degree of diamagnetism and  $\Delta M$  at 970°C is related to the microstructure of the specimen. Figure 7 shows the SEM photo covering the cross section of the specimen heat treated at 970°C, in which we can see that fine  $\text{Yb}_2\text{BaCuO}_5$  grains ( $<1\mu\text{m}$ ) dispersed in the of  $\text{YbBa}_2\text{Cu}_3\text{O}_x$  matrix. In the specimens treated at 950°C such a dispersion of fine  $\text{Yb}_2\text{BaCuO}_5$  grains was noticed, while many impurity phases of  $\text{BaCuO}_5$  and  $\text{Yb}_2\text{BaCuO}_5$  existed on top of  $\text{YbBa}_2\text{Cu}_3\text{O}_x$  phase in the specimens treated at 990°C.

It appeared to us that the sudden increases in diamagnetism degree and  $\Delta M$  at 970°C was brought about by the dispersion of  $\text{Yb}_2\text{BaCuO}_5$  grains in the  $\text{YbBa}_2\text{Cu}_3\text{O}_x$  matrix effectively working as the pinning center to pin the magnetic flux, as reported by Matsushita et al.<sup>6)</sup> This pinning effect is necessary for the oxide superconductor, which is the second type superconductor, to improve the critical current density ( $J_c$ ) in the magnetic field.

Next, we used the  $\Delta M$  obtained by measuring magnetization of the specimens treated at 970°C, and show in Fig.8 dependance on the magnetic field of the  $J_c$  calculated by the

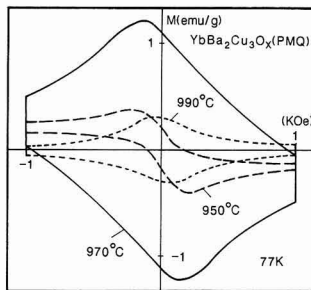


Fig. 6. Magnetization versus magnetic field curves measured at 77K for the  $\text{YbBa}_2\text{Cu}_3\text{O}_x$  sample annealed at 950°C, 970°C and 990°C.

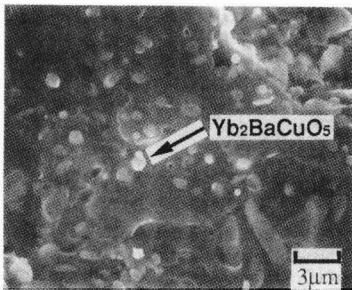


Fig. 7. SEM micrograph of the small  $\text{Yb}_2\text{BaCuO}_5$  ( $<1\mu\text{m}$ ) segregation in the  $\text{YbBa}_2\text{Cu}_3\text{O}_x$  matrix.

Bean Model.<sup>7)</sup> We also show those on the specimens prepared by the solid phase method for comparison's sake. As is clear from the figure, the  $J_c$  of the specimens prepared by the PMQ method was greater by about 5 times, and attenuation of  $J_c$  by the magnetic field was smaller, than that on the specimens prepared by the solid phase reaction method. This attenuation of  $J_c$  is brought about by the weak-link, or the weak superconductive connection between the crystal grains, and the figure shows that this weak-link was improved in the specimens prepared by the PMQ method.

There is another important factor of the flux-creeping phenomenon,<sup>7)</sup> beside the weak-link, for the characteristics of  $J_c$  in the magnetic field, when we consider the application at 77K. Because of the flux-creeping phenomenon, a quantumized magnetic flux pinned down inside a superconductor jumps over to other location, released from the pin by the thermal activity of the inclination of the magnetic field. In such a case, the magnetization of the superconductor decreases as the time goes on, so that permanent current is attenuated.

In order to solve this problem, we show in Fig.9 how the magnetization decreases along with the shift in the line of magnetic flux as the time goes by, measured at 77K. The outside magnetic field is 550 Oe, and the magnetization was standardized by the value at the first measuring point. The magnetization attenuates linearly in proportion to the logarithm of the time ( $\ln t$ ), and agrees well with the theory of flux-creeping. In addition, as the figure clearly shows,

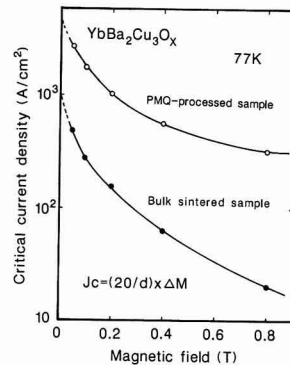


Fig. 8. Magnetic field dependence of  $J_c$  estimated from the Bean critical-state model for the PMQ-processed sample and bulk sintered sample.

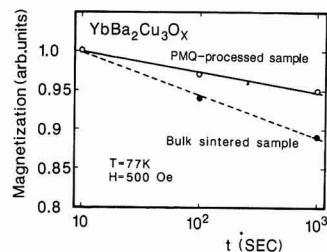


Fig. 9. Magnetic relaxation of the PMQ-processed sample and bulk sintered sample at 500 Oe.

the degree of attenuation in the magnetic field is less in the specimens by the PMQ method than by the solid phase method. This points to the greater pinning force of the former, and the pinning potential was calculated to be  $1.5eV$ .<sup>9)</sup> The value is larger than the metal superconductor, and led us to believe that the pinning force of the oxide superconductor by the PMQ method is very high. We conducted further research on the stability of the surface and the likes, in order to apply this product to superconductive substrates for devices, making full use of these characteristics.

### 3.3. Application to Superconductive Substrates of Device

When we consider the application of the oxide superconductors to the fields of function devices and so forth, we need the layer construction of superconductor / insulator / superconductor (S/I/S) and the likes. Many attempts are now being conducted in this direction, but it is not easy to fabricate a good layer construction, what with the difficulty to obtain stable superconductors with flat surface and what with the problem on the boundary brought about by the dispersion of elements foreign to superconductors and insulators (such as  $ZrO_2$ ,  $MgO$ , etc.). Therefore, we examined the surface stability and others, for the application to the superconductive substrates for devices.

Figure 10 indicates the surface morphology under the

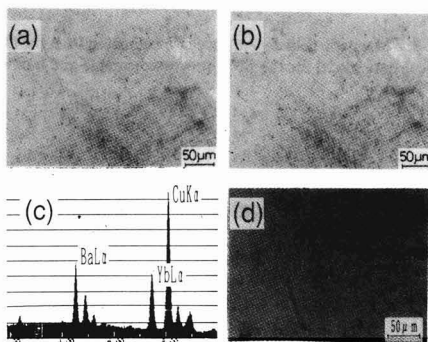


Fig. 10. Surface morphologies of  $YbBa_2Cu_3O_x$  substrate and EDS analysis.  
 (a) at room temperature, (b) at  $700^\circ C$ , 1h in vacuum,  
 (c) Energy dispersive X-ray spectra of (b), (d) at  $800^\circ C$ , 1h in vacuum

various conditions in  $YbBa_2Cu_3O_x$  superconductors, in which (a) covers the untreated ones, pointed to good density and flatness, and (b) covers the specimen treated at  $700^\circ C$  in vacuum for 1hr, showed almost same as in (a) with stable surface and retained the superconductive configuration as shown in (c) by the element quantum analysis (EDS) on EPMA. However, another phase appeared, although very small volume, in the heat treatment at  $800^\circ C$  as indicated in (d). From these facts, we can say that it is possible to retain well the surface stability up to  $700^\circ C$ .

We formed the  $Yb_2BaCuO_5$  insulating layer on the  $YbBa_2Cu_3O_x$  superconductive substrate, making use of the facts that the  $YbBa_2Cu_3O_x$  superconductor made by the PMQ method can retain the surface stability up to  $700^\circ C$  and that the  $YbBa_2Cu_3O_x$  superconductive phase and  $Yb_2BaCuO_5$  insulation phase are in the relation of phase inclusive reaction and easily separated, as seen in section 3.2.

Figure 11 shows the X-ray diffraction pattern on the surface after forming thin films of  $Yb_2BaCuO_5$  in as-grown at  $650^\circ C$  on the  $YbBa_2Cu_3O_x$  superconductive substrate by the sputtering method, in which we can see only the peaks of the  $Yb_2BaCuO_5$  insulating layer and the  $YbBa_2Cu_3O_x$  superconductive substrate, indicating that no deterioration had taken place on the substrate surface.

We further carried out the AES analysis on the problem of boundary between the  $Yb_2BaCuO_5$  insulating layer and the  $YbBa_2Cu_3O_x$  superconductive layer.

Figure 12 shows the results of AES analysis to the direction of depth from the surface of the  $Yb_2BaCuO_5$  insulating layer to the  $YbBa_2Cu_3O_x$  superconductive substrate. The (a) indicates when the film of amorphous  $Yb_2BaCuO_5$  was formed at room temperature where no thermal inter-dispersion of elements takes place, while the (b) is the results when the crystallized  $Yb_2BaCuO_5$  insulating layer was formed at  $650^\circ C$  on the superconductive layer. The widths of the areas (at 5min. of Ar sputtering time) which are regarded to be the boundary are almost same in either case, and we note that the boundary face of the  $YbBa_2Cu_3O_x$  superconductive layer / the  $Yb_2BaCuO_5$  insulating layer are very steep. We are currently attempting to fabricate a layer construction making this fact.<sup>10)</sup>

As stated above, the PMQ method allows to prepare the oxide superconductors dense and superior in flatness and in the surface, and we can expect the application of the superconductive substrates for the functional devices forming

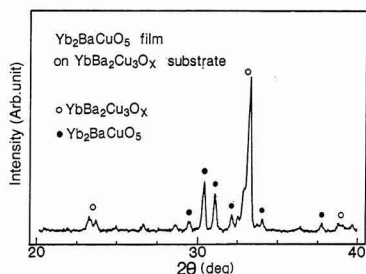


Fig. 11. X-ray diffraction pattern of  $Yb_2BaCuO_5$  film on the  $YbBa_2Cu_3O_x$  substrate.  $Yb_2BaCuO_5$  film was deposited on  $YbBa_2Cu_3O_x$  substrate at  $650^\circ C$ .

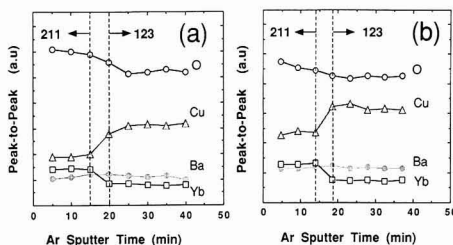


Fig. 12. Auger electron spectroscopy depth profile of a  $Yb_2BaCuO_5/YbBa_2Cu_3O_x$  layered structure.  
 (a)  $Yb_2BaCuO_5$  film was deposited on  $YbBa_2Cu_3O_x$  substrate at room temperature,  
 (b)  $Yb_2BaCuO_5$  film was deposited on  $YbBa_2Cu_3O_x$  substrate at  $650^\circ C$ .

layered construction.

#### 4. Conclusion

We have developed a new Plasma-Arc-Melting and Rapid Quenching Method which can form in short time the oxide superconductors superior in high density and in homogeneity.

This PMQ method can synthesize homogeneous solid solution containing amorphous phases by rapidly quenching the melt instantly at high temperature, and can fabricate oxide superconductors by the subsequent heat treatment, which are highly dense and are superior in homogeneity, with good reproducibility.

The method enabled us to fabricate under the same conditions the  $\text{LnBa}_2\text{Cu}_3\text{O}_x$  superconductors replacing with all of lanthanoid system, and especially the superconductors of  $\text{YbBa}_2\text{Cu}_3\text{O}_x$  have  $T_{ce} = 91\text{K}$  and were highly dense with relative density =  $7.14\text{g/cm}^3$  (98% of the theoretical density), and we were able to incorporate into them the very powerful pinning effect with pinning potential of  $1.5\text{eV}$  by improving the magnetizing characteristics by heat treatment.

From these facts, the PMQ method would be effective in the determination of phase diagrams and in the researches of precipitation process of separate phases and of the pinning center caused by precipitation, through the search for new materials and the examination of the crystallizing process from the amorphous state.

In addition, we examined the stability of the surface with applications to the superconductive substrates for functional devices into consideration, and confirmed that good boundary face was formed after forming the  $\text{Yb}_2\text{BaCuO}_5$  insulating layer, and applications to superconductive substrates for functional devices to fabricate the layered construction.

#### Acknowledgments

Part of this work was performed under the management of the R & D Association for Future Electron Devices as a part of the R & D of Basic Technology for Future Industries sponsored by NEDO (New Energy and Industrial Technology Development Organization).

#### References:

- 1) S. Sakka, H. Kozuka and T. Umeda, *Seramikkusu Ronbunshi*, 96, 468-470 (1988).
- 2) K. Sawano, M. Morita, K. Miyamoto, K. Doi, A. Hayashi, M. Murakami and S. Matsuda, *Seramikkusu Ronbunshi*, 97, 1028-1033 (1989).
- 3) T. Komatsu, T. Ohki, K. Imai and k. Matsushita, *J. Mater. Sci. Lett.*, 8, 1-3 (1989).
- 4) K.B.R. Varma, K.J. Rao and C.N.R. Rao, *Appl. Phys. Lett.*, 54, 69-71 (1989).
- 5) Y. Yoshisato, T. Yokoo, M. Kamino, H. Suzuki, T. Ikemachi, Y. Takai, T. Ienaga, S. Nakano and Y. Kuwano, ext. Abstr., 5th Int. Workshop on Future Electron Devices, 209-213 (1988).
- 6) T. Matsushita, Baorong Ni, M. Murakami, M. Morita, K. Miyamoto, M. Sage, S. Matsuda and M. Tanino, *Jpn. J. Appl. Phys.*, 28, L1545-1548 (1989).
- 7) C.P. Bean, *Phys. Rev. Lett.*, 8, 250-253 (1962).
- 8) Y. Yeshurun and A.P. Malozemoff, *Phys. Rev. Lett.*, 60, 2202-2205 (1988).
- 9) M.R. Beasley, R. Labusch and W.W. Webb, *Phys. Rev.*, 181, 682 (1969).
- 10) M. Kamino, K. Shimaoka, K. Takahashi, T. Usuki, Y. Yoshisato and S. Nakano, *Gakujutsu-Kouenkai-Kouen-Yokoushu, Jpn. Soc. Appl. Phys.*.1 (1990) 180.

---

This article is a full translation of the article which appeared in *Nippon Seramikkusu Kyokai Gakujutsu Ronbunshi* (Japanese version), Vol.99, No.8, 1991.

# Synthesis of SiC from Fine SiO<sub>2</sub>-C Mixed Powders

Norihiro Murakawa and Mutsuo Nakajima

Central Research Institute, Mitsui Toatsu Chemicals, Inc.  
1190, Kasama-cho, Sakae-ku, Yokohama-shi, 247 Japan

Mixed powder containing silica and carbon were chemically synthesized by spraying a mixture of silicon tetrachloride and heavy oil into air-propane flame. The particle size of the mixed powders was less than 1 micron and each particle contained both silica and carbon. Fine SiC powders were obtained by heating compressed tablets of the mixed powders. The powders sintered to high density by pressureless sintering method. SiC whiskers were also obtained by heating the mixed powders without compression. The whiskers had high crystallinity.

[Received March 20, 1991; Accepted May, 23, 1991]

**Key-word:** SiO<sub>2</sub>-C mixed powder, SiC powder, SiC whisker

## 1. Introduction

Silicon carbide powder to be sintered must be very fine (submicron order). Moreover, it is preferably of narrow size distribution, free of secondary agglomeration and of high purity.

Three methods have been commercialized for production of silicon carbide powders; (1) ingots of  $\alpha$ -SiC powders, prepared by the Acheson method, are crushed into very fine particles,<sup>1)</sup> (2) mixed powder of silica and carbon is heated at 2000°C or less to produce coarse particles of  $\beta$ -SiC through the reaction  $\text{SiO}_2 + 3\text{C} \rightarrow \text{SiC} + 2\text{CO}$ , which are further crushed,<sup>2)</sup> and (3) silicon is allowed to react with carbon directly at 1400°C, to produce coarse particles of  $\beta$ -SiC which are further crushed.<sup>3)</sup> However, silicon carbide powders prepared by these methods, being crushed into fine particles in the manufacturing process, tend to have broad size distributions. Another common disadvantage of these methods is inability to produce high-purity powders. For these reasons, attempts have been made to synthesize sub-micron powders by the vapor-phase reaction process,<sup>4-6)</sup> which involve no crushing step.

The authors have conducted experiments in anticipation that heating silica and carbon particles are reacted with each other at an elevated temperature to directly produce very fine particles of silicon carbide, if the starting particles are sufficiently fine, and that the mixed powder of fine silica and carbon particles (hereinafter referred to as Mixed Powder) can be prepared chemically by spraying a silicon compound dispersed in heavy oil into a flame. As a result, it has been found that Mixed Powder can be prepared in which each particle consists of silica and carbon and that its particle size distribution is very narrow.<sup>7,8)</sup> The silicon carbide whiskers can be made, when the conditions under which Mixed Powder is thermally treated are carefully selected.<sup>9)</sup>

Characteristics of these Mixed Powders, silicon carbide

synthesis conditions and characteristics of silicon carbide prepared are discussed.

## 2. Experimental Procedure

### 2.1. Preparation of Mixed Powder

Figure 1 illustrates the reactor lined with refractory material (inner diameter: 300mm, length: 3m), in which a flame was generated by air and propane gas admitted into the reactor through separate ducts. A mixture of SiCl<sub>4</sub> and heavy oil was sprayed into the flame via the feed nozzle, to produce aerosol fume, which was passed from the reactor through the duct to a bag filter, where it was separated into the vapor and solid phases, to produce Mixed Powder.

### 2.2. Characteristics of Mixed Powder

Characteristics of Mixed Powder were assessed by the following properties; (a) Silica/carbon molar ratio: molar fraction of carbon divided by molar fraction of silica, determined by the weight loss and residual silica, the former resulting from combustion of carbonaceous material, when Mixed Powder was heated in air at 650°C.

(b) Specific surface area, determined by BET method with nitrogen; three types of powders, Mixed Powder, silica remaining in Mixed Powder heated at 650°C in air, and carbon remaining in Mixed Powder treated with 55% hydrofluoric acid and then washed with water, to dissolve and remove silica.

### 2.3. Synthesis of Silicon Carbide

Mixed Powder (100 weight parts) and binder of tarry material (25 weight parts) as the forming aid were mixed by a Henschel mixer, and the mixture was formed under a load of 1 ton/mm<sup>2</sup> by a monoaxial press into tablets of 40mm in diameter, 20mm in height and 0.90g/cm<sup>3</sup> in density. Each tablet, placed in a 1ℓ graphite crucible, was heated in a high-frequency oven at a given temperature for 30min in a nitrogen gas atmosphere. The product thus synthesized was treated with hydrofluoric acid, washed with

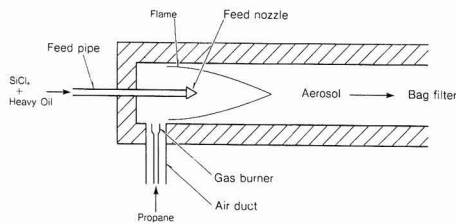


Fig. 1. Model of the reactor to obtain SiO<sub>2</sub>-C mixed powders.

Table 1. Properties of SiO<sub>2</sub>-C mixed powders and SiC powders.

Mixed powders	Properties of mixed powders				Properties of SiC powders		
	C/SiO <sub>2</sub>	BET	SiO <sub>2</sub> -BET	C-BET	BET	Green density	Sintered density
		m <sup>2</sup> /g	m <sup>2</sup> /g	m <sup>2</sup> /g	m <sup>2</sup> /g	g/cm <sup>3</sup>	g/cm <sup>3</sup>
Chemically mixed	7.5	45.2	490 <sup>1)</sup>	459 <sup>2)</sup>	12.7	1.82	3.11
Mechanically mixed	7.5	425	300 <sup>3)</sup>	510 <sup>4)</sup>	11.4	1.58	2.76

1) BET of SiO<sub>2</sub> obtained by burning chemically mixed powder

2) BET of carbon obtained by excluding SiO<sub>2</sub> from chemically mixed powder

3) BET of SiO<sub>2</sub> as raw material of mechanically mixed powder

4) BET of carbon as raw material of mechanically mixed powder

water and then dried, after having been heated at 650°C in air to remove excess carbon, to prepare the sample. No post-crushing was conducted.

The binder-free samples were also prepared, in which 10g of the as-prepared Mixed Powder of 0.08g/cm<sup>3</sup> in density, placed in a 1l graphite crucible, was heated at 1500° or 1700°C for 1h, and treated in the same manner as before.

#### 2.4. Silicon Carbide Powder from Mechanically Mixed Starting Materials

The fine powder of silica (trade name: Aerosil, specific surface area: 300m<sup>2</sup>/g) was mixed mechanically with the fine powder of carbon (trade name: Ketjen Black, specific surface area: 510m<sup>2</sup>/g) by a Henschel mixer in a ratio of 4/6 to result in C/SiO<sub>2</sub> = 7.5, to which the binder was added in the same ratio as before, and the mixture was formed into tablets. They were heated at a given temperature for 30min, to remove excess carbon and silica, in order to prepare the silicon carbide powder.

#### 2.5. Characteristics of Silicon Carbide Powder

Characteristics of the silicon carbide powder were assessed by the following properties:

- Specific surface area of the silicon carbide powder, determined by BET method with nitrogen
- Compact density; 1g of the silicon carbide powder was formed into a tablet of 10mm in diameter by a monoaxial press under a load of 300kg/cm<sup>2</sup>, which was rubber-pressed under a static pressure of 2tons/cm<sup>2</sup>, to prepare the compact.
- Sinter density; the silicon carbide powder (100 weight parts) was mixed with boron powder (0.3 weight parts, Starck's amorphous, metallic boron powder) and carbon (2 weight parts, carbon black of 120m<sup>2</sup>/g in specific surface area) as the sintering aids, and 1g of the mixed powder was formed in the same manner as before, and fired at 2100°C for 15min in an argon atmosphere kept at 1 atm, to prepare the sinter.

#### 2.6. Morphology Observation

The morphologies of Mixed Powder and silicon carbide were observed by a transmission and scanning electron microscope. The whiskers were also analyzed by an electron diffractometer.

### 3. Results

#### 3.1. Mixed Morphologies of Mixed Powder

Table 1 gives the characteristics of Mixed Powder, showing that silica and carbon in Mixed Powder are mixed with each other in a unique morphology, i.e., specific surface area of Mixed Powder is 45.2m<sup>2</sup>/g, as compared with 490m<sup>2</sup>/g of silica remaining in carbon-free Mixed Powder and 459m<sup>2</sup>/g of carbon remaining in silica-free Mixed Powder. Mixed Powder consists of 40.0 wt% of silica and 60.0wt% of carbon from the starting ratio of C/SiO<sub>2</sub>=7.5, and its specific surface area should be 471m<sup>2</sup>/g, if specific surface area were an additive property (490×0.4 + 459×0.6 = 471 (m<sup>2</sup>/g)). The actually measured value, however, was less than 10% of the calculated one. Surface area of the mechanically mixed powder of silica and carbon, on the other hand, was 425m<sup>2</sup>/g, sufficiently close to the calculated value of 426m<sup>2</sup>/g (300×0.4 + 510×0.6). These results mean that silica and carbon in each particle of Mixed Powder contact with each other at the internal surface. Such a mixed condition can be predicted by observation with the aid of an electron microscope. Figures 2(a), (b) and (c) show TEM images of the Mixed Powder particles, silica particles remaining in Mixed Powder whose carbon component was burned and removed, and carbon particles remaining in Mixed Powder chemically treated to remove the silica component, respectively. It was observed that Mixed Powder consisted of the primary particles of 0.02 to 0.1μm agglomerated into secondary particles. The silica particles, though comparable in size with the particles of Mixed Powder when agglomerated, seemed to consist of smaller primary particles, judging from uncleanness of their contours. The agglomerated carbon particles, also comparable in size with the agglomerated particles of Mixed Powder, were more spotted than the latter, some were shell-like. Thus, the single-phase silica or carbon particle differed in morphology from the particle of Mixed Powder, because the dissimilar particles were mixed with each other in the latter particle.

These results indicate that each particle of Mixed Powder, which itself is very fine of submicron size, is a nanocomposite consisting of finer silica and carbon particles. The product yield of Mixed Powder was 98% for

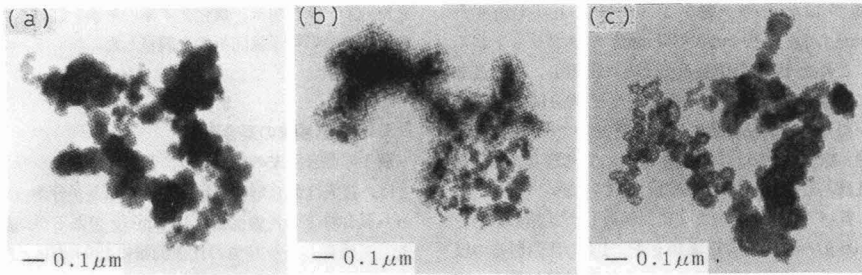


Fig. 2. TEM images: (a) mixed powders, (b) silica powders, (c) carbon powders.

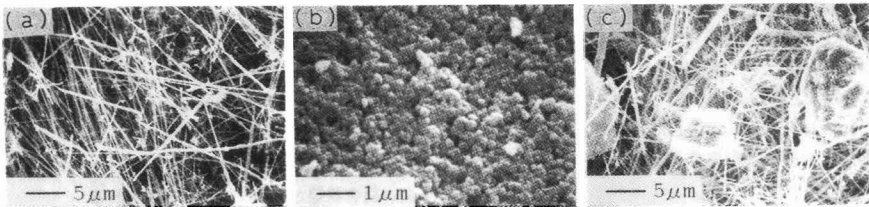


Fig. 3. SEM images of SiC obtained from SiO<sub>2</sub>-C mixed powder. Bulk density of mixed powder and firing temperature: (a) 0.08g/cm<sup>3</sup>, 1500°C (b) 0.90g/cm<sup>3</sup>, 1700°C (c) 0.08g/cm<sup>3</sup>, 1700°C.

remaining silica relative to SiCl<sub>4</sub> charged, as calculated from the silicon balance, and 52% for remaining carbon relative to carbon present in the heavy oil.

### 3.2. Effects of Synthesis Conditions on Silicon Carbide Morphologies

The selected conditions whose effects on silicon carbide morphologies were investigated were bulk density of Mixed Powder from which the silicon carbide powder was synthesized, and firing temperature.

Figure 3(a) presents the SEM image of silicon carbide powder, prepared in a similar manner as were the others by firing Mixed Powder of 0.08g/cm<sup>3</sup> in bulk density at 1500°C for 1h. As shown, the powder consisted mostly of whiskers. Fig.3(b) gives the SEM image of silicon carbide, where Mixed Powder was formed into a tablet which was fired at 1700°C for 30min and then treated to remove excess carbon and silica. The particles were of granular silicon carbide, having no anisotropy. Fig.3(c) presents the SEM image of silicon carbide powder, prepared in a similar manner as were the others by firing Mixed Powder of 0.08g/cm<sup>3</sup> in bulk density at 1700°C for 1h. The powder consisted of whiskers and coarse particles.

Thus, the silicon carbide product was whisker or granular, depending on the synthesis conditions under which the same Mixed Powder was treated.

Figure 4(a) presents the TEM image of the silicon carbide whisker, and Fig.4(b) is its selected area electron diffraction pattern. It is identified to be of single-phase β-SiC by the analysis of the diffraction pattern.

### 3.3. Comparison of Silicon Carbide Grains

Figure 5 shows the effects of firing temperature on surface area of two types of silicon carbide, one from the Mixed Powder tablets prepared chemically by the method developed by the authors, and the other from the mechanically mixed silica/carbon tablets, both fired at 1600° to 2000°C. As shown, the chemically synthesized Mixed Powder gave a higher specific surface than the mechanically mixed one at the same firing temperature.

Figure 6(a) is the TEM image of silicon carbide having a specific surface of 12.7m<sup>2</sup>/g, prepared by firing Mixed Powder at 1800°C, and Fig.6(b) is the TEM image of the silicon carbide powder having a similar specific surface of 11.4m<sup>2</sup>/g, prepared by firing the mechanically mixed powder at 1700°C. The grains shown in Fig.6(a) seem to have a size in a range from 0.1 to 0.4μm, whereas those shown in Fig.6(b) have a wider size distribution, some are smaller than 0.1μm and the others larger at up to around 1μm, and it seems that the grains smaller than 0.1μm are agglomerated to form secondary grains.

Table 1 shows that the former powder gave silicon carbide compact and sinter of higher density than the latter; 1.82 and 3.11g/cm<sup>3</sup> (96.9% of the theoretical level) versus 1.58 and 2.76g/cm<sup>3</sup> (86.0% of the theoretical level).

## 4. Discussion

### 4.1. Fine Mixing Conditions of Mixed Powder

Mixed Powder of silica and carbon, used in this study as

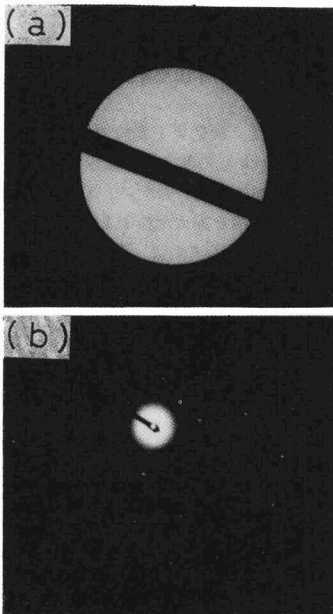


Fig. 4. (a) TEM image of SiC whisker (b) Selected area electron diffraction pattern of the whisker.

the intermediate, was chemically synthesized from  $\text{SiCl}_4$  as the silica source and heavy oil as the carbon source.

It is known that  $\text{SiCl}_4$ , when put in a high-temperature, steam-containing gas, is converted into fine particles of silica through the reaction  $\text{SiCl}_4 + 2\text{H}_2\text{O} \rightarrow \text{SiO}_2 + 4\text{HCl}$ , and that heavy oil, when put in an oxygen-containing flame, is thermally decomposed into fine particles of carbon. The  $\text{SiO}_2$  forming mechanisms involve, first of all, evaporation of  $\text{SiCl}_4$ , and reaction of vapor-phase  $\text{SiCl}_4$  with steam to form the nuclei of  $\text{SiO}_2$  through the above reaction, on which  $\text{SiO}_2$  is deposited, as the reaction proceeds, to grow the  $\text{SiO}_2$  particles. Similarly, the gaseous hydrocarbon compounds are thermally decomposed, in the case of heavy oil, to form the carbon nuclei on which carbon is deposited to grow the carbon particles.<sup>10)</sup> Aerosil consisting of fine silica particles of  $0.1\mu\text{m}$  in diameter and carbon black of fine carbon particles are being produced commercially by the above mechanisms. The authors expected that a mixture of  $\text{SiCl}_4$  and heavy oil, when put in a flame, forms the  $\text{SiCl}_4$  and hydrocarbon vapors, which are well mixed to form fine particles, each consisting of silica and carbon in which carbon is formed on the silica nuclei and silica is formed on the carbon nuclei. The mixture morphologies are as expected, as discussed in Section 3.2.

#### 4.2. Formation of Silicon Carbide Whiskers and Grains

Vapor-solid heterogeneous reactions thought to be responsible for the formation of silicon carbide, where gaseous  $\text{SiO}$  is formed through the reaction  $\text{SiO}_2 + \text{C} \rightarrow \text{SiC} + \text{CO}$ , and  $\text{SiO}$  is then reacted with carbon to form SiC through the reactions  $\text{SiO} + 2\text{C} \rightarrow \text{SiC} + \text{CO}$  and  $\text{SiO} + 3\text{CO} \rightarrow \text{SiC} + 2\text{CO}_2$ .<sup>11)</sup>

It has been demonstrated in this study that the silicon carbide whiskers are formed when Mixed Powder of low

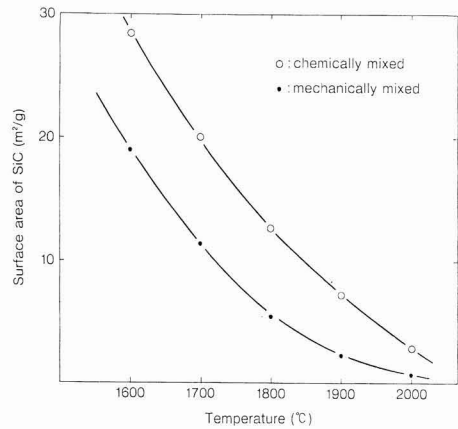


Fig. 5. Relations between firing temperature and specific surface area of SiC powders obtained from chemically mixed  $\text{SiO}_2$ -C powder and mechanically mixed one. Bulk density of mixed powders:  $0.90\text{g}/\text{cm}^3$ .

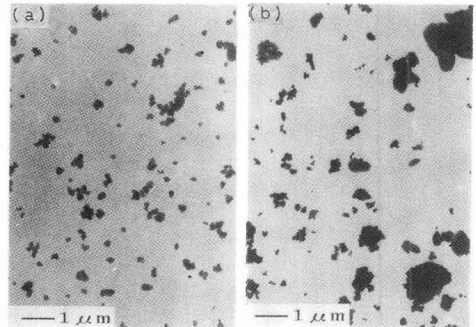


Fig. 6. TEM images of SiC powders from  $\text{SiO}_2$ -C mixed powder (a) from chemically mixed powder (firing  $1800^\circ\text{C}$ ) (b) from mechanically mixed powder (firing  $1700^\circ\text{C}$ )

density is dried at a relatively low temperature, and the grains result from firing of Mixed Powder of high density. Lower bulk density, or higher porosity, favors whiskers, conceivably because of smaller quantity of obstacles to their growth. Moreover, Mixed Powder produces higher partial pressures of  $\text{SiO}$  and  $\text{CO}$  formed by the reaction  $\text{SiO}_2 + \text{C} \rightarrow \text{SiO} + \text{CO}$ , because of larger contact area between silica and carbon, to accelerate the reaction  $\text{SiO} + 3\text{CO} \rightarrow \text{SiC} + 2\text{CO}_2$  which is deeply related to growth of the whiskers. In addition, firing temperature of around  $1500^\circ\text{C}$  gives a growth rate adequate to form SiC of high crystallinity.

Conversely, firing Mixed Powder of high density produces more obstacles to growth of the whiskers, as a result of which the SiC product tends to be less anisotropic, or granular.

#### 4.3. Comparison of Silicon Carbide Particles

The silicon carbide particles from Mixed Powder has a narrower size distribution than those from mechanically

mixed silica/carbon powder, because of silica and carbon distributions being less uniform in the latte powder, which produces higher SiO and CO partial pressures locally in the compact, to cause particle size distribution to be broader.

Moreover, Mixed Powder gives higher compact and sinter density, because of smaller quantities of secondary and coarse particles.

## 5. Conclusions

A mixture of silicon monomer and heavy oil was sprayed into a flame to produce a mixed powder of silica and carbon, which was fired to synthesize silicon carbide.

- 1) The mixed powder, consisting of fine, submicron-size particles, is finely mixed, each particle being a mixture of silica and carbon.
- 2) The mixed powder, when compressed to a high bulk density and fired, is converted into the fine powder of silicon carbide, without being crushed. The silicon carbide powder can be highly densified by pressureless sintering.
- 3) The mixed powder, when fired at a low bulk density, is converted into silicon carbide whiskers.

(Part of the above results were presented to the 6th International Meeting on Modern Ceramics Technologies,

Milan, Italy, June, 1986)

### References:

- 1) S. Somiya and Y. Inomata, Silicon Carbide Ceramics, Uchida Rokaku-ho, (1988), 261-268.
- 2) A. Enomoto, Seramikkusu, 17, 828-833 (1982).
- 3) G. Schwiier, Industrial Rare Metals, 73, 98-102 (1980).
- 4) Y. Okabe, J. Hojo and T. Kata, J. Chem. Soc. Jpn., 188-193 (1980).
- 5) A. Kijima, and M. Konishi, Yogyo Kyokaiishi, 93, 511-516 (1985).
- 6) H. Tanaka, K. Jin and K. Hirota, Seramikkusu Ronbunshi, 98, 607-610 (1990).
- 7) Examined Japanese Patent Publication 61-5647, Mitsui Toatsu kagaku.
- 8) S. Somiya and Y. Inomata, Silicon Carbide Ceramics, Uchida Rokaku-ho, (1988), 237-268.
- 9) Examined Japanese Patent Publication 61-2640, Mitsui Toatsu Kagaku.
- 10) Carbon Black Handbook, Tosho Shuppan, (1971), 238-240.
- 11) S. Somiya and Y. Inomata, Silicon Carbide Ceramics, Uchida Rokaku-ho, (1988) 251-259.

---

This article is a full translation of the article which appeared in Nippon Seramikkusu Kyokai Gakujutsu Ronbunshi (Japanese version), Vol.99, No.8, 1991.

# Preparation of $\text{SiCl}_4$ from Rice Hull Ashes (Part 3) — FT-IR-PAS Analysis of Chlorination Mechanism of Rice Hull Ashes Containing Alkaline and Alakline Earth Metal Salts —

Takeshi Okutani, Yoshinori Nakata and Masao Hino

Government Industrial Development Laboratory, Hokkaido  
2-17, Tsukisamu-Higashi, Toyohira-ku, Sapporo-shi, 062 Japan

The chlorination of a mixture of rice hull ashes and carbon containing alkaline and alkaline earth salts was investigated by FT-IR-PAS. It was thought that the relative ratio of totally symmetric  $\text{SiO}_4$  stretching vibration ( $\nu_1$ ) to antisymmetric  $\text{SiO}_4$  degenerate stretching vibration ( $\nu_3$ ) in infrared frequencies for  $\text{SiO}_2$  whose constituent oxygen atoms occupy the corners of a tetrahedron shows structural changes of  $\text{SiO}_2$  network. The results of  $\nu_1/\nu_3$  of  $\text{SiO}_2$  before and after chlorination showed that the values of  $\nu_1/\nu_3$  increased and the chlorination was accelerated because  $\text{K}^+$  increased. The  $\nu_1/\nu_3$  of  $\text{SiO}_2$  by addition of  $\text{Na}^+$ ,  $\text{Mg}^{2+}$  and  $\text{Ca}^{2+}$  was smaller than that of  $\text{K}^+$  and these additives did not accelerate the chlorination.  $\text{KCl}$ ,  $\text{NaCl}$ ,  $\text{MgCl}_2$  and  $\text{CaCl}_2$  which formed during the chlorination melted at  $900^\circ\text{C}$ . [Received January 25, 1991; Accepted May 25, 1991]

**Key-words:** Rice hull ash, Chlorination,  $\text{SiCl}_4$ , FT-IR-PAS, Structural changes of  $\text{SiO}_2$  network, Alkaline and alkaline earth salt additives.

## 1. Introduction

Silicon tetrachloride ( $\text{SiCl}_4$ ) is used as raw materials for manufacturing  $\text{SiC}$  and  $\text{Si}_3\text{N}_4$  powders by the vapor phase reaction or the method of the thermal decomposition of silicon di-imide ( $\text{Si}(\text{NH})_2$ ). The previous report<sup>1)</sup> clarified that potassium had accelerating effects for chlorination of a mixture of active  $\text{SiO}_2$  contained in rice hull ashes and carbon (C) to produce  $\text{SiCl}_4$ . The mechanism of the chlorination accelerating effect of potassium was presumed that a  $\text{K}^+$  with a radius of  $1.52\text{\AA}$  permeated into  $\text{SiO}_2$  lattice, distorting the lattice of  $\text{SiO}_2$ , thus easing the diffusion of chlorination species (carbon chloride in vapor phase) in the lattice. On the other hand, in cases of Na, Mg, and Ca metal salts,  $\text{Na}^+$ ,  $\text{Mg}^{2+}$  and  $\text{Ca}^{2+}$  did not distort the  $\text{SiO}_2$  lattice sufficiently to ease the diffusion of chlorination species because the ion radii of these metal are smaller than that of  $\text{K}^+$ . Further it was presumed that these salts became chlorides under chlorination conditions, which turned into a molten state at temperature above  $800^\circ\text{C}$ , covering the contact points of  $\text{SiO}_2$  and C and hindering contact with  $\text{Cl}_2$ , thus inhibitory effects on chlorination being observed.

When a substance is irradiated with infrared rays, an absorption band attributable to the proper vibration of the lattice is detected. For this vibration, there are two types: one is symmetric vibration with the total of vector of zero and the other is antisymmetric vibration with the total of vector of non-zero due to the molecular structure of the

substance.  $\text{SiO}_2$  is thought to be of a structure of  $\text{SiO}_4$  tetrahedron having three-dimensional network. The symmetric vibration is inactive for irradiation of infrared ray and no infrared absorption peak is observed if  $\text{SiO}_4$  is assumed to be free ions or gas molecules. In solid states such as crystals, a peak is observed or the degenerate vibration is split due to the influence of crystal field or due to the interaction with ions and crystal water.<sup>2)</sup> In fact, in the IR measurement of the solid  $\text{SiO}_2$ , infrared inactive vibration  $\nu_1$  and  $\nu_2$  are observed if  $\text{SiO}_4^{4-}$  is assumed to be ions.<sup>3)</sup>

The conventional method of measuring infrared spectra is not suitable for the measurements of strongly scattering substances such as powders and amorphous solids and of optically opaque substances. The mixture of rice hull ashes and C dealt with in this report is a powder and black, so the conventional IR spectrum measurement is unapplicable. However, if an infrared ray is irradiated to such a specimen, a part of the light energy generates heat energy in the specimen. The following thermal diffusion makes a part of energy transferred to the surrounding gas, producing compression waves. By detecting the compression waves with a highly sensitive microphone or a piezoelectric elemental device the information on the chemical bond of the specimen that could not be measured with a conventional infrared spectrometer can be obtained. This method is the photo-acoustic spectroscopy (PAS).<sup>4)</sup> Recently, attention has been paid to FT-IR-PAS<sup>5)</sup> which can decrease the measurement time with a high accuracy by combining PAS with the Fourier-transform infrared spectroscopy (FT-IR).

In this report, the mechanism of accelerating and hindering effects of alkaline and alkaline earth metal salts on the chlorination of  $\text{SiO}_2$  in rice hull ashes was investigated by FT-IR-PAS of rice hull ashes before and after chlorination.

## 2. Experimental Procedures

The rice hull ashes, carbon, silicic anhydride, silica sand and alkaline and alkaline earth metal salt additives such as  $\text{KCl}$  and  $\text{KH}_2\text{SO}_4$  used are the same as those used in the previous report.<sup>1)</sup> Also the method of preparation of samples for chlorination is the same.

The chlorination experiments were also conducted in the same way as those of the previous report.<sup>1)</sup> The chlorination was conducted at  $900^\circ\text{C}$  for 1hr, and the conversion of  $\text{SiO}_2$  to  $\text{SiCl}_4$  in rice hull ashes were measured. The reaction residues were used as the specimens for measurement of FT-IR-PAS spectra. To make comparison, the FT-IR-PAS spectra of specimens before chlorination were also measured. In the FT-IR-PAS measurement, the specimens were used as they were. As an FT-IR-PAS apparatus, a

Fourier infrared spectrophotometer (DIGILAB, FTS-15B/D) equipped with a PAS (microphone type) was used.  $\nu_1 \sim \nu_4$  of each specimen were measured, and the peak height of spectra were obtained as a height from the base-line to the top of peak.

### 3. Results and Discussions

Figure 1 shows the FT-IR-PAS spectra of Ash-1, Ash-2, commercial  $\text{SiO}_2$  and silica sand. In the figure,  $\nu_1$  is totally symmetric stretching vibration,  $\nu_2$  is the totally symmetric deformation vibration and  $\nu_3$  and  $\nu_4$  are degenerate stretching vibration.  $\nu_1$  and  $\nu_2$  of normal modes of vibration of tetrahedron  $\text{XO}_4$  molecules/ions are infrared inactive (the total of vectors is 0) and  $\nu_3$  and  $\nu_4$  are infrared active (the total of vectors has a certain plus or minus value).<sup>4)</sup> However, because  $\text{SiO}_2$  has a three-dimension network structure of  $\text{SiO}_4$  tetrahedrons, the spectra of infrared inactive  $\nu_1$  and  $\nu_2$  are also observed due to the effects of crystalline field such as the interaction between  $\text{SiO}_4$  tetrahedrons. The X-ray diffraction showed that Ash-1 and Ash-2 were  $\alpha$ -cristobalite, commercial  $\text{SiO}_2$  was amorphous and the silica sand was  $\alpha$ -quartz. For  $\alpha$ -quartz,  $\nu_1$  has two separate peaks and  $\nu_4$  is not observed. For amorphous  $\text{SiO}_2$ ,  $\nu_1$  has one peak and  $\nu_4$  is not observed. From these results, it was clarified that the detected peaks were different depending on crystals, thus the polymorphism of  $\text{SiO}_2$  could be identified by PAS as by IR.<sup>3)</sup> It is thought that the change in the ratio ( $\nu_1/\nu_3$ ) of peak height of the infrared inactive  $\nu_1$  to that of the infrared active  $\nu_3$  shows some structural change of  $\text{SiO}_2$ . The ratios of the PAS peak heights of  $\nu_1$  and  $\nu_3$  of the specimens before chlorination were measured. The results are shown in Fig.1.

Table 1 shows  $\nu_1/\nu_3$  of the specimens after chlorination at 900°C for 1hr. The specimens were the reaction residues of chlorination of Ash-1 and the mixtures of Ash-1+C, Ash-2+C, commercial  $\text{SiO}_2$ +C and silica sand+C added activated carbon with C/ $\text{SiO}_2$  mole ratio of 2.5 and those with alkaline and alkalin earth metal salts added. The  $\nu_1/\nu_3$  values of the specimens before chlorination of the mixtures of Ash-1, Ash-2, commercial  $\text{SiO}_2$  and silica sand and active carbon or active carbon+KHSO<sub>4</sub> were the same as those of

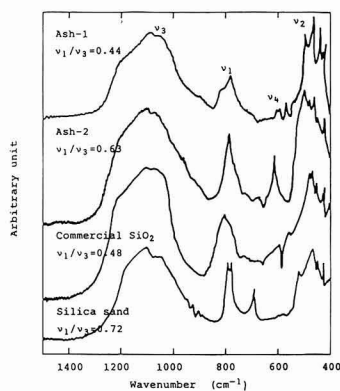


Fig. 1. FT-IR-PAS spectra of rice hull ashes, commercial  $\text{SiO}_2$  and silica sand.

Table 1.  $\nu_1/\nu_3$  of reaction residues of chlorination and conversion of  $\text{SiO}_2$  to  $\text{SiCl}_4$  of rice hull ashes, commercial  $\text{SiO}_2$  and silica sand.

Exp. No.	Sample	$\nu_1/\nu_3$	Conversion (wt%)
1	Ash-1	0.70	60.4
2	Ash-1+KCl	0.73	71.7
3	Ash-1+KHSO <sub>4</sub>	0.73	70.4
4	Ash-1+NaCl	0.59	56.7
5	Ash-1+MgCl <sub>2</sub>	0.53	55.3
6	Ash-1+CaCl <sub>2</sub>	0.47	45.8
7	Ash-1+C	0.69	81.0
8	Ash-1+C+KHSO <sub>4</sub>	0.72	87.9
9	Ash-2+C	0.59	47.9
10	Ash-2+C+K <sub>2</sub> CO <sub>3</sub>	0.76	79.5
11	Ash-2+C+KCl	0.71	79.9
12	Ash-2+C+KHSO <sub>4</sub>	0.76	82.1
13	Ash-2+C+KOH	0.81	76.9
14	Ash-2+C+KNO <sub>3</sub>	0.79	80.4
15	Commercial $\text{SiO}_2$ +C	0.38	7.4
16	Commercial $\text{SiO}_2$ +C+KHSO <sub>4</sub>	0.57	53.8
17	Silica sand+C	0.64	8.7
18	Silica sand+C+KHSO <sub>4</sub>	0.80	26.2

Ash-1, Ash-2, commercial  $\text{SiO}_2$  and silica sand shown in Fig.1.

The  $\nu_1/\nu_3$  of the specimens after chlorination of Ash-2+C, commercial  $\text{SiO}_2$ +C and silica sand+C are the same as or below the values before chlorination. In case that potassium salt is added, the  $\nu_1/\nu_3$  values of the specimens after chlorination are larger than those before chlorination. It seems to be because  $\text{K}^+$  got into  $\text{SiO}_2$ , resulting in a structural change that made the diffusion of chlorination species easier, thus accelerating the chlorination.

The Ash-1 contains 21.3wt% C formed by the pyrolysis of cellulose in the rice hull. As stated in the previous report,<sup>7)</sup> the mixture of  $\text{SiO}_2$  and C obtained from rice hull exhibited a high chlorination reactivity. From the result of the mass balance of the C under chlorination, it seemed that the C reacted with  $\text{Cl}_2$  to form a vapor phase carbon chloride, which contributed to the chlorination. The  $\text{SiO}_2$  and C in the Ash-1 comes from the same rice hull and have a good mutual dispersiveness, resulting in having many points of contact of  $\text{SiO}_2$  and C. When the Ash-1 was treated at 900°C in air for 1hr, the C contained was burnt out and the C content decreased from 21.3 to 2wt%. When the mixture of the ash (C content: 2wt%) and activated carbon is chlorinated at 900°C for 1hr, the conversion of  $\text{SiO}_2$  to  $\text{SiCl}_4$  is 48%, about the same with that of Ash-2+C. From these results it is clear that the  $\text{SiO}_2$  in rice hull and the C formed by the thermal decomposition of cellulose in rice hull have a high chlorination reactivity.

The  $\nu_1/\nu_3$  values of Ash-1 added with NaCl, MgCl<sub>2</sub> and CaCl<sub>2</sub> after chlorination addition are larger than 0.44, the value before chlorination, and smaller than that with potassium salt. Therefore, the degree of structural change of  $\text{SiO}_2$  seems to be smaller than that of the potassium salt. The conversion is lower than the case without additives. The chlorides of Na, Mg and Ca are in a molten state at 900°C, covering points of contact between  $\text{SiO}_2$  and C to restrain the formation of carbon chloride and the contact between carbon chloride and  $\text{SiO}_2$ . Therefore, it can be presumed that the conversion have decreased.

#### 4. Conclusion

When the  $\text{SiO}_2$  in rice hull ashes, the combustion residues of rice hulls, was chlorinated to prepare  $\text{SiCl}_4$ , alkaline and alkaline earth metal salts showed accelerating and hindering effects of chlorination. The mechanism of these effects was investigated by FT-IR-PAS and the following results were obtained.

The relative ratio of totally symmetric stretching vibration ( $\nu_1$ ) to degenerating vibration ( $\nu_3$ ) of  $\text{SiO}_2$  in the FT-IR-PAS spectra of specimens before and after chlorination showed that,  $\text{K}^+$  changed the structure of  $\text{SiO}_2$  and accelerated the chlorination. The structural change by addition of Na, Mg and Ca salts were smaller than that with K salt. It was thought that  $\text{NaCl}$ ,  $\text{MgCl}_2$  and  $\text{CaCl}_2$  formed from these salts during the chlorination were melted at  $900^\circ\text{C}$ , covering the points of contact between  $\text{SiO}_2$  and C, and suppressed rather than accelerated the chlorination reaction.

#### References:

- 1) T. Okutani, Y. Nakada, K. Ishikawa and K. Takeda, *Seramikkusu Ronbunshi*, 99, 315-319 (1991).
- 2) K. Nakamoto, J. Fujita and Y. Morimoto, *Kagaku-no-Ryoiki*, Extra Issue No.54, *Infrared Spectra*, 14-shu, Nankodo (1963), 78.
- 3) J.A. Gadsden, *Infrared Spectra of Minerals and Related Inorganic Compounds*, Butterworth (1975) 33.
- 4) S. Sawada and Y. Goshi, *Hyomen*, 19, 663 (1981).
- 5) S. Ochiai, *Nihon-Denshi-News*, 23, 26-29 (1983).
- 6) Chem. Soc. of Japan (ed.), *Lectures on Experimental Chemistry, Sequel 6, Method for Study on Structure of Inorganics*, Maruzen (1965) 434.
- 7) T. Okutani and Y. Nakata, *Preparation of  $\text{SiCl}_4$  from Rice Hulls in High Tech Ceramics*, ed. by P. Vincenzini, Elsevier Publishing, Amsterdam (1987) 511-516.

---

This article is a full translation of the article which appeared in *Nippon Seramikkusu Kyokai Gakujutsu Ronbunshi* (Japanese version), Vol.99, No.8, 1991.

# Properties of Porcelain Bodies Containing Zirconia

Kouhei Ohta, Tosio Torikai, Takanori Watari and Ohsaku Matsuda

Saga University, Faculty of Science and Engineering, Department of Applied Chemistry  
1, Honjo, Saga-shi, 840 Japan

High grade amakusa pottery clays mixed with 10, 20 and 30wt% zirconia were fired at 1250°, 1300° and 1350°C. Zircon, quartz, mullite, monoclinic- and tetragonal- zirconia were identified in the porcelain bodies with 20 and 30wt% zirconia fired at 1350°C. The content of the tetragonal phase in the fired bodies increased with increasing zirconia and with increasing firing temperature. The bending strength and fracture toughness of porcelain bodies containing zirconia increased with increasing firing temperature and with increasing amount of tetragonal zirconia, and those with 30wt% zirconia fired at 1350°C were 1.5 times higher than those without zirconia.

[Received February 18, 1991; Accepted May 23, 1991]

**Key-Words:** Zirconia, Amakusa Pottery Clay, Strength, Toughness

## 1. Introduction

Recently, attempts are being made to expand the range of porcelain used for manufacturing tableware and containers for school feeding, lighting apparatus, washstands and musical instruments. However, because the conventional porcelain is easy to break, needs for a stronger and tougher porcelain are increasing, and alumina-reinforced porcelain has already been manufactured.<sup>1)</sup> As for with alumina or mullite ceramics, zirconia toughened ceramics with a higher strength and a higher toughness using stress-induced phase transformation and crack branching by zirconia has been manufactured.<sup>2)</sup> However, no report has been made on the effects of zirconia addition on porcelain.

In this paper, the increase in strength and toughness due to the addition of zirconia particles to porcelain was investigated.

## 2. Experimental Procedures

Using high grade amakusa pottery clays ground for 24hr (average grain size: 9.8 $\mu$ m) and unstabilized zirconia (manufactured by Tosoh, average grain size: 1.08 $\mu$ m) as raw materials, each was dispersed in a pH2 acetic water solution for homogeneous mixing and mixed with a stirrer under application of ultrasonic waves using aqueous ammonia being added to keep the mixture at pH4. The slurry was press-formed at 100kg/cm<sup>2</sup> to 5.0cm in dia. and 4.5mm in thickness. The obtained formed bodies were naturally dried for 5 days and using a furnace in reduction atmosphere fired at 1250°, 1300° and 1350°C for 0.5hr at a rate of temperature

rise 100°C/hr. Zirconia contents in the pottery clays were 0, 10, 20 and 30wt%. Regarding the obtained pottery bodies, bulk density was measured by the Archimedes method, the determination of Zirconia crystal phase<sup>3)</sup> was conducted by X-ray diffraction, the structural observation with a scanning electron microscope, bending strength was measured by three-point bending tests and the fracture toughness ( $K_{IC}$ ) using the single edge precracked beam method.<sup>4)</sup>

## 3. Results and Discussion

It is known that the principal minerals in amakusa pottery clays consist of quartz, sericite, kaolinite and feldspar, while the porcelain bodies obtained by firing consist of quartz, mullite and a glass phase.<sup>5)</sup> Figure 1 shows the X-ray diffraction patterns of porcelain bodies with different zirconia contents fired at 1350°C. Although the crystal phases in specimens of pottery clays were quartz and mullite, as for those in specimens with zirconia contents of 20 and 30wt%, zircon as well as quartz, mullite, monoclinic (m) and tetragonal (t) zirconia were observed. On the other hand, no zircon was formed in the pottery bodies fired at temperatures below 1300°C. C.E. Curtis, et al. has reported that the firing temperature more than at 1315°C at the lowest is required to synthesize zircon from zirconia and silica.<sup>6,7)</sup> The results of this study well coincides with the above, and the formation of zircon is thought to be attributable to the reactions of the added zirconia with cristobalite formed from

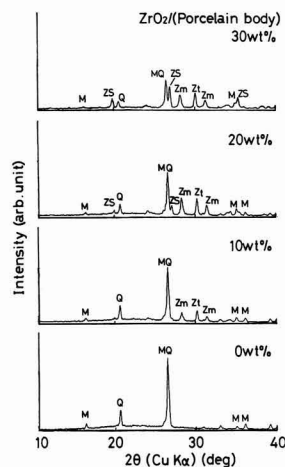


Fig. 1. X-ray diffraction patterns of porcelain bodies fired at 1350°C. M; mullite, Q; quartz, Zt; t-zirconia, Zm; m-zirconia, ZS; zircon

kaolinite or quartz in the pottery bodies. Quantitative determinations of zircon were conducted on specimens with 20 and 30wt% zirconia by X-ray diffraction, showing that amounts of formed zircon were 1 and 12wt% respectively.

**Figure 2** shows the relation between bulk density and contents of zirconia of the porcelain bodies fired at 1250, 1300 and 1350°C. The bulk density increased with increasing contents of zirconia and with increasing firing temperature. It is because the density of zirconia is larger than that of the pottery clays and because the densification of the porcelain bodies progressed with increasing temperature as clearly shown by the relative density in **Fig.3**. **Figure 4** shows the relation between volume fraction of tetragonal zirconia in the porcelain bodies and contents of zirconia. The volume fraction of tetragonal zirconia increased with increasing contents of zirconia and this tendency became

more remarkable with increasing firing temperature.

**Figure 5** shows the relation between bending strength and volume fraction of tetragonal zirconia in the porcelain bodies. The bending strength increased with increasing firing temperature and increasing volume fraction of tetragonal zirconia. **Figure 6** shows the relation between bending strength value divided by bulk density (specific strength) and contents of zirconia. The specific strength increased with increasing firing temperature. Except the specimens with 30wt% zirconia fired at 1350°C, specimens fired at respective temperature shows no increase in specific strength with increasing contents of zirconia. In other words, the strength of specimens at respective firing temperature increases with increasing contents of zirconia, but the specific strength shows little change. The increase in specific strength of specimens with 30wt% zirconia fired

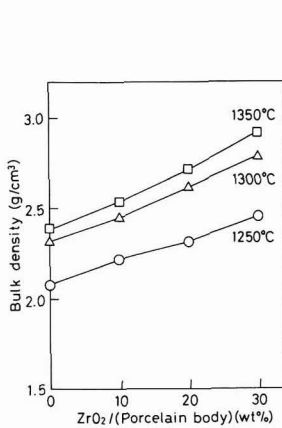


Fig. 2

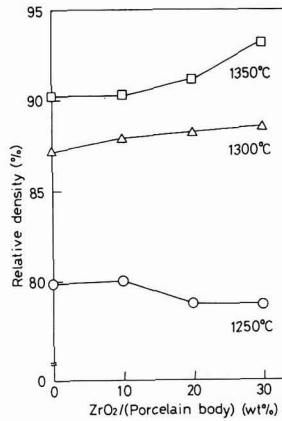


Fig. 3

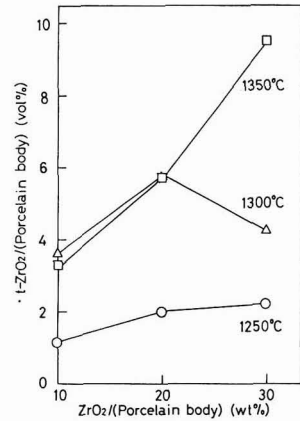


Fig. 4

**Fig. 2.** Relation between bulk density of the porcelain bodies and contents of zirconia.

**Fig. 3.** Relation between relative density of the porcelain bodies and contents of zirconia.

**Fig. 4.** Relation between volume of tetragonal zirconia in the porcelain bodies and contents of zirconia.

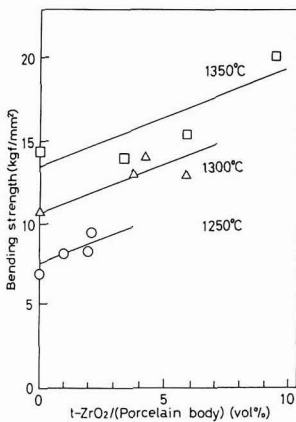


Fig. 5

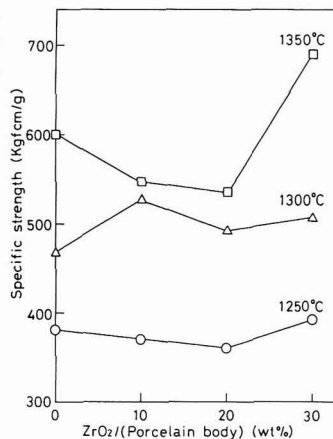


Fig. 6

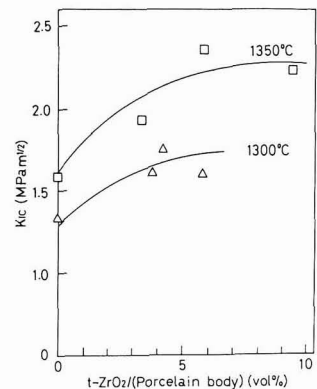


Fig. 7

**Fig. 5.** Relation between bending strength and volume fraction of tetragonal zirconia in porcelain bodies.

**Fig. 6.** Relation between specific strength and contents of zirconia.

**Fig. 7.** Relation between fracture toughness ( $K_{Ic}$ ) and volume fraction of tetragonal zirconia in porcelain bodies.

at 1350°C was largely due to the increase in bending strength with increasing tetragonal zirconia. **Figure 7** shows the relation between fracture toughness ( $K_{IC}$ ) and volume fraction of tetragonal zirconia in the porcelain bodies fired at 1300° and 1350°C. However, the  $K_{IC}$  of the porcelain bodies fired at 1250°C was not measured because of low density. It is thought that the increase in bending strength and fracture toughness is due to the densification of the porcelain bodies with increasing firing temperature as well as to the relaxation of fracture stress resulting from stress-induced-phase-transformation of tetragonal zirconia.

#### Acknowledgments

Authors would like to express thanks to Dr. Hiroshi Tateyama, Government Industrial Research Institute, Kyushu and the staff of Ceramic Industrial Research Institute of Saga Prefectural Government for their kind cooperation in our experiments.

#### References:

- 1) Nikkei New Materials, 66-76 (1988).
- 2) T. Sato, and M. Shimada, *Seramikkusu* 21, 613-620 (1986).
- 3) H. Toratani, M. Yoshimura, and S. Somiya, Determination of Monoclinic-Tetragonal  $ZrO_2$  System by X-ray Diffraction, *Zirconia Ceramics 2*, ed. by S. Somiya and M. Yoshimura, Uchidarokakuho (1984) 53-59.
- 4) Daiichi Research Center, Daiichi Giken, Nippon Steel Corporation, Method for Testing Fracture Toughness by inducing Pre-crack (1986) 2.
- 5) T. Torikai, O. Matsuda and S. Yoshida, Reports of Faculty of Science and Engineering, Saga Univ. 14, 91-96 (1986).
- 6) S. Komameni and R. Roy, *New Materials Series, Zircon-Science and Technique*, ed. by S. Somiya, Uchidarokakuho, (1989) 289-298.
- 7) C.E. Curtis and H.G. Sowman, *J. Am. Ceram. Soc.*, 36, 190-193 (1953).

---

This article is a full translation of the article which appeared in *Nippon Seramikkusu Kyokai Gakujutsu Ronbunshi* (Japanese version), Vol.99, No.8, 1991.

# Mechanical Properties of High Thermal Conductive SiC Ceramics

Yukio Takeda and Kunihiro Maeda

Hitachi Research Laboratory, Hitachi Ltd.  
4026 Kuji-cho, Hitachi-shi, 319-12 Japan

The mechanical properties of high thermal conductive SiC ceramics were studied. The flexural strength was 430MPa at room temperature and raised to 720MPa at 1400°C, but it decreased to 630MPa at 1500°C. The fracture toughness was  $3.8M \cdot \text{Pam}^{1/2}$  at room temperature and increased with increasing temperature, while Young's modulus was 460GPa at room temperature and decreased above 1300°C.

[Received March 7, 1991; Accepted April 19, 1991]

**Key-words:** SiC, BeO, Flexural strength, Fracture toughness, Young's modulus, Mechanical property

## 1. Introduction

SiC ceramics with addition of BeO have excellent properties such as high thermal conductivity electrical insulation and a coefficient of thermal expansion close to that of Si.<sup>1)</sup> SiC ceramics are used for the substrates in semiconductor elements having heat sink functions. On the other hand, SiC had been noted as a high-temperature structural ceramic material, and its mechanical properties have been extensively studied. SiC ceramics with high thermal conductivity has a relatively large bending strength of about 460 MPa; particularly because of its high thermal conductivity, it can possibly be used advantageously in environments subjected to thermal shock.<sup>1-3)</sup> For applications other than as structural materials, it is also necessary to recognize the mechanical properties of this material.

We investigated the bending strength, fracture toughness and Young's modulus as basic mechanical properties of high thermal-conductive SiC in the temperature range from room temperature to 1500°C.

## 2. Experimental Procedure

### 2.1. Samples

SiC ceramics were prepared by hot pressing with 2wt% BeO addition at 2100°C, 30MPa for 1h.<sup>1,2)</sup> The products were machined into the dimensions of 3×4×40mm. Their surfaces were finished to a roughness below 0.8μm and their corners were chamfered to about 0.1mm.

### 2.2. Measurement of Bending Strength

Bending strength was measured by a 4-point bending method with a lower span of 30mm, upper span of 10mm and crosshead speed of 0.5mm/min. This measurement was carried out in air at room temperature and in a vacuum (below 0.1MPa) at high temperature. Jigs for measurement

were prepared from the hot-pressed SiC ceramics by machining from the hot pressed Si ceramics. To measure bending strength at high temperatures, the samples were placed in an electric furnace equipped with a graphite heater and held at the required temperature for about 15min. Temperatures were measured with W-WR<sub>2</sub> thermocouples paced near the samples. At each temperature, 25 samples were measured.

### 2.3. Measurement of Fracture Toughness

To measure fracture toughness, the SENB method was used. The measuring procedure was the same as for bending strength. At each temperature, 10 samples were used.

### 2.4. Measurement of Young's Modulus

Young's modulus was measured under a deflection method over a range from room temperature to high temperature. The samples were prepared of 1×4×40mm and the cross head speed was 0.05mm/min. The conditions were the same as for the measurement of bending strength. 5 samples were tested at each temperature.

## 3. Results

### 3.1. Bending Strength

Figure 1 shows the temperature dependence of bending strength. SiC ceramics have a bending strength of 430MPa (mean) at room temperature. As temperature rises, the bending strength increases, peaking to 740MPa (mean) at 1400°C. At 1500°C, it is lower at 630MPa (mean). Such variations in strength due to temperature are the same as observed with other SiC ceramics.<sup>4)</sup>

Figure 2 shows the Weibull plots and Weibull modulus of bending strengths measured at several temperatures. The Weibull modulus range from 9.5 to 13.5. The fracture surfaces showed that in a temperature ranged from room temperature to 1200°C, grain boundary and transgranular fractures coexist. In a temperature range from 1400°C to 1500°C, intergranular fractures were predominant. Main fracture sources were pores, large grains, agglomerate grains

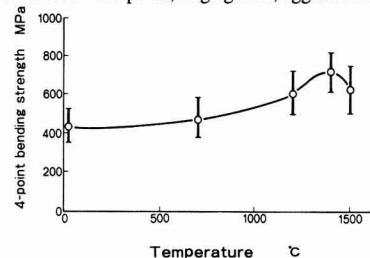


Fig. 1. Flexural strength as a function of temperature.

and flaws by machining. With low strengths, fracture origins at room temperature were observed relatively easily; with high strength, it was difficult to identify fracture origins. At high temperatures in particular, pores, large grains and agglomerate grains were identified as fracture origins but flaws by machining could not be identified as fracture origins.

**3.2. Fracture Toughness**

Figure 3 shows the relation between fracture toughness and temperature. The values of fracture toughness are  $3.8\text{MPa}\cdot\text{m}^{1/2}$  (mean) at room temperature and increase with temperature, peaking at  $5.1\text{MPa}\cdot\text{m}^{1/2}$  (mean) at  $1400^\circ\text{C}$ . At  $1500^\circ\text{C}$ , they are  $4.9\text{MPa}\cdot\text{m}^{1/2}$  (mean) with scatter at a higher level.

**3.3. Young's Modulus**

Figure 4 shows the temperature dependance of Young's modulus. The Young's modulus remains a nearly constant  $460\text{GPa}$  at temperatures up to  $1200^\circ\text{C}$ . As temperature rises above  $1300^\circ\text{C}$ , it decreases to  $420\text{GPa}$  at  $1400^\circ\text{C}$  and rapidly to  $350\text{GPa}$  at  $1500^\circ\text{C}$ .

**4. Discussions**

We investigated the temperature dependence of bending strength, fracture toughness and Young's modulus of of high thermal-conductive SiC ceramics with addition of BeO. As temperature rises up to about  $1400^\circ\text{C}$ , the bending strength and fracture toughness of SiC ceramics increase. At  $1500^\circ\text{C}$ , they are a little lower. The Young's modulus decreases at temperature above  $1300^\circ\text{C}$  and rapidly

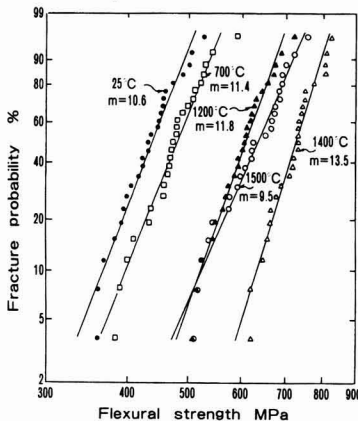


Fig. 2. Weibull plots of flexural strength at various temperatures.

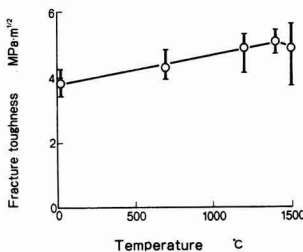


Fig. 3. Fracture toughness as a function of temperature.

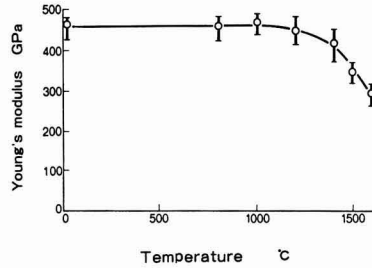


Fig. 4. Young's modulus as a function of temperature.

decreases at around  $1500^\circ\text{C}$ . Such decreases in mechanical properties of SiC ceramics at high temperatures are observed when there is second phase on grain boundaries which softens at high temperature. When SiC ceramics with addition of BeO are observed under a transmission electron microscope, BeO as additive exists as a single crystalline phase at triple points on grain boundaries, but no second phase which softens at high temperature is observed on grain boundaries.<sup>3,5)</sup> In the present study, we also observed grain boundaries under a high-resolution electron microscope, reaching no conclusion whether a secondary phase existed or not. However, the behavior of mechanical properties at high temperatures as described above suggests that there might be a very thin layer which softens at temperature above  $1500^\circ\text{C}$ .

**5. Conclusions**

We investigated the mechanical properties of high thermal-conductive SiC ceramics with an addition of 2wt% BeO obtained by hot-pressing and reached the following findings:

- 1) As temperature rises, the bending strength increases from  $430\text{MPa}$  at room temperature to  $720\text{MPa}$  at  $1400^\circ\text{C}$ , then decreases to  $630\text{MPa}$  at  $1500^\circ\text{C}$ .
- 2) As temperature rises, fracture toughness increases from  $3.8\text{MPa}\cdot\text{m}^{1/2}$  at room temperature to  $5.1\text{MPa}\cdot\text{m}^{1/2}$  at  $1400^\circ\text{C}$  but decreases to  $4.9\text{MPa}\cdot\text{m}^{1/2}$  at  $1500^\circ\text{C}$ .
- 3) Young's modulus is  $460\text{GPa}$  but at temperatures above  $1300^\circ\text{C}$ , it is lower.
- 4) At temperatures above  $1500^\circ\text{C}$ , mechanical properties are degraded. This suggests that a very thin secondary phase might exist on grain boundaries.

**References:**

- 1) T. Takeda, K. Nakamura, K. Maeda and Y. Matsushita, Nippon Seramikkusu Kyokai Gakujutsu Ronbunshi, 95, 860-863 (1987).
- 2) Y. Takeda, K. Nakamura, K. Maeda and M. Ura, Adv. Ceram. Mater., 1, 162-165 (1986).
- 3) Y. Takeda, K. Usami, K. Nakamura, K. Maeda, T. Miyoshi, S. Shinozaki and M. Ura, Advances in Ceramics, 7, 253-259 (1984).
- 4) S. Prochazka and R.J. Charles, Am. Ceram. Soc. Bull., 52, 855-861 (1973).
- 5) A. Soeda and K. Maeda, Nippon Seramikkusu Kyokai Gakujutsu Ronbunshi, 93, 636-648 (1985).

# Solubility of Lanthanum Oxide in Barium Titanate

Akira Hasegawa, Satoru Fujitsu\*, Kunihiro Koumoto and Hiroaki Yanagida\*\*

Department of Industrial Chemistry, Faculty of Engineering, Univ. of Tokyo  
7-3-1, Hongo, Bunkyo-ku, Tokyo, 113 Japan

\*Department of Materials Science and Ceramic Technology, Shonan Institute of Technology  
1-1-25, Tsujido-Nishikaigan, Fujisawa-shi, 251 Japan

\*\*Research Center for Advanced Science and Technology, Univ. of Tokyo  
4-6-1, Komaba, Meguro-ku, Tokyo, 153 Japan

Lattice parameters of La-doped barium titanate were measured to elucidate the mechanism of insulation induced by excess  $\text{La}_2\text{O}_3$  addition from the viewpoint of the second-phase precipitation and the change in the substitutional site for La. Neither second-phase precipitation or anomalous change in lattice parameter was observed even above the critical concentration (0.4mol%) at which  $\text{BaTiO}_3$  is converted to an insulator. The phase transition from tetragonal to cubic system occurs at 5mol%  $\text{La}_2\text{O}_3$  doping, but this is higher than the critical concentration. The concentration at which the second-phase precipitation occurs was higher than 15mol%. The lattice parameter changed according to the Vegard's law, and the substitution of La for B-site was not clearly indicated. It was suggested that the insulation induced by excess  $\text{La}_2\text{O}_3$  addition was not caused by the change in bulk crystal properties.

[Received March 18, 1991; Accepted May 23, 1991]

**Key-words:** Barium titanate, Lanthanum oxide, Semiconducting, Solid solution, Lattice parameter

## 1. Introduction

It is known that barium titanate turned semiconducting by adding a trace of an additive shows PTC effect at around the Curie point. There is an optimal content of the element used to turn the material semiconductive. If the content is above this optimal level, the material is turned insulating again.<sup>1,2)</sup> About the mechanism of this returning to the insulating state due to the additive above the optimal level, there are various theories including precipitation of excess ions on crystal grain boundaries and the substitution of La for the B-site.<sup>3,4)</sup>

Choosing  $\text{La}_2\text{O}_3$ , the most common agent for turning barium titanate semiconducting, we determined the limit of  $\text{La}_2\text{O}_3$  doping in barium titanate and investigated how the lattice parameter of barium titanate changed when  $\text{La}_2\text{O}_3$  content increased.

## 2. Experimental Procedure

For starting materials,  $\text{BaCO}_3$  (99.9% made by Soekawa Rikagaku),  $\text{La}_2\text{O}_3$  (99.9%, Shinetsu Kagaku) and  $\text{TiO}_2$  (99.8%, Fuji Titanium) were used. Adequate amounts of these materials were weighed out to prepare a composition:

$\text{Ba}_{1-x}\text{La}_x\text{TiO}_3$ . This powder was wet mixed with ethanol in a ball mill for 12h. The mixed powder was dried with an infrared lamp and calcined at 1150°C for 2h. It was then molded into round pallets and burned at 1350°C for 1h. The products were annealed at the specified temperature for 1h and plunged into water for rapid cooling. They were then dried, crushed and submitted to powder X-ray diffraction analysis. Burning and annealing were carried out on a zirconia plate dusted with powder. For the lattice parameters, peaks on the high-angle side were measured using silicon powder as an internal standard substance. For the lattice parameter computation from the data obtained, the X-ray structure analysis library (UNICS) at the University of Tokyo was used.

## 3. Results and Discussion

Figure 1 shows changes in the lattice parameter as x of the composition formula  $\text{Ba}_{1-x}\text{La}_x\text{TiO}_3$  was increased at room temperature. Pure barium titanate is tetragonal at room temperature.

The a- and c-axes of pure barium titanate at room temperature were 3.9935Å and 4.0359Å respectively. As La increases, the a-axis grows, while the c-axis shrinks. There was no precipitated phase at the upper limit of the additive content (0.4mol%) for semiconduction, which was not doping limit. Either of this concentration was no sudden change in the lattice parameter observed. For the solid dissolution of La in barium titanate, it is known that La is substitutionally solid dissolved at the A-site (barium site). The ion radii of Ba and La are 1.35Å and 1.16Å, respectively. The crystal lattice shrinks by the substitution of the La ion for the Ba ion site. Figure 2 shows lattice parameter

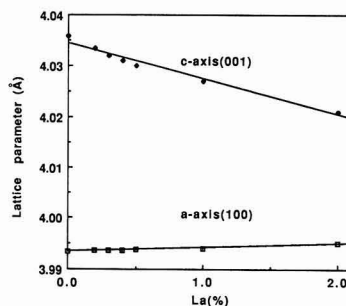


Fig. 1. Lattice parameters of  $\text{La}_x\text{Ba}_{1-x}\text{TiO}_3$  vs. La contents (%) near the insulation starting concentration

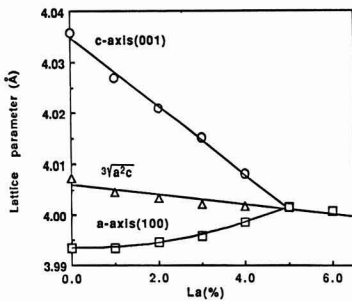


Fig. 2. Lattice parameters of  $\text{La}_x\text{Ba}_{1-x}\text{TiO}_3$  vs. La contents (%) near the tetragonal-cubic transition.

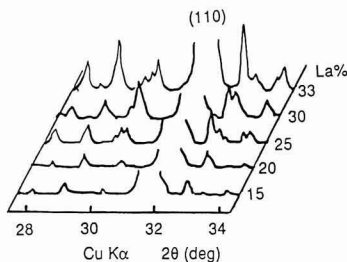


Fig. 3. X-ray diffraction pattern of  $\text{La}_x\text{Ba}_{1-x}\text{TiO}_3$  near (110) peak.

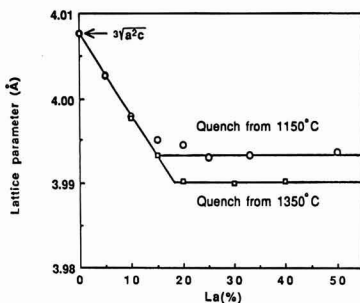


Fig. 4. Lattice parameters change at the limit of solid solution. Plot at 0% of La contents means the cubic root of lattice volume.

changes as the dissolved amount increases. Evidently, when La content is 5.0%, the material turns cubic with  $a=c=4.0016\text{Å}$ . The Curie temperature of pure barium titanate is  $120^\circ\text{C}$ . It is assumed that this was lowered by La substitution down to room temperature when the La content was 5.0%. On the assumption that Curie temperature drops linearly with La substitution, a  $20^\circ\text{C}/\%$  Curie temperature drop results from La substitution. The cubic root of the volume of unit lattice ( $\sqrt[3]{a^2c}$ ) is shown by a solid line in Fig.2. The cubic root of the volume of unit lattice for pure barium titanate was  $4.0076\text{Å}$ . Vegard's law using a lattice parameter of  $3.92\text{Å}^{5,6}$  for  $\text{LaTiO}_3$  (cubic) is shown by a straight line in the figure.<sup>5,6</sup> Evidently, Vegard's law holds

in the area of solid dissolution.

As the La content was increased from  $x=0$ , a second phase came to appear in addition to perovskitic cubic solid solution. Figure 3 shows peaks of the second phase appearing near the (110) face of the solid solution. This proves that perovskitic cubic solid solutions have limits to La solid dissolution. To investigate such limits, we obtained lattice parameters of samples cooled slowly and samples annealed to  $1300^\circ\text{C}$  or  $1150^\circ\text{C}$  and then cooled rapidly. The results are shown in Fig.4. For the La content of 0%, with which the material was tetragonal, the cubic root of the volume of unit lattice ( $\sqrt[3]{a^2c}$ ) was plotted. The doping limits were 20% at  $1350^\circ\text{C}$  and 15% at  $1150^\circ\text{C}$  and that of the samples cooled slowly was the same 15% at  $1150^\circ\text{C}$ . This suggests that in the samples cooled slowly, the state at  $1150^\circ\text{C}$  is frozen. There was probably no La substitution for B-site because the lattice parameters changed in accordance with Vegard's law. As La content increases, barium titanate rapidly turns insulating. Probably, this changed is not caused by the precipitation of excess ions on crystal grain boundaries due to doping limits or La substitution for B-site but caused without changes in radiographically bulk crystals.

## 4. Conclusion

Carrying out a test of doping barium titanate with La, we acquired the following findings:

- 1) No precipitated phase appeared at the upper limit of additive content (0.4mol%) for semiconducting and thus the limit was not a doping limit. There were no rapid changes either in the lattice parameters.
- 2) Transition from tetragonal to cubic took place at 5mol% which was higher than the upper limit (0.4mol%) of additive content for turning the material semiconducting.
- 3) The precipitation of the second phase began to occur with a 15% additive content with samples cooled slowly and those cooled rapidly from  $1150^\circ\text{C}$  and with a 20% additive content with samples cooled rapidly from  $1350^\circ\text{C}$ .
- 4) Lattice parameters changed in accordance with Vegard's law and it seemed that there was no La substitution for B-site.

## References:

- 1) Osamu Saburi, J. Phy. Soc. Jpn., 14 1159-1174 (1959).
- 2) Osamu Saburi, J. Am. Cer. Soc. 44, 54-63 (1961).
- 3) P.K. Gallagher, F. Schrey and F.V. Dimarcello, *ibid.*, 46, 359-365 (1963).
- 4) H.A. Sauer and S.S. Fraschen, Proc. Electronic Component Sympo. (1959) 41-46.
- 5) JCPDS#34-596.
- 6) J. Haffel, M.A. Mnatow, L. Bajars and M. Kundrath, Ind. Eng. Chem., 14, 154 (1975).

# Emission Spectra and Morphology of Carbon Films by ECR Plasma CVD

Kazunori Maruyama, Kiichiro Kamata, Tohru Inoue and Isao Tanabe

Nagaoka University of Technology, Department of Chemistry  
1603-1, Kami-Tomioka-cho, Nagaoka-shi, 940-21 Japan

This paper is concerned with the relationships between the morphology of carbon films and the intensity of emission spectra in ECR plasma CVD of the system  $\text{CH}_4\text{-H}_2$ . A sample holder was connected in series to DC bias and it was negative to the apparatus. The application of negative bias caused an abrupt increase in emission intensity at about -100V bias. At the same time, smooth and flat carbon films were formed. The abrupt increase in emission spectra intensity was caused by the cooperative effects between DC and ECR powers. The formation of flat and smooth surface was attributed to the abrupt increase in plasma density which gives high speed ions, molecules and electrons. They might prevent the formation of secondary particles through aggregation of primary particles and/or enhance the peening effect on the substrate.

[Received March 19, 1991; Accepted April 19, 1991]

**Key-words:** ECR plasma CVD, Amorphous carbon films, Emission spectra intensity, Surface morphology.

## 1. Introduction

ECR plasma CVD process is featured by a high ionization efficiency of reaction gas, which contributes not only to the formation of amorphous silicon films<sup>1)</sup> and amorphous carbon films<sup>2)</sup> with increased hardness and in good quality even at low substrate temperature, but also to the increase of hardness of the formed films and, at the same time, to the obtainment of dense, smooth surfaced and flat films when DC bias voltage is applied to the substrate independent of the RF power source.<sup>3,4)</sup>

As for clarification of the thin film formation mechanism, plasma emission spectrum analysis is popularly used<sup>2,5,6)</sup> in order to identify the kind and the quantity of

atoms and molecules generated in plasma. In our present study, we confirmed the presence of the relationship between the intensity of plasma emission spectra and the surface morphology of formed films by SEM observation.

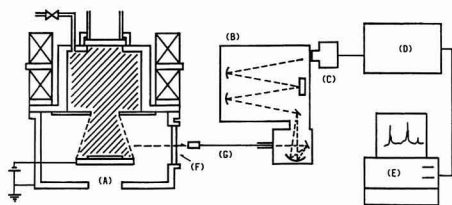
## 2. Experimental Procedure

Figure 1 shows the experimental apparatus, including an ECR plasma CVD apparatus, which we used for emission spectrum measurement. For the spectral analysis of emitting species in plasma, we used an optical spectrometric multichannel analyzer (OSMA), which consisted of a SMA detector (model IRY-700 N/RB, made by Princeton Instruments Inc.), a SMA spectrometer (model HR-320, made by the same), and a controller (model ST-110, made by the same). The conditions for plasma generation were same to the conditions for synthesis of carbon films in our previous study,<sup>3)</sup> namely, substrate temperature of 200°C, microwave (MW) power of 100 to 500W, methane gas flow rate of  $20\text{cm}^3 \cdot \text{min}^{-1}$ , hydrogen gas flow rate of  $30\text{cm}^3 \cdot \text{min}^{-1}$ , and total gas pressure of  $3 \times 10^{-4}$  Torr. DC bias voltage was applied to substrate in negative.

## 3. Results and Discussion

Figure 2 shows the emission spectra patterns of plasma in ECR plasma CVD, the conditions of which consisted of microwave power of 300W and respective bias voltages ( $V_B$ ) of 0 and -150V. Emission peaks attributed to H radical, CH radical and  $\text{H}_2$  molecule are observed in these spectra, in the same manner as in the emission spectra which come out in the formation process of amorphous carbon films by the RF plasma CVD process.<sup>5)</sup>

Figure 3 shows the relationship between the emission peak height attributed to  $\text{H}_\alpha$  radical and CH radical in Fig.2 and the bias voltage. The emission intensity of the system  $\text{CH}_4\text{-H}_2$  becomes slightly weak in the  $V_B$  range of 0 and -90V. In the  $V_B$  range beyond -100V, all of the emission intensities abruptly increase. On the other hand, all of the emission intensities of ECR plasma of  $\text{H}_2$  slightly increase with the increase of  $V_B$ , as seen in Fig.3. Therefore, the abrupt increase of emission peak intensities attributed to  $\text{H}_2$  molecule and CH radical implies the rapidly accelerated dissociation of  $\text{CH}_4$  into CH radical, H radical and  $\text{H}_2$  molecule. In the case of the synthesis of hard carbon films by plasma CVD process, various types of discharge are used for generation of plasma, such as direct current (DC) discharge,<sup>7)</sup> high frequency (RF) discharge,<sup>8)</sup> and microwave (MW) discharge.<sup>9)</sup> High voltage in the order of several



**Fig. 1.** Experimental apparatus for the emission spectra measurements: A; ECR plasma CVD apparatus, B; Spectrometer, C; Detector, D; Controller, E; Console, F; Quarts glass window, G; Glass fiber.

kilovolt is normally required to be applied when DC discharge is only used, but in the case of our present experiments, in which ECR effect and DC effect are simultaneously applied, we assume that the application of a small DC bias voltage effected to abruptly accelerate the discharge due to a synergistic effect of ECR and DC.

When carbon films were formed by ECR plasma CVD process with various bias voltages applied, their deposition rate and their film hardness simply increased with the increase of bias voltage in the same manner as given in our previous report,<sup>3)</sup> but did not abruptly change in correspondence to the abrupt change of emission intensities attributed to CH radical and others as shown in Fig.3. While, SEM photographs in Fig.4 indicated that the morphology of the formed carbon films showed a rough surface containing

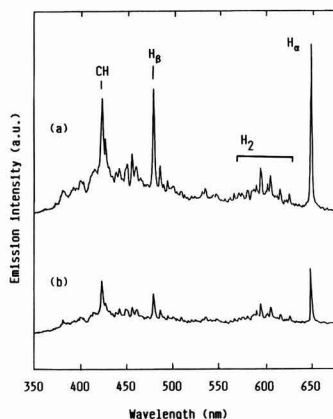


Fig. 2. Observed emission spectra of plasma in ECR plasma CVD: Bias voltages were  $-150\text{V}$  (a) and  $0\text{V}$  (b). Flow rates of  $\text{CH}_4$  and  $\text{H}_2$  were  $20\text{cm}^3\text{min}^{-1}$  and  $30\text{cm}^3\text{min}^{-1}$ , respectively. MW power was  $300\text{W}$ .

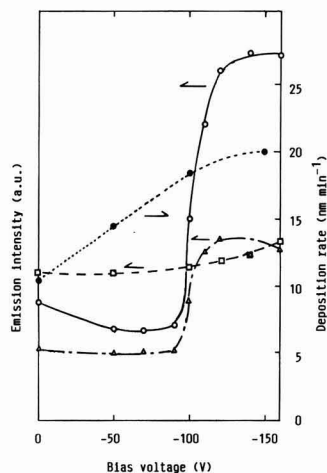


Fig. 3. Relationships among bias voltage, deposition rate (●) and peak height of emission spectra:  $\text{H}\alpha$  (○) and  $\text{CH}$  (Δ) for flow rates of  $20\text{cm}^3\text{min}^{-1}$  ( $\text{CH}_4$ ) and  $30\text{cm}^3\text{min}^{-1}$  ( $\text{H}_2$ );  $\text{H}\alpha$  (□) for flow rate of  $30\text{cm}^3\text{min}^{-1}$  ( $\text{H}_2$ ). MW power was  $300\text{W}$ .

hemispherical coarse grains when  $V_B$  was lower than  $-100\text{V}$ , and a fine-grain, smooth and flat surface when  $V_B$  was higher than  $-150\text{V}$ . Different from the bias voltage dependence of deposition rate and film hardness, this change of morphology of carbon films corresponds to the abrupt change of plasma emission intensity which was caused by the change of bias voltage applied.

In our previous reports on the thin film formation by vapor deposition processes,<sup>10-13)</sup> we confirmed that fine primary particles in size of around  $10\text{nm}$  were formed in the vapor phase, and, in the subsequent stage, they cohered each other to form large secondary particles in size of over several hundred nm. In the case of our present experiments, we similarly assume that the fine primary particles formed in the plasma flow cohered each and grew up to large particles on the way to the substrate. When plasma density is increased, the primary particles are assumed to be impacted more violently by radicals, ions and high speed electrons in plasma, thereby, they are disturbed from the growth to the large secondary particles. As the result, the deposition rate does not show an abrupt increase. We further assume that the peening effect<sup>14)</sup> of various plasma-generated species on the substrate becomes remarkable, thereby, deposition films were formed with smooth surfaces.

Figure 5 shows the relationship between the microwave

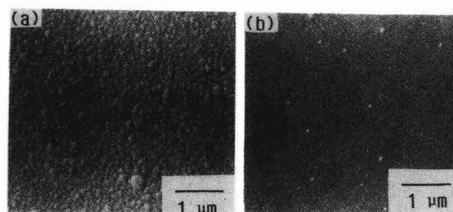


Fig. 4. SEM photographs of carbon films on glass substrates at  $200^\circ\text{C}$ . MW power was  $300\text{W}$  and bias voltages were  $-100$  (a) and  $-150$  (b)V.

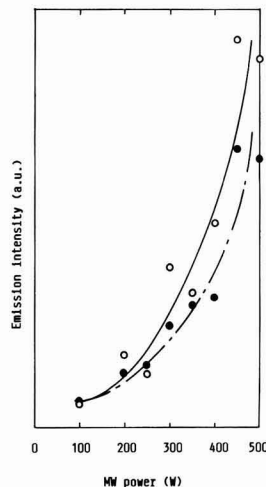


Fig. 5. Relationships between MW power and peak height of  $\text{H}\alpha$  (○) and  $\text{CH}$  (●) in plasma emission spectra. Flow rates of  $\text{CH}_4$  and  $\text{H}_2$  were  $20\text{cm}^3\text{min}^{-1}$  and  $30\text{cm}^3\text{min}^{-1}$ , respectively. Additional bias voltage was not applied.

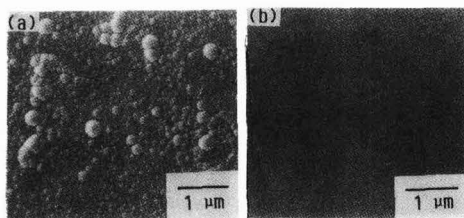


Fig. 6. SEM photographs of carbon films on glass substrates at 200°C. MW powers were 100W (a) and 500W (b). Bias voltage was -100V.

power and the emission peak height attributed to  $H_{\alpha}$  radical and CH radical in the plasma emission spectra. The additional bias voltage was not applied in this experiment, and respective emission peak intensities attributed to  $H_{\alpha}$ ,  $H_{\beta}$ , CH and  $H_2$  are seen to have abruptly increased with the increase of microwave power. If an abrupt increase of emission spectrum intensity should be observed, we can predict that the carbon films obtained should have a smooth surface structure. As the matter of fact, we confirmed that carbon films had surface with hemispherical roughness when microwave power applied was lower than 300W, while, they had dense, smooth and flat surfaces when microwave power applied was 500W, as seen in the SEM photographs in Fig.6.

#### 4. Conclusion

In the synthesis of amorphous carbon films by ECR plasma CVD process, we confirmed that plasma emission intensity abruptly increased when either DC bias voltage or microwave power was changed, and the surface morphology of the formed carbon films became fine and smooth when either of the above mentioned factors became beyond a

certain threshold value.

#### Acknowledgements

This study was partly supported by the 1990 research fund on materials engineering of the Japan Plate Glass Co., Ltd.

#### References:

- 1) K. Kobayashi, M. Hayama, S. Kawamoto and H. Miki, *Jpn. J. Appl. Phys.* 26, 202-208 (1987).
- 2) P. Koidl, Ch. Wild, B. Dischler, J. Wagner and M. Ramsteiner, *Mater. Sci. Forum* 52 and 53, 41-70 (1989).
- 3) K. Kamata, T. Inoue, K. Maruyama and I. Tanabe, *Jpn. J. Appl. Phys.* 29, L1203-L1205 (1990).
- 4) I. Nagai, A. Ishitani and H. Kuroda, *J. App. Phys.*, 67, 2890-2893 (1990).
- 5) K. Kobayashi, N. Matsukura and Y. Machi, *ibid.*, 59, 910-912 (1986).
- 6) Y. Saito, K. Sato, H. Tanaka, K. Fujita and S. Matuda, *J. Mater. Sci.* 23, 842-846 (1988).
- 7) K. Kurihara, K. Sasaki, M. Kawarada and N. Koshino, *Appl. Phys. Lett.* 52, 437-438 (1987).
- 8) S. Matsumoto, Y. Sato, M. Tsutsumi and N. Setaka, *J. Mater. Sci.* 17, 3106-3112 (1982).
- 9) M. Kamo, Y. Sato, S. Matsumoto and N. Setaka, *J. Cryst. Growth* 62, 642-644 (1983).
- 10) K. Kamata, Y. Hosono and T. Yamashita, *Yogyo-Kyokaiishi*, 94, 910-2 (1986).
- 11) K. Kawata, K. Maruyama, S. Amano and H. Fukazawa, *J. Mater. Sci.*, 17, 316-319 (1990).
- 12) K. Kamata, S. Amano, H. Fukazawa, K. Maruyama and I. Tanabe, *Seramikkusu Ronbunshi*, 97, 1535-1536 (1989).
- 13) The authors, under preparation to apply to *Seramikkusu Ronbunshi*.
- 14) No.131 Committee on thin films of Nippon Gakujutsu Shinkokai (ed.), *Handbook on Thin Films*, Ohm-sha, (1983), p.338.

This article is a full translation of the article which appeared in Nippon Seramikkusu Kyokai Gakujutsu Ronbunshi (Japanese version), Vol.99, No.8, 1991.

# Preparation and Some Properties of Porous Mullite Ceramics Using Needle-like Crystals

Hiroaki Katsuki, Akihiko Kawahara, Hiromichi Ichinose, Sachiko Furuta and Ohsaku Matsuda\*

Ceramics Industrial Research Institute of Saga Prefectural Government  
3100-5, Chubu, Arita-machi, Nishimatsuura-gun, Saga, 844 Japan

\*Department of Applied Chemistry, Faculty of Science and Engineering, Saga University  
1, Honjyo-machi, Saga-shi, 840 Japan

Porous mullite ceramics with porosity of 26-57% were prepared with needle-like mullite crystals of 3-5 $\mu$ m length and 0.5-1.0 $\mu$ m diameter synthesized by firing New Zealand kaolin at 1650°C. Pore characteristic (porosity, pore diameter), three points bending strength and the thermal conductivity were examined on the porous mullite ceramics sintered at 1550-1700°C in air. With increasing the sintering temperature, the pore volume decreased, leading to the increase in the bending strength. However, the pore size distribution was almost independent of the sintering temperature. The average pore diameters for the porous mullite ceramics sintered at 1550-1700°C were in the range of 0.46-0.58 $\mu$ m. Thermal conductivity at room temperature decreased linearly with increasing porosity.

[Received April 4, 1991; Accepted May 23, 1991]

**Key-words:** Needle-like mullite, Porous ceramics, Kaolin, Porosity, Thermal conductivity

## 1. Introduction

Porous ceramics have great features in their pore structures in textures (pore volume, pore diameter, specific surface area etc.), and are widely used as insulators, filters, absorbers, catalyst carriers, and fixed enzyme carriers and others.<sup>1-5)</sup>

At present, porous materials with various pore characteristics are being produced by using ceramic particles with different sizes or burnable organic materials. Moreover, some other porous materials have been developed which adopt fiber ceramics such as alumina, silica and mullite.<sup>5-9)</sup>

The authors previously reported<sup>10)</sup> that porous ceramics having needle-like mullite densely entangled with each other is obtained by extruding New Zealand kaolin to prepare a sheet which is sintered over 1550°C and then dipped in hydrofluoric acid to remove a glassy phase coexisting in the sintered body. It was also found that this needle-like mullite is stable in air up to 1650°C.<sup>11)</sup> However, prolonged leaching by hydrofluoric acid greatly lowers the strength of porous bodies because the acid attacks needle-like mullite as well. On the other hand, if leaching is insufficient, a glassy phase containing alkali components melts at high temperatures so that problems arise such as the deformation of the porous body and affected pore characteristics.

Consequently, this study was intended to prepare mullite

porous bodies stable at elevated temperatures, and only needle-like mullite powder obtained by the sufficient leaching of a glassy phase in New Zealand kaolin was used to prepare sintered porous bodies. They were subjected to tests for various properties such as pore characteristics, strength, coefficient of thermal expansion, and thermal conductivity.

## 2. Experimental Procedure

### 2.1. Synthesis of Needle-Like Mullite

The used raw material was New Zealand kaolin, the same as that in the previous report,<sup>10)</sup> and a sheet was sintered at 1650°C. After sintering, sintered bodies were ground into particles 2 to 3mm in size to facilitate the leaching of a glass phase. The hydrofluoric acid 9.2wt% in concentration was added to this powder in the plastic container, which was rotated at room temperature for the whole day to promote the leaching treatment. As glass phase leaching progressed, needle-like mullite crystals began to disperse and cloud the solution. Then the solution was filtered to recover needle-like mullite which were rinsed fully with pure water. The morphology of the obtained needle-like mullite was examined with a transmission electron microscope (type: 100U, JEOL), and chemical composition with a fluorescent X-ray analyzer (type: 3070, Rigaku Denki).

### 2.2. Preparation of Needle-Like Mullite

Needle-like mullite (15g) was charged in a metal mold 60mm in diameter and compacted by a uniaxial press (18MPa). No additives were mixed such as organic binders and sintering agents like oxides. These compacted bodies were sintered at 1500°, 1550°, 1600°, 1650°, and 1700°C for 2hrs to obtain needle-like mullite porous bodies. The heating rate was 100°C/hr.

### 2.3. Evaluation of Properties of Porous Bodies

The bulk density of sintered porous bodies was measured by a water substitution method (20°C). Pore size distribution and pore volume were determined with a mercury porosimeter (type: 9310; Shimadzu Seisakusho). Additionally, the sintered bodies were cut into columns 5 $\times$ 5 $\times$ 30mm in size, polished with emery paper (N.1000), and subjected to a 3-point bending test under the conditions of 25mm for a span and 0.5mm/min for a crosshead speed. The measured strength was represented by the average of 5 specimens. The coefficient of thermal expansion from room temperature to 1400°C was examined with a high-temperature-type

thermo-mechanical analysis system (Rigaku Denki) and thermal conductivity was measured in air by a laser flash method (type: A-8510B; Rigaku Denki). The diameter of a sample was 10mm, and its thickness was 1.3~1.5mm to reduce the influence of thermal leak from the sample after laser application. The specific heat was measured in vacuum higher than  $1.3 \times 10^{-3}$ Pa.

### 3. Results and Discussion

#### 3.1. Sinterability and Pore Characteristics of Needle-Like Mullite Porous Bodies

Figure 1 shows the morphology of needle-like mullite prepared at 1650°C before sintering. Crystals 10~20 $\mu$ m long and about 1 $\mu$ m thick are grown from adopted New Zealand kaolin by calcination at 1650°C<sup>(10)</sup>, and yet in this study, sintered bodies were ground into particles 2~3mm in size so that obtained crystals were smaller with an average length of 3~5 $\mu$ m, thickness of 0.5~1.0 $\mu$ m, and aspect ratio of 3~5. The chemical composition of needle-like mullite examined by fluorescent X-ray analysis was 2.97Al<sub>2</sub>O<sub>3</sub>·2SiO<sub>2</sub> and the total content of Na<sub>2</sub>O, K<sub>2</sub>O, CaO, and MgO was 0.1wt% or less. Table 1 gives bulk density and pore characteristics of porous bodies of needle-like mullite sintered after compacting. Sintering did not effected below 1500°C, and the samples were too brittle to achieve the measurement of physical properties. As shown in Table 1, samples sintered at 1550~1650°C had a porosity of 48~57%, while in the case of 1700°C, advanced densification reduced the porosity to 26%. Nevertheless, pore diameter was almost constant (0.46~0.58 $\mu$ m) regardless of sintering temperature. Figure 2 presents the textures of fracture surfaces of samples sintered at 1650 and 1700°C. The porosity decreased with an increase in sintering temperature, and inside those sintered at 1650°C pores submicron in size were observed between crystals of needle-like mullite as shown in Fig.2(a); the result of this SEM observation almost agreed with pore diameter measured with a mercury porosimeter. Whereas,

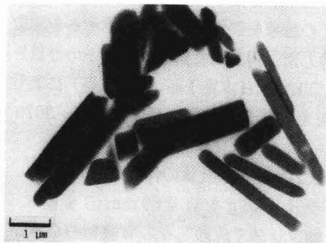


Fig. 1. Morphology of needle-like mullite crystals synthesized by firing New Zealand kaolin at 1650°C.

Table 1. Density and pore characteristic of porous mullite ceramics.

Properties	Sintering temperature (°C)			
	1550	1600	1650	1700
Bulk density (g/cm <sup>3</sup> )	1.37	1.52	1.65	2.32
Relative density (%)	43.6	48.3	52.4	73.5
Porosity (%)	57.4	52.5	48.1	26.1
Pore volume (cc/g)	0.43	0.35	0.29	0.11
Average pore diameter (μm)	0.58	0.53	0.54	0.46

at 1700°C, sintering proceeds as in Fig.2(b) but particles maintain needle shapes. Figure 3 gives the pore size distribution of samples sintered at 1550 and 1700°C. Both pore size distributions are sharp showing that the effect of sintering is low. The main reason is probably that no substantial change occurred in the morphology of particles even after sintering at 1700°C. Moreover, the sum of relative density

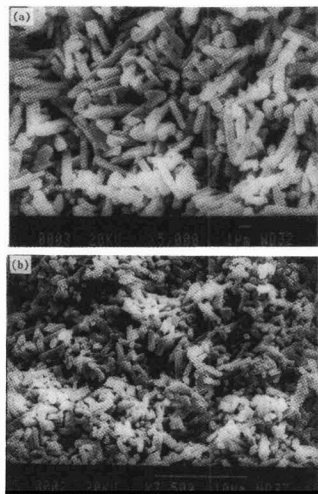


Fig. 2. Fracture surface of porous mullite ceramics sintered at (a) 1650°C and (b) 1700°C.

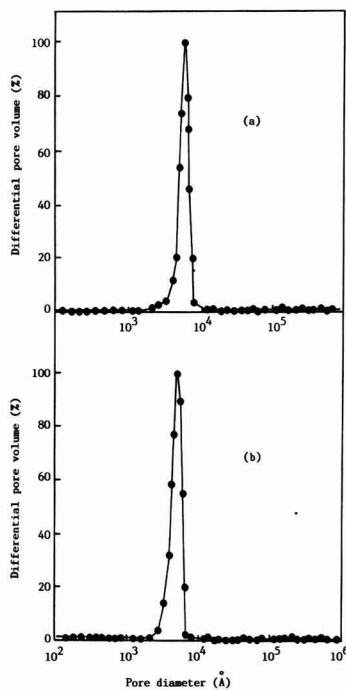


Fig. 3. Pore size distribution of porous mullite ceramics sintered at (a) 1550°C and (b) 1700°C.

of a sample calculated from bulk density and porosity measured with a mercury porosimeter is almost 100%; hence it can be concluded that most of pores in the sample are open pore structure.

3.2. Thermal and Mechanical Properties of Mullite Porous Bodies

Figure 4 shows changes in the coefficients of thermal expansion of porous bodies sintered at 1550-1700°C. The coefficient of thermal expansion by linear approximation up to 1400°C was 4.8-5.0x10^-6/°C, and a difference by sintering temperature was small. In the previous report, a thermal change in the lattice constants of needle-like mullite was determined by high-temperature X-ray diffraction and the coefficients of thermal expansion in the a-, b-, and c-axis direction were 2, 3.9, and 4.5x10^-6/°C(11) respectively. The coefficient of needle-like mullite porous bodies prepared in this study are close to that of a single crystal in the c-axis direction (the direction of crystal growth).

Since mullite is one of the ceramics with relatively low thermal conductivity, needle-like mullite porous bodies having high porosity could be used as insulators. Figure 5 plots the thermal conductivity at room temperature of porous bodies sintered at 1550-1700°C as a function of porosity. The specific heat of porous bodies in vacuum was 0.196-0.201J/°C.g, and no difference was encountered by

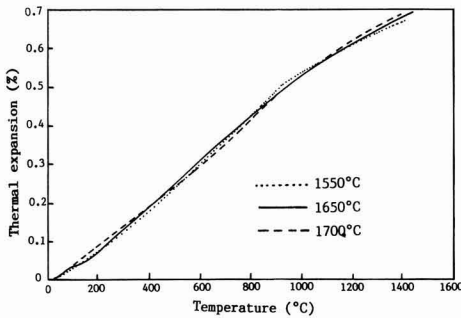


Fig. 4. Thermal expansion curves of porous mullite ceramics sintered at 1550°C, 1650°C and 1700°C.

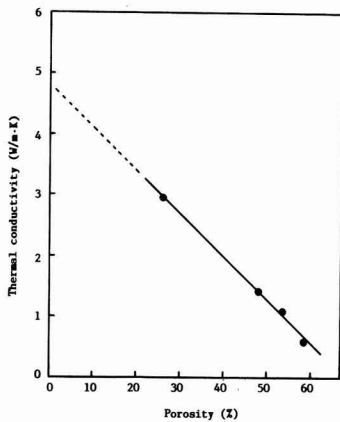


Fig. 5. Effect of porosity on the thermal conductivity of porous mullite ceramics.

sintering temperature. On the other hand, thermal conductivity decreased linearly with an increase in porosity, and reached 0.63W/m.K for a porous body (porosity: 57.4%) sintered at 1550°C. The value is about 1/10 that of commercial dense mullite ceramics, and such a porous texture leads to lower thermal conductivity as is the case with other porous ceramics.<sup>13)</sup>

Generally, the thermal conductivity of porous ceramics decreases with an increase in porosity, and the thermal conductivity (K<sub>m</sub>) of a sample with porosity P in which closed pores are so small as to be negligible is expressed as follows according to Maxwell-Eucken's equation<sup>14,15)</sup>:

$$K_m = K_c(1 - \beta P) \dots \dots \dots (1)$$

where K<sub>c</sub> is thermal conductivity in the case of a porosity of 0%, and β a constant depending on a pore diameter and morphology. In Fig.5, the line was extrapolated to P=0 to obtain K<sub>c</sub>: 4.8W/m.K.

Figure 6 presents 3-point bending strength of porous bodies. Sintering proceeded very little at 1550°C and the strength was less than 10MPa. Densification was notable at 1700°C providing a strength of about 72MPa.

4. Conclusion

In order to study the feasibility of needle-like mullite synthesized from NeW Zealand kaolin as porous ceramics, needle-like mullite 3-5μm long and 0.5-1.0μm thick grown at 1650°C was compacted and sintered to form porous ceramics. The various properties of these porous bodies were examined to obtain the following results.

- 1) The porosity of porous bodies of densely-entangled needle-like mullite decreased with a rise in sintering temperature, and yet samples sintered at 1650°C had a porosity as high as 48.1%. At 1700°C sintering proceeded and the porosity decreased to 26.1%. The pore size distribution of mullite porous bodies obtained at 1550-1700°C was sharp, and the average pore diameter was 0.46-0.58μm.
- 2) The average coefficient of thermal expansion of porous bodies from room temperature to 1400°C was 4.8-5.0x10^-6/°C, close to that of needle-like mullite in the c-axis direction. The thermal conductivity of porous

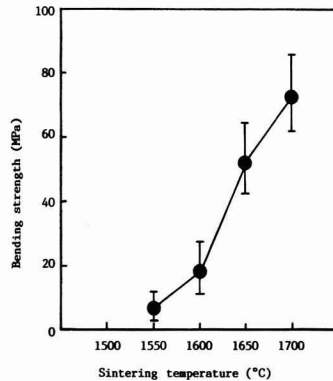


Fig. 6. Three points bending strength of porous mullite ceramics sintered at 1550°C-1700°C.

bodies at room temperature decreased linearly with an increase in porosity, and 0.63W/mK in the case of samples sintered at 1550°C with a porosity of 57.4%. The value was about 1/10 that of commercial dense mullite sintered bodies. The bending strength of needle-like mullite porous bodies increased with sintering temperature to reach 72MPa at 1700°C.

**Note:**

A part of this study was published at First International Congress on Silicate Ceramics (Abstract P.16) held in Nuremberg, West Germany on September 26 and 27, 1989, as well as at 29th Seramikkusu Kiso-kagaku Toronkai (Lecture No. 1D-26) held in Nagaoka, Japan on January 24 and 25, 1991.

**Acknowledgements**

The authors wish to thank Mr. F. Muta of Rigaku Keisoku Co. for his guidance in the measurement of thermal conductivity.

**References:**

- 1) T. Hioki, Seramikkusu, 20, 168-174 (1985).
- 2) N. Yamamoto, Proc. Int. Sympo. on Fine Ceramics Arita'87, (1987) p.87-95.
- 3) S. Sakuhana, Seramkkusu, 23, 702-706 (1988).
- 4) C.E. Baumgartner, J. Am. Ceram. Soc., 73, 516-520 (1990).
- 5) J.F. Zievers, P. Eggerstedt and E.C. Zievers, Am. Ceram. Soc. Bull., 70, 108-111 (1991).
- 6) T. Yasue, Y. Kojima and Y. Arai, Seramikkusu-Ronbunshi, 97, 728-734 (1989).
- 7) G.M. Simon and T.L. Stark, SAE paper, No. 850016, February (1985).
- 8) T. Mihara, S. Kuwano, T. Kusuda, M. Yoneyama, M. Nakamoto and M. Takigawa, *ibid.*, No. 860010, February (1986).
- 9) T. Kusuda, Seramikkusu, 23, 723-726 (1988).
- 10) H. Katsuki, S. Furuta, H. Ichinose and H. Nakao, Seramikkusu-Ronbunshi, 88, 1081-86 (1988).
- 11) H. Katsuki, A. Kawahara, H. Ichinose, S. Furuta and S. Yoshida, *ibid.*, 97, 1521-24 (1989).
- 12) The latest values of thermal conductivity of mullite sintered bodies in Japan are published in Shin-Sozai Series, Mullite 2, ed. by S. Munemiya, Uchida-Rokakuho (1987) in Japanese.
- 13) T. Yamaguchi and H. Yanagida (ed.), Seramikkusu to Netsu, Ceramics Science Series 6, Gihodo Suppan (1987) p.87.
- 14) J. Francl and W.D. Kingery, J. Am. Ceram. Soc., 37, 99-107 (1954).
- 15) K. Hamano, (ed.) Fine Ceramics Handbook, Asakura Shoten (1984) p.567.

---

This article is a full translation of the article which appeared in Nippon Seramikkusu Kyokai Gakujutsu Ronbunshi (Japanese version), Vol.99, No.8, 1991.

# Information & Communications

## News

### Black-Color Substrate of Nitride

Toshiba has developed, for the first time in the world, a black-color substrate of aluminum nitride high, in thermal conductivity and capable of preventing transmission of ultraviolet rays which may damage software. The substrate contains trace amounts of a metallic compound such as titanium sintered under carefully controlled conditions with respect to nitrogen flow and temperature. The metallic compound added is dispersed uniformly in the aluminum nitride crystallites, to absorb light and prevent its transmission, making the substrate black in color. The substrate (thermal conductivity: 180 to 250W/m·K) is more thermally conductive than metallic aluminum, and comparable with the conventional white-color substrate of aluminum nitride in electrical resistance, resistance to pressure and mechanical strength. Ceramic substrates are being produced at a monthly rate of some 200 million yen. Of these, demand for substrates of non-oxide compounds such as aluminum nitride is growing faster than for others at 30 to 50% per year, because of their heat-radiation capacity. The black-color substrate of aluminum nitride, therefore, is expected to increase demand.

### Mass Production of Al Nitride

Toyo Aluminum has started mass production of aluminum nitride which has been attracting attention as a material for IC substrates and automobile structures. Sintered aluminum nitride is mainly characterized by its high electrical insulating capacity and by being comparable with metallic aluminum in thermal conductivity. It is high in heat-radiation capacity, being more than 10 times higher in thermal conductivity than alumina ceramics.

The company's aluminum nitride sinter is prepared by firing powdered aluminum of ten or more microns in size in a nitrogen gas atmosphere. It is expected to find wide use in IC substrates, power transistors and laser-related devices. Moreover, it has a bending strength of 50kg/mm<sup>2</sup>, very close to that of silicon carbide or nitride, which allows application to automobile structures. The company, which started production of sintered aluminum nitride at around 1 ton/mo in 1987, plans to increase the volume to 2.5 tons/mo soon and to 5 tons/mo 1 year later. At present, Tokuyama Soda is leading production of aluminum nitride with its 11 tons/mo plant; Toyo Aluminum plans to expand production to increase its market share.

### High-Quality cBN Membranes

RIMS has succeeded in production of high-quality membranes of cubic boron nitride, using the ion-beam-assisted deposition method. The deposition apparatus the company has developed consists of a vessel kept under vacuum in which argon ion beams are directed towards boron as the target to deposit boron atoms on the substrate; at the same time, nitrogen ions are emitted to allow boron to react with nitrogen over the substrate. The substrate temperature is set at 350°C, to form the cBN film on the glass or silicon substrate at a rate of 2000Å/hr. The apparatus produces large-size films of 10cm<sup>2</sup> or more. The film is spread uniformly over the entire surface of the substrate, as revealed by the electron beam diffraction and infrared spectral analyses.

The new method is more controllable and repeatable than the conventional plasma-aided process. It is expected to expand use of the thin cBN films for iron-base cutting tools difficult to cut and for superhigh-speed semiconductor elements.

### Zinc Oxide Whiskers

Matsushita Amtech has started full-scale mass production of zinc oxide whiskers. The product is a new material of single needle-shape crystals characterized by a three-dimensional structure, derived from the zinc powder massively emitted by Matsushita Sangyo Kiki as waste from its film condenser production lines. These whiskers, being of zinc oxide, have a high specific gravity of 5.78 and other favorable properties such as vibration-controllability, electrical conductivity, wave-absorption capacity and resistance to heat (up to 1730°C). Furthermore, they are low in thermal expansion coefficient, being of an inorganic ceramic.

The whiskers are used as vibration absorbers, after being compounded into resins or metals, for chassis frames in VTR hardware, in external cases for stereo headphones, frames for radio cassettes and vibrators for common speakers. The company established the mass production techniques in 1988, producing the whiskers in a monthly volume of 50 tons, and is now expanding the business from the original scale of supplying them to the Matsushita group.

### Joint R&D for Ceramic Materials

The Industrial Science and Technology Agency's Government Industrial Research Institutes of Osaka, Nagoya and Kyushu plan to start joint programs for the development of fiber-reinforced composite ceramics for high-

temperature use and techniques to assess them in a 3-year plan beginning in 1991. Each institute is proficient at different materials and processes for fiber-reinforced ceramics based on their own techniques.

Osaka is responsible for the development of the whisker-reinforced oxide-base ceramics for high-temperature use, Nagoya for the ceramics reinforced with fibers of organic silicon polymer, and Kyushu for the carbon-carbon composite ceramics for high-temperature use. The fiber-reinforced ceramics prepared will be analyzed for properties such as bending strength, hardness and modulus of elasticity at room temperature and high temperature. Furthermore, they will be brought to the New Materials Technical Center at the Osaka's institute, where they will be injected with ions by an ion accelerator to improve their mechanical properties. This is the first joint R&D program in Japan in high-technological and basic areas.

### Aspiring Fine Ceramic Center

Mr. Masaaki Ohashi, managing director of Toyota Motors, has assumed the second chairmanship of the Fine Ceramic Center (established in 1985 as the nation-wide technical trustee in Nagoya, where the ceramic-related industries are concentrated). The municipal government enthusiastically invited the establishment of the institution in the city. Its business scope covers wide areas, including R&D efforts, commissioned research, training scientists and engineers, and international exchanges and enlightenment in its advanced facilities. "Independent institution" is its motto, and securing stable research funds is one of the greatest problems for the center. A special system was started in 1990 to invite many participants (target: 180 enterprises) as a means of securing funds. So far, 60 enterprises have joined the system. The center will provide these participants with various services such as testing, researching and training. The center is appealing for more support, because its future is totally dependent on the conscientiousness of ceramic-related enterprises.

### Single Crystalline Barium Titanate

Fujikura Ltd. has developed single crystalline barium titanate with the world's highest optical characteristics, having a light amplification factor more than 20% higher than the conventional level. 11.5mm in length and 3.9 × 3.1mm<sup>2</sup> in area, the substance is produced by a new method in which an impurity such as iron or cobalt is doped or the single crystals are thermally treated in a

reducing atmosphere. Increase in crystal size and improved properties are realized simultaneously. The company has also discovered a new phenomenon where light entering the large-size crystal generates optical-path patterns different from the conventional ones. Its phase conjugate wave reflection factor is approximately 30%, which is 15 times as high as that of the conventional one. These characteristics will allow it to find use in compact, practical systems for analyzing light interference. Moreover, the device has a light amplification factor with two lights more than 20% higher than that of the conventional one, and is thus capable of amplifying by 6 times the power of signal-carrying light. This may drastically accelerate the development of optical computers.

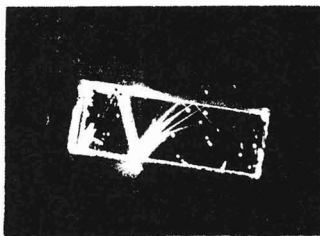


**Photo1.** The newly discovered light-path patterns

### Small-Size Ceramic Heater

The Tokyo Electric Power Co. has developed, jointly with Noritake, small-size ceramic heaters using far-infrared ray which are capable of withstanding a 1100°C surface temperature and consume 40% less power than the conventional Nichrome heater. The newly developed heater, 0.7 to 2.0mm in thickness, is made of a monolithic sinter in which the heating element of lanthanum is sandwiched by thin alumina-base ceramic sheets. It is resistant to 1100°C, with improved surface temperature distribution. Improved fabricability of the ceramic material allows the heater to assume various shapes (such as sheets and rod) and to heat desired spots selectively according to the shape of the object to be heated, thereby greatly diminishing heat loss caused by radiation. The price is around 15,000 yen for a 50×50mm sheet-like heater. The companies have been jointly developing the heaters since 1988 with a total investment of 100 million yen. They expect to attain initial sales of one billion yen by targeting the units for the heating and/or drying of precision device insides and laminated resin films.

### Ceramic Liner

Japan Encera Co., Ltd. has been producing ceramic liners for seven years utilizing the wear-resistant characteristics of fine ceramic materials. They are going into various areas, including those portions exposed to abrasive

atmospheres in pneumatic transportation systems for powder and fine solids, slurry transportation systems and conveyor systems. The company is providing packaged series including ceramic production, installation and maintenance. Three liner types of alumina, silicon nitride and silicon carbide are available at present, to be selected for specific purposes. Each can be adaptable to a pipe of any size and shape above 1 inch. The market, originally steel-making plants, is now expanding to include power generating plants. The company is commanding a share of 70 to 80% of the ceramic liner market for coal transportation and ash-handling systems in coal-fired power plants.

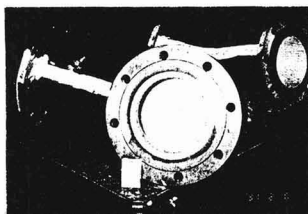


**Photo 1.** Pulverized coal supply pipe for coal burning thermal station

### Stable 4500rpm Flywheel

Mitsubishi Electric Corp. has developed a flywheel of oxide superconductor which rotates at 4500rpm; a faster rotation speed is expected in a vacuum environment. The flywheel has a permanent magnet measuring 65mm in diameter by 20mm thick and weighing 1.1kg, sandwiched by Y system superconductor 75mm in diameter and 5m thick. As mentioned on the facing page, the Superconducting Engineering Laboratory has manufactured a 37.5kg flywheel, which although much larger than that of Mitsubishi operates on the same principle.

### Safe Coil for SC Generator

The Superconducting Power Generation Related Equipment and Material R&D Association has established technology to manufacture superconducting coils which operate safely at cryogenic temperature and high speed. This will allow favorable prospects for the manufacture of 70,000kW superconducting generators. The coils rotate at 3600rpm and cryogenic temperature of 4K; each of them measures 7m long and withstands current of 3000A.

Such coils tend to undergo quench phenomena when current is input rapidly, but this one does not, even when a change ranging from 0 to 20 tesla is impressed in one second, and no quench is generated at rated current of 2400A. With current of 2600A (2400 + 200), the coil caused quench, but when current was reduced to the rated 2400, conditions returned to normal (i.e. no

quench).

### 0.1 T Under 6 T Ext. Magnetic Field

Kobelco, Kobe Steel Co. has succeeded in generation of 0.1 tesla magnetic field in the environment of 6 tesla external magnetic field, while Sumitomo Electric Industry succeeded in generating a magnetic field under 23 tesla magnetic field. The Kobelco record is inferior than that of Sumitomo and the 1.15 tesla of Toshiba and Showa Cable and Wire. However, many companies are now succeeding in generating a magnetic field in high magnetism, which indicates they are making progress in the application of high Tc superconductor to the energy industry.

Kobelco's Jc is 15,000A/cm<sup>2</sup> under 1 tesla, 11,000A/cm<sup>2</sup> under 6 tesla. The company is to carry out experiments under 20 tesla this autumn.

### Facility for SC Power Generator

CRIEPI has completed an experimental facility to test conductors used for superconducting power generators under conditions equivalent to operational ones. With this equipment, CRIEPI is testing conductors to be used for a 70,000kW superconducting generator currently under development as a national R&D project. The experimental facility will be used to test the performance of armature conductors. Conductor performance can not only be tested under ordinary conditions, but also under those of centrifugal force, magnetism, and so on.

### Nuclear Fusion Test Facility

A cryogenic temperature experimental facility (Nuclear Fusion Science Laboratory of the Ministry of Education, Science and Culture) has been completed and is ready to begin test work. The facility, part of the Helical Nuclear Fusion Experimental Facility, will be used for the development of SC coil conductors. The facility includes a large experiment room with floor space of 2650m<sup>2</sup>×13.2m(high), and small experimental, control and clean rooms. Testing equipment is capable of loading 1000t at room temperature and 500t at liquid helium temperature. The apparatus features 1000t rigidity testing equipment which can measure Jc of SC magnets under high intensity magnetic field, and a 75kW DC power source used for measurement of Jc of coils.

Tokamak type experimental facilities are now under development in the world, for which Japan constructed the JT-60. Against the Tokamak type, Kyoto University proposed a helical type nuclear fusion facility. Those who are engaged in the helical type facility are confident regarding the realization of high temperature and density of plasma necessary for nuclear fusion, however they have not yet clearly established how to maintain such high temperature and density of plasma for one second. Yet they expect this problem to be solved by 2001.

### Oblique Crystal Growth

Toshiba has succeeded in development of process technology to grow Bi system superconducting thin film in oblique orientation. Such thin film has 100 times the current density of ordinary (vertically grown) thin film. The technique can be applied for fabrication of JJ (Josephson Junction) elements. When TiOSr crystal substrate is cut obliquely, thin film grows at an angle of 48° against the substrate surface. The process employs MBE (Molecular Beam Epitaxy).

### Niobium-Aluminum Superconductor

Tokai University's Faculty of Engineering has developed a new process for making niobium-aluminum superconductor having a critical magnetic flux density of 30 to 40 tesla. Until now there existed no adequate method to produce wires of niobium-aluminum superconductor, which has a 1.5 to 2 times higher magnetic flux density than metallic superconductor currently being commercialized. The new process is more simple than the conventional one and produces the wires more easily. The research group believes that this may pave the way to the development of superconducting magnets generating flux density of 20 tesla or more for superconductor-driven ships, NMR analyzers and nuclear fusion.

The superconductors presently being used are of niobium-titanium alloy and niobium-3 tin, which generate a magnetic flux density of 11.5 and 20 tesla, respectively. These cannot be made into superstrong magnets generating a flux density above 20 tesla, because they generate lower flux density when made into wires and wound around a magnet.

By contrast, niobium-aluminum superconductor generates much higher flux density, 30 tesla by niobium-3 aluminum and 40 tesla by niobium-3 aluminum-germanium, and is promising as a material for superconductor magnets capable of generating a flux density above 20 tesla.

It is necessary for the conventional method, which depends on direct diffusional reactions between niobium and aluminum, to produce a very thin film (about 0.1μm thick)

of aluminum, which makes it difficult to fabricate the superconductor into wires. Another problem is degraded characteristics resulting from the thin aluminum film, which causes reduced aluminum concentration in the niobium-3 aluminum structure.

The new process uses a niobium-2 aluminum compound as the starting material. This is diffusion-reacted with niobium to produce niobium-3 aluminum compound, in which a mixture of powdered niobium-2 aluminum and niobium is formed into strips and then thermally treated. No thin film of aluminum is required, resulting in no reduction in aluminum concentration.

The niobium-3 aluminum-germanium superconductor produced by the new process has been confirmed to have a critical current density (the largest current available under a superconducting condition) of 500mA/cm<sup>2</sup> or more at 4.2K (approximately -268°C) and a magnetic field flux of 28 tesla. The research group has also formed the niobium-aluminum superconductor into a tape 2m long × 5mm wide × 0.4mm thick, and a multi-core wire containing 7 niobium-aluminum cores.

### Electric Power Storage Flywheel

The Superconductivity Research Laboratory of ISTEC has succeeded in development of a flywheel which stores electric power by means of superconductivity. The prototype system can store 100Wh of electric power.

The rotation unit is an aluminum wheel (30cm in diameter, 3.5cm thick and weighing 37.5kg) containing an Fe/Ne/Br permanent magnet. The stationary unit has Y system superconductor as shown in Fig.1. Through the magnetic levitation effect, the flywheel is suspended 1cm above the superconductor. In experiments, the flywheel rotated at 3600rpm to store 100Wh. When the system operates in a vacuum environment, the flywheel can rotate forever, therefore it can store energy. An experiment demonstrated that the electric power storage device could light an electric lamp. If the flywheel weighs 500kg, such a system could store 10kWh; the Laboratory plans to manufacture such a device. The key technology is how to arrange per-

manent magnets without reduction of magnetism caused by the increase in size of the permanent magnet and large superconducting body.

### 370kVA SC Transformer

The Superconducting Magnet Research Center of Kyushu University has completed a 370kVA superconducting transformer measuring 3.1m high by 1.13m in diameter and weighing 4.5t. NbTi alloy multi-filamentary wire composed of 3 twisted wires of 6 filaments is used. When liquid helium cooled the coil directly, the transformer registered secondary current of 365kVA, though this was only 60% of the target current.

### Switch for SC Circuits

Toshiba, together with Prof. Shioda (Tokyo Institute of Technology) and Showa Electric Cable and Wire Co., has developed a new type of switch which can supply and cut off current during ordinary conduction according to superconducting circuit cooling to permit the flow of superconducting current. The new switch applied Nb<sub>3</sub>Sb multi-filamentary wire instead of the NbTi wire employed in conventional switches. Base material of the new switch wire is copper/nickel alloy. The switch is 60mm in outer diameter and 44mm long; length of the superconducting wire is 55m. Tc is 18k, and Jc at 4k is 2300A/mm<sup>2</sup> under 7 tesla.

### Aspheric Glass Lens Production

Microengineering Co., has jointly with Nakanoume Lens Co., Ltd. and Toyonari Ltd., developed technology for mass production of aspheric glass lenses. As processing is difficult, glass has not been used for aspheric lenses; plastic has been used as material which permits easy processing. In the new process, aspheric lenses are formed roughly prior to polishing with a ceramic mold at 600°C. Error rate of a roughly formed glass lens is 0.1mm for 100mm in radius, therefore the thickness to be removed by polishing is largely reduced.

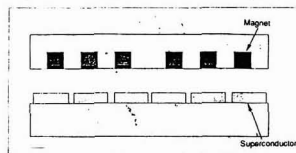


Fig.1. Cross sectional view of flywheel

# Abstracts of Articles on Ceramics from the Selected Journals of the Academic Societies

Japanese Journal of Applied Physics  
Vol.30 No.4 April 1991  
p.639-644

## Bi-Sr-Ca-Cu-O Superconducting Oxides Synthesized from Different Diffusion Couples

Kyoji TACHIKAWA, Takayuki WATANABE, Takayuki INOUE  
and Kenji SHIRASU

*Department of Materials Technology, Faculty of Engineering, Tokai University, Hiratsuka, Kanagawa 259-12*

Thick Bi-Sr-Ca-Cu-O (BSCCO) layers have been synthesized by a reaction diffusion between a Sr-base oxide substrate and a Bi-base oxide coating layer. Effects of the composition of diffusion couples on superconducting properties and structures of resulting reaction layers have been studied. The most favorable diffusion couple to form a uniform 2212 layer was 2001 (Bi<sub>2</sub>CuO<sub>4</sub>) and 0212 (Sr<sub>2</sub>CaCu<sub>2</sub>O<sub>7</sub>). The Pb substitution for Bi in the coating layer produced a thick 2223 layer with no crystal orientation, unlike the 2212 reaction layer which showed a strong a-axis orientation. The Li substitution for Bi significantly enhanced the reaction diffusion, and an offset  $T_c$  of 83 K was obtained after a heat treatment at 800°C for 10 min. A study was also performed on the powder-diffusion process in which powders of a Sr-base oxide and a Bi-base oxide were mixed and sintered.

**KEYWORDS:** BSCCO, reaction diffusion, Pb substitution, Li substitution,  $T_c$ ,  $J_c$ , crystal orientation

Japanese Journal of Applied Physics  
Vol.30 No.4 April 1991  
p.645-649

## X-ray Photoelectron Spectroscopy Study in Bi<sub>2</sub>Sr<sub>2</sub>Ca<sub>1-x</sub>Nd<sub>x</sub>Cu<sub>2</sub>O<sub>8+d</sub>

Hidetoshi YAMANAKA, Hiroyuki ENOMOTO, Jae Soo SHIN,  
Takeshi KISHIMOTO, Yoshiki TAKANO<sup>1</sup>, Natsuki MORI<sup>2</sup>  
and Hajime OZAKI

*Department of Electrical Engineering, Waseda University, Ohkubo 3-4-1, Shinjuku-ku, Tokyo 169*

<sup>1</sup>*Department of Physics, Nihon University, Kanda-Surugadai 1-8, Chiyoda-ku, Tokyo 101*

<sup>2</sup>*Department of Electrical Engineering, Oyama National College of Technology, Nakakuki 771, Oyama 323*

X-ray photoelectron spectroscopy (XPS) measurements were performed in Bi<sub>2</sub>Sr<sub>2</sub>Ca<sub>1-x</sub>Nd<sub>x</sub>Cu<sub>2</sub>O<sub>8+d</sub> (0 ≤ x ≤ 1) in order to investigate the change in the electronic states through the decrease of the holes in this system. The negative chemical shifts of the Cu 2p main peaks were observed, while their satellites did not shift but decreased in areas. These behaviors indicated that the holes at both Cu and O sites decrease with increasing Nd concentration x.

**KEYWORDS:** Bi<sub>2</sub>Sr<sub>2</sub>Ca<sub>1-x</sub>Nd<sub>x</sub>Cu<sub>2</sub>O<sub>8+d</sub>, 2212 phase, hole concentration, XPS, Cu core-level spectra, hole at Cu site, hole at O site

Japanese Journal of Applied Physics  
Vol.30 No.4 April 1991  
p.650-655

## Preparation of Lateral Isolation Structures by Controlling Bi or Ca Compositions in Bi-System Superconducting Films

Tatsuro USUKI, Ichiro YASUI, Yorinobu YOSHISATO  
and Shoichi NAKANO

*Functional Materials Research Center, SANYO Electric Co., Ltd., 1-18-13, Hashiridani, Hirakata, Osaka 573*

Two kinds of monolithic lateral isolation structures have been obtained by controlling Bi or Ca compositions in the lateral direction using a Bi-oxide system for the first time. One is a BiSrCaCuO/SrCaCuO/BiSrCaCuO structure, which was made from a Bi-O/SrCaCuO layer. The other is a BiSrCaCuO/BiSrCuO/BiSrCaCuO structure, which was made from a Ca-F/BiSrCuO layer. Each BiSrCaCuO area is composed of a 2-2-1-2 phase and a 2-2-2-3 phase, with high crystallinity in the c-axis orientation. A SrCaCuO area indicates semi-insulation. The BiSrCuO area showed a flat temperature dependence of resistivity above 25 K and exhibited a resistivity of about 6 mΩ·cm.

**KEYWORDS:** Bi-Sr-Ca-Cu-O high- $T_c$  phase, Sr-Ca-Cu-O, Bi-Sr-Ca-O, rf magnetron sputtering, electron beam deposition, annealing, diffusion, patterning

Japanese Journal of Applied  
Physics  
Vol.30 No.4 April 1991  
p.656-660

### Photo Chemical Vapor Deposition of Metal Oxide Films Relating to Bi-Sr-Ca-Cu-O Superconductor

Hideomi KOINUMA, Kaliq A. CHAUDHARY, Masaaki NAKABAYASHI<sup>1</sup>,  
Tadashi SHIRAIISHI<sup>1</sup>, Takuya HASHIMOTO<sup>2</sup>, Koichi KITAZAWA<sup>2</sup>,  
Yuuichi SUEMUNE<sup>3</sup> and Takakazu YAMAMOTO<sup>4</sup>

*Research Laboratory of Engineering Materials, Tokyo Institute of Technology,  
4259 Nagatsuta, Midori-ku, Yokohama 227*

<sup>1</sup>*Department of Communications, Faculty of Engineering, Tokai University,*

*1117 Kitakaname, Hiratsuka 259-12*

<sup>2</sup>*Department of Industrial Chemistry, Faculty of Engineering, University of Tokyo,  
7-3-1 Hongo, Bunkyo-ku, Tokyo 113*

<sup>3</sup>*Nihon Kagaku Sangyo Co., Ltd., 80 Nakane-cho, Souka, 340*

<sup>4</sup>*Research Laboratory of the Resources Utilization, Tokyo Institute of Technology,  
4259 Nagatsuta, Midori-ku, Yokohama, 227*

Oxide films relating to high- $T_c$  superconducting Bi-Sr-Ca-Cu-O system were prepared by an oxidative photochemical vapor deposition using a low pressure mercury lamp. Bismuth oxide film was prepared by the photo decomposition of  $\text{Bi}(\text{C}_6\text{H}_5)_3$  in the presence of oxygen (20 Torr) at 300°C, while no film was obtained without the UV light irradiation. The UV light irradiation increased X-ray diffraction peak intensities of  $\text{CuO}$ ,  $\text{CaCO}_3$ , and  $\text{SrCO}_3$  films prepared from  $\text{Cu}(\text{dipivaloylmethanate})$ :  $\text{DPM}_2$ ,  $\text{Ca}(\text{DPM})_2$ , and  $\text{Sr}(\text{DPM})_2$ , respectively, at temperatures of 400°C. By simultaneous supply of  $\text{Ca}(\text{DPM})_2$  and  $\text{Cu}(\text{DPM})_2$ ,  $\text{Ca}_2\text{CuO}_3$  crystalline film without  $\text{CaCO}_3$  contamination was formed at 400°C. Without the UV irradiation, amorphous Ca-Cu-O film was obtained by thermal CVD. Photochemical reactions using  $\text{N}_2\text{O}$  and  $\text{NO}_2$  instead of  $\text{O}_2$  were also examined.

**KEYWORDS:** high- $T_c$  superconductor, Bi-Sr-Ca-Cu-O system, photo CVD, oxide film, low temperature growth, Ca-Cu-O

Japanese Journal of Applied  
Physics  
Vol.30 No.4 April 1991  
p.661-664

### Heterodyne Detection of Microwaves Using Granular-Type $\text{Y}_1\text{Ba}_2\text{Cu}_3\text{O}_{7-x}$ Superconductors

Yorinobu YOSHISATO, Akio TAKEOKA, Minoru TAKAI, Kazuya NIKI,  
Shuichi YOSHIKAWA, Toshimasa HIRANO and Shoichi NAKANO

*Functional Materials Research Center, SANYO Electric Co., Ltd.,  
1-18-13 Hashiridani, Hirakata, Osaka 573*

A heterodyne mixing experiment of microwaves at about 20 GHz was performed using a microwave detector made from granular-type  $\text{Y}_1\text{Ba}_2\text{Cu}_3\text{O}_{7-x}$  (YBCO) superconductors. Although the bridge included many boundaries, voltage steps corresponding to the Josephson frequency and step height dependence for microwave power similar to those of a single weak-link bridge were clearly observed. The IF signal showed peak amplitudes corresponding to the peak dynamic resistance due to nonlinearity resulting from the Josephson effect. It was confirmed for the first time that this detector operates stably for the heterodyne mixer at 60 K or below and has a potential for high sensitivity due to its large dynamic resistance.

**KEYWORDS:** YBCO superconductor, microwave detector, granular, Josephson effect, grain boundary, heterodyne mixing

Japanese Journal of Applied  
Physics  
Vol.30 No.4 April 1991  
p.665-666

### Field-Induced Anisotropy in $\text{Bi}_{1.7}\text{Pb}_{0.3}\text{Sr}_2\text{Ca}_2\text{Cu}_3\text{O}_y$ High- $T_c$ Superconductors

Joo-Il LEE, Mun-Seog KIM, Seong-Cho YU, Suhk-Kun OH, Woo-Young LIM<sup>1</sup> and Min-Su CHANG<sup>2</sup>

*Dept. of Physics, Chung-buk National Univ., Cheongju 360-763, Korea*

<sup>1</sup>*Dept. of Physics, Korea Univ., Seoul, 136-701, Korea*

<sup>2</sup>*Dept. of Physics, Pusan National Univ., Pusan 609-735, Korea*

The angular dependence of the magnetization of  $\text{Bi}_{1.7}\text{Pb}_{0.3}\text{Sr}_2\text{Ca}_2\text{Cu}_3\text{O}_y$  was studied by rotating the sample relative to the applied magnetic field. At low fields and at the nitrogen temperature, the irreversible part of the field-cooled magnetization,  $M_{irr}$ , rotates with the sample like a rigid body. Above some angle  $\phi^*$ , the rigid nature of the sample is diminished, and a part of  $M_{irr}$  disappears. This feature is quite similar to what had been observed in  $\text{Y}_1\text{Ba}_2\text{Cu}_3\text{O}_y$  compounds.

**KEYWORDS:** angular dependence, high  $T_c$  superconductor, irreversible magnetization, field-cooled, zero-field-cooled, magnetic anisotropy

Japanese Journal of Applied  
Physics  
Vol.30 No.4A April 1991  
p.L587-L589

### DC Superconducting Quantum Interference Device of $\text{YBa}_2\text{Cu}_3\text{O}_{7-x}$ Step-Edge Junctions

Mitsuyoshi YOSHII, Jun-ichi KITA, Osamu NAKATSU  
and Yasuharu YAMADA

*Central Research Laboratory, Corporate R/D Operations, Shimadzu Corporation,  
1 Nishinokyo-Kuwabaracho, Nakagyo-ku, Kyoto 604*

DC superconducting quantum interference devices (DC-SQUIDS) are made of  $\text{YBa}_2\text{Cu}_3\text{O}_{7-x}$  (YBCO) thin films by conventional photolithography and argon ion milling. The YBCO thin films are prepared on magnesia substrates with step edges by the rf magnetron sputtering method. The step-edge junctions for the SQUIDS exhibit clear DC and AC Josephson effects. The SQUIDS respond well to change of magnetic flux and have a white flux noise at 51.4 K of  $8.1 \times 10^{-5} \Phi_0/\text{Hz}^{1/2}$  at 1 Hz,  $5.8 \times 10^{-5} \Phi_0/\text{Hz}^{1/2}$  at 10 Hz and a noise increase at a low-frequency range of less than 10 Hz.

**KEYWORDS:**  $\text{YBa}_2\text{Cu}_3\text{O}_{7-x}$  thin films, rf magnetron sputtering, DC-SQUID, Josephson effect

Japanese Journal of Applied  
Physics  
Vol.30 No.4A April 1991  
p.L578-L581

### Electron-Irradiation Enhancement of the Critical Magnetization Current in the $\text{Bi}_{1.4}\text{Pb}_{0.6}\text{Sr}_2\text{Ca}_2\text{Cu}_3\text{O}_{10}$ Superconductor

Kensuke SHIRAISHI, Yukio KAZUMATA<sup>1</sup> and Takahiko KATO<sup>2</sup>

*Takasaki Radiation Chemistry Research Establishment, Japan Atomic Energy Research Institute,  
Watanuki-machi, Takasaki, Gunma 370-12*

<sup>1</sup>*Department of Physics, Japan Atomic Energy Research Institute,  
Tokai-mura, Ibaraki 319-11*

<sup>2</sup>*Hitachi Research Laboratory, Hitachi Ltd., Kuji-cho, Hitachi, Ibaraki 319-12*

The  $\text{Bi}_{1.4}\text{Pb}_{0.6}\text{Sr}_2\text{Ca}_2\text{Cu}_3\text{O}_{10}$  ceramic was irradiated with 1 MeV electrons of  $1.1\text{--}27.5 \times 10^{14} \text{ cm}^{-2} \cdot \text{s}^{-1}$  dose rate to a dose of  $1.0 \times 10^{15} \text{ cm}^{-2}$  at ambient temperature, and the magnetization measurements were carried out at 5, 20 and 50 K in magnetic fields up to 5 T. Whereas the magnetization current density at 5 and 20 K was increased by the irradiation, the current density measured at 50 K was decreased in low magnetic fields. The enhancement of 17–25% in the current density at 5 K, which was dependent on dose rate, changed slightly with an increase in strength of the magnetic field.

**KEYWORDS:** superconductor, (Bi, Pb)<sub>2</sub>Sr<sub>2</sub>Ca<sub>2</sub>Cu<sub>3</sub>O<sub>10</sub> ceramic, electron irradiation, magnetization, critical current density

Japanese Journal of Applied  
Physics  
Vol.30 No.4B April 1991  
p.L690-L693

### Study on Annealing Treatment and Sr/Ca Ratio for Pb-Sr-Y-Ca-Cu-O Ceramics with "1212" Structure

Seiji ADACHI, Hideaki ADACHI, Kentaro SETSUNE  
and Kiyotaka WASA

*Central Research Laboratories, Matsushita Electric Industrial Co., Ltd.,  
3-15 Yagumo-Nakamachi, Moriguchi, Osaka 570*

The annealing effects of "1212" lead cuprate in a Pb-Sr-Y-Ca-Cu-O system were investigated. Samples with a nominal composition of  $(\text{Pb}_{0.7}\text{Cu}_{0.3})\text{Sr}_2(\text{Y}_{1-x}\text{Ca}_x)\text{Cu}_2\text{O}_y$  ( $x=0.4\text{--}0.7$ ) were annealed at various temperatures in oxygen. The  $x=0.5$  sample, which was annealed at 800°C and then quenched, exhibited the highest  $T_c$  (zero resistivity) of 48 K. It was found that there were three different types, two tetragonal phases and one orthorhombic phase, in the "1212" of  $x=0.5$ . It was considered that the phase transformation was caused by different oxygen contents. Samples with a nominal composition of  $(\text{Pb}_z\text{Cu}_{1-z})\text{Sr}_{2+z}(\text{Y}_{0.5}\text{Ca}_{0.5-z})\text{Cu}_2\text{O}_y$  ( $z=\pm 0.3$ ) were also prepared. Deviation from  $z=0.0$  in the composition induced degradation of the superconductivity.

**KEYWORDS:** oxide superconductor, high- $T_c$  superconductor, lead cuprate, annealing treatment, 1212 structure, phase transition, Sr/Ca ratio

Japanese Journal of Applied  
Physics  
Vol.30 No.4B April 1991  
p.L697-L699

### Preparation of Superconducting $\text{Bi}_2\text{Sr}_2\text{CaCu}_2\text{O}_x$ Ceramics by Low-Temperature Heat Treatment

Won-Hyuk LEE and Yoshihiro ABE

*Department of Materials Science and Engineering, Nagoya Institute of Technology,  
Gokiso-cho, Showa-ku, Nagoya 466*

Superconducting ceramic rods ( $T_c \approx 80$  K) of  $\text{Bi}_2\text{Sr}_2\text{CaCu}_2\text{O}_x$  were successfully prepared by heat treatment in air at 700°C for 20–50 h; the temperature of 700°C is believed to be the lowest temperature reported so far. The precursor rod specimens were made by vacuum casting the stoichiometric melts into silica tubes; the as-cast rods are spontaneously devitrified during cooling and are composed of crystalline phases of  $\text{Bi}_2\text{Sr}_2\text{CuO}_y$  (2201 phase) and small amounts of  $\text{Cu}_2\text{O}$  and unidentified crystalline phases.

**KEYWORDS:** bismuth-oxide-based superconductor, glass ceramics, low-temperature heat treatment, melt quenching, critical temperature, vacuum casting

Japanese Journal of Applied  
Physics  
Vol.30 No.4B April 1991  
p.L703-L705

### Preparation of BiSrCaCuO Superconducting Thin Film by Microstructure and Microwave Properties of $\text{Tl}_2\text{Ba}_2\text{CaCu}_2\text{O}_8$ Thin Films on $\text{CaNdAlO}_4(001)$

K. H. YOUNG, D. ARNEY, E. J. SMITH  
and D. STROTHER

*Superconductor Technologies Inc., 460-F Ward Drive, Santa Barbara, CA 93111, U.S.A.*

High-quality epitaxial  $\text{Tl}_2\text{Ba}_2\text{CaCu}_2\text{O}_8$  superconducting thin films have been grown on  $\text{CaNdAlO}_4(001)$  substrates by a two step process. Analysis results from secondary ion mass spectroscopy and X-ray energy dispersive spectroscopy of a film annealed at 850°C indicated non-uniform Nd and Ca interdiffusion from the substrate into the film. A second film, annealed at 800°C, exhibited better superconducting properties with a  $T_c$  of 100.7 K, transition width of 2.5 K, and  $J_c$  of  $3.5 \times 10^6 \text{ A/cm}^2$  at 77 K. Microwave measurement at 77 K of a 2.3 GHz microstrip resonator made from the 800°C annealed film on a  $\text{CaNdAlO}_4$  substrate exhibited a low power  $Q$  of 2,100.

**KEYWORDS:** high  $T_c$  superconductor, Tl-Ba-Ca-Cu-O thin film,  $\text{CaNdAlO}_4$ , microstructure, microwave resonator

Japanese Journal of Applied Physics  
 Vol.30 No.4B April 1991  
 p.L728-L731

**Changes of Superconductivity and Crystal Structure on  $\text{Ba}_2\text{YCu}_3\text{O}_{7-x}$  by 1 MeV  $\text{Ar}^+$  Ion Irradiation**

Takayuki TERAI, Tai FURUTA, Tamaki MASEGI,  
 Kazuyuki KUSAGAYA and Yoichi TAKAHASHI

Department of Nuclear Engineering, Faculty of Engineering,  
 University of Tokyo, Hongo, Bunkyo-ku, Tokyo 113

Effects of 1 MeV  $\text{Ar}^+$  ion irradiation on thin films of high- $T_c$  oxide superconductor  $\text{Ba}_2\text{YCu}_3\text{O}_{7-x}$  (BYCO) were investigated in the fluence range between  $1.7 \times 10^{10}$  ions/cm<sup>2</sup> and  $9.9 \times 10^{11}$  ions/cm<sup>2</sup>. Increase of transport critical current density ( $J_c$ ) by irradiation was observed with a fluence below  $1.3 \times 10^{11}$  ions/cm<sup>2</sup>, while the critical temperature ( $T_c$ ) was unchanged in this fluence region. With a fluence above  $3.4 \times 10^{11}$  ions/cm<sup>2</sup>, both  $T_c$  and  $J_c$  decreased with increasing fluence. Regarding the change of the crystal structure, expansion of the c-axis lattice constant and an increase of full width at half maximum (FWHM) value of the peak in X-ray diffraction were observed above a fluence of  $1.0 \times 10^{11}$  ions/cm<sup>2</sup>. These results suggest that the radiation induced defects act as pinning centers in the low fluence region, and they cause the destruction of the crystal structure in the high fluence region.

**KEYWORDS:** superconductor,  $\text{Ba}_2\text{YCu}_3\text{O}_{7-x}$ , thin film,  $\text{Ar}^+$  irradiation, critical current density, critical temperature

Japanese Journal of Applied Physics  
 Vol.30 No.4B April 1991  
 p.L732-L734

**Laser Excitation Effects on Laser Ablated Particles in Fabrication of High  $T_c$  Superconducting Thin Films**

Hiroshi CHIBA, Kouichi MURAKAMI, Osamu ERYU,  
 Kazuhiko SHIHOYAMA<sup>1</sup>, Takayasu MOCHIZUKI<sup>1</sup> and Kohzoh MASUDA

Institute of Materials Science, University of Tsukuba, Tsukuba Academic City, Ibaraki 305  
<sup>1</sup>Center for Optonics Products, HOYA Corporation, Musashino 3-3-1, Akishima, Tokyo 196

Improvement in the characteristics of  $\text{YBa}_2\text{Cu}_3\text{O}_x$  superconducting thin films was performed by a second laser irradiation method. Particles in the laser ablated plume were decomposed and/or excited by the second laser irradiation. By controlling a time delay of the second laser from the ablation laser, ablated particles with average velocities of  $1 \times 10^6$  cm/s and  $2 \times 10^7$  cm/s were irradiated with the second laser. Notable improvement was observed when the slower ablated particles were irradiated with the second laser.

**KEYWORDS:** second laser irradiation effect, laser ablation, high  $T_c$  superconducting thin films,  $\text{YBa}_2\text{Cu}_3\text{O}_x$ , ablated particles

Japanese Journal of Applied Physics  
 Vol.30 No.4B April 1991  
 p.L735-L738

**$^{119}\text{Sn}$ -Mössbauer Study on the Normal Lattice Vibration of Superconducting  $\text{Bi}(\text{Pb})_2\text{Sr}_2\text{Ca}_2\text{Cu}_3\text{Sn}_{0.015}\text{O}_{10-y}$**

Tetsuaki NISHIDA, Motomi KATADA<sup>1</sup>, Norio MIURA<sup>2</sup>,  
 Yuichi DESHIMARU<sup>2</sup>, Tetsuya OTANI<sup>2</sup>, Noboru YAMAZOE<sup>2</sup>,  
 Yasukuni MATSUMOTO<sup>3</sup> and Yoshimasa TAKASHIMA

Department of Chemistry, Faculty of Science, Kyushu University, Hakozaki, Higashiku, Fukuoka 812

<sup>1</sup>Department of Chemistry, Faculty of Science, Tokyo Metropolitan University,  
 Fukasawa, Setagayaku, Tokyo 158

<sup>2</sup>Department of Materials Science and Technology, Graduate School of Engineering Sciences,  
 Kyushu University, Kasuga-shi, Fukuoka 816

<sup>3</sup>Department of Electrical Engineering, Faculty of Engineering, Kinki University in Kyushu,  
 Iizuka, Fukuoka 820

The  $^{119}\text{Sn}$ -Mössbauer spectrum of superconducting  $\text{Bi}(\text{Pb})_2\text{Sr}_2\text{Ca}_2\text{Cu}_3\text{Sn}_{0.015}\text{O}_{10-y}$  ceramic, having the  $T_c$  of 108 K, consists of an intense doublet peak with the  $\delta$  of  $0.18 \text{ mm} \cdot \text{s}^{-1}$  and the  $\Delta$  of  $1.01 \text{ mm} \cdot \text{s}^{-1}$  at room temperature. The  $\delta$  and  $\Delta$  indicate that the  $\text{Sn}^{4+}$  is substituted for the copper ion in the triangular  $\text{CuO}_3$  site of the  $\text{CuO}_4$  layer. The  $\delta$  and the absorption area increase gradually with decreasing temperature and become saturated at about 30 K, being consistent with the theoretical curves obtained from the "combined Debye and Einstein model". Only the normal vibration without the softening is observed in the  $\text{CuO}_4$  layer.

**KEYWORDS:** superconducting  $\text{Bi}(\text{Pb})$ - $\text{Sr}$ - $\text{Ca}$ - $\text{Cu}(\text{Sn})$ - $\text{O}$ , "high- $T_c$  2223 phase",  $^{119}\text{Sn}$ -Mössbauer spectroscopy,  $\text{Sn}^{4+}$  present in the  $\text{CuO}_4$  layer, normal lattice vibration, softening of lattice vibration, "combined Debye and Einstein model", Debye temperature

Bull. Chem. Soc. Jpn.  
Vol.64, 1991  
p.1383-1385

## Reaction between Nitrogen Monoxide and Carbon Monoxide over Superconducting Bi-Sr-Ca-Cu and Related Mixed Oxides

Noritaka MIZUNO,<sup>†</sup> Hisashi TOYAMA,<sup>††</sup> Mika TANAKA, Mika YAMATO,<sup>†††</sup> and Makoto MISONO\*

Department of Synthetic Chemistry, Faculty of Engineering,  
The University of Tokyo, Hongo, Bunkyo-ku, Tokyo 113

**Synopsis.** Bi-Sr-Ca-Cu-O mixed oxides having a Bi<sub>2</sub>Sr<sub>2</sub>CaCu<sub>2</sub>O<sub>7</sub> structure were very active for reactions between nitrogen monoxide and carbon monoxide among the prepared catalysts having perovskite and related structures.

<sup>†</sup> Present address: Catalysis Research Center, Hokkaido University, Sapporo 060.

<sup>††</sup> Present address: Central Research Laboratory, Hitachi Ltd., Kokubunji, Tokyo 185.

<sup>†††</sup> Present address: Asahi Chemical Industry Co., Ltd., Yako, Kawasaki-ku, Kanagawa 210.

Zairyo  
Vol.40 No.451 April 1991  
p.374-378

## Preparation of YBa<sub>2</sub>Cu<sub>3</sub>O<sub>7-x</sub> Superconductor by Sol-Gel Method Using Metal Carboxylates as Starting Materials

Jisun JIN\*, Hiromitsu KOZUKA\* and Sumio SAKKA\*\*

Suppression of the bloating of the Y-Ba-Cu-O metal acetate gels during heating for the conversion of gel-to-superconducting oxide was attempted by three different approaches: the use of metal formates characterized with less numbers of carbon and hydrogen atoms in a molecule than corresponding metal acetates, the vacuum drying of the gel fiber before heating, and the reduction of the rate of heating of the acetate gel. Vigorous bloating was seen in metal formate gels as well in the temperature range where the copper formate complexes were decomposed, and thus the use of metal formates as the starting materials was not effective in suppressing the bloating. The vacuum drying of the gel was not effective either. On the other hand, the reduction in the rate of heating for gel-to-superconductor conversion was effective in suppressing vigorous bloating, leading to the formation of solid ceramic superconducting fibers with  $T_c$  (end) of 86.3 K.

**Key words:** Superconducting oxide, Sol-gel method, Fiber, Formate, Acetate, Thermal decomposition

Zairyo  
Vol.40 No.451 April 1991  
p.385-389

## Grain Growth and Dielectric Properties of SrO-Sm<sub>2</sub>O<sub>3</sub>-Ta<sub>2</sub>O<sub>5</sub> Ceramics

Keisuke KAGEYAMA\* and Mitsuhiro TAKATA\*\*

In order to survey new microwave dielectric resonators, complex perovskite compounds having A(B'<sub>1/2</sub>B''<sub>1/2</sub>)O<sub>3</sub> composition have been investigated. It was reported previously that the dielectric ceramics fabricated from a stoichiometric powder mixture in Sr(Sm<sub>1/2</sub>Ta<sub>1/2</sub>)O<sub>3</sub> composition (SST ceramics) had a high  $Q$  value at microwave frequencies and a negative temperature coefficient, and also reported that long time sintering had considerable effects on the densification, grain growth and the improvement of microwave  $Q$  for SST ceramics.

In this study, HIP'ed SST ceramics were prepared in order to investigate the relation between grain growth and microwave  $Q$  with taking notice of the effect of HIP process on the acceleration of grain growth under certain conditions. The results were summarized as follows:

- (1) Long time sintering was effective to the densification and grain growth of SST ceramics. HIP after long time sintering accelerated the densification and grain growth of SST ceramics.
- (2) The relative dielectric constants of both normally sintered and HIP'ed SST ceramics increased according to the densification of SST ceramics.
- (3) Microwave  $Q$  of HIP'ed SST ceramics was not improved from that of normally sintered ceramics in spite of the increases of density and grain size.

**Key words:** Strontium samarium tantalum oxide, Complex perovskite, Grain growth, Dielectric resonator, Microwave properties

ISIJ International  
Vol.31 No.4 1991  
p.372-378

## Erosion of Ceramic Particle Composite Products for Pipe Transportation

Yoshiyasu MORITA, Hisakazu KAWASHIMA and Manabu SEGUCHI<sup>(1)</sup>

Iron & Steel Research Laboratory, Sumitomo Metal Industries, Ltd., Fuso-cho, Amagasaki, Hyogo-ken, 660 Japan.

<sup>(1)</sup> Sumikin Techno Research, Ltd., Fuso-cho, Amagasaki, Hyogo-ken, 660 Japan.

The erosion of the metal-ceramic particles dispersion composite materials was experimented for the purpose of improving the erosion resistance of the elbow for the transportation line of solid particles. The composite flat plates were made by casting method adding the alumina particles of 3 mm diameter into each matrix. The effects of the impingement particle and the impingement angle on the erosion of the composite were investigated. It was made clear that the erosion ratio of the composite was decreased to a half of the average value of the matrix only. Then, the improvement of the erosion resistance of the trial composite elbow was confirmed.

**KEY WORDS:** composite material; ceramics; erosion; maintenance; mechanical testing; wear.

Zairyo  
Vol.40 No.451 April 1991  
p.431-437

Study on Strength Distribution and Size Effect of  
Ceramics by Computer-Simulated Experiments  
(Continued Report : In the Case that the  
Lower Limit Exists in Strength)

Yoshifumi TANIGUCHI\*, Junichi KITAZUMI\* and Toshiro YAMADA\*\*

Following the previous report, the strength distribution of ceramics was simulated by the Monte-Carlo method for the case in which the lower limit existed in the strength of ceramics. In this study, the tensile strength, 3-point and 4-point bending strengths of specimens of four different sizes were calculated, by using the model specimens with a number of penny-shaped inner cracks. In order to investigate the change of strength distribution of ceramics due to the size effect, the strength obtained was plotted on the Weibull probability paper. It was found that the shape of strength distribution was convex for the specimens of large effective volume, while it was concave for those of small effective volume. The strength distribution function for this model was also expressed and compared with the simulation results. As a result, both distributions showed good agreement in the range of fracture probability greater than a few percents.

Furthermore, the relation between the mean strength and the effective volume was discussed. As the strength of the specimens varied between the lower and upper limits, its relation was represented by a inverse S-shape curve on the logarithmic graph paper.

**Key words :** Ceramics, Strength, Monte-Carlo simulation, Inner crack, Size effect

Zairyo  
Vol.40 No.451 April 1991  
p.438-443

Strength Properties of Structural Ceramics at Elevated Temperatures  
(Relationship between Fracture Toughness and  
Fracture Strength of Smooth Specimen)

Nobushige KOISO\*

Flexural strength tests and fracture toughness tests on two kinds of ceramics (silicon nitride and silicon carbide) were carried out by four-point bending at room temperature and elevated temperatures. The fracture toughness was measured by using the chevron-notched specimens and by using the controlled surface flaw specimens which have a semi-circular surface crack induced by a knoop indenter.

Furthermore, the fracture toughness of smooth specimen was evaluated by using  $\sqrt{\text{area}}$ , which is the square root of the area of the defect projected to the direction of the principal stress. These results were discussed in comparison with the fracture toughness values obtained by the chevron-notched specimens and the controlled surface flaw specimens.

The results obtained are as follows :

- (1) The fracture toughness values depended on the method of measurement. The values of silicon nitride and silicon carbide obtained from the chevron-notched specimens were higher than those obtained from the controlled surface flaw specimens at elevated temperatures.
- (2) The fracture toughness values of silicon nitride obtained from the controlled surface flaw specimens decreased rapidly when the temperature exceeded 1000°C. It was clear that its rapid decrease was caused by slow crack growth.
- (3) The fracture toughness values of silicon carbide obtained from the controlled surface flaw specimens were influenced by the healing of crack at about 1200°C.
- (4) The temperature dependency of the fracture toughness value of silicon nitride obtained from the smooth specimens coincided with that of the fracture toughness obtained from the controlled surface flaw specimens.

**Key words :** Structural ceramics, Elevated temperatures, Flexural strength, Knoop-indented specimen, Chevron-notched specimen, Fracture toughness, Equivalent crack length

Journal of The Japan Institute  
of Metals  
Vol.4 No.4 1991  
p.466-471

Evaluation of Thermal Shock Fracture Resistance of Ceramics  
by Quenching-Small Punch (SP) Test

Jing-Feng Li\*, Akira Kawasaki\*\*,  
Zi-Zhang Xie\*\*\* and Ryuzo Watanabe\*\*

A simple test method using small sized specimens is often required for the effective development of ceramic materials. In the present work, the Modified Small Punch (MSP) test was employed for evaluating the thermal shock resistance of  $Y_2O_3-ZrO_2$  and SiC ceramics.

The change in strength after quenching from various temperatures was evaluated accurately by the MSP test. The load vs. deflection curves obtained by the MSP test provided more detailed information about the thermal shock by quenching. It has been found that the measured values of the critical temperature difference which indicates the thermal shock resistance of the ceramics are in good agreement with the theoretically calculated values for the materials investigated in the present work. The results show that the combination of water quenching and MSP test is effective for the evaluation of thermal shock resistance of ceramics.

**Keywords:** material evaluation, thermal shock resistance, quenching, small punch test, zirconia, silicon carbide

Journal of The Japan Institute  
of Metals  
Vol.4 No.4 1991  
p.472-480

Microstructure and Superconducting Properties of Nb<sub>3</sub>Al Multifilamentary Wires  
Processed by Nb-Tube Method\*

Takao Takeuchi\*\*, Michio Kosuge\*\*, Yasuo Iijima\*\*,  
Akira Hasegawa\*\*, Tsukasa Kiyoshi\*\*,  
Fumiaki Matsumoto\*\* and Kiyoshi Inoue\*\*

Microstructure of Nb tube processed Nb<sub>3</sub>Al multifilamentary wires was studied by an X-ray diffractometer, a transmission electron microscope, etc., and its effect on superconducting properties was discussed from the viewpoint of Al-core sizes, heat treatments and additive elements. Samples with various Al-core diameters were prepared by arranging the filament numbers and final composite diameters. With decreasing Al-core sizes, the volume ratio of A15 phase to other intermediate phase increased, but the lattice parameter of A15 phase decreased conversely. This was accompanied by an increase in  $T_c$  and  $H_{c2}$  (4.2 K), suggesting that the small diffusion spacing between Nb and Al, which was realized by reducing the Al-core size, facilitates to form the metastable A15 phase with the composition near stoichiometry. However, both the  $n$  value of voltage-current characteristics and its magnetic field dependence were remarkably decreased when the Nb/Al composite was heavily cold-drawn into Al-core sizes below 50 nm, suggesting that the Al filament "sausaging" caused by heavy cold-drawing is one of the reasons for degradation in superconducting properties at small Al-core sizes. TEM microstructures were in good agreement with reported ones of Nb/Al multilayer thin films. Alloying Al-cores, which are essential to improve the workability of Nb/Al composites, influences the superconducting properties through the diffusion reaction. Additive elements of Ag and Mg facilitate the formation of the A15 phase with excellent superconducting properties at a low reaction temperature (below 1200 K). They enable the Nb/Al composite to be used for alternating current (ac) superconductors, since ac conductors consisting of resistive Cu alloy matrix must be heat treated below 1200 K. On the other hand, the addition of Cu, which depresses the A15 phase formation rate, is suitable for the high-field superconductors, since it makes it easy to control the high temperature heat treatments for short periods.

**Keywords:** multifilamentary superconductor, Nb<sub>3</sub>Al, diffusion spacing, additive element, X-ray, transmission electron microscopy, critical temperature, critical current density

Journal of The Physical Society  
of Japan  
Vol.60 No.4 April 1991  
p.1185-1188

### Two-Dimensional Weak Localization in Electron High- $T_c$ Superconductor Nd<sub>2-x</sub>Ce<sub>x</sub>CuO<sub>7</sub> under High Magnetic Field

Yoshikazu HIDAKA, Yukimichi TAJIMA, Kiyohiro SUGIYAMA,<sup>†</sup>  
Futoshi TOMIYAMA,<sup>†</sup> Akio YAMAGISHI,<sup>††</sup> Muneyuki DATE<sup>†</sup>  
and Makoto HIKITA<sup>††,\*</sup>

*NTT Applied Electronics Laboratories, 162 Tokai, Ibaraki 319-11*

*<sup>†</sup>Department of Physics, Faculty of Science, Osaka University,*

*Toyonaka, Osaka 560*

*<sup>††</sup>Research Center for Extreme Materials, Osaka University,  
Toyonaka, Osaka 560*

Electron high- $T_c$  superconductor Nd<sub>2-x</sub>Ce<sub>x</sub>CuO<sub>7</sub> single crystals are studied under high magnetic field of up to 20 tesla. The superconducting state is completely destroyed by the field when the field is applied along the  $c$ -axis and the normal electrical resistivity is obtained at all temperatures. The temperature dependence of the normal resistivity is plotted down to 1.3 K and a clear resistance minimum is found. The result is understood in terms of the two-dimensional weak localization model and this means that the materials are regarded as the intrinsic two-dimensional conduction system.

[ high- $T_c$  superconductor, high magnetic field, normal resistivity,  $\ln T$  dependence, two-dimensional weak localization ]

Journal of The Physical Society  
of Japan  
Vol.60 No.4 April 1991  
p.1189-1192

### Effect of Oxygen Deficiency on the Compressibility of High- $T_c$ Superconductor YBa<sub>2</sub>Cu<sub>3</sub>O<sub>7- $\delta$</sub>

Kazufumi SUENAGA and Gendo OOMI

*Department of Physics, Faculty of General Education,  
Kumamoto University, Kumamoto 860*

The effect of pressure on the lattice constant and crystal structure of YBa<sub>2</sub>Cu<sub>3</sub>O<sub>7- $\delta$</sub>  (YBCO) has been studied up to about 120 kbar at room temperature in the wide range of  $\delta$ ,  $0 < \delta < 1$ . It is found that the lattice compression of all samples is anisotropic, and the volume compressibility of superconducting YBCO increases with  $\delta$ , having a peak near the orthorhombic-tetragonal phase boundary  $\delta = 0.8$ .

[ high- $T_c$  superconductors, crystal structure ]

## Bibliographic Information

1. Title	Journal of Ceramic Society of Japan, International Edition	ISSN : 0912-9200
2. Frequency	Monthly	1 volume per year (No.1 Jan. - No.12 Dec.)
3. Volume No.	100	
4. Cover data of (Vol. 95, No1)	January 1987	Vol.95 No.1 is the first Issue of English version
5. Index of contents	Given annually	bound in
6. Size	21cm×29.7cm	1700 pages per annum
7. Subscription rates (Air speed)	¥200,000	(12 issues)

### ORDER FORM

To: Circulation Div., the Journal of  
Ceramic Society of Japan, Inter-  
national Edition  
c/o Fuji Technology Press Ltd.  
Daini Bunsei Bldg., 1-11-7 Toranomon  
Minato-ku, Tokyo 105, Japan

Date: \_\_\_\_\_

Please enter my subscription to the **Journal of Ceramic Society of Japan, International Edition**  
(for \_\_\_\_\_ copy/ies)

Name: \_\_\_\_\_  
Position: \_\_\_\_\_  
Address: \_\_\_\_\_  
Signature: \_\_\_\_\_

Payment enclosed  Bill me  
(Payment by credit card is preferred) Air speed ¥200,000

Attention: Please indicate our ref. No.(AUTO, TEC, TECJ, CER, ROB, ...) when you make the remittance.  
All subscriptions can be paid in advance through any of the following methods.

- 1) Charge my:  
 AmEx  Visa  MC  
 Card No. . . . . Exp. Date . . . . .  
 Mr/Mrs./Ms. . . . .  
 Address . . . . . City . . . . .  
 Zip code . . . . . Country . . . . .
- 2) Transfer to Fuji Technology Press Ltd      A/C No.10667 Fuji Bank Toranomon Branch, Minato-ku Tokyo
- 3) Bank Draft
- 4) Transfer to Fuji Gijyutsu Shuppan K.K.(Fuji Technology Press Ltd.) A/C No. Tokyo 7-145130, Postal Saving

### Attention!!

**You are now able to make remittance by credit card!**  
**You can enter subscriptions with only your name, card number and its  
 expiry date. No bank charge nor preparation of Japanese yen bank  
 draft is necessary.**



